Institut de physique
Université de Neuchâtel

Quantum cascade Lasers at terahertz frequencies

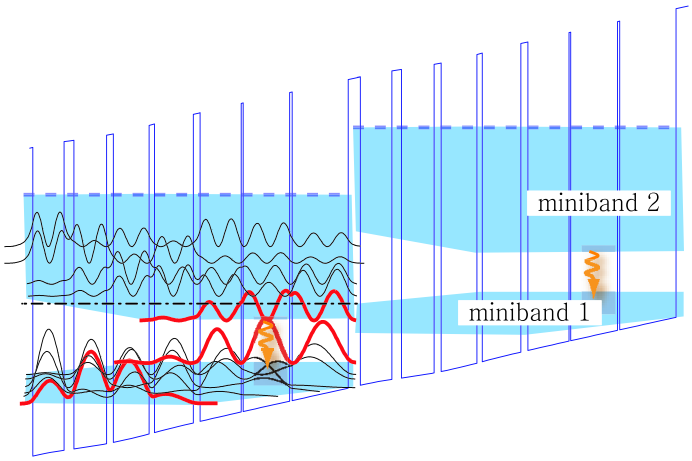

THESE

présentée à la Faculté des Sciences
de l'Université de Neuchâtel en vue d'obtenir le grade de

DOCTEUR EN SCIENCES

Lassaad Ajili

Soutenue le 25 Avril 2007 en présence d'un jury composé de
Prof. Jérôme Faist, Directeur de thèse, Université de Neuchâtel
Prof. Daniel Hofstetter, Université de Neuchâtel
Dr. Hideaki Page, Teraview, Cambridge, U.K

Neuchâtel, Avril 2007

Université de Neuchâtel

FACULTE DES SCIENCES
Secrétariat-Décanat de la faculté
- Rue Emile-Argand 11
- CP 158
- CH-2009 Neuchâtel

IMPRIMATUR POUR LA THESE

Quantum Cascade Lasers at Terahertz Frequencies

Lassaad AJILI

UNIVERSITE DE NEUCHATEL

FACULTE DES SCIENCES

La Faculté des sciences de l'Université de Neuchâtel,
sur le rapport des membres du jury

MM. J. Faist (directeur de thèse),
D. Hofstetter et H. Page (Cambridge UK)

autorise l'impression de la présente thèse.

Neuchâtel, le 4 juin 2007

Le doyen :
T. Ward

UNIVERSITE DE NEUCHATEL
FACULTE DES SCIENCES
Secrétariat-décanat de la faculté
Rue Emile-Argand 11 - CP 158
CH-2009 Neuchâtel

À la mémoire de mon père,

À ma mère et mon frère,

Keywords

Semiconductor heterostructures, intersubband transitions, quantum cascade lasers, Terahertz.

Mots clés

Hétérostructures semiconductrices, transitions intersousbandes, lasers à cascade quantique, Térahertz.

Abstract

The thesis which I have pleasure to present you is the fruit of the research work during four years in the laboratory of mesoscopic physic located at the institute of physics of neuchâtel. The extraordinary progress realized at the end of the seventy years, in the control of the growth, atomic layer by atomic layer, of semiconductor heterostructures have developed a true quantum engineering of the components. A new generation of devices called quantum cascade laser was developed putting at a profit these quantum effects to design laser devices innovents. Contrary to the diode lasers (semiconductors inter-band lasers), these new lasers involving only one type of carriers, the electrons (where unipolar appellation), and the emission can be tuned in the Mid and Far-infrared region simply by varying the thickness or the composition of the quantum wells. Today , the quantum cascade lasers seem to be one of the most promising ways to realize coherent sources in a solid state, emitting in the infrared range i.e., in the frequential band extending between 300 GHz and 30 THz. However, currently the Far-infrared remains difficult to reach and for this reason an intense activity of research concentrates on the QCL emitting in this spectral region. The Far-infrared is particularly interesting, because many physical phenomena have a characteristic frequencies in this spectral region.

The objective of this work was to achieve and to develop QCL's emetting at terahertz frequenties (Far-infrared). Laser action requires both an active region and a low loss resonnator in the considered spectral region. A single plasmon waveguide, where a semi-insulated GaAs substrate is used as lower cladding was designed to achieve low losses. With an optimisation of processing, this concept allowed to reduce notably the waveguide losses (1.2 cm^{-1}) and to achieve the first continuous wave operation of terahertz QCL's (4.6 THz). Many active region

designs were proposed and allowed an increase of the performances. These structures have been experimentally characterized, which yield valuable information about the transport and optical properties of terahertz devices. The highest operating temperatures are achieved by designs based on LO-phonon scattering and single surface plasmon. Additionally, the first terahertz QCLs have been demonstrated that use $In_{0.52}Al_{0.48}As$-$In_{0.53}Ga_{0.47}As$/InP material system, where the optical waveguide exploits a combination of metallic and dielectric confinement. Various fabrication methods have been developed, including a distributed-feedback QCL emetting around 87 μm.

Résumé

La thèse que j'ai le plaisir de vous présenter est le fruit du travail de recherche pendant 4 ans dans le laboratoire de physique mésoscopique situé à l'institut de physique de neuchâtel. Les extraordinaires progrès réalisés dès la fin des années soissante-dix dans la maîtrise de la croissance, couche atomique par couche atomique, d'hétérostructures semiconductrices ont dévéloppé une véritable ingénierie quantique des composants. Une nouvelle génération de dispositifs appelé laser à cascade quantique a été développée mettant à profit ces effets quantiques pour concevoir des dispositifs laser innovents. Contrairement aux diodes lasers (Lasers semi-conducteurs inter-bandes), ces nouveaux lasers n'impliquent qu'un seul type de porteurs de charge, les électrons (d'où l'appellation unipolaire), et l' emission peut être accordée dans tout le domaine moyen et lointain infrarouge simplement en changeant l'épaisseur ou la composition des puits quantiques. Les lasers à cascade quantique semblent être aujourd'hui une des voies les plus prometteuses pour réaliser des sources cohérantes à l'état solide émettant dans le domaine infrarouge i.e., dans la plage fréquentielle s'étendant entre 300 GHz et 30 THz. Cependant, actuellement l'infrarouge lointain reste difficilement accessible et c'est pour cette raison qu'une intense activité de recherche se concentre sur les LCQ rayonnant dans cette région spectrale. L'infrarouge lointain est particulièrement intéressant, car de nombreux phénomènes physiques ont des fréquences caractéristiques dans cette région spectrale.

L'objectif de ce travail était la réalisation et le développement des lasers à cascades quantiqes emettant aux fréquences terahertz (infrarouge lointain). Afin d'obtenir un effet laser, il est nécessaire d'avoir un milieu amplificateur avec un gain suffisant (Phénomènes complexes, surtout au THz) et un résonateur avec de faibles pertes. Un guide d'onde simple

plasmon utilisant un substrat GaAs semi-isolant a été utilisé pour obtenir des pertes de guide faibles. Avec une optimisation de procesing, ce concept a permis de réduire notablement les pertes (1.2 cm^{-1}) et d'accomplir le premier laser à CQ fonctionnant en régime continue aux fréquences terahertz (4.6 THz). Plusieurs regions actives ont été proposé et ont permis d'améliorer les performences des laser à CQ. Ceux structures ont été caractérisé expérimentalement, et ils ont accédé à des informations précieux sur le transport et les propriétées optiques des échantillons emettant dans la région terahertz. Les plus haute températures de fonctionnement sont accomplis par les structures basées sur l'extraction par emission des phonons optiques longitudinaux et un guide d'onde simple plasmon. De plus, le premier LCQ aux fréquences terahertz utilisant une alternance de couches $In_{0.52}Al_{0.48}As$-$In_{0.53}Ga_{0.47}As$/InP ont été démontré, òu le guide d'onde optique exploite une combinaison de confinement métallique et dielectrique. Plusieurs méthode de fabrications ont été développé, y compris un laser à CQ à contre-réaction répartie emettant autour de 87 μm.

Contents

Abstract **3**

Résumé **5**

List of figures **11**

1 Introduction **1**
1.1 Historical overview . . . 1
1.2 Terahertz sources and their applications . . . 3
1.2.1 Terahertz sources . . . 5
1.2.2 Direct generation . . . 6
Diodes . . . 6
Transistor . . . 8
Semiconductor laser . . . 8
Tubes . . . 10
Gas laser . . . 10
1.2.3 Indirect generation . . . 11
Harmonics generation . . . 11
1.3 Terahertz applications . . . 12
1.3.1 gas spectroscopy . . . 12
1.3.2 THz imaging and tomography . . . 14
1.3.3 Telecommunication . . . 17
1.4 Thesis overview . . . 18

2 Intersubband transitions and quantum cascade lasers **19**
2.0.1 semiconducting heterostructures . . . 19
2.0.2 Electronics states in heterostructures . . . 20
2.0.3 effective mass . . . 26
2.1 Optical properties of heterostructures . . . 28
2.1.1 Radiatives transitions . . . 29
2.1.2 Oscillator strength . . . 31
2.1.3 Non-radiatives transitions . . . 32
2.1.4 Resonant tunneling transport . . . 36
2.2 Quantum cascade lasers . . . 39

2.2.1 basic properties . . . 41
Optical gain . . . 41
Threshold current . . . 43
Losses . . . 43
Slope efficiency . . . 45
2.3 Terahertz quantum cascade lasers . . . 46
2.3.1 The various proposed structures of terahertz QCL . . . 47
Chirped-superlattice . . . 49
Bound-to-continuum transition . . . 50
Structure based on a resonant phonon extraction . . . 51
2.4 Waveguide design . . . 52
2.4.1 Mid-infrared waveguides . . . 55
2.4.2 Drude model . . . 59
2.4.3 Terahertz-waveguide . . . 60
2.4.4 Distributed feedback quantum cascade lasers . . . 65
Mid-infrared QC-DFB lasers . . . 66
Single-mode tuning of distributed feedback lasers . . . 69

3 Experimental Setup and Fabrication 71
3.1 Experimental setup . . . 71
3.1.1 Spectral measurements . . . 71
3.1.2 Terahertz detectors . . . 74
3.2 Fabrication . . . 77
3.2.1 FP Fir-processing . . . 77
3.2.2 DFB Fir-processing . . . 81

4 First generation of terahertz quantum cascade lasers structures 83
4.1 Introduction . . . 83
4.2 Chirped superlattice active region . . . 83
4.3 Experimentals results . . . 85
4.3.1 Optimisation of the processing . . . 85
4.3.2 Low-threshold quantum cascade laser at $\lambda = 65\ \mu$m . . . 91
4.3.3 Continuous wave operation at $\lambda = 65\ \mu$m . . . 93
4.3.4 Spectral measurements . . . 94
4.3.5 Losses . . . 96

5 Second generation of terahertz QCL's structures. 97
5.1 Introduction. . . . 97
5.2 High power terahertz QCL's . . . 98
5.2.1 Lasers based on a bound-to-continuum transition emitting at $\lambda \simeq 87\,\mu$m . . . 98
Laser design and characterization . . . 98
Lifetimes and slope effeciency . . . 105

5.2.2 Lasers based on a bound-to-continuum transition emitting at $\lambda \simeq 130\,\mu$m . . . 111
Laser design and characterization . . . 111
Spectral measurements . . . 117
5.3 Doping in terahertz GaAs/AlGaAs quantum cascade lasers . . . 119
5.3.1 Samples preparations . . . 119
5.3.2 Doping characterisations . . . 121
5.3.3 Waveguide losses . . . 124
5.3.4 Threshold current and spectra vs temperature measurements . . . 127
5.4 Growth requirements . . . 129

6 Third generation of THz QCL's. 133
6.1 Introduction. . . . 133
6.2 Design and operation of GaAs/AlGaAs QCL's . . . 134
6.3 Experimental results . . . 135
6.3.1 Samples N464 . . . 136
6.3.2 Samples N465 . . . 139
6.3.3 Comparison . . . 141

7 Distributed feedback terahertz quantum cascade lasers. 149
7.1 Introduction. . . . 149
7.2 Loss-coupled distributed feedback far-infrared Quantum Cascade lasers. . . . 150
7.2.1 spectra as a function of grating period. . . . 150
7.2.2 Liiv curves. . . . 151
7.2.3 Lasing spectra . . . 152
7.3 Continuous wave operation of distributed feedback terahertz quantum cascade lasers. . . . 153
7.3.1 Optical measurements . . . 154
7.3.2 far-field measurements . . . 160

8 InGaAs-AlInAs/InP terahertz quantum cascade laser. 165
8.1 Introduction. . . . 165
8.2 Waveguide design. . . . 166
8.3 Stucture based on a Bound-to-cntinuum transition with optical phonon extraction. . . . 169
8.4 Samples processing. . . . 170
8.5 Experimental measurements. . . . 171
8.5.1 Optical spectra. . . . 171
8.5.2 Liiv curves. . . . 173
8.5.3 Waveguide losses. . . . 174

9 Conclusion. 177

Acknowledgements 181

Bibliography **183**

Appendix **195**

A Samples parameters **195**

Published work **197**

List of Figures

1.1 Schematic timeline of significant QC-laser developments. 2
1.2 Position of terahertz spectrum. 4
1.3 Performance of some CW sources in the sub-millimeter wave range. 5
1.4 Radiated energy versus wavelength showing 30-K blackbody, typical interstellar dust, and key molecular line emissions in the submillimeter. 13
1.5 T-ray computed tomography image of two plastic cylinders. 15
1.6 THz image of an onion cell membrane. 16

2.1 Semiconductor of type I. 20
2.2 schematic representation of the Bloch wavefunction with fast variation modulated with the envelope wavefunctions slowly varying at this shells. 21
2.3 Schematic representation of the subband energies as a function of the in-plane wavevector $k_\perp$, for potential barriers E_c. 25
2.4 Energy of the first two subband energies as a function of the in-plane wavevector $k_\perp$. The right arrow represents the non-radiatively relaxation assisted by the optical phonon emission, the arrow corrugated corresponds to photons emission. 28
2.5 Schematic representation of the effective mass variation of electrons as a fuction of the gap energy of semiconductor with direct gap. 32
2.6 Schematic view of important intersubband scattering mechanisms for narrow (a) and wide (b) quantum wells, where the energy separation E_{fi} is larger or smaller than the optical phonon energy $E_{LO} = \hbar\omega_{LO}$, respectively. 35
2.7 Kazarinov and Suris's superlattice 37
2.8 Quantum cascade design philosophy: each repeated period consists of an active (gain) region followed by a relaxation/injection region. 39
2.9 A simpliefed dynamic diagram of population in quantum cascade laser, three level model of the active region is used where n=3 and n=2 are the upper and lower states of the laser transition, respectively. The ground state n=2 is depopulated through a sequential tunneling to the relaxation/injection region of the structure. 42
2.10 Schematic diagrams of successful terahertz QCL active regions. 48
2.11 a) Waveguide geometry of wave plane. b) Wveguide ridge in quantum cascade laser. 52
2.12 Mode intensity of dielectric Waveguide of quantum cascade laser. 56
2.13 Mode intensity of single (a) and double (b) surface plasmon Waveguide of quantum cascade laser. 61
2.14 single plasmon quantum cascade laser Waveguide 63

2.15 Refractive index and optical mode intensity as a function of distance of the far-IR waveguides used in this study. Both are formed with the same core, consisting successively, from the surface, of a 80 nm thick heavily doped ($n = 5 \times 10^{18}\,\mathrm{cm}^{-3}$) GaAs contact layer, an undoped, 10 nm thick $Al_{0.15}Ga_{0.85}As$ layer, an undoped 320 nm thick $Al_xGa_{(1-x)}As$ ($x : 0.15 \rightarrow 0$) parabolic grating, 120 periods of the active region, a bottom 320 nm thick $Al_xGa_{(1-x)}As$ ($x : 0 \rightarrow 0.15$) parabolic grating, and an undoped, 15 nm thick $Al_{0.15}Ga_{0.85}As$ layer. a) Double plasmon waveguide. The core is grown on a 1 μm thick heavily doped ($n = 5 \times 10^{18}\,\mathrm{cm}^{-3}$) GaAs contact layer, on top of the heavily doped ($n = 2 \times 10^{18}\,\mathrm{cm}^{-3}$) GaAs substrate. b) Single plasmon waveguide. The core is grown on a 300 nm thick, $n = 2 \times 10^{18}\,\mathrm{cm}^{-3}$ GaAs buried contact layer on top of an undoped GaAs substrate. 64

3.1 Experimental setup. 72
3.2 Blackbody spectra taken using Si bolometer 75
3.3 Schematic of the sample processing. The dashed line is the optical mode intensity in the transverse direction. 77
3.4 Schematic of the sample processing. The dashed line is the optical mode intensity in the transverse direction. 79
3.5 Schematic of the sample processing with isolation layer. 80
3.6 Schematic of the sample processing with isolation layer. 81

4.1 Chirped superlattice structure. 84
4.2 Schematic of the front facet coated. 86
4.3 (a) Laser spectrum at a 0.25 % duty cycle for a 210 μm-wide, 2.2-mm-long device. (b) V-I and L-I characteristics for the laser with 2 facets coated as a function of temperature. Operation up to 30 K is observed. 87
4.4 Peak optical output power versus injected current in pulsed mode at a duty cycle of $5 \cdot 10^{-5}$ at various temperatures, as indicated. 88
4.5 The simulations of the ratio Γ/α of the overlap factor and the waveguide losses have been performed for a far-infrared radiation at $65\mu m$ and assuming zero losses in the semi-insulating GaAs. 89
4.6 Computed transverse mode profile of 100 μm-wide, 13 μm-high ridge structure and a substrate thickness of 250 μm for an identical active region and waveguide. The distance separation between the lateral alloyed ohmic contacts and the edge of the ridge are 15 (left) and 45 μm (rigth). 90
4.7 Liiv curves. 91
4.8 Liiv curves. 92
4.9 Liiv curves in CW. 93
4.10 CW spectra as a function of injection current and temperature. 94
4.11 Peak position of CW spectra as a function of injection current and temperature. . . 95
4.12 The threshold current density versus reciprocal cavity length. 96

5.1 structure based on a bound-to-cntinuum transition emitting at $\lambda \simeq 87\,\mu$m. 99
5.2 Diagram of cone used for radiation emission measurements. Radiation originating within the smaller aperture will emerge with an angle of divergence $\theta < \theta_{max}$. 100
5.3 Peak optical output power versus injected current. 101

5.4 The pulsed threshold current density as a function of inverse laser length with backfacet coating measured at 10 K. 102
5.5 Optical output power versus injected current in CW operation. 103
5.6 Bias voltage as a function of injection current density and differential resistance deduced from the V-I curve of the A2986 (continuous line) and A2771 (dashed line) samples. 104
5.7 An approximative geometry model of the sample is used to determine the relation between V_{app}, V_{AR} and the residual series resistance of the buried contact layer. . . 107
5.8 Bias voltage as a function of injection current for applied and extrapolated voltages. 108
5.9 Bias voltage as a function of injection current density for applied and extrapolated voltages. 109
5.10 Spectra recorded at 10 K under continuous operation at six different injection currents. At low current levels the laser emits on a multimode; passing a certain threshold additional serie of modes appear in the spectra. 111
5.11 Computed conduction band profile at T=40 K of one stage of the structure (130 μm) under an average applied electric field of 2.55 kV/cm. The optical transition occurs between level n = 8, isolated in the minigap, and the state n = 6 of the lower miniband. 112
5.12 Light-current characteristics at different temperatures as measured from a 3-mm-long and 430μm-wide laser stripe with backfacet coating. In the inset, threshold current density vs inverse laser length with backfacet coating measured at 10 K. . . 113
5.13 The pulsed thrshold current density as a function of inverse laser length with backfacet coating measured at 10 K. 114
5.14 CW optical power from a single facet and bias of a 2.1 mm long and 200 μm wide laser stripe as function of drive current for various heat sink temperatures. 115
5.15 The ratio Γ/α_W of the overlap factor and the waveguide losses are shown versus the doping density of the 600 nm thick buried contact layers. The simulations have been performed for a far-infrared radiation at $\lambda = 130\mu m$, using the bulk Drude model, where scattering times of $\tau = 0.1$ ps and 0.5 ps were used for the heavily doped and lightly doped GaAs regions respectively. They show a maximum of the ratio Γ/α_W at N=9 $\times 10^{17}$. 116
5.16 Lasing spectra of a 150 μm-wide and 1 mm-long QCL with high reflectivity back and frontfacet coating at different temperatures between 15 and 47 K. The curves are vertically displaced for clarity. 117
5.17 Spectra recorded at 10 K under continuous operation at four different injection currents. At low current levels the laser emits on a multimode; passing a certain threshold the laser emitson a single mode. 118
5.18 Computed conduction band profile at T=20 K of the structure under an average applied electric field of 3.1 kV/cm and an Si doped layer of $n = 4.2 \times 10^{16}\,\mathrm{cm}^{-3}$. The optical transition occurs between level n = 8, isolated in the minigap, and the state n = 7 of the lower miniband. 120
5.19 Peak optical output power and voltage versus injected current density in pulsed mode at a duty cycle of 2% of various sheet doping density, as indicated. The sample is processed into a 2.5-mm-long and 200 μm-wide waveguide. 121
5.20 Threshold current density (J_{th}) and the maximum current density before appearance NDR (J_{NDR}) as a function of doping density. 123
5.21 Experimental and calculated waveguide losses versus n_{eff}. 125

5.22 Simulations of the waveguide losses. 126

5.23 Comparison of the relative tempertature dependence of the threshold current density for the QCL's with different doping levels, as indicated. The solid lines correspond to fits of the data with the following relation $J_{th} = J_0 + J_1 \exp(T/T_0^*)$. Samples dimensions are 210 μm wide and 5.4, 1.8, and 2.5 mm-long for N299, N301, and N310 respectively. The improvements in the maximum operating temperature arise from successively increasing the sheet doping density. The squares show superior temperature dependence and a maximum operating temperature of 78 K. 128

5.24 Lasing spectra of 210-μm-wide and 2.5 mm long QCL's taken at 10 K for different doping density (4.4, 6.6, 8.8 $\times$ $10^{10}\,cm^{-2}$), as indicated. The spectra are vertically displaced for clarity. The redschift observed is in agreement with the calculated optical transition. 129

5.25 (a)Threshold current density and (b) peak power measured for samples N301, N310 grwon in Neuchâtel and A2986 grown in Combridge. We attribute the slightly lower performance of sample N301 and N310 to the larger background doping of the epitaxial growth system at the time it was grown. 131

6.1 THz QCL's design based on a bound-to-continuum transition combined with an optical phonon extraction. 134

6.2 THz QCL's design based on a bound-to-continuum transition combined with an optical phonon extraction. 136

6.3 Average power data as a function of duty cycle taken at 10 K. The cavity length are 1-mm with a stripe width of 210 and 160 μm-wide waveguides. 138

6.4 L-I and V-I taken in pulsed mode for 210-μm-wide, 4.3mm-long ridge after the evaporation of a HR coating on the backfacet. Data was measured using 100-ns pulses repeated at 100 kHz. 139

6.5 Devices with low doping in the active region (N465) worked in continuous wave up to 40 K. emitted power has been measured with a calibrated thermopile from a 1.7-mm-long, 210-mm-wide waveguide laser ridge. 140

6.6 Threshold current density as a function of the heatsink temperature in pulsed mode for both devices (N464 and N465). The curves correspond to the usual exponential fit $j_{th} = j_0 exp(T/T_0)$. 142

6.7 Threshold current density (J_{th}) and the maximum current density before appearance NDR (J_{NDR}) as a function of doping density. 143

6.8 Threshold current density vs inverse laser length with backfacet coating for both samples (N464 and N465) measured at 10 K. 144

6.9 experimental and calculated waveguide losses versus n_s. The waveguide losses are calculated using the Drude model with $\tau = 0.5$ ps for the active region, 0.15 ps for the heavily doped regions, and 0.05 ps for gold. 145

6.10 Lasing spectra of 210-μm-wide and 1.7 and 0.6 mm long for N465 and N464 QCL's respectively taken at 10 K for different doping density (5.7, 11.4 $\times$ $10^{10}\,cm^{-2}$), as indicated. The spectra are vertically displaced for clarity. The redschift observed is in agreement with the calculated optical transition. 146

7.1 (a) Lasing spectra of DFB QC laser as a function of different grating periods. (b) Good agreemnet is obtained between the calculated (squares symbols) and the experimental (cycles symbols) bragg wavelengths as a function of the grating periods. The slope of the line fit to the data, give $n_{eff} = 3.40$ close to the calculated value (3.68). 150
7.2 (a) Liiv curves of the laser operating at $\Lambda = 11.7$ μm measured at different temperatures. (b) Applied bias as a function of injection current in pulsed mode of the DFB (continuous line) and FP (dashed line) devices. 152
7.3 (a) Spectra of the laser operating at $\Lambda = 11.7$ μm measured at different current injection. (b) shows lasing spectra of the same device taken at different temperatures between 20 and 60 K. 153
7.4 Lasing spectra of DFB QCL in pulsed mode for different grating periods. 155
7.5 Lasing spectra of DFB QCL in CW operation for different grating periods. 156
7.6 Good agreement is obtained between calculated (circles) and experimental Bragg wavelengths in pulsed (squares) and CW operation (triangles) against grating period. 157
7.7 (a) CW optical power from a single facet and bias of a 110 μm-wide and 1.25 mm-long DFB QCL as function of drive current for various heat sink temperatures. (b) Lasing spectra of the same device measured at different temperatures. 158
7.8 Spontaneous emission spectrum of a 110 μm-wide and 1.25 mm long DFB QC laser for Λ=11.9 μm grating period measured at 10 K. 159
7.9 (a) This figure gives the definition of the angular coordinates for the orientation of the samples. The x-axis is perpendicular to the cryostat window. (b) Beam profile for DFB Quantum Cascade with Λ=11.7 μm grating period measured at 10 K. . . . 162
7.10 The section of the far-field distributions in the parallel (for φ=0; (a)) and perpendicular(θ=0; (b)) grown layers directions, represented by a Gaussian profile (Solid line). 163

8.1 Solid line: Optical mode intensity profile in an $In_{0.52}Al_{0.48}As$-$In_{0.53}Ga_{0.47}As$/InP waveguide structure. Solid line is the mode computed assuming the current is injected by a two-dimentional electron gas (2DEG). For comparison, the mode computed assuming a $In_{0.53}Ga_{0.47}As$ heavily doped buried contact layer is also shown (dashed line). The growth, on a semi-insulating InP substrate, starts by a two dimentional electron gas formed successively of 2 1/2 period of a 5 nm $In_{0.53}Ga_{0.47}As$ / 5 nm $In_{0.52}Al_{0.48}As$ superlattice, a 120 nm thick undoped $In_{0.52}Al_{0.48}As$ layer, a 5 nm thick doped ($n = 2\times10^{18}$ cm^{-3}) $In_{0.52}Al_{0.48}As$ layer, an undoped 10 nm thick $In_{0.52}Al_{0.48}As$ spacer layer, and finishing by a an undoped 100 nm thick $In_{0.53}Ga_{0.47}As$ layer. The growth follows by 70 periods of the active region, and followed by an undoped, 40 nm thick $In_{0.53}Ga_{0.47}As$ layer. The latter consists of a an undoped 5 nm thick $In_{0.52}Al_{0.48}As$ layer, an undoped, 1 nm thick $In_{0.53}Ga_{0.47}As$ layer, a 60 nm thick heavily doped ($n = 1.5 \times 10^{19}$ cm^{-3}) $In_{0.53}Ga_{0.47}As$ contact layer. 168
8.2 Computed conduction band profile at T = 10 K of one stage of the structure under an average applied electric field of 3.3 kV/cm. 169
8.3 Spectra recorded at heat sink temperature of 10 K from a 1.25 mm long and 110 μm wide device under pulsed excitation with a duty cycle of 2 at different currents. The threshold curent of the deviceis 630 mA. Spectra are offset for clarity. 171

8.4 Solid line, emission spectra measured as a function of current for a 110 μm-wide and 1.25 mm-long device. For comparison, the same measurement performed from the side of a device that has been cleaved along the length of the stripe is shown (dashed line). Inset: High resolution spectra of the same laser taken above threshold. The spectra are vertically displaced for clarity. 172
8.5 Peak optical output power versus injected current in pulsed mode at a duty cycle of 0.008 % at various temperatures, as indicated. The sample is processed into a 1.25-mm-long and 110 μm-wide waveguide. 174
8.6 Pulsed threshold current as a function of inverse laser length measured at 10 K. . . . 175

Chapter 1

Introduction

1.1 Historical overview

Historically, heterojunction superlattices (SL) and their transport properties were first investigated by Esaki and Tsu in 1970 [1]. The use of intersubband transitions for electromagnetic wave (radiation) amplification was first proposed in 1971 by Kazarinov and Suris [2] in a superlattice structure. This intersubband emission was observed in 1985 by West [3] and the first sequential resonant tunneling through a multiquantum-well superlattice was reported in 1986 by Capasso and al [4]. Such a structure is practically useless as a quantum cascade active region and is electrically unstable. In 1994, Faist et al [5] demonstrated the first intersubband laser, designed to emit at 4.3 μm wavelength and grown by molecular beam epitaxy (MBE). They named the new laser the QC laser. Progress advanced quickly after that [6, 7, 8, 9, 10, 11, 12]; Figure. 1.1 shows a timeline. Already a year after their invention the lasers operated in cw at cryogenic temperatures [6], and in pulsed mode up

to room temperature (RT) [7]. Distributed feedback (DFB) lasers were first introduced in 1996 [8], providing continuously tunable single-mode laser output and the first QC laser in the GaAs/AlGaAs on GaAs material system was demonstrated in 1998 by Sirtori [9]. The first far-infrared QC lasers with wavelengths longer than 20 μm, were demonstrated late in 2000 [10]. In 2002, continuous wave operation of a Mid-Infrared quantum cascade lasers was reported up to a temperature of 312 Kelvin [11].

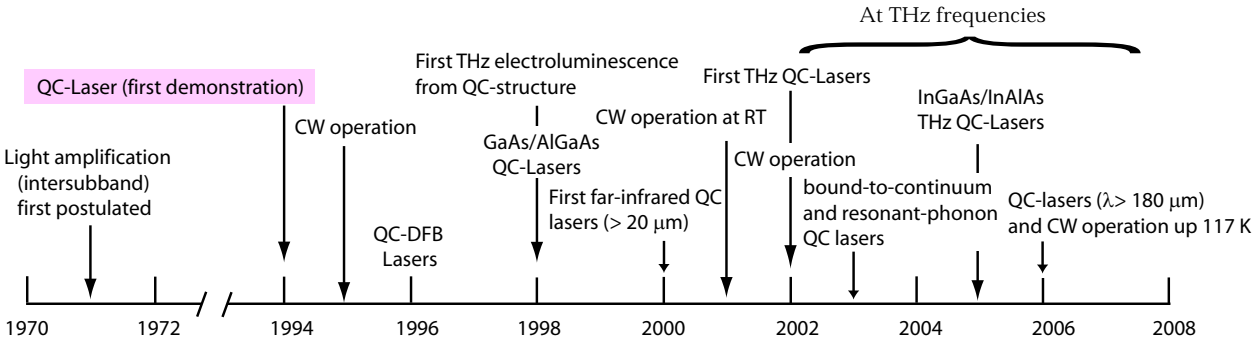

Figure 1.1: Schematic timeline of significant QC-laser developments.

Despite this progress, the emission wavelength was always limited in the mid-infrared. The first encouraging step towards the accomplishement of a terahertz QC laser emitting at frequencies below 8 THz was made in 1998 by Rochat et al. [13] through the observation of THz (4.5 THz) electroluminescence from a QC structure, which triggered the investigation of several similar structures [14, 15, 16, 17, 18]. Lasing was achieved only in 2002 [19] at 4.4 THz (68 μm), in the chirped superlattice based quantum cascade structure placed in a new type of low-loss waveguide (semi-insulating surface plasmon waveguide) (Sec. 2.4.3). Soon afterward, in January 2002 Jerome Faist's group at Neuchâtel reported lasing in a similar structure at 4.5 THz (66 μm) [20]. By an optimisation of the device processing, this structure show the

first continuous wave operation at terahertz frequencies [21]. While less than four years have passed since the advent of the terahertz quantum cascade laser, much improvement has taken place. The first major performance improvement came with a bound-to-continuum-QC laser design embedded in SI surface-plasmon waveguide [22, 23]. The development of this laser is described extensively in Chap. 5. THz QCLs based on $In_{0.52}Al_{0.48}As$-$In_{0.53}Ga_{0.47}As$/InP material system was demonstrated in 2005 [24]. The best temperature performance for terahertz QCLs has been demonstrated using metal-metal waveguides with the resonant-phonon depopulation scheme [25], which has allowed operation up to 164 K in pulsed mode and 117 K in cw mode [26]. The emitting wavelength range are presently from 4.5 THz (66 μm) [19] down to 1.6 THz ($\approx$ 190 μm) ([27, 26, 28]). In addition two-color quantum cascade laser emitting at 1.39 and 2.3 THz have been demonstrated using active regions based on an intrawell transition which exploit magnetic field-induced confinement to enhance population inversion [29]. The field is rapidly progressing, and terahertz lasers promise to soon make an impact on scientific and hopefully even commercial applications.

1.2 Terahertz sources and their applications

The terahertz (THz) region of the electromagnetic spectrum has proven to be one of the most elusive. Terahertz radiation is loosely defined by the frequency range of 0.1 to 10 THz (10^{12} cycles per second). Being situated between infrared light and microwave radiation (see Fig. 1.2), THz radiation is resistant to the techniques commonly employed in these well-established neighbouring bands. High atmospheric absorption constrained early interest

and funding for THz science. Historically, the major use of THz spectroscopy has been by chemists and astronomers in the spectral characterization of the rotational and vibrational resonances and thermal-emission lines of simple molecules. The past 20 years have seen a revolution in THz systems, as advanced materials research provided new and higher-power sources, and the potential of THz for advanced physics research and commercial applications was demonstrated. Terahertz technology is an extremely attractive research field, with interest from sectors as diverse as the semiconductor, medical, manufacturing, space and defence industries. Several recent major technical advances have greatly extended the potential and profile of THz systems. These advances include the development of a quantum cascade THz laser [19], the demonstration of THz detection of single base-pair differences in femtomolar concentrations of DNA [30, 31] and the investigation of the evolution of multiparticle charge interactions with THz spectroscopy [32]. In this chapter we will provides an overview of these and many other important recent developments of the THz sources and his applications.

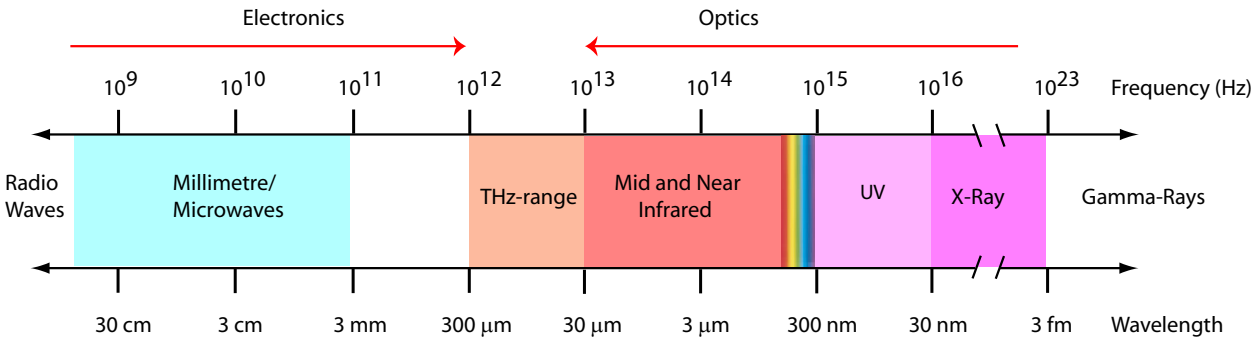

Figure 1.2: Position of terahertz spectrum (1-10 THz). This range is also known as the far-infrared, or sub-millimeter range, and the lower limit is often extended down to 300 GHz ($\lambda = 1$ mm) or even 100 GHz ($\lambda = 3$ mm).

1.2.1 Terahertz sources

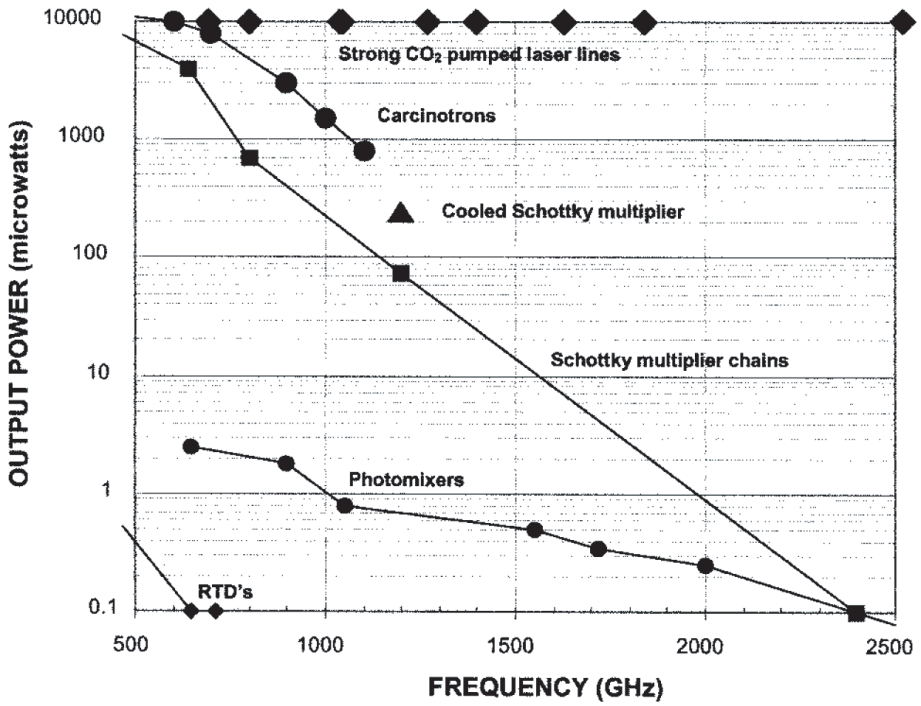

Figure 1.3: Performance of some CW sources in the sub-millimeter wave range. Figure is reprinted from Siegel (2002) [33].

The lack of a high-power, low-cost, portable room-temperature, THz source is the most significant limitation of modern THz systems. However, there is a vast array of potential sources each with relative advantages, and advances in high-speed electronics, laser and materials research continue to provide new candidates. Fig. 1.3 shows the typical power levels of some CW sources in the submillimeter-wave range [33]. Sources may be broadly classified as either direct sources or indirect. This classification is only one possibility among many others. Indeed, the sources could be classified according to various angles: for example, one can separate the components with coherent emission of those with incoherent emission,

or the photonic from the electronic ones. Let us see more in details the principal devices while starting with the direct generation.

1.2.2 Direct generation

Diodes

- Gunn diode

A Gunn diode, also known as a transferred electron device (TED) is a form of diode used in high-frequency electronics. It is somewhat unusual in that it consists only of N-doped semiconductor material, whereas ordinary diodes consist of both P and N-doped regions. In the Gunn diode, three regions exist: two of them are heavily N-doped on each terminal, with a thin layer of lightly doped material in between. When a voltage is applied to the device, the electrical gradient will be largest across the thin middle layer. Eventually, this layer starts to conduct, reducing the gradient across it, preventing further conduction. In practice, this means a Gunn diode has a region of negative differential resistance. The oscillation frequency is determined partly by the properties of the thin middle layer, but can be adjusted by external factors. Gunn diodes are therefore used to build oscillators in the 10 GHz and higher (THz) frequency range, where a resonant cavity is usually added to control frequency.

Various sorts of semiconductor show this effect, but the types used most often for commercial purposes are GaAs and InP. The fundamental oscillation frequency is typically around 200 GHz [34, 35]. However operation in a second or higher harmonic mode opens new horizons,

for diodes manufactured on InP a 325 GHz was obtanied in a second harmonic with significant level power and 400-560 GHz from InP gunn diode devices in a third or higher harmonic mode [36].

- IMPATT diode

An IMPATT diode (IMPact ionization Avalanche Transit-Time) is a form of high power diode used in high-frequency electronics and microwave devices. They are typically made with silicon carbide owing to their high breakdown fields.
They operate at frequencies between about 3 and 140 GHz [37] or more. A main advantage is their high power capability (100 mW) [37]. These diodes are used in a variety of applications from low power radar systems to alarms. A major drawback of using IMPATT diodes is the high level of phase noise they generate. This results from the statistical nature of the avalanche process. Nevertheless these diodes make excellent microwave generators for many applications.

- Tunnel diode

A tunnel diode or Esaki diode is a type of semiconductor diode which is capable of very fast operation, well into the microwave region GHz, by utilizing quantum mechanical effects. It was named for Leo Esaki, who recieved the Nobel Prize of 1973 for discovering the electron tunneling effect used in these diodes. These diodes have a heavily doped p-n junction only some 10 nm wide. The heavy doping result in a broken bandgap, where conduction band electron states on the n-side are more or less aligned with valence band hole states on the

p-side. At room temperature, an InAs/AlSb double-barrier resonant-tunneling diodes were reported up to 712 GHz with a power estimated at 300 nW [38].

Transistor

HEMT stands for High Electron Mobility Transistor, and is also called heterostructure FET (HFET). A HEMT is a Field effect transistor with a junction between two materials with different band gaps (i.e. a heterojunction) as the channel instead of an n-doped region. A commonly used combination is GaAs with AlGaAs. The effect of this junction is to create a very thin layer where the Fermi energy is above the conduction band, giving the channel very low resistance (or to put it another way, "high electron mobility"). This layer is sometimes called a two-dimensional electron gas. As with all the other types of FETs, a voltage applied to the gate alters the conductivity of this layer. A HEMT transistors were recently demonstrated at frequencies between 0.4 and 1.0 THz by Knap et al [39].

Semiconductor laser

- Ge and Si terahertz laser

Semiconductor lasers are a further technique with extreme promise for narrowband THz generation. The first such laser was demonstrated over 20 years ago in lightly doped p-type germanium as a result of hole population inversion induced by crossed electric and magnetic fields [40, 41]. These lasers are tunable by adjusting the magnetic field or external stress. Terahertz lasing in germanium has also been demonstrated by applying a strong uniaxial stress to the crystal to induce the hole population inversion [42]. Several watts of peak power

have been obtained in broadband lasing (linewidths of 10-20 cm^{-1}) that can be tuned from 1-4 THz and cw lasing that is tunable with pressure from 2.5 to 10 THz was demonstrated by Gousev et al. in 1999 [42]. Such lasers have many inherent limitations including low efficiency, low output power and the need for cryogenic cooling to maintain lasing conditions. An interesting project is also the one aimed to develop a laser in the Si/SiGe quantum wells, with some experimental report also about THz emission from such structures [43, 44, 45, 45]. The mechanism used is the same of lasing as in uniaxially stressed P-Ge THz lasers. This is a promising method which eliminates the need for externally applied strain, but no laser is achieved untill now and high voltage is required.

- Quantum cascade lasers

Quantum cascade (QC) lasers are unipolar mid- to far-infrared emitters in which the laser transition occurs between quantized energy levels within e.g., the conduction band. As the emission wavelength is determined by quantum confinement, a broad wavelength range can be covered by tuning the thicknesses of the individual layers without changing the material compositions. The properties and the advantages of these lasers are described extensively in Sec. 2.2. Since their first demonstration in 1994 employing GaInAs/AlInAs grown on InP substrate [46] these novel devices have made tremendous progress, including operation spanning the mid- to far-infrared wavelength range from 3.5 to 24 μm, peak power levels in the Watt range and above-room-temperature (RT) pulsed operation for wavelengths from 4.5 to 17 μm and CW operation from 10 μm. The development of terahertz quantum cascade lasers that operate below the semiconductor Reststrahlen band of the semiconductor is the

topic of this thesis, and the background on this subject is given in more detail in Sec. 2.3.

Tubes

Terahertz tube sources [47] based on emission from bunched electrons spiraling about in strong magnetic fields (backward-wave-oscillators or carcinotrons) offer the most power and frequency tuning range at submillimeter wavelengths. Bench-top commercial units extend to 1.2 THz with mW levels of available power. Tubes also suffer a strong roll-off of power with increasing frequency due to physical scaling and metallic losses, and so are unlikely candidates for operation at higher terahertz frequencies. Perhaps more importantly they can now only be obtained from Russia, and suffer from a relatively short operating lifetime [33].

Gas laser

Optically pumped gas lasers have been the other dominant source of THz radiation. These are usually based on grating tuned CO_2 pump lasers (20-100 W) injected into low-pressure flowing-gas cavities that lase to produce the terahertz signals. Population inversion is thus obtained in some of the rotational levels of the excited vibrational state. Although discrete lines can be obtained between 0.1 and 8 THz [48, 33], most strongly pumped lines are below 3 THz. For these strongly pumped lines continuous-wave power of 1-20 mW is typical [33]. However, the selection of laser frequencies is limited by available gasses, and tunability is extremely limited. Additionally, such gas lasers are expensive, bulky, and power hungry, which makes them less than ideal for space light applications.

1.2.3 Indirect generation

Harmonics generation

Alternative approaches to generate THz radiation are associated with optical techniques, that use a coherent output at the difference frequency ≈ equal to the difference between the frequencies of radiation emitted by two lasers (Photomixing) [49] or a response of photoconductive structures to femtosecond optical pulses.

- Photomixing

The technique of photomixing operates by illuminating a fast photoconductive material with two optical lasers detuned by the desired terahertz frequency. The laser induced photocarriers short the gap producing a photocurrent, which is modulated at the laser difference frequency. This current is coupled to an RF circuit or antenna that couples out or radiates the terahertz energy. The resulting power is narrow-band, phase lockable, and readily tuned over the full terahertz band by slightly shifting the optical frequency of one of the two lasers. Power levels available are on the order of 1-10 μW below 1 THz, and sub-microwatt above 1 THz.

- Femtosecond pulse generation

This technique is based on using a short pulse (femtosecond) optical laser (argon-laser-pumped Ti : sapphire laser) to illuminate a gap between closely spaced electrodes on a photoconductor (e.g., silicon-on-sapphire or LTG GaAs) generating carriers, which are then accelerated in an applied field ($<$ 100 V) [33]. The resulting current surge, which is coupled

to an RF antenna, has frequency components that reflect the pulse duration, i.e., terahertz rates. The same terahertz output spectrum can be obtained by applying short laser pulses to a crystal with a large second-order susceptibility (field-induced polarization) like zinc telluride. Since the higher order susceptibility terms are indicative of nonlinear response, mixing occurs, producing a time-varying polarization with a frequency-response representative of the pulse length, i.e., terahertz oscillation. As with the photomixers, RF power may be radiated by antennas printed on the photoconductor or crystal, and typically have frequency content from 0.2 to 2 THz or higher depending on the laser pulse parameters. While the average power over the entire spectrum are very low (nanowatts to microwatts) and pulse energies tend to be in the femtojoule to nanojoule range. Fiber coupled systems have been developed and continual improvements are being made to these RF generators in order to increase the signal-to-noise of the Terahertz imagers [50].

1.3 Terahertz applications

1.3.1 gas spectroscopy

Astronomy and space research have been two of the strongest drivers for THz research because of the vast amount of information available concerning the presence of abundant molecules such as oxygen, water and carbon monoxide in stellar dust clouds, comets and planets. In recent years, THz spectroscopy systems have been applied to a huge variety of materials both to aid the basic understanding of the material properties, and to demonstrate potential applications in sensing and diagnostics.

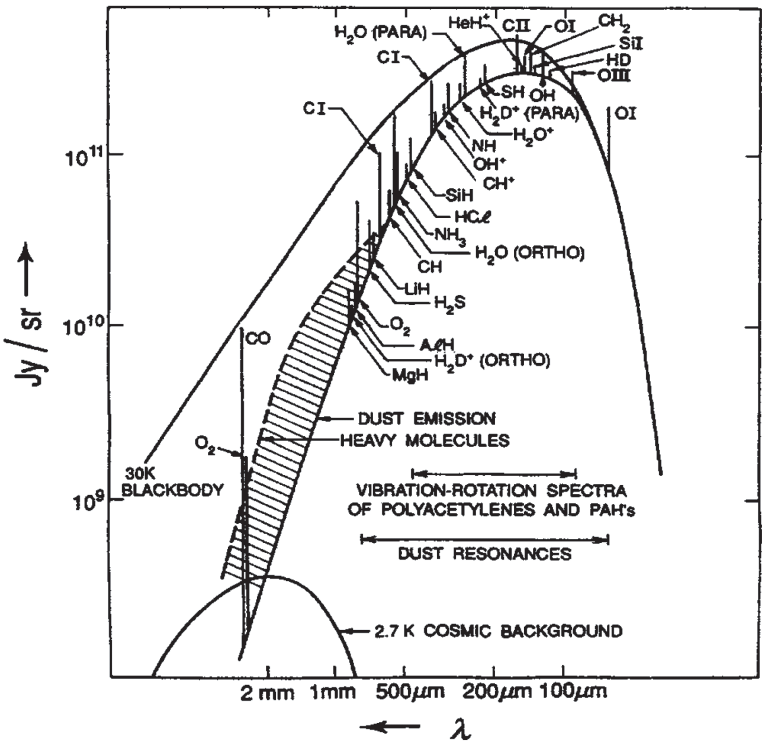

Figure 1.4: Radiated energy versus wavelength showing 30-K blackbody, typical interstellar dust, and key molecular line emissions in the submillimeter (reprinted from [33]).

A quick look at the spectral signature of an interstellar dust cloud (Fig. 1.4), however, explains why astronomers are so interested in terahertz sensor technology. Results from the NASA Cosmic Background Explorer (COBE) Diffuse Infrared Background Experiment (DIRBE) and examination of the spectral energy distributions in observable galaxies, indicate that approximately one-half of the total luminosity and 98% of the photons emitted since the Big Bang fall into the submillimeter and far-IR. Individual emission lines such as C^+ at 158 μm (1.9 THz), the brightest line in the Milky Way submillimeter-wave spectrum, provide a detailed look at star forming regions where surrounding dust is illuminated by hot

young ultraviolet emitting stars. Many other abundant molecules, e.g., water, oxygen, carbon monoxide, nitrogen, to name a few, can be probed in the terahertz regime. Since these signals are obscured from most Earth-based observations (except from a very few high-altitude observatories, aircraft, or balloon platforms), they provide strong motivation for a number of existing or upcoming space astrophysics instruments, most notably the Submillimeter Wave Astronomy Satellite (SWAS), launched in December 1998, and currently sending back data on water, oxygen, neutral carbon, and carbon monoxide in interstellar space; and in the near future, the European Space Agencys (ESA) Herschel scheduled for 2007 and NASAs proposed Submillimeter Probe of the Evolution of Cosmic Structure (SPECS), SPace InfraRed Interferometric Telescope (SPIRIT), and Filled Aperture InfraRed telescope (FAIR), which will examine this spectral region in great detail in the decade beyond 2010. For interstellar and intragalactic observations, both high resolving power (large apertures) and high spectral resolution (1-100 MHz) are generally required.

1.3.2 THz imaging and tomography

Pulsed THz-wave imaging, or 'T-ray imaging', was first demonstrated by Hu and Nuss [51] in 1995, and since then has been used for imaging a wide variety of targets including semiconductors [50], cancerous tissue [52] and flames [53]. The attraction of THz imaging is largely due to the availability of phase-sensitive spectroscopic images, which holds the potential for material identification or 'functional imaging'.

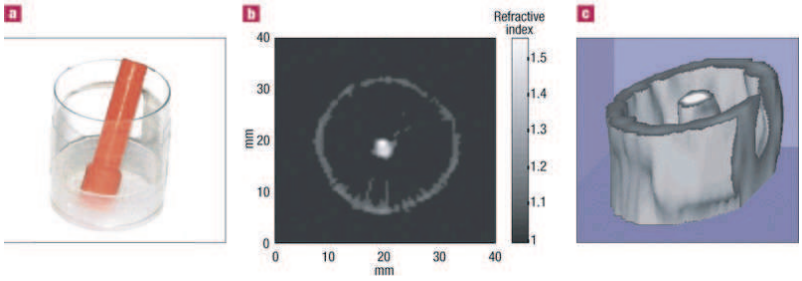

Figure 1.5: T-ray computed tomography image of two plastic cylinders (after ref.[54]). a, An optical image of the test structure. b, The target was imaged using the tomography system, and the refractive index of each cross-sectional slice was reconstructed. The central slice is shown. The greyscale intensity indicates the refractive index of the two different types of plastic. c, The cross-sectional slices are combined to form a 3D image. A surface-rendered image is shown.

THz systems are ideal for imaging dry dielectric substances including paper, plastics and ceramics. These materials are relatively non-absorbing in this frequency range, yet different materials may be easily discriminated on the basis of their refractive index, which is extracted from the THz phase information. Many such materials are opaque at optical frequencies, and provide very low contrast for X-rays. THz imaging systems may therefore find important niche applications in security screening and manufacturing quality control. An important goal in this context is the development of three-dimensional (3D) tomographic T-ray imaging systems [54]. Figure. 1.5 illustrates a reconstructed cross section and 3D-rendered image of two plastic cylinders with differing refractive index. The system is based on the same principles as X-ray computed tomography, but provides a wealth of information about the material's frequency-dependent optical properties through broadband, phase-sensitive THz

detection [55].

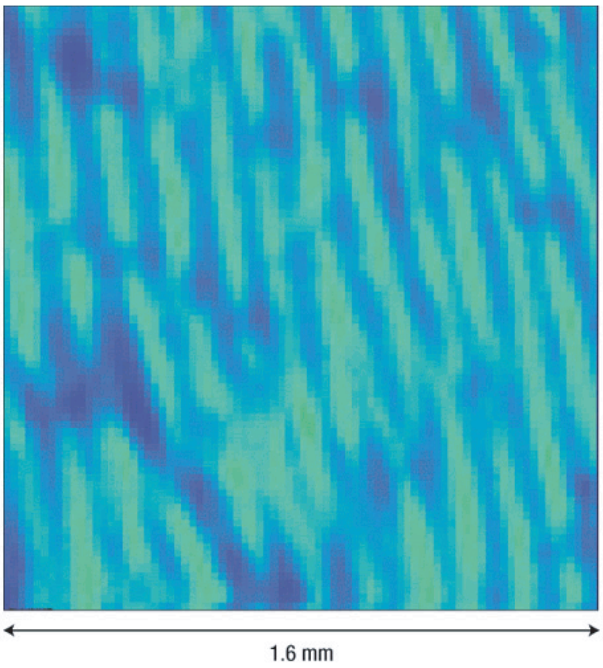

Figure 1.6: THz image of an onion cell membrane (after ref. [56]). A THz imaging system based on optical rectification and free-space electro-optic sampling in ZnTe crystals 30 μm thick was used with a bandwidth up to 40 THz. This allowed a spatial resolution of less than 50 μm to be achieved. The cellular structure of the tissue membrane is clearly visible.

Interest in using THz imaging to study cellular structure is also increasing. A fundamental limitation in this context is the resolution of current systems. The Rayleigh criterion limits the far-field resolution of an imaging system to the order of the wavelength (0.3 mm at 1 THz). For this reason, researchers are relying on imaging in the near-field to achieve improved spatial resolution. Using near-field techniques, similar to those used in near-field optical microscopy, resolutions of 7 μm have been demonstrated using radiation with a centre

wavelength of 600 μm [55]. An alternative method to improve the resolution is to use higher-frequency THz pulses. Figure. 1.6 shows a THz image of a membrane of onion cells. The resolution of approximately 50 μm is achieved by using very broadband THz pulses extending into the mid-infrared. The contrast in the image is attributed primarily to differences in the water content of the cells and the intercellular regions [56].

1.3.3 Telecommunication

The development of the future multi-media applications (wideband internet, digital television, fast calculators) requires the development of a circuit with a high-speed. The flows of optical transmission of the current systems are at 10 Gbit/s. The prototypes with 40 Gbit/s were already developed, and it is now necessary to conceive future systems with wideband. Moreover, the fast internal lifetimes of the devices should allow modulation at frequencies of several hundreds of gigahertz and possibly up to $\approx$ 1 THz assuming negligible parasitics. These systems will require stages of amplification, but also a structures of propagation and local oscillators functioning at the THz frequencies. Highspeed modulation and free-space optical audio/video transmission are demonstrated using mid-infrared quantum cascade lasers. In fact, Martini et al. published results of an optical data link using a high-speed modulated, liquid nitrogen-cooled Mir-QC laser over a distance of 70 m under laboratory conditions [57]. They also succeeded in transmitting a video image via a common TV channel frequency. Blaser et all are also demonstrated an optical data link between two different buildings separated by 350 m and using a Peltier-cooled QC laser as well as a room-temperature HgCdTe detector, taking full advantage of the existing technology [58].

1.4 Thesis overview

The developments and the improvements of the terahertz QC-lasers that operate below the semiconductor Reststrahlen band are the topic of this thesis. Three distinct designs of the active region, have been developed, and are used with SI-surface-plasmon waveguides. We begin in Chapter 2 with a few theoretical aspects concerning intersubband transitions, including calculation of radiative and non-radiative intersubband transition rates, and description of the resonant tunneling transport. The basic considerations and equations of QC lasers that allow us to estimate and predict a lasers performance are briefly discussed with the usually employed resonators. Chapter 3 is a presentation of the fabrication techniques and experimental methods used throughout this work. The first generation of terahertz quantum cascade lasers (chirped-superlattice) is discussed in chapter 4. In chapter 5, a second generation of QC structures are designed and characterized. These structures are based on a bound-to-continuum transitions and are expected to have increased gain compared with the first generation. Chapter 6 prsents a third generation of THz QCL's, which are based on a bound-to-continuum transition combined with an optical phonon extraction. A high power has been achieved in pulsed mode, however in CW operation no particular temperature improvement is showed compared to the best performance from bound-to-continuum designs. Distributed feedback lasers that provide single-mode emission in the far-infrared wavelength range are presented in chapter 7. The first terahertz QC laser based on a new material system (InGaAs:AlInAs/InP) is demonstrated in chapter 8. A conclusion and outlook section completes the thesis.

Chapter 2

Intersubband transitions and quantum cascade lasers

This chapter summarizes a few theoretical aspects employed in this thesis. It first discusses the computation of energy levels and wavefunctions in a heterostructure, the intersubband transitions between them and its electrical properties, and then gives a short review of the quantum cascade lasers basics and properties.

2.0.1 semiconducting heterostructures

The heterostructure is obtained by sandwiching a semiconductor layer A between two layers of semiconductor B whose bandgap energy E_g^B is larger than that of material A(E_g^A)(see Fig 2.1), the wavefunctions in layer A becomes spatially confined in the direction perpendicular to the interface. The motion of electrons along that direction becomes quantized, and their energy is raised with respect to that of the unconfined electron by the confinement

energy. Within the plane of layer A the electrons are still free to move, they form thus a quasi-two dimentional electron system. Such a system is also called a quantum well.

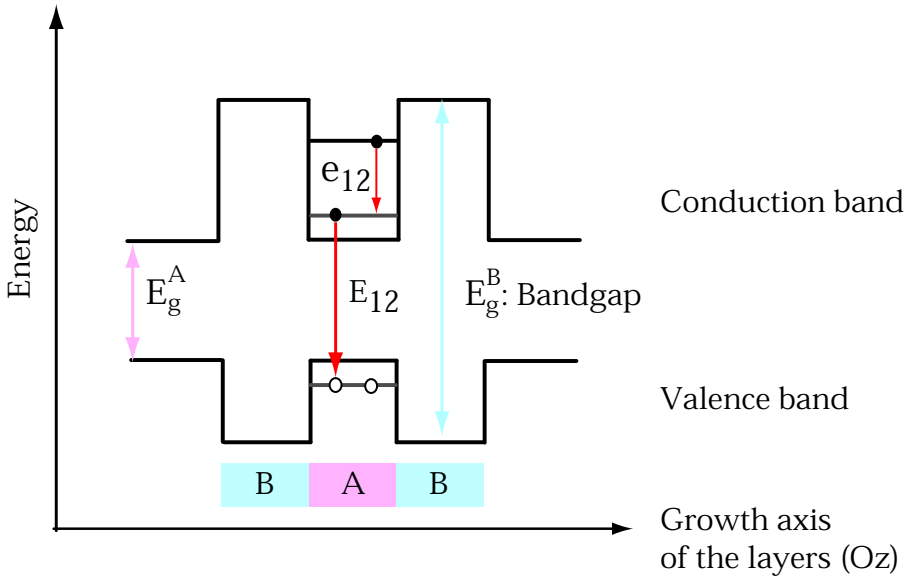

Figure 2.1: Schematic drawing representing a quantum well formed with two different semiconductors whose bandgap energy differs. e_{12} and E_{12} are the intersubband and interband transitions respectively.

2.0.2 Electronics states in heterostructures

The electronic states (more specifically the energy eigenvalues and the wavefunctions of the states) of the heterostuctures are very often calculated using the envelope function approximation [59, 60]. This formalisme is valid if the electronic wave functions have Bloch symmetry with well-defined $\vec{k}$ in the alloy region and the periodic parts of the Bloch functions are the same throughout the heterostructure [61, 62]. All two conditions are well fullfilled in the GaAs/AlGaAs and InGaAs/AlGaAs materials systems used throughout this thesis. The wavefunctions of electrons in a bulk crystal are given by the product of a plane wave

$\exp i[\vec{k}.\vec{r}]$ with the appropriate Bloch factor $u_k(\vec{r})$ as illustrated in Fig 2.2.

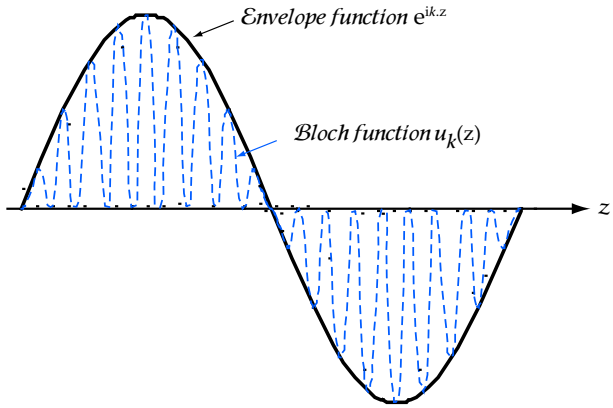

Figure 2.2: schematic representation of the Bloch wavefunction with fast variation modulated with the envelope wavefunctions.

The envelope function formalisms permits to describe the systems, where the confinement potential varying slowly on the scale of host units cells to be superimposed with the periodic potential of cristal. In the each layer A and B of the heterostructure, the wavefunction of an electron around a $\vec{k}_0$-symmetry point of the Brillouin zone (Γ, L, X) [63] is developed on the periodic part of Bloch functions:

$$\psi_{jk_\perp}(\vec{r}) = \sum_n f^{(A)}_{njk_\perp}(\vec{r}) u^{(A)}_{n,\vec{k}_0}(\vec{r}). \tag{2.0.1}$$

if $\vec{r}$ corresponding to material A and,

$$\psi_{jk_\perp}(\vec{r}) = \sum_n f^{(B)}_{njk_\perp}(\vec{r}) u^{(B)}_{n,\vec{k}_0}(\vec{r}). \tag{2.0.2}$$

if $\vec{r}$ corresponding to material B. where the index A, B denotes the material, z is the growth

direction, i.e., the direction in which the motion is quantized, n and j are the band and subband index respectively, $\vec{k_\perp}$ is the wave vectors in the plane of layer, $u_{n,\vec{k}_0}$ the periodic part of the Bloch functions which varied rapidly at the shells of lattice and $f^{(B)}_{njk_\perp}$ is the envelope wavefunctions slowly varying at this shells.

As A and B materials systems have an identical lattice parameters and they cristallize in the same structure, the periodic part of the Bloch function $u_{n,\vec{k}_0}$ is the same for each band of the different materials (III-V semiconductors like GaAs, InP, InAs and AlAs) which constitute the heterostructure.

$$\psi_{jk_\perp}(\vec{r}) = \sum_n f^{(A,B)}_{njk_\perp}(\vec{r}) u_{n,\vec{k}_0}(\vec{r}). \tag{2.0.3}$$

From this equation, we deduce a continuously relation of the wavefunction at the interface z=z_0 between the two materials:

$$f^{(A)}_{njk_\perp}(r_\perp, z_0) = f^{(B)}_{njk_\perp}(r_\perp, z_0). \tag{2.0.4}$$

The invariance of structure by translation in the plane of layers which suggest the factorisation of the enveloppe function into the product of a plane wave propagating along the layer $\exp i[\vec{k_\perp}.\vec{r_\perp}]$ with two-dimensional in-plane wavevector by an envelope function $\chi^{(A,B)}_{nj}(z)$ variant slowly in the atomic shells:

$$f^{(A,B)}_{njk_\perp}(r_\perp, z) = \frac{1}{\sqrt{S}} \cdot e^{i[\vec{k_\perp}.\vec{r_\perp}]} \cdot \chi^{(A,B)}_{nj}(z). \tag{2.0.5}$$

Where $\vec{r_\perp}$, is the position in the plane of layer and S is the normalization area.

In what follows, we limit ourselves to the model at conduction band, the coupling between valence and conduction band can be introduced in the effective mass m*. The varying material composition is represented by a spatially varying effective mass m*(z) and the potential V(z), which represents the conduction band edge profile, including any externally applied field and local variations due to space charge. If the envelope function of the conduction band $f_{njk_\perp}(r_\perp, z)$ is introduced in the Schrodinger equation, one obtains the BenDaniel-Duke eqution[64, 65] which is described as:

$$\left[-\frac{1}{\hbar^2}\frac{\partial}{\partial z}\frac{1}{2m^*(z)}\frac{\partial}{\partial z} + V(z) + \frac{\hbar^2\vec{k_\perp}^{\,2}}{2m^*(z)}\right]\chi_j(z) = E_j(\vec{k_\perp})\chi_j(z) \tag{2.0.6}$$

Where $E_j(\vec{k_\perp})$ is the energy in-plane wavevector $k_\perp$. The spatially dependent effective mass introduces a coupling between the in-plane and z directions. This coupling is usually neglected and this equation becomes the one-dimensional Schrodinger equation:

$$\left[-\frac{1}{\hbar^2}\frac{\partial}{\partial z}\frac{1}{2m^*(z)}\frac{\partial}{\partial z} + V(z)\right]\chi_j(z) = E_j\chi_j(z) \tag{2.0.7}$$

Where the total energy is given by:

$$E_j(\vec{k_\perp}) = E_j + \frac{\hbar^2\vec{k_\perp}^{\,2}}{2m^*(z)} \tag{2.0.8}$$

Where E_j is the confinement energy corresponding to the coulombic potential V(z). This is the sum of the z-direction energy and the in-plane free particle kinetic energy.

In the simple quantum well confined between two potential barriers, the envelope function and their derivatives are continuous at the interface $\pm\frac{L}{2}$. If the effective masses do not differ between the two materials, the solutions in the quantum well are the lineare combinations of plane-waves:

$$\chi_j(z) = A_j e^{ik_{zj}z} + B_j e^{-ik_{zj}z} \tag{2.0.9}$$

The allowed values for the wavevctors can be obtained from the continuity relations of the envelope functions and their derivatives at the well boundaries ($\pm\frac{L}{2}$).

$$\chi_{j,A}(\pm\frac{L}{2}) = \chi_{j,B}(\pm\frac{L}{2}) \tag{2.0.10}$$

$$\frac{1}{m_A^*}\frac{\partial\chi_{j,A}}{\partial z}(\pm\frac{L}{2}) = \frac{1}{m_B^*}\frac{\partial\chi_{j,B}}{\partial z}(\pm\frac{L}{2}) \tag{2.0.11}$$

In the infinite quantum well approximation, the confinement energies deduced from the equation. 2.0.7 are:

$$E_j = j^2\,\frac{\hbar^2\pi^2}{2\mathrm{m}^*\mathrm{L}^2} \tag{2.0.12}$$

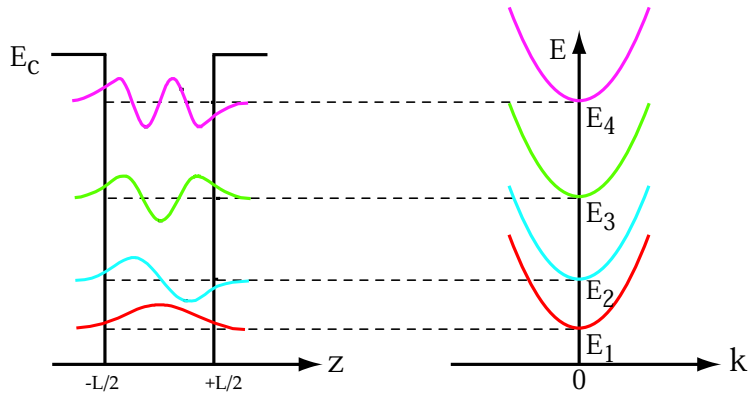

Figure 2.3: Schematic representation of the subband energies as a function of the in-plane wavevector $k_\perp$, for potential barriers E_c.

In the more general case of an arbitrary potential, the solution is obtained numerically by the method of the transfer matrices [66]. In this method, the potential is decomposed into sufficiently small section so that it is practically constant in each section. The continuity relations of the envelope functions and their derivatives to each interface give a 2x2 matrix. The solution is obtained starting from the multiplication of all the matrices.

In this work, Eq. 2.0.7 is solved using a finite-difference method, where the structure of interest is divided into slices with constant material parameters. Although the states calculated are typically assumed to be stationary states, this is not strictly true. Under the application of an electric field, the states become metastable, i.e. they may escape into the continuum. However, usually only a limited spatial extent of the quantum-well structure is simulated, and the states are assumed to be bound. Escape to continuum is considered via an escape time, and is usually much longer than intersubband scattering times. Population of the electronic states by electrons introduces space charge which con- sequently affects the

conduction band profile V(z). For this reason, it is necessary to solve the Poisson equation.

$$\left[\frac{\partial}{\partial z}\,\epsilon(\mathrm{z})\frac{\partial}{\partial \mathrm{z}}\right]\phi(z) = -\rho(z) \tag{2.0.13}$$

where $\phi(z)$ is the electrostatic potential, $\epsilon(z)$ is the spatially varying permittivity, and $\rho(z)$ is the charge density. The Poisson and Schrodinger equations are iteratively solved to obtain a self-consistent solution. The method used and the iterative procedure for obtaining self-consistent Schrodinger and Poisson solutions is described in details in Ref [67].

2.0.3 effective mass

In the one band approximation described in the equ. 2.0.7, in which the effective mass is independent of energy, all electronic subbands have the same curvature. This, however, is not true anymore if the coupling between the conduction band and valence is considered. The effective mass then increases with increasing energy, which leads to a correction of the eigenenergies towards lower values and a different curvature of different subbands. The effective mass becomes energy-dependent. This effect is called non-parabolicity. To take into account the non-parabolicity, the standard theoretical approach considers the envelope-function Hamiltonian in the Kane approximation (with the in-plane wavevector $\vec{k}_{\perp}$ of the carrier being zero) [68]. In this formalism, we can show for the conduction band, the confinement energies of heterostructure can be calculated while using in equ. 2.0.7, an effective mass depending on energy in the form:

$$\frac{1}{m^*(E,z)} = \frac{1}{m_0}\left[\frac{2}{3}\frac{E_p}{E - E_{lh}(z)} + \frac{1}{3}\frac{1}{E - E_{so}(z)}\right] \tag{2.0.14}$$

where E_{lh} and E_{so} are respectively the light-hole and split-off position-dependent band energies, E_p is the Kane energy ($\sim$ 20eV in III-V semiconductors). This three-band model can be simplified through a unitary transformation which allows one to replace light-hole and split-off bands with an *effective* valence band v [69], leading to an effective two-band model. In this case, the energy-dependent effective mass is given by

$$\frac{1}{m^*(E,z)} = \frac{1}{m_0}\left[\frac{E_p}{E - E_v(z)}\right] \tag{2.0.15}$$

The Kane energy can be obtained from the measured effective mass m^* via relation $m^* = |E_c - E_v|/E_p$ with

$$|E_c - E_v| = \frac{\hbar^2}{2m^\star\gamma} \tag{2.0.16}$$

Where γ is the non-parabolicity coefficient [64]

In this thesis, the non-parabolicity $\gamma = 0.014 \cdot 10^{-11}$ cm^2 and the effective mass of GaAs $m^* = 0.067m_0$ are used. For the effective mass of $Al_xGa_{1-x}As$ a linear interpolation $m^*(x) = (0.067 + x \times 0.057)m_0$ is used. Likewise the conduction band offset in eV is computed as $E_c(x) = 8.94 \times x$.

For typical InGaAs wells, with values of $m^\star = 0.043m_0$ and $\gamma = 1.13 \cdot 10^{-14}$ cm^2, and InAlAs barriers with $m^\star = 0.072m_0$, one obtains a Kane energy of $E_p = 18.3$ eV and an effective energy gap $|E_c - E_v| = 0.79$ eV.

2.1 Optical properties of heterostructures

The discussion of the optical properties of heterostructures including the spatial dependence of the effective mass and non-parabolicity can be found in ref. [69]. Here, for the sake of simplicity, and since the physics is easier to understand in this case, we restrict ourselves to the parabolic case.

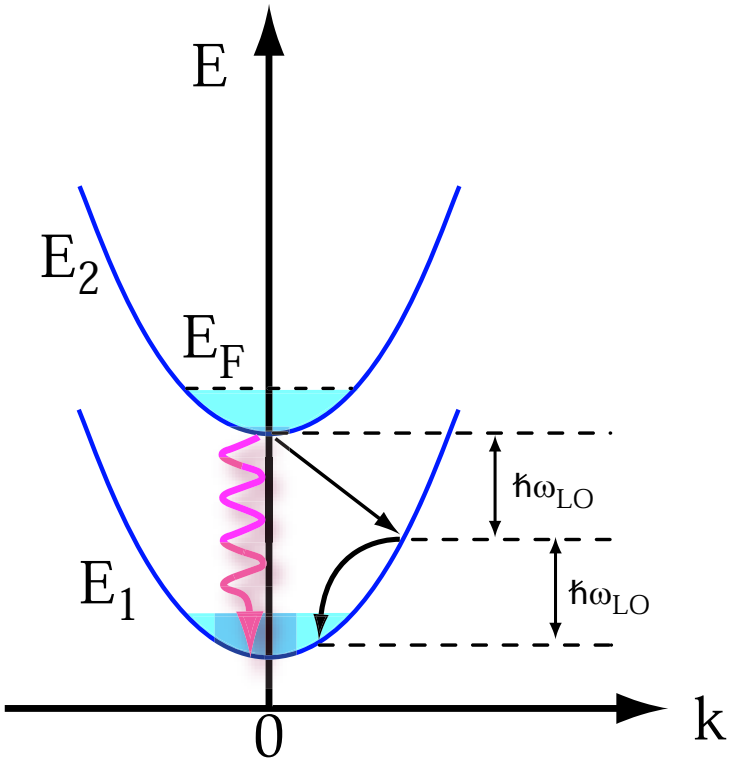

Figure 2.4: Energy of the first two subband energies as a function of the in-plane wavevector $k_\perp$. The right arrow represents the non-radiatively relaxation assisted by the optical phonon emission, the arrow corrugated corresponds to photons emission.

The term " inter sub-band transition" commonly indicates a transition between the energy levels in the conduction (or the valence) band. As shown in figure. 2.4, if one injects electrons

in the excited state, they can relax radiatively by emitting a photon (corrugated arrow), or non-radiatively by emitting longitudinal (LO) optical phonons (right arrow).

2.1.1 Radiatives transitions

Transitions between initial $|i\rangle$ and final $|f\rangle$ states in quantum wells occur at a rate given by Fermi's golden rule:

$$\wp_{if} = \frac{2\pi}{\hbar} \left|\langle \psi_f \left| W \right| \psi_i \rangle\right|^2 \delta(E_f - E_i \pm \hbar\omega) \tag{2.1.17}$$

Where

$$W(\vec{r}, t) = \frac{e}{2m^* c}(\vec{p} \cdot \vec{A} + \vec{A} \cdot \vec{p}) \tag{2.1.18}$$

is the interaction Hamiltonian and $\vec{p}$ is the dipole interaction. The Lorentz-gauge vector potential for a harmonic interaction can be written as $\vec{A}(\vec{r}, t) = -\frac{\vec{e}cF}{2i\omega}\left\{e^{i(\omega t - \vec{q}\cdot\vec{r})} - e^{-i(\omega t - \vec{q}\cdot\vec{r})}\right\}$, where e is electronic charge, F is the amplitude electric field, c is speed of light in vaccum, $\vec{e}$ is the polarization vector and $\vec{q}$ is the photon wavevector at ω frequency. Because $\left[\vec{A}, \vec{p}\right] = 0$ and since the potential vector varied more slowly than the vector position ($\vec{q} \ll \vec{r} \Rightarrow e^{\pm i\vec{q}\cdot\vec{r}} \cong 1$), the equation (2.1.17) can be writen:

$$P = -\frac{2\pi}{\hbar} \frac{e^2 F^2}{4m^{*2}\omega^2} \left|\langle f \left| \vec{e} \cdot \vec{p} \right| i \rangle\right|^2 \delta(E_f - E_i \pm \hbar\omega) \tag{2.1.19}$$

The wavefunction of an electron in state j and band n can be writen as $\psi_j(\vec{r}) = f_j(\vec{r}) u_{n,j}(\vec{r})$.

Due to the properties of the periodic Bloch functions and the slowly varying envelope functions, the complete matrix element can be split up in the following way [68].

$$\langle \psi_j \left| \vec{e} \cdot \vec{p} \right| \psi_i \rangle = \vec{e} \cdot \langle u_{mj} \left| \vec{p} \right| u_{ni} \rangle \cdot \langle f_j \left| \right| f_i \rangle + \vec{e} \cdot \langle u_{mj} \left| \right| u_{ni} \rangle \cdot \langle f_j \left| \vec{p} \right| f_i \rangle \tag{2.1.20}$$

Where i and j, and n and m are the subband and band indices of the initial and final states, respectively. The first term describes interband transitions, which are accompanied by a change of the band index n. If the initial and the final bands are the same, as in the case of intersubband transitions in the conduction band, this term vanishes. The second term, which describes transitions between subbands in the same band, become relevant.This term can be decomposed as the sum of a parallel and perpendicular component to the growth direction:

$$\langle f_j \left| \vec{e} \cdot \vec{p} \right| f_i \rangle = \left\langle e^{ik'_{\perp j} \cdot r} \chi_j \left| e_\perp p_\perp + e_z p_z \right| e^{ik_{\perp i} \cdot r} \chi_i \right\rangle \tag{2.1.21}$$

Using $p_z = -i\hbar \frac{\partial}{\partial z}$, one obtains:

$$\langle f_j \left| \vec{e} \cdot \vec{p} \right| f_i \rangle = \hbar e_\perp k_\perp \delta_{k_{\perp i}, k'_{\perp j}} \delta_{i,j} + e_z \delta_{k_{\perp i}, k'_{\perp j}} \langle \chi_j \left| p_z \right| \chi_i \rangle \tag{2.1.22}$$

The terms proportional to $e_\perp$ vanish, except when initial and final states are identical (i=j and $k_\perp = k'_\perp$). The physical meaning of these terms is the free-carrier absorption in the two-dimentional electron gas, which is finite only at zero frequency when no scattering processes are included. This is due to the impossibility of conserving energy and momentum

simultaneously during the absorption of a phonon by an electron.

Only the term proportional to e_z yields a contribution at finite frequency. In addition, only transitions with the F field polarized along the growth axis ($\hat{z}$) are permitted. The delta function $\delta_{k_{\perp i},k'_{\perp j}}$ ensures conservation of in-plane momentum over a transition. The matrix element which determines the intersubbands transition probability is proportional to:

$$\langle \chi_j \left| p_z \right| \chi_i \rangle = \int \chi_j^*(z) p_z \chi_i(z) dz \tag{2.1.23}$$

The operator p_z being odd, the matrix element will be not null if the two states implied in the transition are of opposite parity. The first intersubband absorption in a GaAs-AlGaAs multi-quantum well was performed by West and Eglash in 1985 [3]. Intersubband electroluminescence of GaAs/AlGaAs heterostructure was observed five years later (1989) [16].

2.1.2 Oscillator strength

Instead of a dipole matrix element, the optical transitions between states are commonly described in terms of a dimensionless oscillator strength f defined by[60, 70]

$$f_{ij} = \frac{2m_0}{\hbar^2}(E_j - E_i)\langle \psi_i \left| Z \right| \psi_j \rangle^2 = \frac{2m_0}{\hbar^2}(E_j - E_i) z_{ij}^2 \quad . \tag{2.1.24}$$

Where z_{ij} denotes the optical dipole matrix element. This definition of the oscillator strength allows the comparison with different systems, because it obeys the sum rule $\sum_j f_{ij} = \frac{m_0}{m^\star}$. For an infinite quantum well, the oscillator strength between the two first confined states is inversely proportional to the effective mass $m^\star$ and is $f_{12} = 0.96\frac{m_0}{m^\star}$ [3]. One sees then

the advantage of using a material with a small effective mass. Figure. 2.5 show a linear dependence of electron effective mass with the gap energy of semiconductor. As the low effective mass means large oscillator strength, it is prefered to choose a material with a small band gap semiconductor as InAs/AlSb [71, 72].

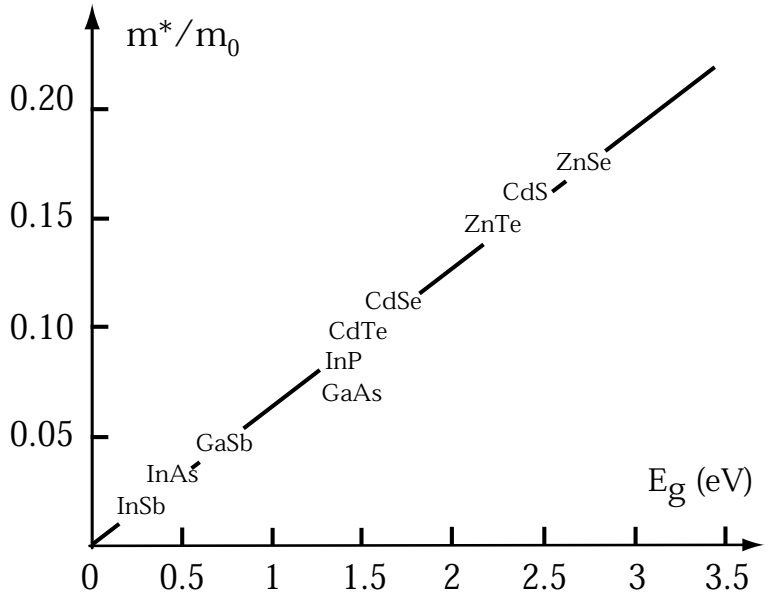

Figure 2.5: Schematic representation of the effective mass variation of electrons as a fuction of the gap energy of semiconductor with direct gap.

2.1.3 Non-radiatives transitions

Besides the emission of photons, electrons can also relax non-radiatively. Such relaxation processes are e.g. the scattering of electrons with impurities, interface roughness, and acoustic and optical phonons. With the exception of scattering with phonons all others scattering processes are elastic, i.e., the total energy of the electron remains unaltered in the scattering process. Nevertheless, potential energy, considered as the kinetic energy in the quantized

z-direction, can be converted into kinetic energy in the x,y-plane of the quantum well. A particular elastic scattering process is electron-electron scattering: in this case the total energy of a particular electron can indeed change, but the total energy of the whole of electron remains constant.

The scattering of electrons with phonons is the only process by which the electron distribution can thermalize with the lattice. The assumed electron-phonon hamiltonian takes the form

$$H_{e-ph} = \sum_{q} \left[\alpha(q) e^{(-i\vec{q}.\vec{r})} a_{\vec{q}}^{+} + c.c. \right] \tag{2.1.25}$$

Where $a_{\vec{q}}^{+}$ is the creation operator for the phonon in the mode $\vec{q}$. The Fröhlich interaction strength for electron-optical-phonon scattering is given

$$|\alpha(\vec{q})|^2 = 2\pi\hbar\omega_{LO} \frac{e^2}{\epsilon_r \Omega q^2} \tag{2.1.26}$$

where $\epsilon_r^{-1} = \epsilon_\infty^{-1} - \epsilon_s^{-1}$, ϵ_s and ϵ_∞ are the static and high frequency permittivities, Ω is the volume of elementary lattice cell, $E_{LO} = \hbar\omega_{LO}$ is the energy of the optical phonon which has been assumed to be dispersionless while a linear dispersion is taken for the acoustic phonons. The strength of the electron-acoustical-phonon interaction is given by.

$$|\alpha(\vec{q})|^2 = \frac{C_0}{\Omega} \hbar\omega_q \tag{2.1.27}$$

Ferreira and Bastard have evaluated some scattering times for electrons in quantum wells and have also explicitly calculated lifetimes for the GaAs/AlGaAs material system [73].

Using Eqs. 2.1.25 and 2.1.26 the scattering rate from an initial state $|i, k_i\rangle$ to all final states $|f, k_f\rangle$ due to longitudinal-optical-phonon emission at zero temperature can be computed from [73]

$$\tau_i^{-1} = \frac{m^* e^2 \omega_{LO}}{2\hbar\epsilon_r} \sum_j \int_0^{2\pi} d\theta \frac{I^{ij}(Q)}{Q} \tag{2.1.28}$$

Q is given

$$Q = (k_i^2 + k_f^2 - 2k_i k_f cos\theta)^{1/2} \tag{2.1.29}$$

$$k_f^2 = k_i^2 + \frac{2m^*}{\hbar^2}(E_i - E_f - \hbar\omega_{LO}) \tag{2.1.30}$$

E_i, E_f are the energy of initial and final state, respectively and θ is the angle between the in-plane wavevectors k_i and k_f. $I^{ij}(Q)$ is defined as

$$I^{ij}(Q) = \int dz \int dz' \chi_i(z)\chi_j(z) e^{\left[-Q\left|z-z'\right|\right]} \chi_i(z')\chi_j(z') \tag{2.1.31}$$

Which is equal to δ_{ij} if $Q = 0$ and which decays like Q^{-1} at large Q values.

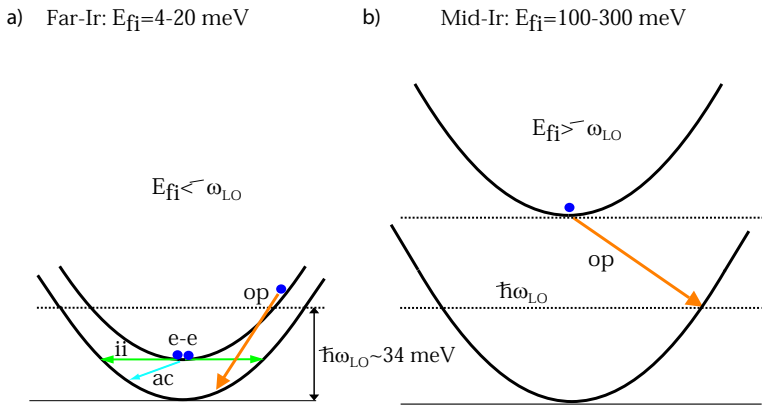

Figure 2.6: Schematic view of important intersubband scattering mechanisms for narrow (a) and wide (b) quantum wells, where the energy separation E_{fi} is larger or smaller than the optical phonon energy $E_{LO} = \hbar\omega_{LO}$, respectively. For (a), the mechanisms dominant are the electron-electron scattering (e-e), ionized-impurity scattering (ii), acoustic phonon emission (ac) and thermally activated LO-phonon scattering (op). For (b), optical phonon emissions is the dominant scattering mechanism (op).

Only the high energy tail of the thermal electron distribution can emit LO-phonons.

In a terahertz QCL, the radiative state separation is less than the longitudinal-optical-phonon energy $E_{fi} < E_{LO}$ (Fig 2.6.(a)), and relaxation by phonon emission is blocked at low temperature. The rate of non-radiative relaxation is then fixed by the ionized impurities or the acoustic phonons. These processes are relatively slow with the characteristic times located between 10 ps and 1 ns for polar semiconductors like GaAs for example [74, 75]. For intersubband energies larger than the optical phonon energy $E_{fi} \geq E_{LO}$ (Fig. 2.6.(b)), optical phonon emissions is the dominant scattering mechanism. The associated typical lifetime is about 1ps [73, 76]. It is a function of the wave-vector Q intervening to satisfy the rule of conservation of the momentum. It increases when the vector Q and intersubband

energy increase. A typical life time value of $\approx 0.2 - 0.3$ps for an intersubband transition separated by $E_{fi} \approx E_{LO}$ and, of ≈ 0.6 ps for $E_{fi} \approx 3E_{LO}$.

2.1.4 Resonant tunneling transport

The original proposal of optical gain via photon-assisted tunneling for a strongly biased superlattice in which the ground state is lifted above the first excited of the adjacent well has been given by Kazarinov et al [2]. This theoretical treatment based on a detailed density matrix analysis marks the basic idea of unipolar lasers based on intersubband transitions in semiconductor heterostructures.

As illustrated in Fig. 2.7.a, at zero electric fields, the states of superlattice are characterized by minibands E_j with a width δ_j assumed much smaller than the minigaps of width Δ ($\delta_j << \Delta$). Under an applied electric field F in the growth direction of SR, the energy of mini-band j of the (n)-th period is given by:

$$E_j^n(\vec{k_\perp}) = E_j - edFn + \frac{\hbar^2 \vec{k_\perp}^2}{2m^*} \tag{2.1.32}$$

where d is the superlattice period. When the transmitted energy (edF) to the electron by the electric field for one period is larger than the width of mini-band δ_j, the electrons become localised within one period, and can tunnel to the next site along the electric field and transfer the energy edF to the lattice vibrations or to the transverse motion because of the scattering.

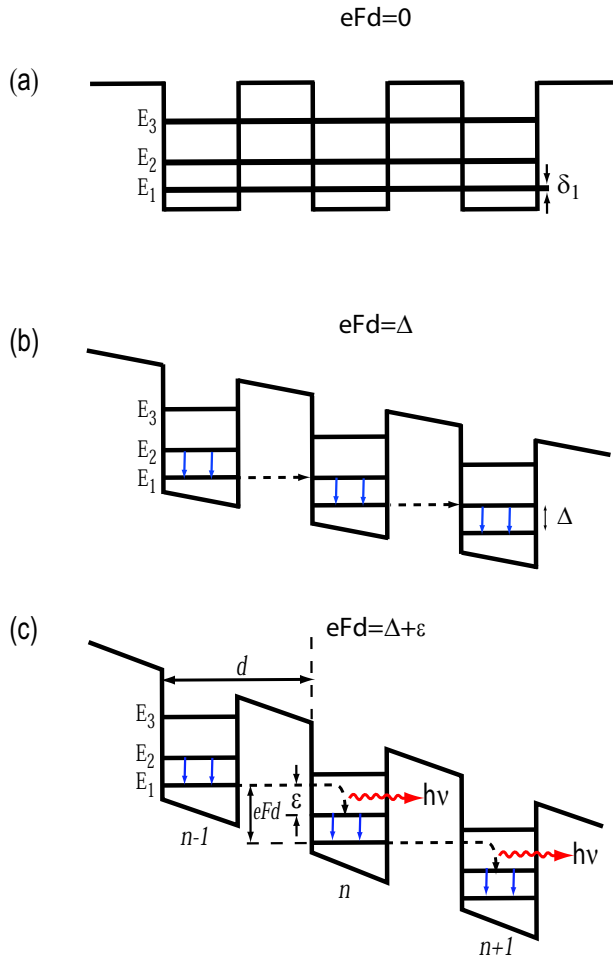

Figure 2.7: Schematic representation of the superlattice proposed by Kazarinov and Suris for far-infrared emission. The photon should be emitted during an interwell or diagonal photon-assisted tunneling transition between the ground state of the n-th well and the first excited state of the adjacent $(n+1)$-th well.

If $edF > E_2$-E_1=Δ, where d is the superlattice period, E_1 and E_2 are the energies of the ground state and the first excited state respectively, the first excited level in the n-th well lies below are ground-state level in the $n-1$-th well. Under these conditions (see Fig. 2.7), Kazarinov and Suris predicted that amplification may occur due to the possibility of

tunneling of electrons from the ground state in the $n-1$-th well to the excited state in the (n)-th well accompanied by the simultaneous emission of a photon of energy $\varepsilon = eFd-(E_2-E_1)$. Following non-radiative transitions from the excited to the ground state within one well the electrons are "recycled" for another photon-assisted tunneling process.

Calculations give the following expression of the current density J [2, 77]

$$J = edN_s(1 - e^{-\frac{\Delta}{kT}})\frac{2|\Omega|^2\tau_\perp}{1 + \epsilon^2{\tau_\perp}^2 + 4|\Omega|^2\tau_2\tau_\perp} \tag{2.1.33}$$

$$\hbar\epsilon = edF - \Delta \tag{2.1.34}$$

Where e is the electronic charge, N_s is the electron sheet density, Ω is the Rabi frequency given by:$\Omega = F\left\langle \phi_1^n \left| z \right| \phi_0^{n+1} \right\rangle$, $\tau_\perp$ is the relaxation time for the momentum in the plane of the layers, the time constant τ_2 represents the lifetime of an electron in the upper laser level and $\varepsilon = eFd - (E_2 - E_1)$ is the emitted photon energy. The factor $(1 - exp(-\Delta/kT))$ takes into account the difference between the populations of the ground and first excited states of an electron in a cell.

When the two energy levels are in resonance, i.e., when $\varepsilon = eFd-(E_2-E_1)$ is equal to zero, equ. 2.1.33 gives the maximum attainable current density:

$$J_{max} = edN_s(1 - e^{-\frac{\Delta}{kT}})\frac{2|\Omega|^2\tau_\perp}{1 + 4|\Omega|^2\tau_2\tau_\perp} \tag{2.1.35}$$

Even if this structure makes it possible to have a population inversion between two subbands,

on the other hand it has an intrinsic instability due to the absence of resonant injection which does not make it possible to establish a stable electron operation. Infact, the essential difficulty which appears in the realization of such structure, comes from inhomogeneous electric field along the superlattice due to space charge injection. This problem was solved in 1994 by Faist, by the introduction of collector/injector regions between the active quantum wells. In the following section I will discuss the principle of this idea.

2.2 Quantum cascade lasers

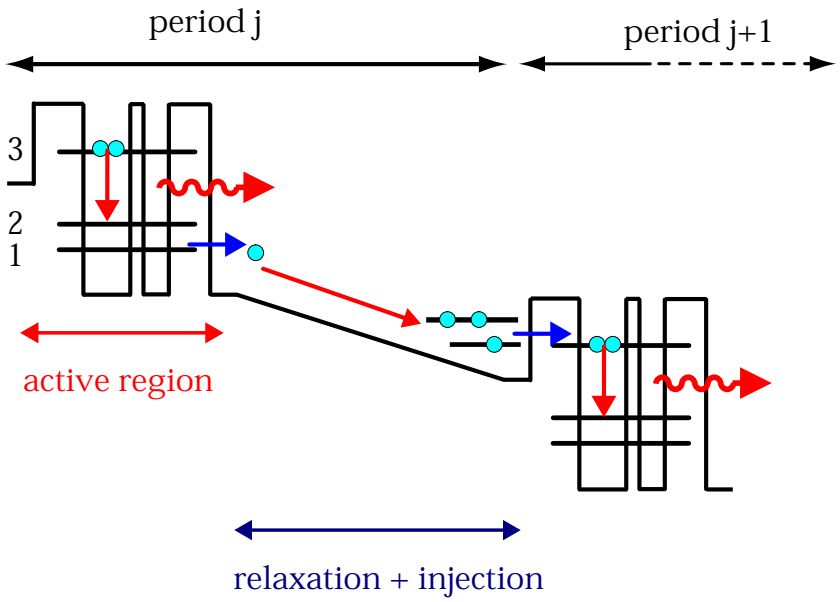

Figure 2.8: Quantum cascade design philosophy: each repeated period consists of an active (gain) region followed by a relaxation/injection region. From the injector region the electrons are injected into the upper laser energy level (3) of the active section. Here the laser transition takes place. After that, the electrons loose energy via a non-radiative transition (between level 2 and 1) and enter the next stage by tunnelling.

The Quantum Cascade laser is a semiconductor laser involving only one type of carriers (electrons) and is therefore called a unipolar laser. It was invented and first demonstrated in 1994 [46]. The Quntum Cascade consists of a repeating structure in which each repeat unit is made up of an injector and an active region. In the active region a population inversion exists and electrons transition to a lower energy level emitting photons at a specific wavelength. The electrons then tunnel between quantum wells and the injector region couples them to higher energy level in the active region of the subsquent repeat unit (Fig. 2.8).

Compared to conventional (interband) lasers, the quantum cascade laser has the following advantages: First, the emission wavelength is primarily a function of the QW thickness. For this reason, the quantum cascade laser can be designed to emit at any wavelength over an extremely wide range using the same combination of materials in the active region. Second, it is based on a cascade of identical stages (typically 20-50), allowing one electron to emit many photons, emitting more optical power. Finally, intersubband transitions are characterized by an ultrafast carrier dynamics and a small linewidth enhancement factor, with both features being expected to have significant impact on laser performance. It is intrisically more robust (no surface recombination) since the dominant non-radiative recombination mechanism is optical phonon emission and not Auger effect (as it is the case in narrow-gap materials), it allows intrinsically higher operating temperature. As of now, it is still the only mid-infrared semiconductor laser operating at and above room temperature.

2.2.1 basic properties

Optical gain

We start with basic three-level model system shown in Fig. 2.2.43. The laser transition occurs between $|3\rangle$ and $|2\rangle$ levels with densities n_3 and n_2. Electrons are injected into level $|3\rangle$ with a current density J and an injection effeciency η, where they either relax to level $|2\rangle$ and $|1\rangle$ and to the injector wih a total rate $\tau_3^{-1} = \tau_{32}^{-1} + \tau_{31}^{-1} + \tau_{esc}^{-1}$, where τ_{32} and τ_{31} are optical-phonon-emission processces and τ_{esc} is the electron escape by tunneling in the continuum. The depopulation rate of the lower level is τ_2^{-1}. At terahertz frequencies the spontaneous emission lifetime is typically much longer (microseconds) compared to the non-radiative lifetimes (picoseconds), so radiative relaxation plays no role in transport below threshold. The rate equations relating the sheet densities n_2 and n_3, The photon density S (per unit length per period) and their derivatives read.

$$\frac{dn_3}{dt} = \eta\frac{J}{q} - g_c S(n_3 - n_2) - \frac{n_3}{\tau_3} \tag{2.2.36}$$

$$\frac{dn_2}{dt} = (1-\eta)\frac{J}{q} + \frac{n_3}{\tau_{32}} + g_c S(n_3 - n_2) - \frac{n_2}{\tau_2} \tag{2.2.37}$$

$$\frac{dS}{dt} = \frac{c}{n}\left\{[g_c(n_3 - n_2) - \alpha]\right\} S + \beta\frac{n_3}{\tau_{sp}} \tag{2.2.38}$$

Where g_c is the gain cross section, c is the velocity of light in vacuum, and n is the mode refractive index. The total optical losses $\alpha = \alpha_W + \alpha_m$ are the sum of the waveguide α_W and mirror α_m losses.

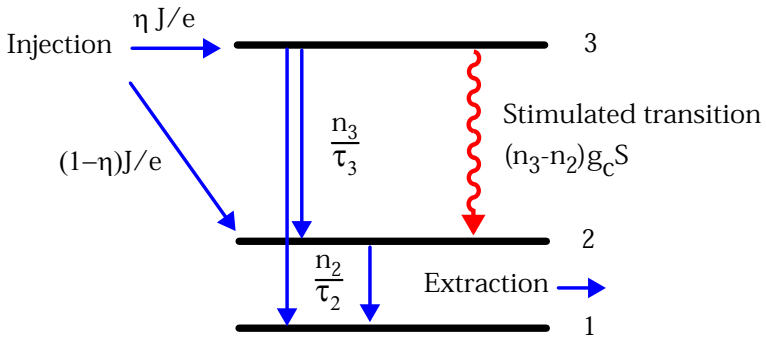

Figure 2.9: A simpliefed dynamic diagram of population in quantum cascade laser, three level model of the active region is used where n=3 and n=2 are the upper and lower states of the laser transition, respectively. The ground state n=2 is depopulated through a sequential tunneling to the relaxation/injection region of the structure.

Solving for the rate equations in the stationary state ($\frac{dn}{dt} = 0$), we obtain population inversion:

$$\Delta n = n_3 - n_2 = \frac{\frac{J}{q}(\eta + \frac{\tau_2}{\tau_3}(1-\eta) - \frac{\tau_2}{\tau_{32}})}{\frac{1}{\tau_3} + g_c S\left[1 + \tau_2(\frac{1}{\tau_3} - \frac{1}{\tau_{32}})\right]} \tag{2.2.39}$$

Assuming a unity injection effeciency (perfect injector $\eta = 1$) into the upper state $|3\rangle$, The equilibrium inversion at the absence of an optical field is obtained from Eq. 2.2.39 by setting S=0 and is:

$$\Delta n = n_3 - n_2 = \frac{J}{q}(1 - \frac{\tau_2}{\tau_{32}})\tau_3 \tag{2.2.40}$$

It is evident from Eq. 2.2.40 that gain in quantum cascade laser requires $\tau_{32} > \tau_2$, i.e., extraction of carries from the lower laser level must be more rapid than re-population by

carries which have been non-radiatively scattered from the upper laser level.

Threshold current

The threshold condition is obtained from Eq. 2.2.38 by setting the derivatives and S to zero. Neglecting the spontaneous emission, the threshold current J_{th} is

$$J_{th} = \tau_3 \frac{1}{q} \frac{\alpha / g_c}{1 - \frac{\tau_2}{\tau_{32}}} \tag{2.2.41}$$

With

$$g_c = \frac{4\pi q^2}{\epsilon_0 n \lambda} \frac{z_{32}^2}{2\nu_{32} L_p} \tag{2.2.42}$$

Using Eq. 2.2.40 the gain coefficient g (in m/A) of a QC laser can be writen.

$$g = \tau_3 (1 - \frac{\tau_2}{\tau_{32}}) \frac{4\pi q}{\epsilon_0 n_{eff} \lambda} \frac{z_{32}^2}{2\nu_{32} L_p}, \tag{2.2.43}$$

Where z_{32} is the dipole matrix element between states 3 and 2, λ is the wavelength of the emitted ligth in vacuum, ϵ_0 the vacuum dielectric constant, $2\nu_{32}$ is the full-width at half maximum (FWHM) of the intersubband electroluminescence, n_{eff} the effective refractive index of the mode and L_p is the the length (thickness) of one period of active region and injector.

Losses

After determining the gain coefficient, i.e. gain per current density, the second important factor for the threshold current are the losses experienced by the light traveling in the

waveguide. Three major losses are discernible. First, the laser resonator will be formed by two semitransparent mirrors, typically un-coated, as-cleaved, and parallel semiconductor facets. They provide a reflectivity that can be approximate by $R = (\frac{n_{eff}-1}{n_{eff}+1})^2$ each.

$$\alpha_m = -\frac{1}{2L} \ln(\mathrm{R}_1 \, \mathrm{R}_2) \tag{2.2.44}$$

Where L is the length of the resonator, R_1 and R_2 are the reflectivity . This loss can certainly be reduced using high-reflection coating at the mirror facets. $R_1 = 0.31$ and $R_2 = 0.98$ for a GaAs/air interface and GaAs/ZnSe-Au interface, respectively.

The second important source of losses is free-carrier absorption in the doped semiconductor regions and the metallic contact layers. While the influence of the metallic layers can be partially suppressed as will be shown later in section. 2.4, the semiconductor Drude losses are unavoidable. We shall call them waveguide losses α_W.

A third source of potential absorption losses are resonant intersubband transitions. Due to the considerable optical dipole matrix element of interminiband transitions, it is in general conceivable that the electrons in the injector region can cause significant absorption if there are optical transitions resonant with the laser wavelength present. It is therefore necessary, but generally achievable, during the design of the QC-laser active regions and injectors that such resonantly absorbing intersubband or interminiband transitions are avoided.

The threshold current density is determined by the condition. [46, 78].

$$Re^{(\Gamma G_p - \alpha)L} = 1 \tag{2.2.45}$$

Where $G_p = gJ_{th}$ is the peak material gain at threshold and α is the total loss. We can then recast Eq. 2.2.45 in the form:

$$g\Gamma J_{th} = \alpha_W + \alpha_m, \tag{2.2.46}$$

Where Γ is the fraction of the guided optical mode that overlaps with the active region of the laser. Γ is called the confinement factor and the quantity $g\Gamma$ is called the modal gain as opposed to the material gain.

Slope efficiency

After the calculation of the laser threshold, knowledge of the loss mechanisms also lets us estimate the slope efficiency, i.e. the increase in optical power (per outcoupling facet) per unit current, as

$$\frac{\partial P}{\partial I} = N_p h\nu\alpha_m \frac{\partial S}{\partial J} = N_p \frac{h\nu}{q} \frac{\alpha_m}{\alpha_W + \alpha_m} \frac{\tau_{eff}}{\tau_{eff} + \tau_2}, \tag{2.2.47}$$

Where P is the optical output power, I is the injection current, $h\nu$ is the photon energy, $\tau_{eff} = \tau_3 (1 - \tau_2/\tau_{32})$ is the effective lifetime and N_p the number of stages of active regions and injectors. In the rate equations just described, we assumed implicitly that the injection effeciency η is unity into state 3, i.e., each electron leaving the injector is going into state 3. It is obvious that a large number of stages will result in a large slope efficiency, and subsequently a large optical output power in general; values in the range of W A^{-1} and Watts, respectively, are common. A study of the performance of QC lasers as a function of the number of stages

also demonstrated what we termed unit cascade efficiency, i.e. that within the experimental error all stages of a cascade are in fact participating in laser action [79].

2.3 Terahertz quantum cascade lasers

QC electroluminescence in the 1-10-THz region was reported by several groups of researchers, [13, 14, 15, 16, 17, 18] lasing was achieved only in 2002 [19]. Significant issues to be addressed included the difficulty of obtaining population inversion at such small transition energies and the need for low-loss waveguide that will provide sizable confinement of the optical mode in a thickness compatible with available growth techniques.

For a long time, it had been assumed that achieving intersubband laser threshold would be easier in the far-infrared (i.e., for photon energies below the optical phonon energy: $h\nu < \hbar\omega_{LO}$) than in the midinfrared because of the absence of optical phonon emission at low temperatures [2, 4, 80, 81].

In fact, it is established that the emission probability of a polar optical phonon is reduced considerably as soon as the intersubband energy transition is lower than $\hbar\omega_{LO}$, consequently, the upper state lifetime increases, which is favorable to keep the population inversion. However, other non-radiative mechanisms, like the electron-electron (e-e) scattering, electron-impurity scattering, interface roughness scattering, or the interaction on acoustic phonons, become the interactions limiting the performances at terahertz frequency, when $h\nu < \hbar\omega_{LO}$. The e-e interaction is not easily controllable with the temperature as in the case of the interaction with the phonons. It depends on many parameters, like the sheet doping density, and of

multiple space covering.

The problem related to the waveguide was overcome by use of a special low-loss waveguide (α_w= 5-10 cm^{-1}) with confinement factors of as much as 30 %. This waveguide exploits the surface plasmons that exist at the interfaces that separating materials with negative dielectric constants (metals and highly doped semiconductors) from the low-doped stack of active regions and the semi-insulating substrate [19, 82, 83](see Sec. 2.4.3).

The first terahertz spontaneous emission in intrawell transition was observed in QCL by Rochat et al. [13] in 1998, where depopulation was dependent solely upon resonant tunneling in a narrow-band superlattice, rather than by LO-phonon depopulation. The breakthrough finally came in October 2001 from Köhler et al. [19] demonstrated the first terahertz quantum cascade laser based on GaAs superlattice structure, which operated at 4.4 THz ($\lambda = 68\mu$m).

2.3.1 The various proposed structures of terahertz QCL

Since their first demonstration in 2001 many designs of terahertz QC lasers have emerged, and can basically be characterized by three active region types: chirped superlattice (SL), bound-to-continuum, and resonant phonon (Fig. 2.10). A few characteristic and high-performance of each structures will be reviewed in the following.

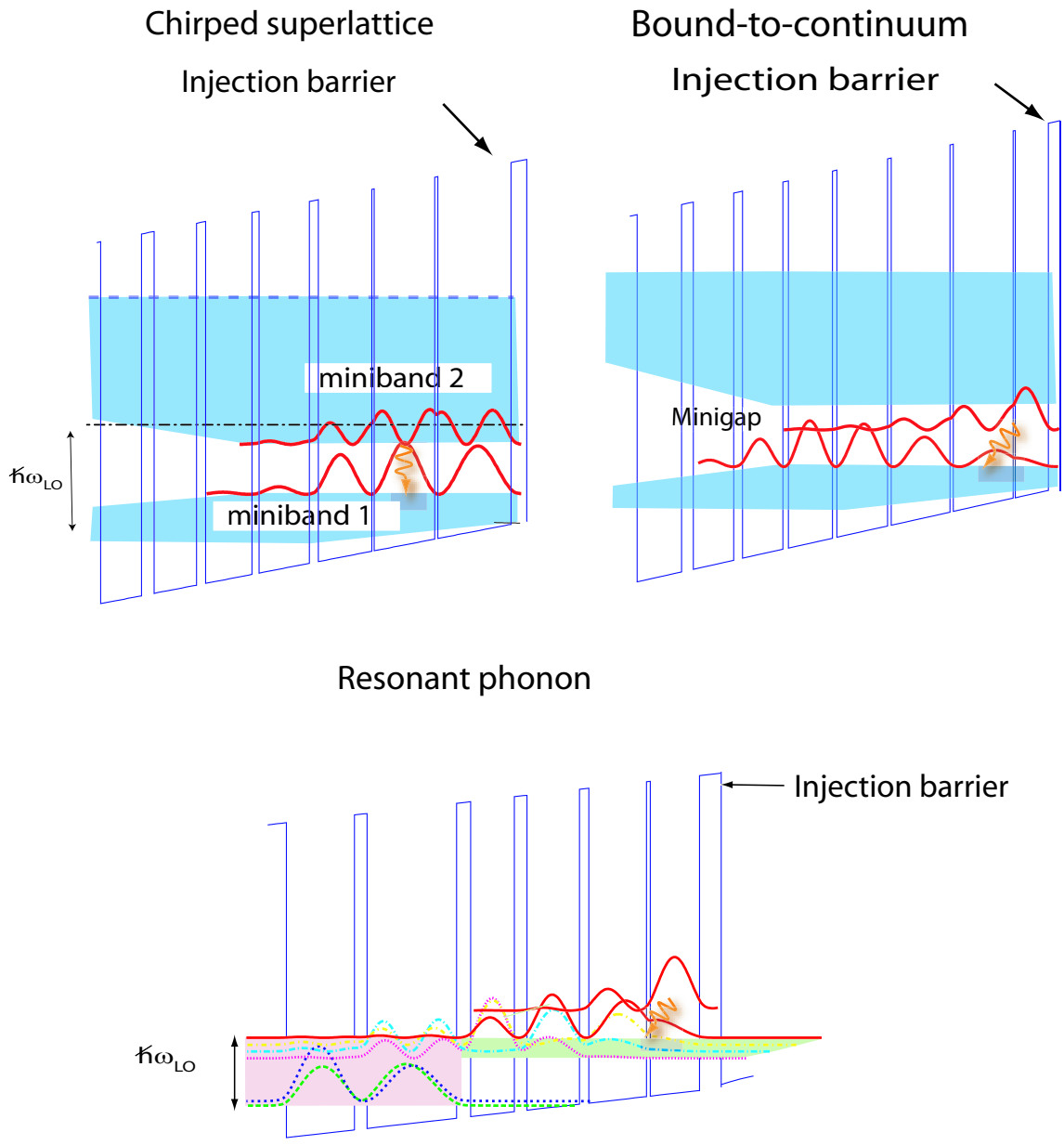

Figure 2.10: Schematic diagrams of successful terahertz QCL active regions.

Chirped-superlattice

The Chirped superlattice is the first successful stuctures showed an operation quantum cascade laser in the terahertz frequency [19, 20], which have been previously used for mid-infrared QCLs [84]. Active regions based on chirped superlattices [84] are promising candidates for long wavelength operation because the population inversion mechanism is based on a phase space argument and not specifically on optical phonon emission. Figure. 2.10 illustrates an example interminiband SL-QC laser concept based on GaAs/$Al_{0.15}Ga_{0.85}As$ material system. In short, laser action takes place between minibands, rather than between the subbands of few- and single [85] well active region QC-lasers. To first order, the miniband width is determined by the barrier thickness, and the minigap is determined by the well width.

In terahertz QCLs where the miniband width is typically less than the LO-phonon energy, the electrons of the lowest miniband was extracted by electron-electron scattering, electron-impurity scattering, and interface roughness scattering and inject them into the second miniband of the following one. This design facilitates electron extraction and simultaneously reduces the probability of non-radiative scattering from the upper laser level into the lower laser level. This type of structure has the advantage that the applied electric field is compensated by a gradually varying SL and at minibands can be obtained without dopants. In addition, SL-QC lasers excel through their high gain, and very large oscillator strengths due to the large spatial extent and overlap of the wavefunctions [86].

Using this concept, at 3.5 THz, low-threshold-current densities of 95 and 115 A/cm^2 were demonstrated, in pulsed and continuous-wave operation, respectively by Köhler et al [87].

Bound-to-continuum transition

In the active region presented in the previous paragraph, the upper and lower state wavefunctions extend (for THz lasers) over few (3-8) coupled quantum wells. "Chirping" the quantum well and barrier thickness restores the large dipole matrix element existing between the states at the edge of the minigap [88]. The main limitations in slope efficiency and maximum operating temperatures for these devices were attributed to a thermal backfilling of the lower miniband and a weak population inversion. For this reason, Scalari et al investigated anoher design conept, based on a bound-to-continuum transition [89, 22, 23]. Instead of an inter-miniband transition, the emission process takes place between an isolated state created inside a minigap by a thin well adjacent to the injection barrier and the lower miniband. As the chirped superlattice, depopulation of this design occurred via electron-electron scattering and resonant tunneling inside a wide ($\simeq$ 17 meV) miniband. Due to the diagonal nature of the laser transition, both the injection efficiency and lifetime ratio (upper to lower state) are maximised, while miniband transport is employed as an efficient extraction mechanism to minimize the lower state population. It is the combination of long lifetime and good injection efficiency of the upper state with an excellent extraction efficiency of the lower state that is especially advantageous in terahertz QC lasers, where population inversion is difficult to achieve. Long-wavelength ($\lambda \simeq 16\mu m$), high performance QC lasers based on this design concept operating above room have already been demonstrated [90]. At terhertz frequency, the bound-to-continuum design has displayed improved performance over the original chirped superlattice design. Notably, pulsed operation up to 100 K at 3.5 THz has been observed, with CW powers up to 50 mW at 10 K [23].

Structure based on a resonant phonon extraction

A new class of terahertz quantum cascade lasers based on resonant phonon depopulation have been presented, latest two years [91, 25, 92, 93, 94]. This design is fundamentally different than the two previous terahertz QCL designs, as it does not rely on a superlattice for depopulation, but rather uses combination of resonant tunneling and direct electron-LO-phonon scattering. The use of direct LO-phonon depopulation has two potential advantages. First, depopulation via LO-phonon emission is a fast, robust mechanism which doesn't depend very much on temperature or the electron distribution. Second, the large energy separation between the injector states and the lower radiative state ($\geq$ E_{LO} = 36 meV) provides intrinsic protection against thermal backfilling of the lower radiative state. Recently, a design that combines the advantages of the bound-to-continuum approach together with the use of an LO phonon resonance to enable fast scattering of the carriers out of the lower miniband has been demonstrated high performance operation [94]. At this time, in pulsed mode, the maximum operating temperature is 164 K from a resonant-phonon design with a low-loss metal-metal waveguide [92] (92 K in a SI-surface-plasmon waveguides) [25], and is 116 K from a bound-to-continuum transition combined with an optical phonon extraction design where a double-metal waveguide is used (98 K in a SI-surface-plasmon waveguides) [94]. A laser has recently been demonstrated at 3.6 Terahertz in the $In_{0.52}Al_{0.48}As$-$In_{0.53}Ga_{0.47}As$/InP material system using the same concept design [24].

2.4 Waveguide design

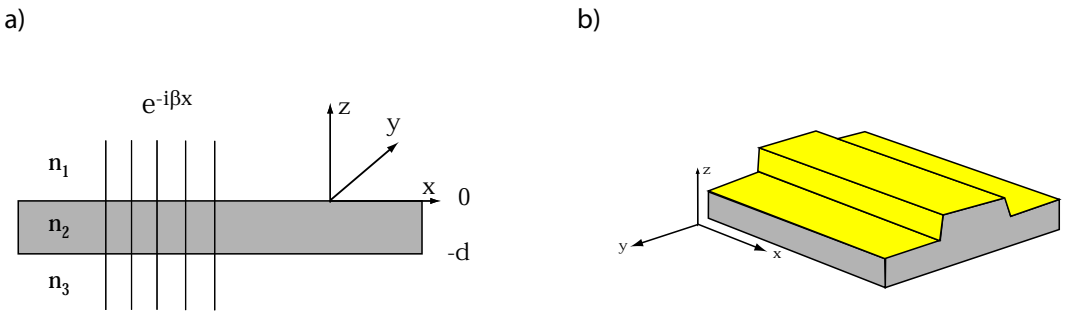

Figure 2.11: a) Waveguide geometry of wave plane. A dielectric waveguide is composed of a core with an index of refraction n_2 and a cladding with a refractive index n_1, n_3. A light beam inside the core will be totally reflected at the interface if $n_2 > n_1$, n_3 and if its angle of incidence θ than a critical angle θ_c. b) Waveguide ridge in quantum cascade laser.

There are two main components to obtain laser action semiconductor: a low-loss waveguide resonator with large optical confinement, and gain, which is conveniently derived from population inversion. Basically, a resonator used in quantum cascade lasers is a ridge-waveguide schematized in fig. 2.11.a. Light propagates along the ridge ($\vec{x}$-direction) and is reflected at the back and front mirrors. Mode confinement in the $\vec{y}$-direction results from the etching of the ridge. In the mid-infrared, dielectric waveguides is employed to achieve confinement in the growth direction ($\vec{z}$-direction) and is obtained by growing low refractive index cladding below and above a high refractive index active region (Fig. 2.11.b). Such a waveguide can be modeled in a slab model, where the structure is assumed to be infinitely extended in the x, y directions and processes a finite dimention in the z-direction. A mode of a dielectric waveguide at a frequency ω is a solution of the wave equation that, can be written as

$$\nabla^2\vec{E}(\vec{r}) + k^2n^2(\vec{r})\vec{E} = 0, \tag{2.4.48}$$

where $\vec{E}$ is the optical electric field, n($\vec{r}$) is the refractive index, $\vec{r}$=(x,y,z) and $k = \omega/c$, with c is the speed of light in vacuum.

The mode is given by a wave traveling in x direction with a propagation constant β

$$\vec{E}(\vec{r},t) = E(y,z)e^{[i(\omega t-\beta x)]} \tag{2.4.49}$$

The wave equation. 2.4.48 becomes

$$(\frac{\partial^2}{\partial y^2} + \frac{\partial^2}{\partial z^2})\vec{E}(y,z) + \left[k^2n^2(\vec{r}) - \beta^2\right]\vec{E}(y,z) = 0. \tag{2.4.50}$$

The basic features of the behavior of dielectric waveguide can be extracted from a planar model in which no variation exists in one (e.g., y) direction ($\Rightarrow \frac{\partial}{\partial y} = 0$). Putting $\frac{\partial}{\partial y} = 0$ in 2.4.50 and writing it separatly for regions 1, 2, 3 yield

$$\frac{\partial^2}{\partial z^2}E(y,z) + \left[k^2n_j^2(\vec{r}) - \beta^2\right]E(y,z) = 0, \tag{2.4.51}$$

With j=1, 2 and 3 if $x > 0$, $-d < x < 0$ and $x < -d$, respectively. Guided mode is obtained only if the propagation constant β satisfies $kn_1 < kn_3 < \beta < kn_2$ (i.e., the refractives indices of the three layers satisfay $n_2 > n_1$, n_3). In this propagation regime, modes decaying exponentially in layer 1 and 3 and having a sinusoidal shape within layer 2, the values of allowed β are discrete, the number of modes depends on the width d, the frequency and the

refractives indices of the three layers.

A detailed derivation for transverse-electric (TE) and transverse magnetic (TM) modes in symetric and antisymetric waveguides can be found in ref. [78]. For TE modes of the waveguide in the symetric case ($n_1 = n_3$), introdusing the following solutions

$$E_y(z) = \begin{cases} Aexp(-kz) & forz \geq 0 \\ Bcos(\alpha z) + Csin(\alpha z) & for - d \leq z \leq 0 \\ Dexp(k(z+d)) & forz \leq -d \end{cases} \tag{2.4.52}$$

in the Eq. 2.4.51 and, applying the continuity conditions for these solutions and their derivates ($\partial E_y(z)/\partial z = 0$) at both z=0 and z=-d, one obtained.

$$\begin{cases} tan(\alpha d) = \frac{2k\alpha}{\alpha^2 - k^2} \\ \beta^2 + \alpha^2 = n_1^2 k^2 \\ \beta^2 - k^2 = n_2^2 k^2 \\ k = \omega/c \end{cases} \tag{2.4.53}$$

The problem is thus to find, for a radial frequency ω and a given thickness d of guide, the constant of propagation β which satisfies simultaneously all the conditions (2.4.53). The multilayer equation is solved according to a transmission matrix formalism [95], to yield the propagation constants β for the guided modes of the waveguide. The various modes of a guide is represented by the dispersion curve $n_{eff}(\lambda)$, where n_{eff} is the effective index given by $n_{eff} = \beta/k = \beta c/\omega$). The effective index n_{eff} is the eigenvalue for the mode. For lossless

guides, n_{eff} is real. For guides with complex valued of permittivity electric ϵ, the effective index is complex, and is given by $n_{eff} = n + i\kappa$ where $\kappa > 0$ corresponds to loss, and $\kappa < 0$ to gain.

2.4.1 Mid-infrared waveguides

In the mid-infrared quantum cascade lasers, dielectric waveguides can be used to confine mode radiation in the vertical (growth) direction [96]. In the material system most commonly used with QC lasers at present, the InP substrate with a refractive index $n_{InP} \cong 3.10$ and AlInAs with a refractive index $n_{AlInAs} \cong 3.20$ are natural cladding layers for the waveguide core. The latter consists of the stack of 500 or more alternated ultra-thin layers of InGaAs and AlInAs. The refractive index of this stack is usually modelled through a linear interpolation between the refractive indices of AlInAs and InGaAs ($n_{InGaAs} \cong 3.49$) according to the volume fraction of the two constituents. It is therefore clearly higher, often around $n_{QC-stack} \cong 3.35$, than the refractive indices of the cladding layers. In order to increase the average refractive index of the waveguide core even more, in particular when the actual cascade stack is chosen rather thin, i.e. with a small number of stages, the active region and injector stack is sandwiched between two several hundred nanometres thick InGaAs layers.

So far, we have only given the refractive indices of the materials without taking into account their doping levels. However, being the QCL a current injection laser, all or at least a significant portion of the waveguide layers have to be doped for carrier transport(fig. 2.12). Free-carrier absorption in these layers, and at high doping levels the strongly noticeable onset of the plasma edge, usually reduce the refractive index by a few per cent over the

purely dielectric value. In addition a noticeable attenuation coefficient is introduced, which is ultimately responsible for the waveguide loss α_W.

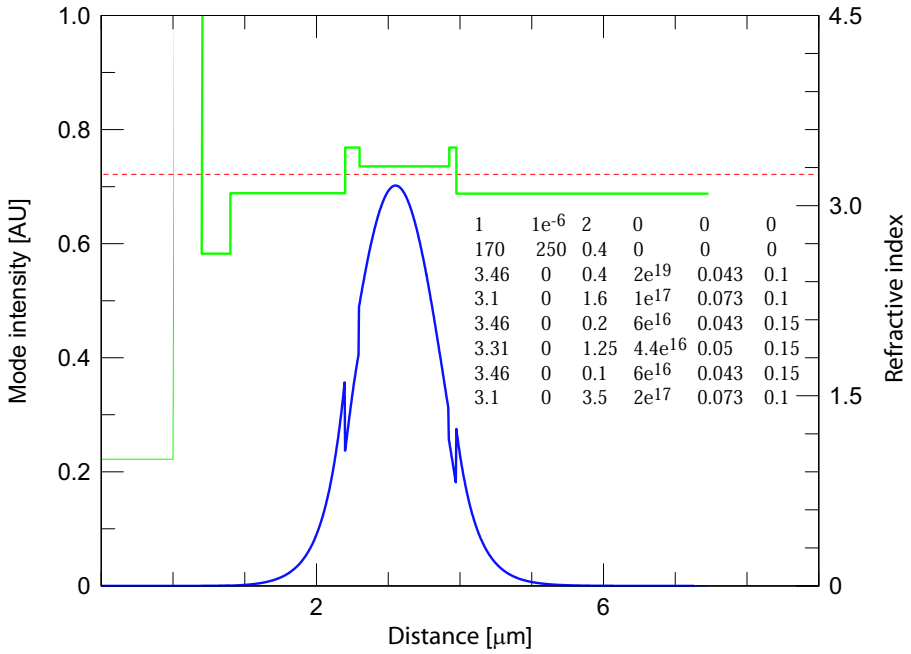

Figure 2.12: Mode intensity of dielectric Waveguide of quantum cascade laser for a laser wavelength of 3.5 μm.

In addition to the free-carrier loss from the doped semiconductor layers, the coupling of the mode with the metal can introduce a large additional waveguide loss. This problem was solved by the introduction of a thin highly doped InGaAs layer between the top metal contact and the semiconductor [83]. In this case, we raised the refractive index of the plasmon mode resulting an enhancing of the difference of the effective refractive indices of the plasmon and laser modes. Nevertheless, a combined study of the reduction of the refractive index and the increase of the attenuation coefficient with doping level suggests using InGaAs for wavelengths longer than $\cong$ 5 μm, while using AlInAs for shorter wavelengths.

QC lasers have not only been fabricated in the InGaAs/AlInAs on InP material system but also in the GaAs/AlGaAs system. There, the substrate, GaAs, has the highest refractive index, and does not, therefore, provide a natural cladding layer. Furthermore, in order to achieve a strong index contrast between the GaAs/AlGaAs multilayer core and AlGaAs cladding layers, a high-AlAs-mole-fraction material would have to be used for the latter. This is, however, generally ill advised as it difficult to dope this material at a sufficiently high level for efficient current transport [9]. Sirtori et al [97] and other groups [98, 99, 100, 101] working on GaAs-based QC lasers therefore employ with great success plasmon-enhanced dielectric waveguides with highly doped GaAs for both claddings.

At longer wavelength QC lasers, dielectric waveguide is hindered for two reasons. First, the thickness of the cladding layers is at least in the order of $\lambda/2$ in the material, becomes incompatible with MBE growth yet. These layers would increase the growth time, add to the thermal resistance and increase dramatically the number of defects below the active region. Second, loss due to free carrier absorption increases as λ^2 for frequencies above the plasma frequency.

The solution introduced by Sirtori et al [102] is the surface-plasmon waveguide [103, 10]. Surface plasmons are a peculiar solution of Maxwell's equations at the interface between materials posessing dielectric constants of opposite sign.

The modes are not supported by a layered transparent medium but are electromagnetic surface waves (surface plasmons) at a metal-semiconductor interface. No additional confinement layer is needed because the amplitude of the optical wave decreases exponentially in the two directions normal to that interface. These guided TM modes occur at the interface

between two media that have dielectric constants opposite in sign, as is the case with a metal and a semiconductor. Therefore the metal layer, which is usually deposited as an electrical contact upon the top surface of a semiconductor laser, is now deposited directly above the active region of the device and used as a guiding interface. However, surface waves at a metal-dielectric interface suffer from high optical losses because the mode penetrates partly into the metal.

For electromagnetic surface waves the modal losses depend strongly on the dielectric constants of the materials. The attenuation coefficient α can be written as [5]

$$\alpha \cong \frac{4\pi n n_d^3}{\kappa^3 \lambda} \tag{2.4.54}$$

where n and κ are the real and the imaginary parts of the complex refractive index of the metal, respectively, n_d is the refractive index of the dielectric, and λ is the wavelength in vacuum. The approximate equality holds because the dispersion of the metals in the mid-IR is such that the value of κ is typically much larger than those of n and n_d. In the previous equation, it is apparent that the losses at the interface are inversely proportional to λ and can be minimised by choosing metals having a refractive index with a strong imaginary component ($\kappa >> n$, i.e., dielectric constant almost real and strongly negative). The free carrier loss in the doping level and active region is calculated using the Drude-Jensen model which is discussed in the next section (2.4.2).

The advantages of this approach are the complete suppression of the cladding layers, a higher confinement factor of the laser-active region compared with those of a conventional layered

semiconductor waveguide, and strong coupling to the active material, which could be used in devices such as distributed-feedback lasers. These advantages have to be traded against the disadvantage of increased absorption losses. A QC laser device based on this waveguide configuration has been demonstrated at long wavelengths with a so-called three quantum well [104] or chirped superlattice [105, 106, 103, 10] QC structures.

2.4.2 Drude model

The Lorentz-Drude (LD) model is a simple phenomenological approach based on the classical dispersion theory. In this model, conduction electrons are treated as free to move under the influence of an applied field $E(t) = \Re eE(\omega)e^{-i\omega t}$, subject only to a collisional damping force. The probability of a collision during an interval dt is dt/ τ , where τ is the scattering time, or equivalently, the average time between collisions.

The equation predicts a frequency dependent conductivity for the Drude model is as follows:

$$\sigma = \frac{ne^2\tau}{m^*(1 - i\omega\tau)} \tag{2.4.55}$$

where n is the carrier density, τ is the critical scattering time, ω is the light pulsation, and m^* is the effective carrier mass. The Drude theory for conductivity is used to obtain the contribution to the complex permittivities for the semiconductor and metal layers that results from free carrier effects. If the frequency dependent permittivity $\epsilon(\omega) = \epsilon_{core} + i\frac{\sigma}{\tau}$

The dielectric constant (or function), which describes the optical properties of media, is then defined as:

$$\epsilon(\omega) = \epsilon_{core} + i\frac{\sigma}{\tau} = \epsilon_{core}\left[1 - \frac{\omega_p^2\tau^2}{1+(\omega\tau)^2} + i\frac{\omega_p^2\tau}{\omega(1+(\omega\tau)^2)}\right] \tag{2.4.56}$$

where $\omega_p^2 = \frac{ne^2}{m^*\epsilon_{core}}$ is the plasma frequency of the materia and ϵ_{core} is the core permittivity. For a given frequency, the semiconductor can be made to behave either as a dielectric ($\Re(\epsilon) > 0$) or a plasma ($\Re(\epsilon) < 0$) by the proper choice of carrier concentration. When $\omega\tau >> 1$ the conductivity is purely imaginary ($\sigma = i\frac{ne^2}{m^*\omega}$) and the dielectric permittivity expressed in Eq. 2.4.56 have the folowing form.

$$\epsilon(\omega) = \epsilon_{core}\left[1 - \frac{\omega_p^2}{\omega^2} + i\frac{\omega_p^2}{\omega^3\tau}\right] \tag{2.4.57}$$

When the radiation frequency is lower than the plasma frequency ($\omega < \omega_p$) the permittivity is negative ($\epsilon < 0$) and the index of refraction $\bar{n} = n + i\kappa = \sqrt{\epsilon}$ is purely imaginary ($\bar{n} = i\kappa$). For $\omega >> \omega_p$ the dielectric constant is slightly reduced by the factor $\left[1 - \frac{\omega_p^2}{\omega^2}\right]$ and the free carrier loss is given by

$$\alpha_{fc} = \frac{\omega_p^2}{\omega^2}\frac{1}{c\tau}\sqrt{\frac{\epsilon}{\epsilon_0}} = \frac{ne^2\lambda^2}{4\pi^2 m^* c^3\tau\epsilon_0}\sqrt{\frac{\epsilon_0}{\epsilon}} \propto \frac{\lambda^2}{\tau} \tag{2.4.58}$$

2.4.3 Terahertz-waveguide

Despite the single surface-plasmon waveguide solution provides very high performance for longwavelength ($\lambda = 17 - 24\mu$m) QC lasers [105, 106, 103, 10], it is clear from waveguide calculations that for the realization of far-infrared QC lasers ($\lambda \geq 50\mu$m)(fig. 2.13.a), the waveguide design must be further improved.

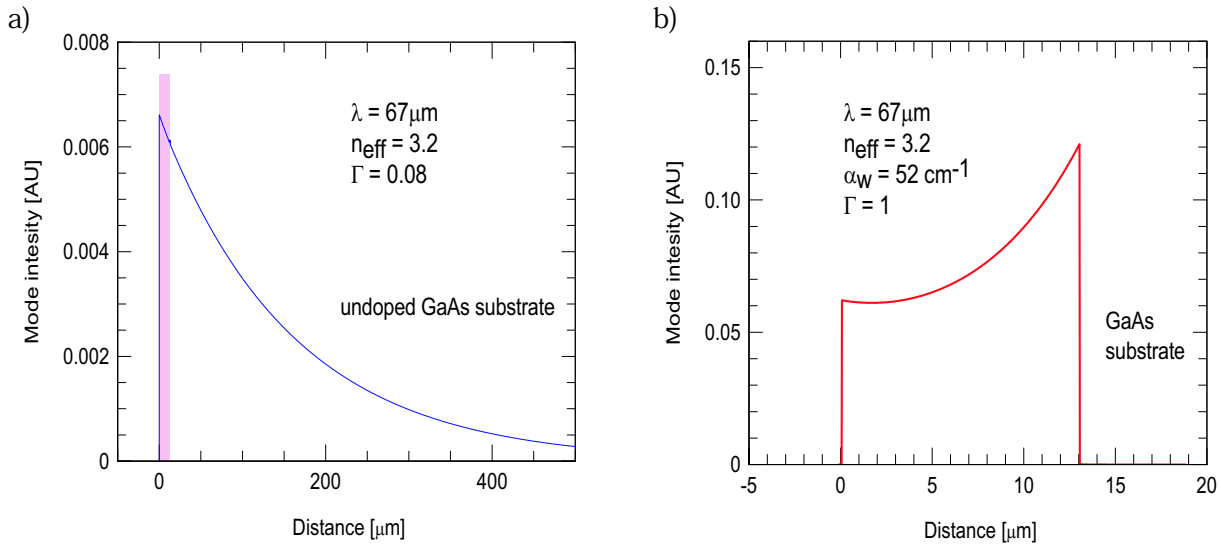

Figure 2.13: a) The computation for a mode of 67 μm wavelength bound to the interface between a gold layer and an undoped GaAs substrate. The very long decay into the semiconductor renders the overlap with any active core of reasonable thickness very small;to highlight this the 0.08 averlap with a 13 um thick stack has been shaded. b) The computation for a mode of 67 μm wavelength in a doped 13 μm-thick GaAs layer sandwiched between gold on the left and a high-doped GaAs substrate on the right. a close to unity confinement is achieved but at the expense of high propagation losses.

Ideally, at THz frequencies, the waveguide should be based on a metal-semiconductor-metal geometry, but fabrication difficulties suggest that replacing the bottom metal with a highly doped n^{++} semiconductor layer to obtain high mode confinement. For this reason, the low-doped GaAs layer directly below the cascade stack was replaced by a thick (1-2 μm) highly doped ($n = 5 \times 10^{18}\,\mathrm{cm}^{-3}$) InGaAs layer [107]. This highly doped semiconductor acts as a bottom metal, thus realizing a double surface-plasmon waveguide, with an extremely high

confinement factor $\Gamma = 0.99$ (fig. 2.13.b).

In this waveguide, the mode is confined between the upper metallic contact and a thick (1-2 μm) heavily semiconductor doped ($n = 5 \times 10^{18}\,\mathrm{cm}^{-3}$) GaAs layer grown over the n+ GaAs substrate $n = 1 - 2 \times 10^{18}\,\mathrm{cm}^{-3}$.

Despite the fact that the first observation of intersubband electroluminescence in the terahertz frequency took place in the double surface-plasmon waveguide QC, no terhertz laser from this approach has been achieved due to the high optical losses of the waveguide. The optical loss at THz frequencies of such a waveguide was measured by Rochat et al [108] at $\lambda = 75\mu$m by mean of a multisection single-pass technique. They found a value $\alpha_W = 42 \pm 20 cm^{-1}$m, in agreement with calculations based on free carrier absorption. It is obvious from waveguide calculations that the majority part of the optical losses is due to free carrier absorption in the lower cladding layer and doped substrate due to the significant skin depth. For this reason, Koehler et al [19] designed and fabricated a wavegide based on a semi-insulating GaAs substrates (Fig. 2.14).

This technique was first used in QC structures by Ulrich et al [82] in waveguides where the modes are bound to the upper metallic contact and a thin (0.1-0.7μm) heavily doped contact layer grown directly beneath the active region and above the semi-insulating (SI) GaAs substrate. Because the doped layer is thinner than its own skin depth, the mode extends substantially into the substrate. However, because the mode overlap with the doped contact layer is small, the free carrier loss is minimized. Surface plasmons at the interfaces between the burried contact layer and the core on one side and the semi-insulating substrate on the other exist, if the constant dielectric constant of the bottom contact layer is negative.

This can be achieved by adjusting the doping of the lower contact layer.

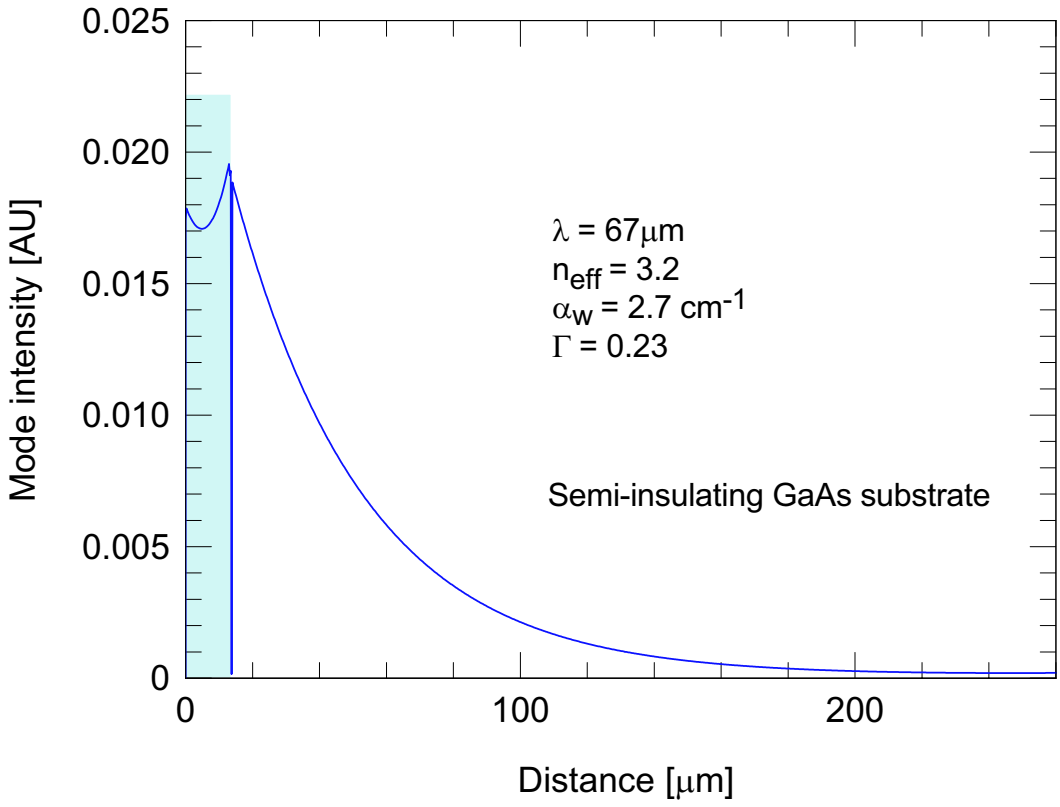

Figure 2.14: single plasmon quantum cascade laser Waveguide.

To investigate, the importance of this waveguide design compared to the double-plasmon structure in terahertz QCLs, Rochat et al have reported a comparison of the performances of a device based on the same three quantum well active region structure inserted in these two different waveguide designs [20]. The two waveguide sructures are displayed in Fig. 2.15 and are described in detail in the figure caption. The first waveguide is based on a double-plasmon structure formed by the Al metallic contact, grown in-situ in the MBE system on the upper side and a heavily n doped ($n = 5 \times 10^{18}\,\mathrm{cm}^{-3}$) GaAs layer on the other. The devices were then processed by etching successively the Al and the epitaxial layers down to

the substrate, to form 500 μm wide waveguides.

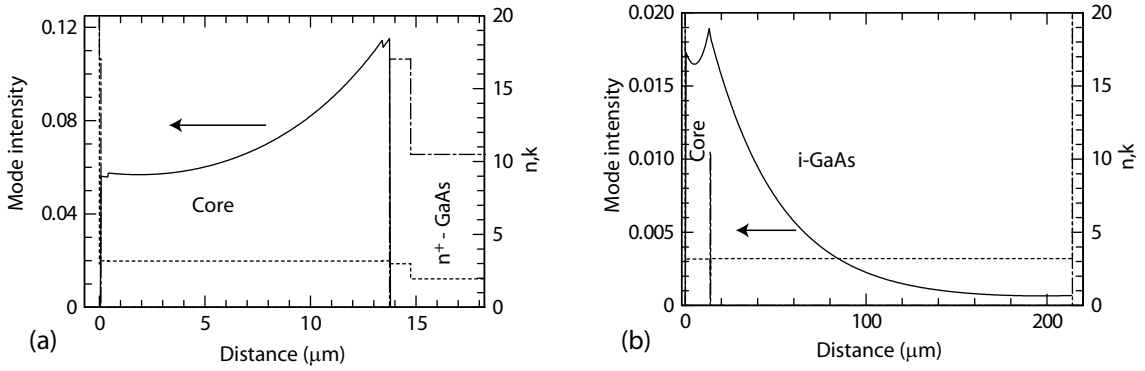

Figure 2.15: Refractive index and optical mode intensity as a function of distance of the far-IR waveguides used in this study. Both are formed with the same core, consisting successively, from the surface, of a 80 nm thick heavily doped ($n = 5 \times 10^{18}\,\mathrm{cm}^{-3}$) GaAs contact layer, an undoped, 10 nm thick $Al_{0.15}Ga_{0.85}As$ layer, an undoped 320 nm thick $Al_xGa_{(1-x)}As$ ($x : 0.15 \rightarrow 0$) parabolic grating, 120 periods of the active region, a bottom 320 nm thick $Al_xGa_{(1-x)}As$ ($x : 0 \rightarrow 0.15$) parabolic grating, and an undoped, 15 nm thick $Al_{0.15}Ga_{0.85}As$ layer. a) Double plasmon waveguide. The core is grown on a 1 μm thick heavily doped ($n = 5 \times 10^{18}\,\mathrm{cm}^{-3}$) GaAs contact layer, on top of the heavily doped ($n = 2 \times 10^{18}\,\mathrm{cm}^{-3}$) GaAs substrate. b) Single plasmon waveguide. The core is grown on a 300 nm thick, $n = 2 \times 10^{18}\,\mathrm{cm}^{-3}$ GaAs buried contact layer on top of an undoped GaAs substrate.

The computed value [20] of α_w for the waveguide used in this study is $\alpha_w = 47\,\mathrm{cm}^{-1}$ and the overlap factor displays also a large value $\Gamma = 0.95$. The second waveguide [82], similar to the single-plasmon waveguide used for long-wavelength mid-IR QC lasers [109], relies on the confinement provided by the interplay between a metallic reflection at the top metalization and the quasi-metallic confinement provided by a thin (0.3μm), heavily doped ($n = 2 \times$

$10^{18}\,\mathrm{cm}^{-3}$) buried contact. However, because of the large dielectric constant of the doped buried contact, the overlap factor between the field and the buried contact is very small, enabling a much lower computed value of the waveguide losses ($2.7\,\mathrm{cm}^{-1}$) than the double plasmon one. Even if the overlap factor has decreased to $\Gamma = 0.23$, the figure of merit $\Gamma/\alpha_w = 8.1 \times 10^{-2}\,\mathrm{cm}$ for the buried contact waveguide is much larger than for the double plasmon case, where $\Gamma/\alpha_w = 2 \times 10^{-2}\,\mathrm{cm}$. The buried contact layer must be heavily doped (in order for its dielectric constant to become negative); a thicker buried contact layer will lead to a larger value of the active region confinement at the cost of a larger loss, with an overall decrease of Γ/α_w.

The experimental results show, no lasing is obtained in the structure based on a double-plasmon waveguide. However, the single plasmon interface device reaches threshold at a current of $210\,\mathrm{A/cm}^2$.

Ideally, at THz frequencies, the waveguide should be based on a metal-semiconductor-metal geometry. A QC laser device based on a metal-semiconductor-metal configuration has been recently demonstrated by Williams and Scalari [92, 94].

2.4.4 Distributed feedback quantum cascade lasers

In the preceding paragraph, we describe QC lasers waveguides based on Fabry-Perot cavities. These lasers exhibited a relatively broadband, multimode operation which are acceptable for some spectroscopy applications targeting liquids and solids, where the characteristic absorption features are broad continuous bands-is not useful for demanding gas sensing applications. Applications such as remote chemical sensing and pollution monitoring require

a tunable source with a narrow linewidth. Distributed feedback (DFB) QC lasers provide a very elegant and reliable method to achieve the required single-mode operation. DFB QC lasers were first introduced in 1996 [8, 110] in mid infrared, providing continuously tunable single-mode laser output. Very rapidly they have evolved [110, 111, 112, 113, 114, 115] and have shown great promise in many different gas sensing applications [116, 117, 118, 119, 120]. As described in section 2.4.1, the top cladding of the conventional QC-laser waveguide is usually composed from several layers, low-doped inner ones capped by a highly doped layer. This characteristic QC-laser waveguide [83] provides several possibilities to produce a grating modulation strong enough to supply the necessary wavelength selective feedback. In essence, a grating with period Λ is incorporated into the waveguide, which lowers the threshold gain-by reducing the outcoupling loss-for a distinct wavelength close to the Bragg wavelength $\lambda_B = 2n_{eff}\Lambda$ (first order grating). Until now, two fundamentals methods are used to achieve single-mode operation for QC-DFB lasers: loss coupled QC-DFB lasers [8] and Index coupled lasers [110].

Mid-infrared QC-DFB lasers

- Complex-coupled QC-DFB lasers

In the Loss-coupled DFB lasers, the grating is etched into the surface of the waveguides. If the highly doped topmost waveguide layer is made thin or entirely removed and then directly overlaid with metal in a grating pattern, two fundamental phenomena appear. First, the waveguide loss in the position of the grating grooves is higher than in the non-etched portion of the grating, leading to a loss modulation of the waveguide. Secondly, the metal layer in

the grating grooves pulls the mode towards itself, giving it some characteristics of a surface plasmon. As the mode is pulled into the top-cladding layer, its effective refractive index is modulated. For these reason, these DFB lasers are are complex-coupled structures; i.e. they had both a modulation of the loss and the refractive index. The highly doped topmost waveguide (plasmon-enhancement) layer thickness was $> 0.6\mu$m and was only partly etched by the grating. The manufacture of these distributed feedback lasers is very simple and requires only one growth step at the beginning. The grating periodicity Λ can be adjusted a posteriori by trial and error on the grown layer.

Since the waveguide parameters (n_{eff}) strongly depend on the metal's dielectric function, a Bragg grating fabricated from alternating stripes of two different metals can have sufficient strength for single-mode operation at far-infrared wavelengths. Single-wavelength emission (17 μm) is achieved using a grating of alternating gold and gold-over-titanium stripes [106].

The grating strength can be roughly approximated by the coupling coefficientκ [95, 5, 121], which quantifies the amount of coupling between the forward and backward waves traveling in the cavity.

$$\kappa = \frac{\pi}{\lambda_B}\,\mathrm{n}_1 \; + \mathrm{i}\frac{\alpha_1}{2} \tag{2.4.59}$$

where n_1 is the amplitude of the periodic modulation of the real part of the effective index (n_{eff}) of the mode, induced by the grating of periodicity Λ. The corresponding modulation of the absorption coefficient has an amplitude α_1. For optimum performance in slope efficiency and threshold current, the product $\kappa L_{cav} \approx 3 - 5$ where L_{cav} is the cavity length, must be

kept close to unity.

Although this top grating approach yields quite good results and provides for a straight forward time-saving processing technology, it is located away ($\geq 2\mu$m) from the active region and the region of maximum intensity of the laser mode. Strong coupling is only attainable with a reduced upper cladding layer thickness. This increases the waveguide loss through the absorbing top metal layer and in turn decreases the performance of the DFB laser. A still higher level of performance can be reached using a grating etched directly inside the active region because it allows strong coupling with negligible additional loss. The characteristic of this DFB laser is described in the next paragraph.

- Index coupled QC lasers

Therefore, Gmachl et al took another, approach to QC-DFB lasers, which positions the grating close to the active waveguide core, where the mode intensity is high [110, 122]. In the first MBE cycle, the QC active regions section is grown embedded between two InGaAs layers. The upper InGaAs layer serves as the host region for the first-order grating. The latter is transferred by contact lithography and wet chemical etching. The wafer is then transferred back into another growth chamber, where an InP top cladding is grown on top of the Bragg grating using solid-source MBE. The grating strength is controlled by the grating depth and duty-cycle during grating fabrication (etching) and the reflow of material in the regrowth process.

Single-mode tuning of distributed feedback lasers

The heat dissipated in the device by the current is responsible for the temperature increase that leads to the red-tuning of the wavelength. As the temperature is increased both the Bragg resonance via the temperature dependence of the refractive index n_{eff} and the gain spectrum via the temperature dependence of the intersubband structure are shifted to longer wavelength. Changing the heat-sink temperature can certainly control the laser temperature The more common approach to temperature tuning QC lasers is through adding a dc current-ramp to the laser drive current. A larger current dissipates more heat in the laser and, therefore, very locally changes the temperature. Since a much smaller volume is involved, rapid temperature cycling, with rates around several 10 kHz, is possible.

Chapter 3

Experimental Setup and Fabrication

3.1 Experimental setup

In the first sections of this chapter, we describe the experimental setup which was developed to perform spectrum of THz radiation emitted due to spontaneous and/or stimulated emission. The second section of the chapter is devoted to the devices processing, both for FP and DFB samples emittinf at THz frequenties.

3.1.1 Spectral measurements

For terahertz spectral emission measurements, a Fourier transform infrared (FTIR) spectrometer is used as shown in Fig. 3.1. The central component of an FT-IR spectrometer is a Michelson interferometer and the signal is recorded as a function of the optical path difference between the fixed and the movable mirror. The light coming from the sample is collected by an off-axis parabolic mirror with an $f/1.5$ aperture and sent through a FTIR

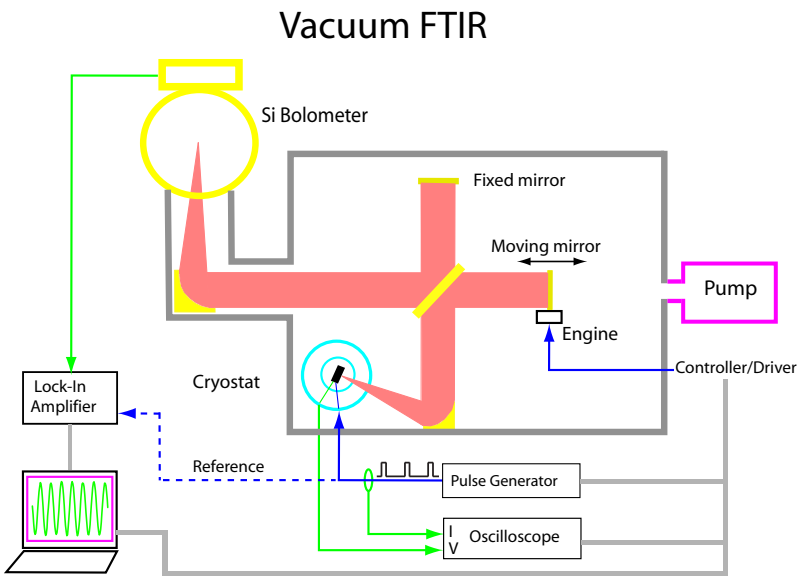

Figure 3.1: Experimental setup.

spectrometer in a liquid-helium cooled Si bolometer. The advantages of this techniques are e.g. the higher spectral resolution achievable.

Spectral measurements in the terahertz spectral range are complicated by the presence of strong atmospheric absorption, most of which is due to water. Not only does this reduce the total detected power, but the presence of pressure broadened absorption lines can make interpretation of spectra more difficult. This has been reasolved with a vacuum FTIR. It has been designed and built by our mechanical workshop. The spectrometer is mounted inside a vacuum chamber, and the sample mounted in vacuum on a copper cold plate, that could be cooled to 6 K with liquid helium (LHe) and is placed at the collecting mirror focal point and is positioned by the outside with a x-y-z manipulator. The bolometer is connected to the side of the vacuum chamber. The whole light path, from the sample to the detector is under vacuum. A dedicated LabView program fully controls the stepper motor together

with the sample current injection and light detection allowing fully automated multiple runs of spectral measurements.

Basically two different techniques are used: the rapid-scan and the step-scan technique. In the step-scan measurement the mirror is positioned and stabilized at every position x and then the measurement for this position is done. This technique is suited for long integration-times and when only very low signals are available. We used this technique together with an external Si bolometer detector and a lock-in amplifier to measure the electroluminescence or amplified spontaneous emission of our devices. The injected current is measured using a Model 711 calibrated current probe by ALS. This probe is an electrical transformer placed around the injection current line. The current and the bias on the device are measured by a LeCroy 9384L digital oscilloscope. The far-infrared emission was amplified by a EG G 7260 DSP lock-in amplifier synchronized with the pulse generator.

The whole experiment is driven via a GPIB network by a computer. Due to the slow response time of the bolometer, the injected current is modulated into low frequency macro pulses with a repetition rate of 1/T = 413 Hz matching the bolometers maximum detector frequency. To prevent as much as possible device heating, trains of 627 micro-pulses with a repetition rate of 520 kHz are produced during the macro-pulse durations. The maximum possible overall duty factor is 50 %.

In a rapid-scan measurement the mirror moves fast and continuously. We used this technique typically for measuring laser spectra where the signal is much stronger than the blackbody radiation of the environment which is a major noise source in this case.

Due to the low resolution achieved in the vacuum FTIR (0.24 cm^{-1}), high resolution (0.09

cm^{-1}) spectral measurements of the laser are performed using a commercial Nicolet 800 FTIR (Fig. 2.15 (a)) in the rapid-scan mode. In contratst to the Vacuum FTIR system which uses a stepper motor, the position being monitored by counting the steps, our Nicolet 800 system uses a linear motor with a HeNe laser fringe counter to monitor of position of the moving mirror. In this setup the cryostat is placed out the FTIR. Far-infrared transparent polyethylene windows are used to isolate the cryostat vacuum from atmospheric pressure. The light coming out from the sample is collected by a gold coated off-axis parabolic mirror with 60 degree collection aperture. The collimated light beam is then sent through the Fourier transform infrared spectrometer used with a 12 micron Mylar beam splitter(240-70 cm^{-1}). Leaving the FTIR, the light is collected with a 90 degrees aluminum plane mirror and sent on Deuterated Triglycine Sulfate (DTGS) detector operated at room temperature. The entire optical path is purged with dry air with a 20 to 30 % decrease of the water vapor absorption [123].

3.1.2 Terahertz detectors

The infrared detector translates the incoming infrared light into an electric signal. The detector element is a crystal of various chemical composition, mounted in a casing and behind an infrared transparent window to protect it from the environment. Infrared detectors can be divided into types: thermal detectors (As Bolometers, Deuterated Triglycerine Sulfate (DTGS) pyroelectric detectors) and quantum detector(As Mercury Cadmium Telluride (MCT) detectors). In terahertz frequencies, a thermal detectors are used. Thermal detectors, as the name implies, senses a change in temperature and convert this to a thermal

electromotive force (thermocouples), a change in resistance of a conductor (bolometers), or a movement acting on a diaphragm by an expansion of a gas (pneumatic detectors). Because of their slow response time, the thermal detectors are seldom used in modern FTIR systems. The exception is the pyroelectric bolometer.

Depending on the power of the laser, we used a silicon composite bolometer for the picowatt level range (Terahertz spontaneous emission), or a Deuterated Triglycerine Sulfate (DTGS) pyroelectric detectors for a power above $\cong$ 100 nW.

- Bolometers

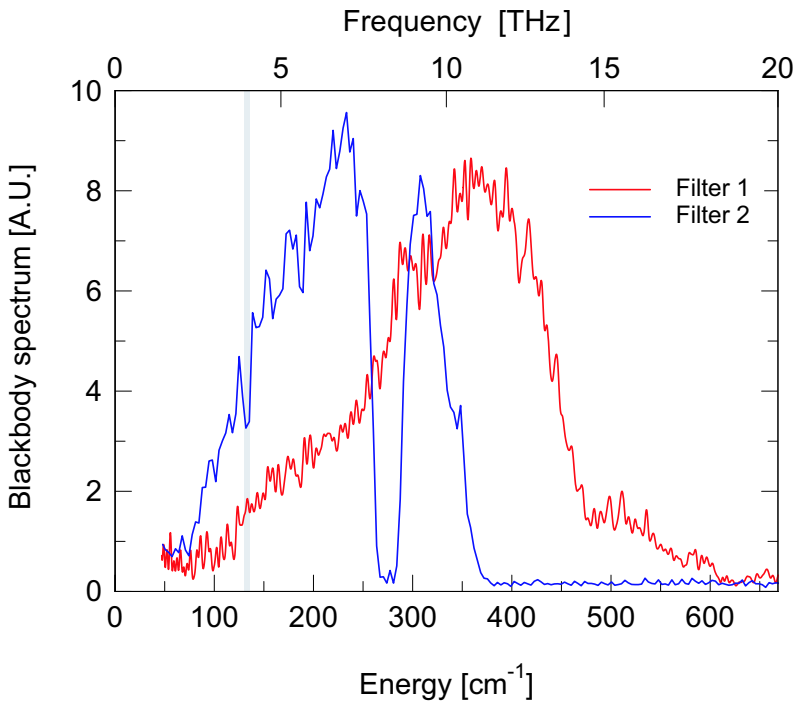

Figure 3.2: Blackbody spectra taken using Si bolometer at 4.8 cm^{-1} resolution with filters 1 and 2.

Terahertz spontaneous emission can be performed using either a silicon composite bolometer,

or a gallium doped germanium (Ge:Ga) photodetector, both of which required cryogenic cooling with LHe. A bolometer consists of an absorber attached to a thermal sensor. Incident radiant energy heats the absorber and is detected as a temperature rise.

The incoming light is collected via a windows onto the detector element, which is a blackened diamond thermal absorber 6 mm in diameter thermally bonded to a small silicon element. Since the detection is limited by the thermal response of the element which is on the order of milliseconds, the bolometer operates with a chopping frequency of not higher than 400 Hz (for the Si bolometer). The chopper frequency is then used as reference frequency for the lock-in amplifier. Ones Si bolometer has a response value of 35500 [V/W], not counting the preamplifier gain, which is usually set to 200. Two filters available have cut-on frequencies of 600 cm^{-1} (18 THz) and 350 cm^{-1} (10.5 THz) and are labeled 1-2, respectively. At 300 K, the measured spectral responses curves of the Si bolometer for both filters are shown in Fig. 3.2. We observe an absorption line at 132 cm^{-1} originates from the quartz window.

- Deuterated Triglycerine Sulfate (DTGS) pyroelectric detectors

Deuterated Triglycerine Sulfate (DTGS) pyroelectric detectors may also be used at THz frequencies, but typically have noise-equivalent powers in the μW range. DTGS detectors are the most common used infrared detectors because of their simplicity, their relatively low price and their robustness. Major drawbacks are the reduced sensitivity compared with Si bolometer detectors. The principle of working is the one of a pyroelectric bolometer: Changes in the amount of the incident infrared radiation result in a change of temperature of the DTGS element. The change of temperature is measured as a voltage across the detector

element. Our DTGS detector is equipped with two windows, a KBr and a polyethylene window, to cover the full spectral range. The KBr window can be used over the mid-infrared range from 4000 to 400 cm^{-1} and the polyethylene window can be used over the far-infrared range from 350 to 35 cm^{-1}.

3.2 Fabrication

3.2.1 FP Fir-processing

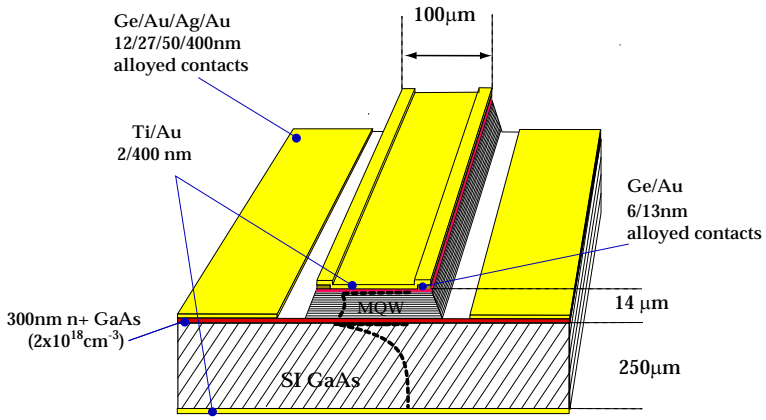

Figure 3.3: Schematic of the sample processing. The dashed line is the optical mode intensity in the transverse direction.

Our designs were grown by molecular beam epitaxy (MBE) first by Dr. Harvey Beere of cavendish laboratory (cambridge), and later by Dr. Mattaias Beck and Dr. Marcella Giovannini of the University of Neuchâtel. In general, a quantum cascade (QC) structure starts with a higly doped contact layer followed by the QC heteterostructure and is terminated by a top contact layer (Fig. 3.4). The FIR waveguides used for the samples in this thesis are based

on single interface plasmon grown on semi-insulating GaAs or InP crystals substrate [19, 24]. For the active region, $Al_{0.45}Ga_{0.65}As/GaAs$ or $In_{0.52}Al_{0.48}As/In_{0.53}Ga_{0.47}As$ materials systems were used as heterojunction material which were lattice-matched on a semi-insulating GaAs or InP substrate, respectively. The most commonly fabricated structures were edge emitting ridges, as shown in Fig. 3.3 [21].

The most generic processing sequence proceeds as schematized in Fig. 3.4. The processing starts by a cleaning sequence of trichloroethylene, acetone and isopropanol baths. The samples are then deshydrated at a temperature of 110 °C for 1 minutes. This deshydratation of the samples has shown to significantly increase the adherence of the photo-resist to the semi-conductor surface. AZ1518 photo-resist is then deposited on the samples and spinned at 5000 RPM. This allows to obtain an average thickness of 2 μm. The samples are then heated for 1 min at a temperature of 110 °C to dry the resist. The samples are then exposed to ultra violet light through a quartz window with patterns during 15 s. The exposed surface is then removed chemically by immersion of the sample into a developer (Microposit Developer/H_2O in the ratio of 1:3) for 45 seconds leaving the unexposed patterns. Stripes with a width of $60 - 100 - 150 - 200\,\mu$m and separated by a period of 500 μm are defined by a first photolithography step (a). Then the active region is etched down to the buried contact layer. Two bottom contacts are then evaporated on both sides of the stripes (Ge/Au/Ag/Au 12/27/50/400 nm alloyed at 400 °C during 1 minute) via electron-beam evaporation, and patterned via lift-off in acetone. A second photolithography is used (e) for deposited two $10\,\mu$m wide stripes (Ge/Au 6/13 nm alloyed at 320 °C for 1 minute) along the edges of the ridge (f). Another photolithography follows for the top contact (g). A Ti/Au confining

layer is furthermore evaporated which completely covers the top of the stripe (h). Substrate thinning down to 250 μm, and backside metallization (Ti/Au), complete the processing of the devices (i).

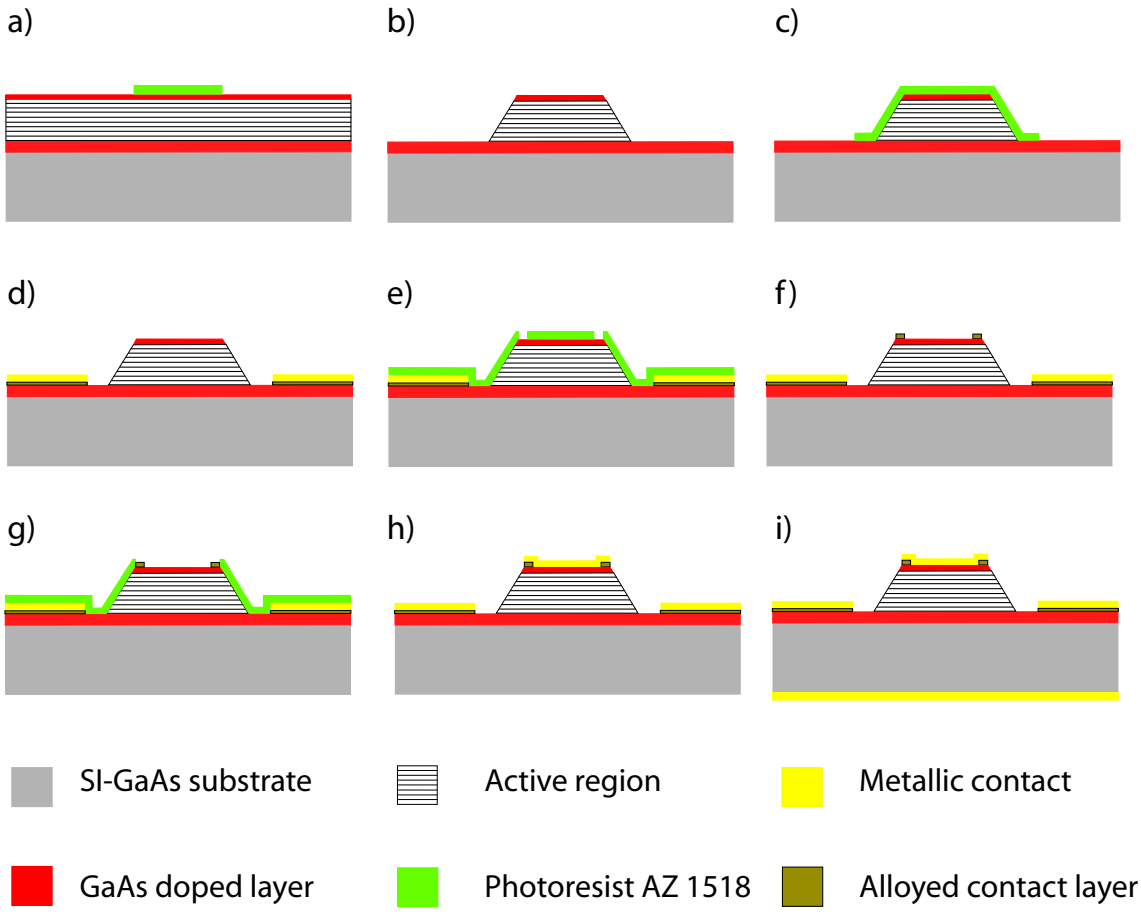

Figure 3.4: Schematic of the Steps for a simple stripe processing (Fabry-Perot cavity).

The etching is performed by the use of H_2SO_4 : H_2O_2 : H_2O for GaAs material system. The relative concentration of the various components is 1:8:1 that yield an etching rate of 0.16μm/s at room temperature while shaking the sample at 1 Hz. The rate can be controlled by changing the relative concentration of H_2O_2. The etch rate decreases with a decrease of

its concentration. In the InP material system, HBr : HNO_3 : H_2O or H_3PO_4: H_2O_2 : H_2O etching solution is used in the ratio of 1:1:10 or 3:4:3, respectively.

In contrary to HBr : HNO_3 : H_2O, the etchant H_3PO_4: H_2O_2 : H_2O (3:4:3) has the characteristic that it produces outwardly sloping sidewalls along both (011) and $(01\bar{1})$ sections.

A Fir processing with isolation layer was also performed (Fig. 3.5). This processing is similar to the one described obove for far-infrared measurements, but involves additional steps to enable a 600 μm-thickness Si_3N_4 isolation layer. As shown in figure. 3.5, 200 μm-wide nitride-injection sections which had a separation of 300 μm between each other were deposited. Top metallization of the 200 μm wide ridges was realized by egun-evaporation of Ti/Au (10/400nm). This processing was used for Fabry-perot and in particular for distributed feedbak quantum cascade laser described in the next section.

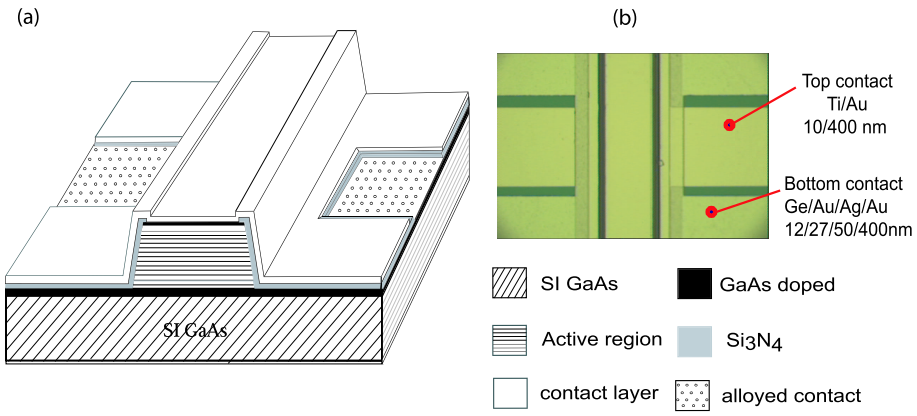

Figure 3.5: Schematic of the sample processing with isolation layer(Fabry-Perot cavity).

3.2.2 DFB Fir-processing

First order Bragg gratings of periodicity $\Lambda = \lambda/2\ n_{eff}$ (11.7, 11.9, 12, 12.2, 12.5 μm) were defined by contact photolithography and subsequently etched to a depth of 200 nm by wet chemical etching (see Fig3.6). A photoresist was then deposited in the etched portion of the grating, and alloyed contacts (Ge/Au/Ag/Au 12/27/50/400 nm alloyed at 400 C for 1 minute) evaporated along the stripe (above both mesa and photoresist). Ridge waveguides were next fabricated as similar to the one described in section. 3.2.1 with an isolation layer (fig. 3.5).

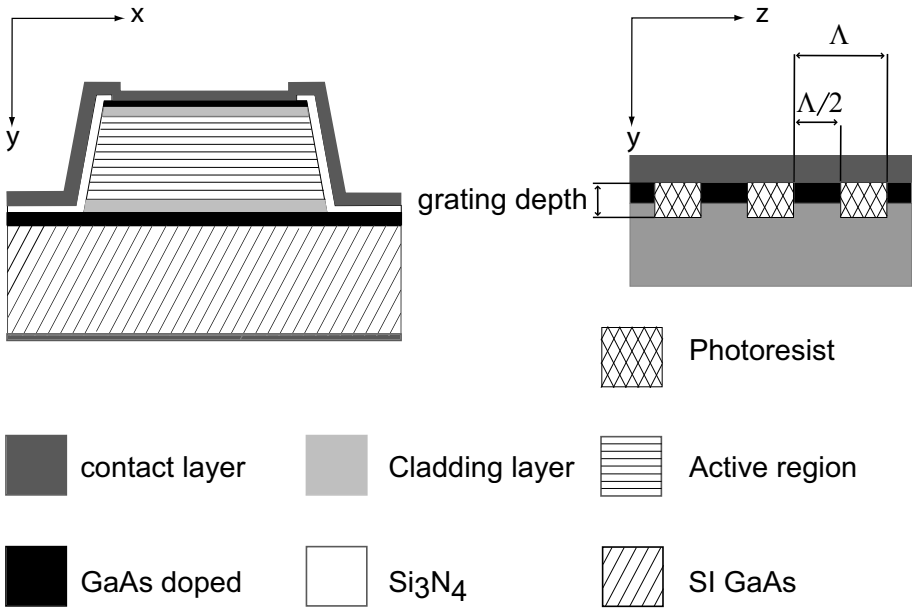

Figure 3.6: Schematic of the sample processing with isolation layer(Fabry-Perot cavity).

First-order Bragg gratings of periodicity $\Lambda = \lambda/2\ n_{eff}$ (= 11.5, 11.7, 11.9, 12, 12.1, 12.2, 12.5 μm) were exposed using optical contact lithography and subsequently etched into the surface

of the GaAs top contact layer and $Al_{0.15}Ga_{0.85}As$ cladding layer by wet chemical etching to a depth of $\cong$ 300 nm. The ridge waveguides were fabricated using standard processing techniques [124] with 600 nm of Si_3N_4 served as an electrical passivation layer and Ti/Au (10/400 nm) was used as top contact metal. Thinning, back contacting and cleaving into 1.25 mm-long cavities completed the processing.

Chapter 4

First generation of terahertz quantum cascade lasers structures

4.1 Introduction

The first terahertz QCLs were based on chirped superlattice designs [19], first proposed by Tredicucci et al. [84, 88], where miniband depopulation is used. In this chapter, we demonstrate that continuous wave operation of far-infrared may be achieved in structures based on a similar active region with a low-loss waveguide and cavity design.

4.2 Chirped superlattice active region

The structure, shown in Fig. 4.1, was composed of a chirped superlattice active region embedded in a single-plasmon waveguide. This structure consists of a three quantum

well active region followed by a four quantum well relaxation/injection region [125] in the $GaAs/Al_{0.15}Ga_{0.85}As$ material system.

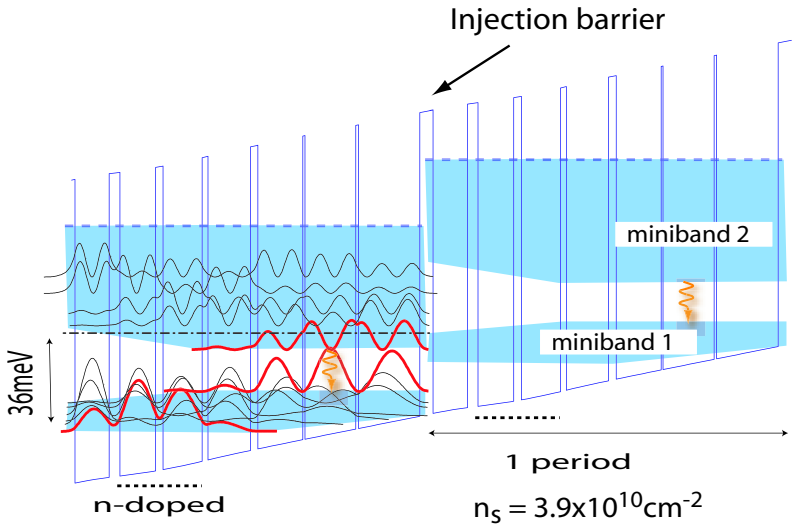

Figure 4.1: Computed conduction band profile of one stage of the structure under an average applied electric field of 3.15 kV/cm. The moduli squared of the relevant wavefunctions are shown. The layer sequence of one period of the structure, in nanometers, left to right and starting from the injection barrier is **3.0**/18.6/**0.7**/15.4/**0.5**/13.6/**2.3**/12.8/**1.8**/ 11.8/**2.3**/10.8/**3.2**/10.4 where $Al_{0.15}Ga_{0.85}As$ layers are in bold, GaAs in Roman and underlined number correspond to Si doped regions with $n = 1.6 \times 10^{16}\,\mathrm{cm}^{-3}$.

The computed band diagram and squared wavefunctions are displayed in Fig. 4.1 for an applied electric field of 3.15 kV/cm; the layer sequence is given in the figure caption. In a similar structure designed at $\lambda = 65\,\mu$m, a peak gain of 31 cm^{-1} at T = 80 K has been predicted by Monte-Carlo studies [126]. The states involved in the lasing transition with wavelength $\lambda = 65\ \mu$m (19.3 meV) between the two minibands are uniformly delocalized

over at least three quantum wells, which ensures a large dipole matrix element Z_{87}= 8.5 nm (f=37) with a scattering life-time τ_{87}=0.75 ps. The device was grown to use a Semi-insulating-surface-plasmon waveguide described in Sec. 2.4.3, using an 300 μm-thick lower contact layer doped at n = 2 $\times 10^{18}$ cm^{-3}. The waveguide was calculated to have α_W = 2.7 cm^{-1} and Γ = 0.23.

4.3 Experimentals results

4.3.1 Optimisation of the processing

The first processing (A2672b) used to characterise this wafer was fabricated similar to the standard processing described in the Sec. 3.2.1, except for two principal differences. An alloyed ohmic contacts (Ge/Au/Ag/Au) were deposited on top of the ridge and the lateral contacts were positioned away $\approx 15\mu m$ from the ridge. The purpose is to decrease the parasitic resistance outside the active region associated to the top and lateral contacts. The rear facet was HR coated with Au evaporated over ZnSe used as insulator to prevent short circuits. Lasing was not seen in any devices, with the longest tested being 2.7-mm-long and 210-μm-wide. A second ZnSe/Au HR coating was deposited on the front facet device except a window with a width of 30 μm in which the ligth intensity can be transmitted (Fig. 4.2), and a 210 μm-wide, 2.2-mm-long ridge was tested.

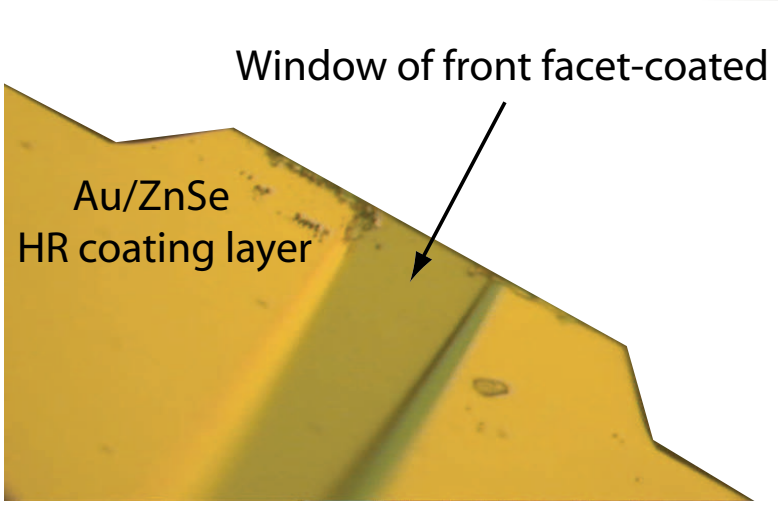

Figure 4.2: Schematic of the front facet coated. The ZnSe/Au HR coating was deposited on the front facet device, except a line covered by a gold wire bonds placed in the center, in the perpendicular growth direction to fabricate a window in which the ligth intensity can be transmitted.

Lasing at 4.65 THz ($\lambda = 65$ μm) was immediately obtained at a threshold current density of 295 A/cm^2 at 12 K. Typical emission spectrum above threshold are shown in Fig. 4.3(a). The emission frequency corresponds to an energy of 19.25 meV, in agreement to the calculated value of 19.30 meV. Measured optical power versus current (L-I) curves at low duty cycle (0.25%) are plotted in Fig. 4.3(b). Lasing is observed in pulsed mode up to 30 K with a peak power level of 4.2 μW at 12 K. The narrow width of the window would cause low slope efficiency (10 μW/A, at 12 K), which would explain the low peak output powers. Clearly the large threshold current density of our first generation of processing devices (A2672b) is an impediment to cw operation. Therefore, reduction of J_{th} is a priority for improving the performance of these devices.

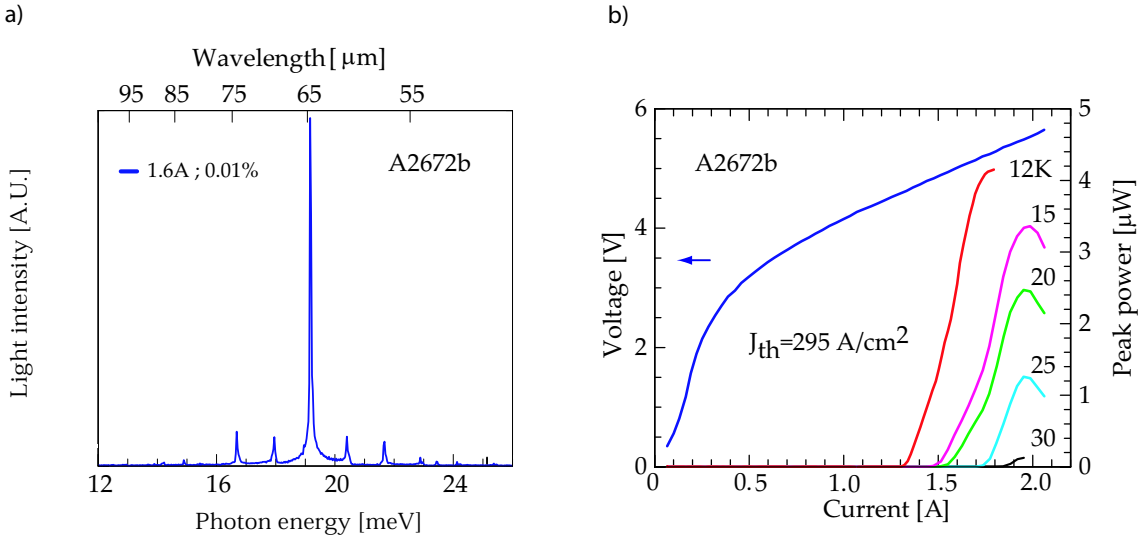

Figure 4.3: (a) Laser spectrum at a 0.25 % duty cycle for a 210 μm-wide, 2.2-mm-long device. (b) V-I and L-I characteristics for the laser with 2 facets coated as a function of temperature. Operation up to 30 K is observed.

A reduction of the threshold current density can be obtained by a reduction of the waveguide losses associated to the top and lateral metallic contact layers. To disentangle the separate influences of these factors on the threshold cureent density, first we compare this processing device (A2672b) to another device (A2672a) performed in another work [20] one based on the same wafer (A2672). The processing fabrication of A2672a is similar to A2672b, except for the top alloyed metalisation which is replaced by two small 10 μm wide Ge/Au/Ag/Au contacts stripes evaporated on the top side of the ridges followed by a 10/400 nm Ti/Au top metalisation.

Figure. 4.4 shows light output-current-voltage (L-I-V) of representative device of A2672a. The threshold current density $J_{th} \approx 210$ A/cm^2 is lower of about 85 A/cm^2 than that of our first laser processing (A2672b). From this comparison, we can conclude that the high

threshold current density of A2672b was partially due to the large waveguide loss brought about by the diffusion of Ge atoms towards the active region.

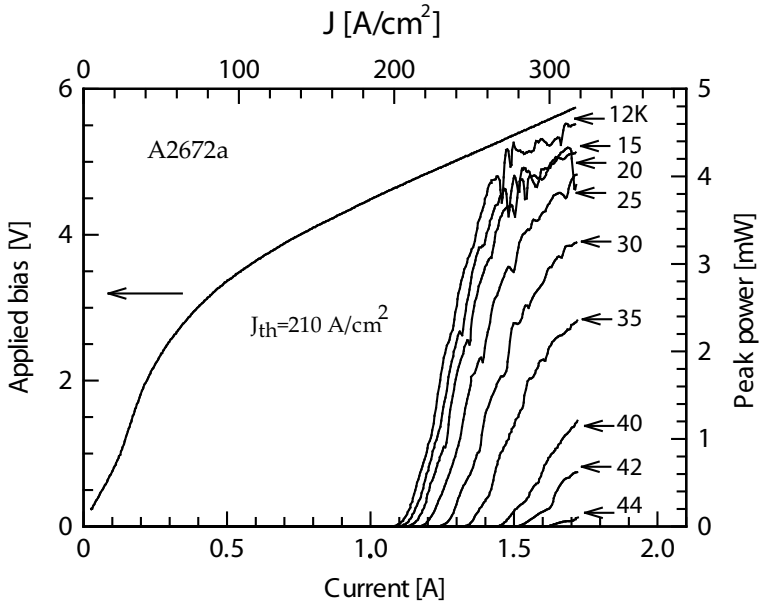

Figure 4.4: Peak optical output power versus injected current in pulsed mode at a duty cycle of $5 \cdot 10^{-5}$ at various temperatures, as indicated.

It was suspected that the coupling of the optical mode with the lateral contacts increase the waveguide losses. To investigate this point, a simulations have been performed at different separation distance D between the ridge and the edges of the lateral contacts for a far-infrared radiation at 65 μm and assuming zero losses in the semi-insulating GaAs substrate and a perfect edge of the lateral contacts. The metal used in the modeling was gold. Fig. 4.5 displays the variation of the ratio Γ/α with the separation distance D. For D $>$ 45 μm, the ratio Γ/α are almost constant, confirming that the ratio Γ/α becomes independent of D for D above 45 μm. However, Γ/α is decreased for D below 45 μm. Sidewall roughness may also play an increased role for narrower ridges, but this is unlikely, since the length scale of

the roughness ($< 3\,\mu$m) is smaller than $\lambda/10$.

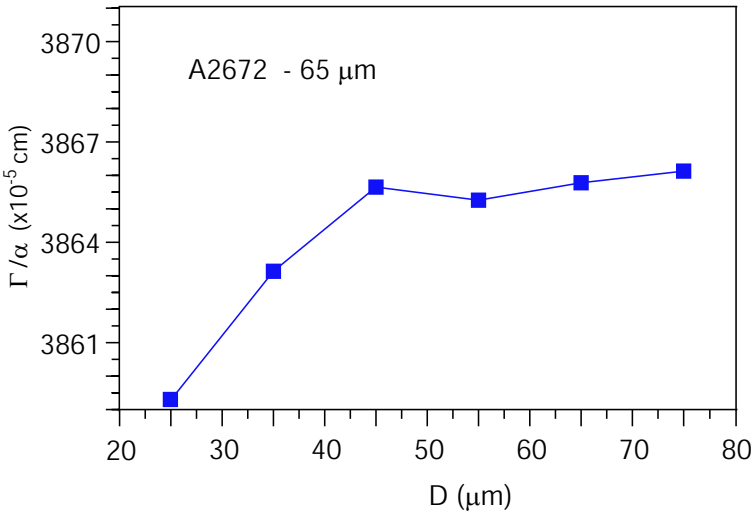

Figure 4.5: The simulations of the ratio Γ/α of the overlap factor and the waveguide losses have been performed for a far-infrared radiation at $65\mu m$ and assuming zero losses in the semi-insulating GaAs.

Fig. 4.6 shows the THz mode for a sample with a ridge width of 110 μm, and two lateral contacts separated by 15 (left) and 45 μm (rigth) from the ridge. The mode, typical of a THz QCL, has a significant part decaying within the substrate. At a separation distance D = 15 μm, a coupling between the mode intensity and the lateral contacts are clearly showed. However, at D = 45 μm this coupling becomes negligible and the mode intensity is confined in the active region.

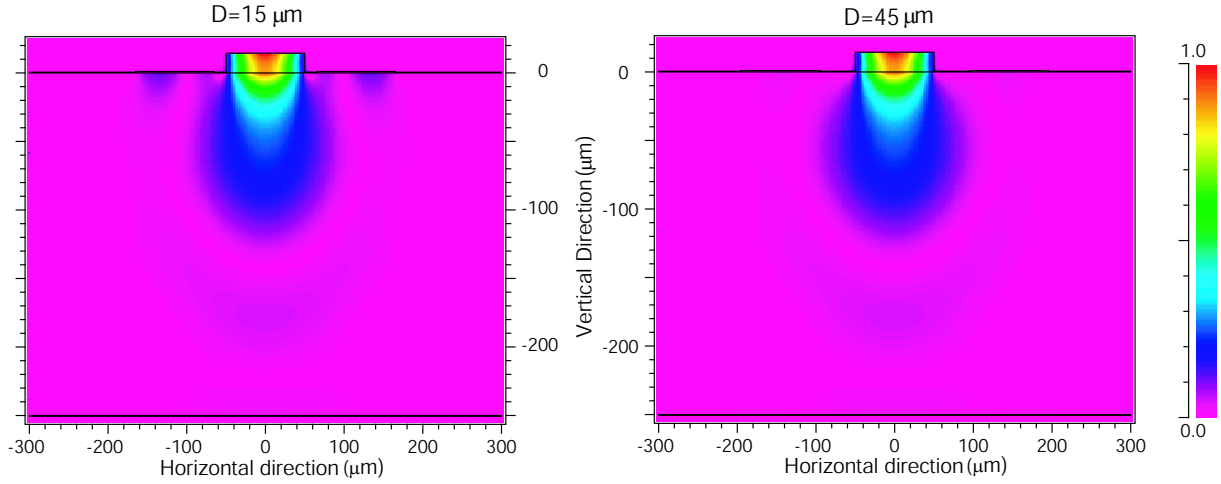

Figure 4.6: Computed transverse mode profile of 100 μm-wide, 13 μm-high ridge structure and a substrate thickness of 250 μm for an identical active region and waveguide. The distance separation between the lateral alloyed ohmic contacts and the edge of the ridge are 15 (left) and 45 μm (right).

For these reasons, this wafer was reprocessed using wet etching in H_2SO_4 : H_2O_2 : H_2O (1:8:1), and a new mask was used so that the lateral contacts were positioned $45\mu m$ away from the ridge (see Sec. 3.3). This was expected to reduce the waveguide loss by minimizing the Ge diffusion in the active regiuon, as well as by reducing the coupling and the scattering of the lateral mode overlap with the roughness of the edges of the lateral contacts. This optimization of the processing was required to reduce the threshold current even further. As will be shown in the next section, a very low threshold current density is obtained using this new processing devices (A2672d).

4.3.2 Low-threshold quantum cascade laser at $\lambda = 65\ \mu$m

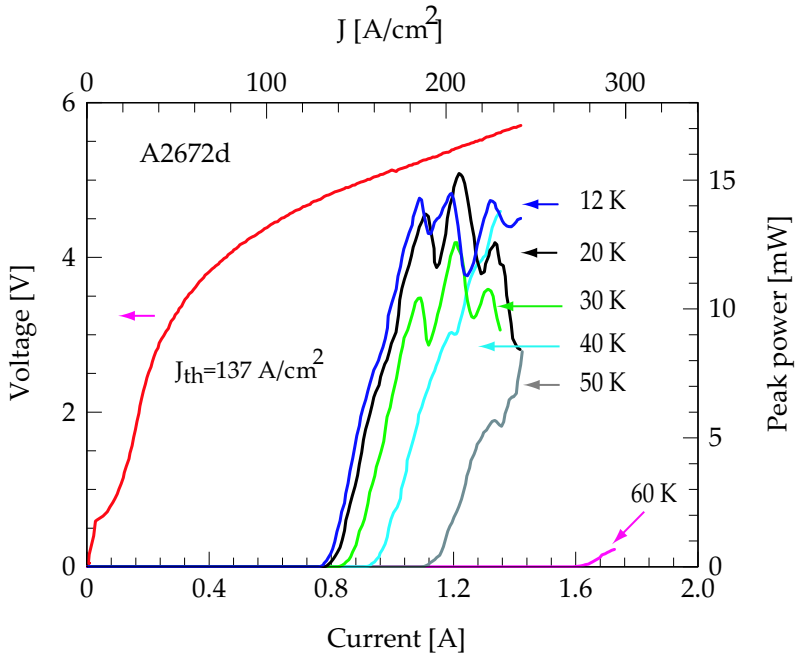

Figure 4.7: Peak optical output power versus injected current in pulsed mode at a duty cycle of 0.005% at various temperatures, as indicated.

A 2.8 mm long and 210 μm wide device (A2672d) was processed in the way described in Sec. 3.3 (with back facet coating) and could be operated up to 60 K with a current density of $J_{th} = 137$ A/cm^2 in pulsed mode(Fig. 4.7), which is an improvement of about 30 K of temperature and 158 A/cm^2 of current density, compared to the previous devices (Fig. 4.3b). This sample could not be operated in continuous wave although the threshold current density was very low, because the large device area required a relatively high threshold current (767 mA) and this to a too large power dissipation from He-flow cryostat.

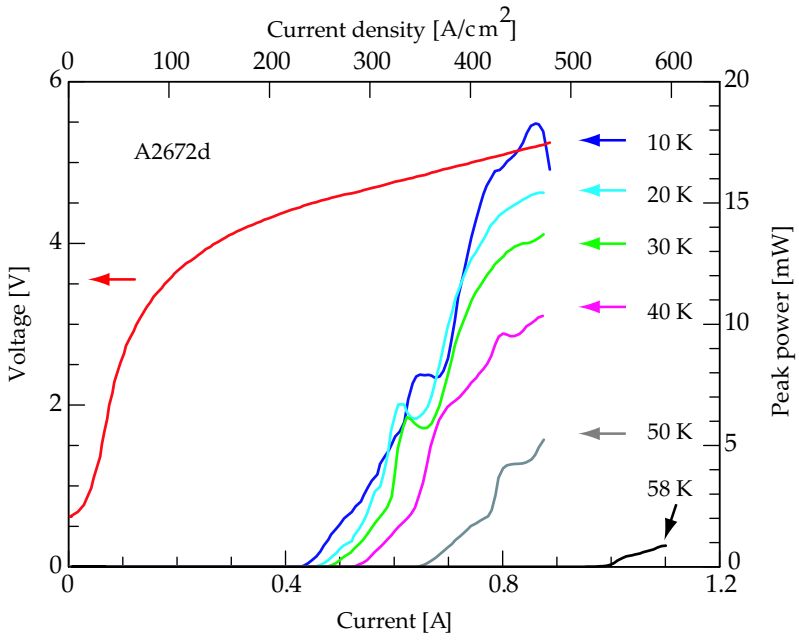

Figure 4.8: Peak optical output power versus injected current in pulsed mode at a duty cycle of 0.005% at various temperatures, as indicated.

For this reason a small device, 1.85mm long and 110μm wide, was tested. The light versus current (L-I) curves in the pulsed mode from this device are shown in Fig. 4.8 for temperatures ranging from 10 K up to 58 K. Knowing the duty cycle(0.005%) we were able to compute the peak power from the measurement of the average power, which we determined with a liquid He-cooled Si-bolometer. The slope efficiency is dP/dI = 47 mW/A at 10 K (where P is optical power and I is current), while the threshold current density is 235A/cm^2, with a maximum power of 18 mW at this temperature. At 58 K the threshold current density increased to a value of 540 A/cm^2 and the maximum output power dropped to about 0.8 mW.

4.3.3 Continuous wave operation at $\lambda = 65\ \mu$m

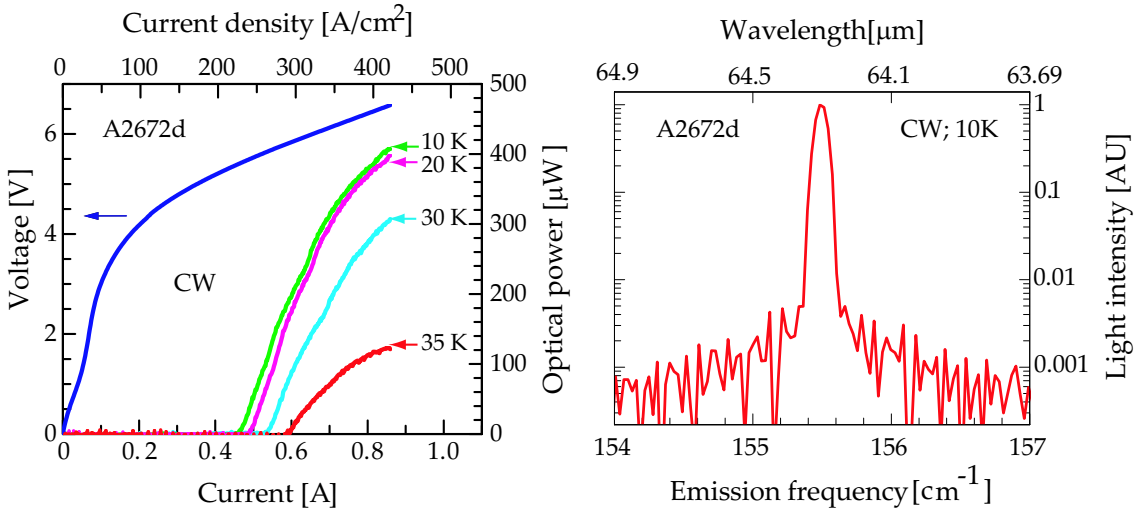

Figure 4.9: (a)CW optical power from a single facet and bias of a 1.85 mm long and 100 μm wide laser stripe as function of drive current for various heat sink temperatures. (b) CW emission spectrum measured at drive current of 700 mA and at a constant temperature of 10 K.

The CW optical output power emitted from the front facet of this device, was measured with a calibrated thermopile detector mounted directly in front of the cryostat window and is shown in Fig. 4.9(a). At 10 K temperature, the laser exhibited a threshold current of 460 mA (corresponding to a threshold current density $J_{\mathrm{th}} = 227\,\mathrm{A/cm^2}$ at a voltage bias V = 5.4 V) and a slope efficiency $dP/dI = 1.3\,\mathrm{mW/A}$. A maximum optical power of 410 μW at 10 K was detected at a driving current of 855 mA. CW operation was observed up to 35 K where the threshold current increased to 595 mA (J_{th} = 291 A/cm^2), while still more than 120 μW of output power was emitted at 850 mA. The electrical transport of the device are shown in the same figure.

4.3.4 Spectral measurements

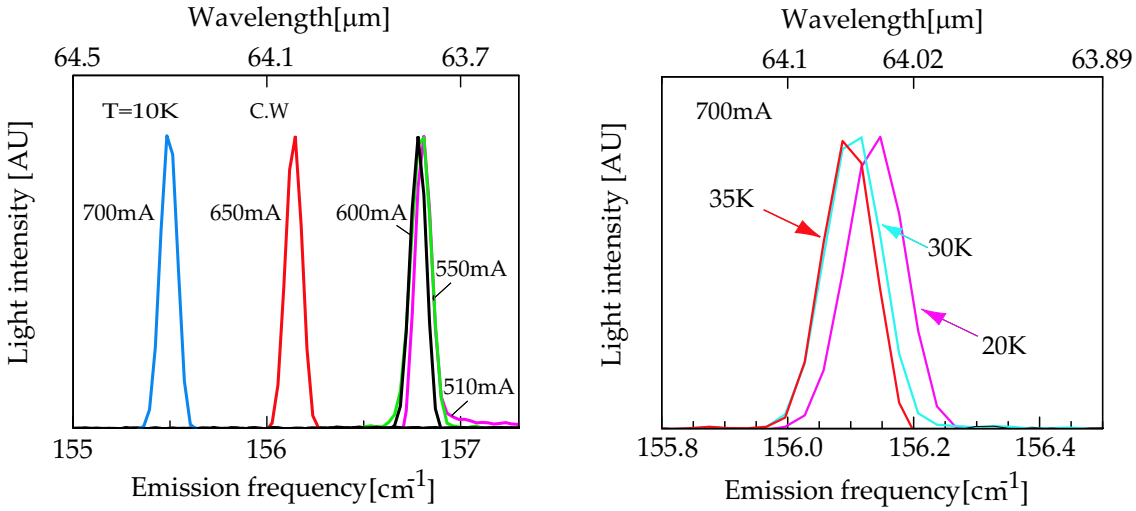

Figure 4.10: (a) High-resolution ($0.1\,\mathrm{cm}^{-1}$) CW spectra as a function of injection current. The emission spectra were measured at a constant temperature of 10 K for various drive currents ranging from 510 mA up to 700 mA. The curves are normalized to one and plotted in linear scale. (b) Series of CW emission spectra as a function of temperature at a constant drive current of 700 mA. The temperature varies from 20 K to 35 K and the intensities are normalized.

The emission frequency ν of this far-infrared QCL can be tuned over a small range of a few cm^{-1} by changing the current and temperature. The CW spectral properties were analyzed collecting the light by an off-axis parabolic mirror and sending it through a FTIR spectrometer with 0.09 cm^{-1} resolution operated in rapid scan mode. The emission spectra (Fig. 4.10(a) collected at a constant heat sink temperature of 10 K and at various currents between 510 and 700 mA reveal a frequency tuning from 156.8 cm^{-1} to 155.2 cm^{-1}.

As shown in Fig. 4.10(a), the main emission peak shifts discontinuously towards smaller

energies when the current is increased while maintaining a constant sample-holder temperature. Between 510 mA and 600 mA, the laser heats while maintaining the initial longitudinal mode. Between 600 mA and 650 mA and between 650 mA and 700 mA, mode-hops to the adjacent longitudinal mode take place. From these data, we extract the current tuning rate (0.3 A^{-1} cm^{-1}).

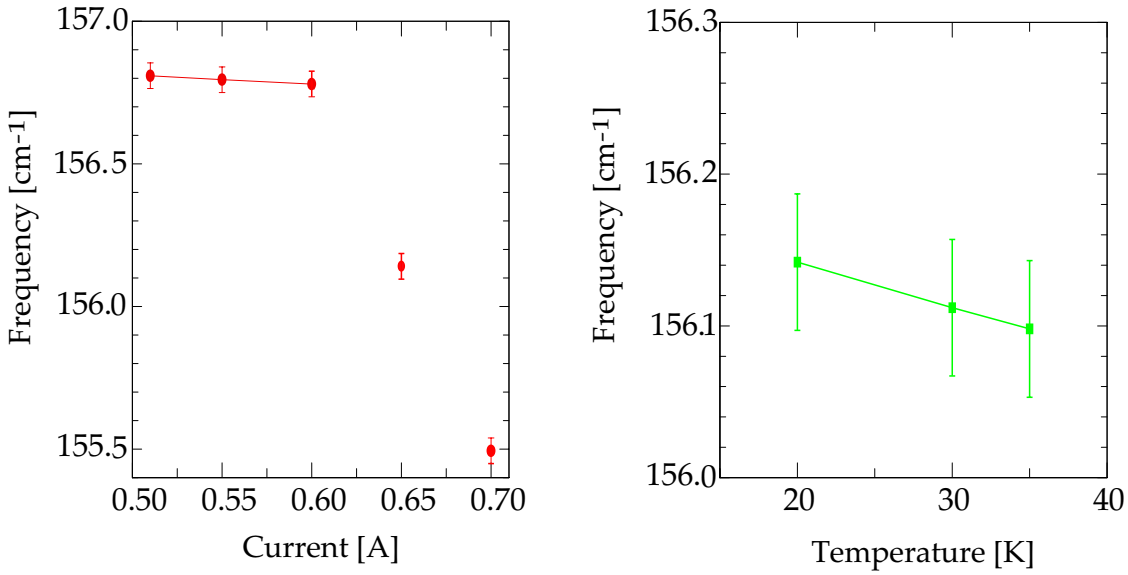

Figure 4.11: Peak position of the CW spectra as a function of injection current and temperature. Left, the emission spectra were measured at a constant temperature of 10 K for various drive currents ranging from 510 mA up to 700 mA. Right, the current is kept at 700 mA and the temperature is varied between 20 and 35 K.

The laser tuning is studied as a function of tempeature at a fixed current of 700 mA. As shown in Fig. 4.10(b), the mode is tuned, as expected, towards the red, with a tuning rate of $\frac{1}{\lambda}\frac{\Delta\lambda}{\Delta T} = 1.9\,10^{-5}$ K^{-1}.

Fig. 4.11 shows a peak position of CW spectra as a function of a cw injection current (Left) and temperature (Right). The measured data of the tuning with temperature can be fitted

by a linear relation. However, The tuning with current is also noticeably nonlinear.

4.3.5 Losses

Using the threshold condition. 2.2.46, we can extract α_W and the modal gain coefficient $g = g_d \Gamma$ from the slope and the intercept of the straight line at $1/L = 0$ of Fig. 4.12. The waveguide loss deduced from the data of devices with one facet coated is 1.2 cm^{-1} which is close to the calculated waveguide loss (2.7 cm^{-1}), and the material differential gain g_d extracted is 100 cm/kA. This low waveguide loss proves the high quality of the waveguide used and the processing optomized.

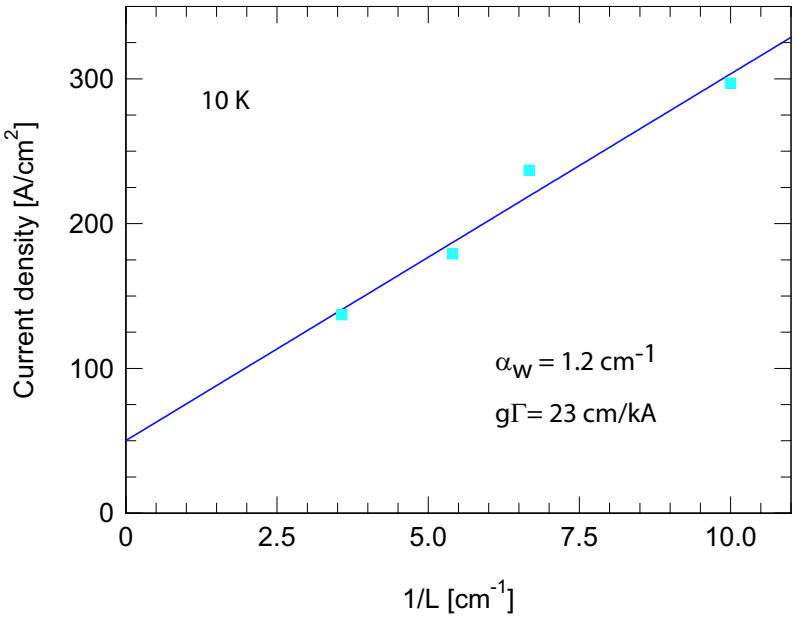

Figure 4.12: The threshold current density versus reciprocal cavity length (1/L), the data (squares) are very well fitted by using a linear dependence relation (straight line).

Chapter 5

Second generation of terahertz QCL's structures.

5.1 Introduction.

Despite the low threshold densities obtained in the chirped superlattice structures [87, 21], this design displayed a poor slope efficiency and a disappointing temperature behavior; those two were attributed to a thermal backfilling of the lower miniband and a weak population inversion. A structure based on a bound-to-continuum transition should increase the injection efficiency of the carriers and thus increase slope effeciency and temperature performances. This method, first proposed by Scalari et al. [22], offers two distinct advantages. First, a very good efficient injection of the upper state transition. Second, an excellent extraction efficiency of the lower state. Both properties are important in allowing higher temperature operation of lasers at longer wavelengths.

In this chapter we demonstrate that the bound-to-continuum approach enables the extension of the wavelength range as well as the achievement of high power operation, and high power QCL's emitting at $\lambda \simeq 87$ and $130\,\mu$m are demonstrated. An experimental study of the lasing and transport properties of GaAs/$Al_{0.15}Ga_{0.85}$As QCLs based on this design are also investigated with varying sheet doping density n_s.

5.2 High power terahertz QCL's

5.2.1 Lasers based on a bound-to-continuum transition emitting at $\lambda \simeq 87\,\mu$m

Laser design and characterization

The active region of this bound-to-continuum laser is composed of 120 repeated periods grown via molecular beam epitaxy (MBE) in the GaAs/$Al_{0.15}Ga_{0.85}$As material system embedded in a waveguide based on a single interface plasmon. The computed band structure of such a laser, based on a bound-to-continuum transition emitting at $\lambda \simeq 87\,\mu$m (3.4 THz) is shown in Fig. 5.1. The radiative transition occurs between level n=8, isolated in the minigap, and a group of three states n=7,6 and 5 in the lower miniband. Because of level broadening, caused by interface roughness and impurities, we were not able to identify these states individually in the intersubband luminescence or magnetotransport measurements. Because of the diagonal nature of the laser transition, the total oscillator strength of the radiative transition, f = 29, is significantly lower than the one computed in our previous work

on chirped superlattices (f = 37). This active region design is similar to the one (A2771) described in the ref. [22], except that the injection barrier thickness has been increased from 3.5 to 4.2 nm, in order to limit the leakage current, and the doping level in the active region increased, with a Si concentration of $3 \times 10^{16}\,\mathrm{cm}^{-3}$ instead of $2.5 \times 10^{16}\,\mathrm{cm}^{-3}$. Thickening the injection barrier has the effect of increasing the injection selectivity and reducing the lasing threshold [23].

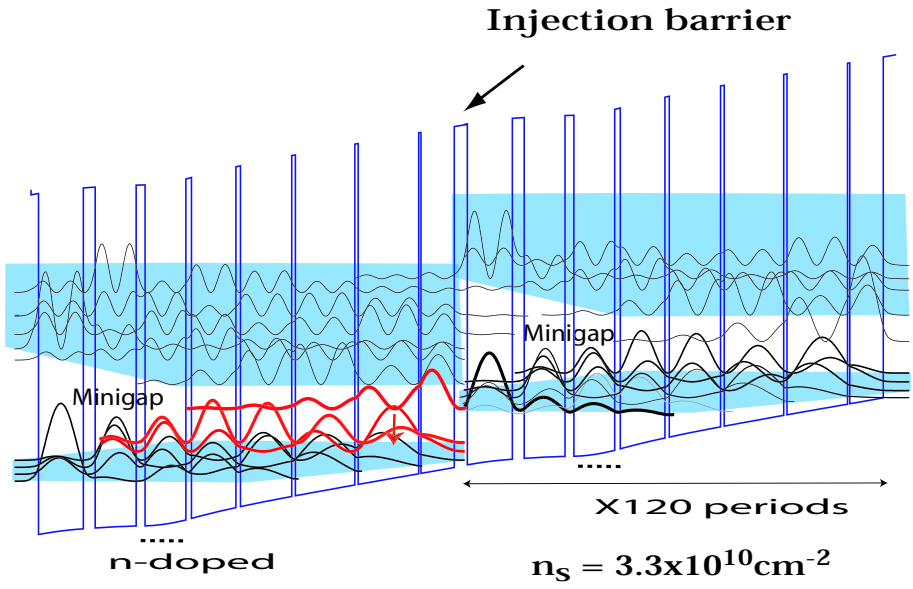

Figure 5.1: Computed conduction band profile at T=20K for one stage of the active structure under an average applied electric field of 2.55 kV/cm. The $GaAs/Al_{0.15}Ga_{0.85}As$ layer sequence for one period of the active layers (starting from the injection barrier) is as follows: **4.2**/9.0/**0.6**/16.3/**0.9**/16.0/**1.0**/13.8/**1.2**/12.0/**1.5**/<u>11.0</u>/**2.4**/11.0/**3.2**/12.1. Thicknesses are in nanometers, $Al_{0.15}Ga_{0.85}As$ barriers are in bold and the doped layer (Si $3 \cdot 10^{16}$) is underlined.

As compared to the structure operting at $\lambda = 65\,\mu$m, [20], the longer operating wavelength

of this laser enabled the use of a waveguide that employed a thicker (700 nm instead of 300 nm) buried heavily ($2 \cdot 10^{18} cm^{-3}$ Si) doped layer while still keeping a large value of the Γ/α_w parameter (where Γ is the overlap factor and α_w are the waveguide losses). The device was processed into ridge structures using standard photolithographic techniques, illustrated schematically in Fig. 3.3, and mounted on the cold finger of a helium-flow cryostat.

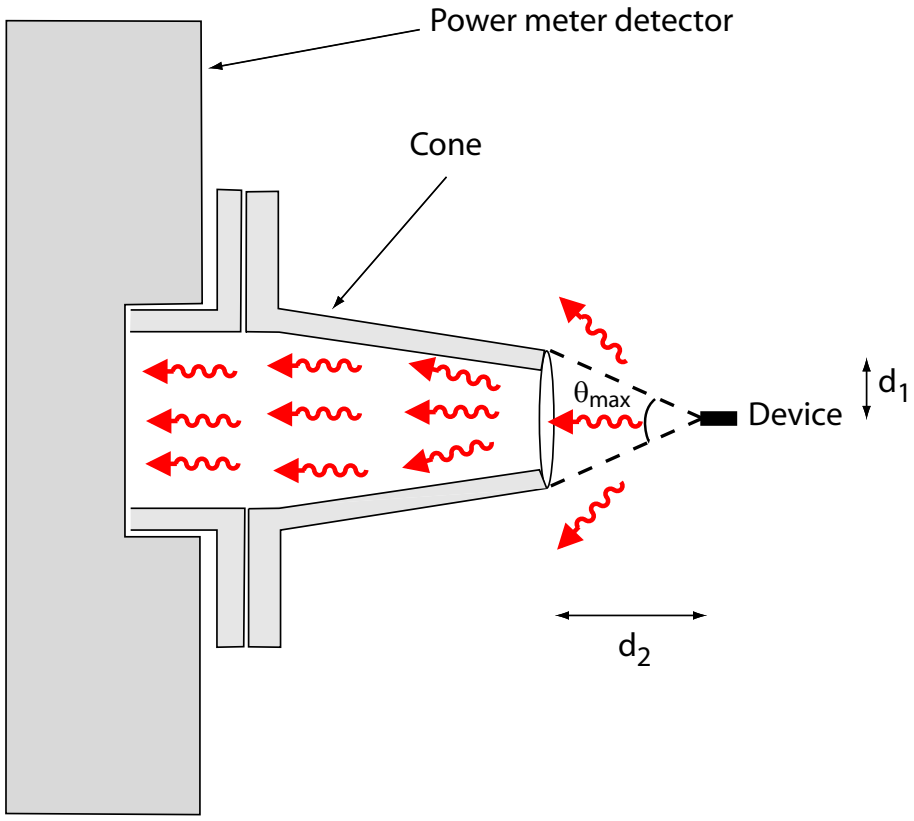

Figure 5.2: Diagram of cone used for radiation emission measurements. Radiation originating within the smaller aperture will emerge with an angle of divergence $\theta < \theta_{max}$.

As illustrated by Fig. 5.2, a cone manufactured by our mechanical workshop is used to collect the emitted light from the QC devices and transmit it to the receiver's power meter detector.

For a device placed at 1.2 mm from the smaller aperture of the cone, radiation emitted at any angle will be detected by the broadband thermopile power meter at an angle θ (azimuth angle) and φ (polar angle) smaller than some maximum angle

$$\theta_{max} = \varphi_{\max} = 2 \times \text{arctg}(\frac{\mathrm{d}_1}{\mathrm{d}_2}) \tag{5.2.1}$$

where $\mathrm{d}_1 = 2$ mm is the radius of the smaller aperture of the cone, and $\mathrm{d}_2 = 1.2$ mm is the distance between the origin (facet of laser) and the smaller aperture, yielding $\theta_{max} = \varphi_{\max} = 118°$. Using Eq. 7.3.3, the calculated collection efficiency is $\eta_{coll} \approx 100\,\%$.

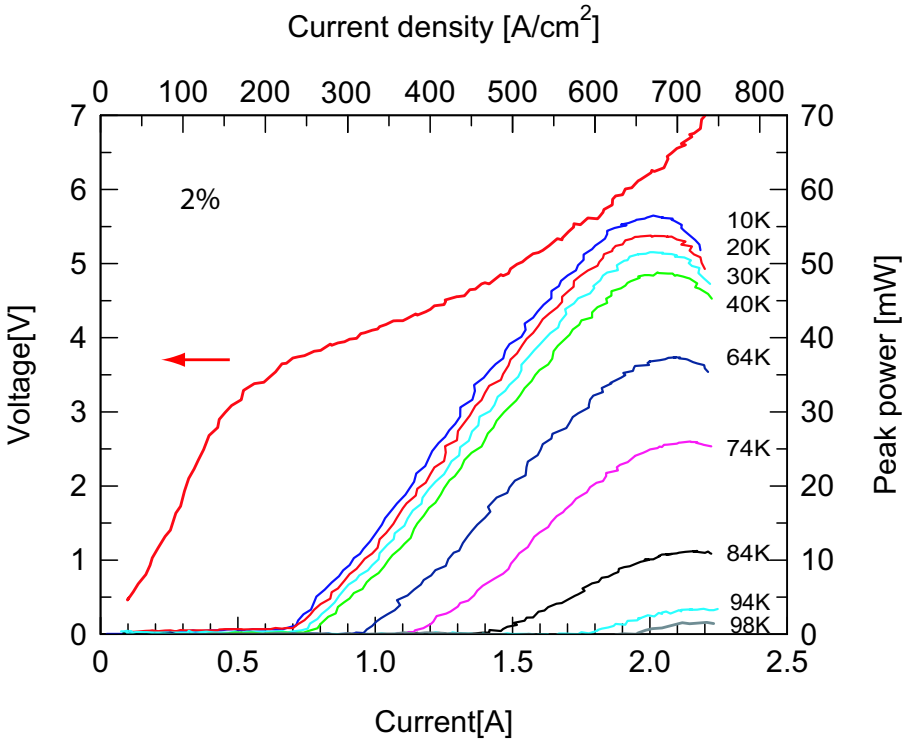

Figure 5.3: Peak optical output power versus injected current in pulsed mode at a duty cycle of 2 % at various temperatures, as indicated. The sample is processed into a 1.6-mm-long and 210μm-wide waveguide with backfacet coating.

The light-current characteristics of a 210 μm-wide and 1.6 mm long device are shown in Fig. 5.3 for temperatures ranging from 10 K up to 98 K. The collected peak power at 10 K reaches a value of 56 mW, with a threshold current density of $J_{\mathrm{th}} = 205\,\mathrm{A/cm^2}$. This represents a significant improvement as compared to the 22 mW and $J_{\mathrm{th}} = 248\,\mathrm{A/cm^2}$ obtained in the previous devices [22] of the same size. Still more than 2 mW is detected at 98 K. A 2.7 mm long and 210 μm-wide device operated in pulsed mode up to 103 K temperature, which is an improvement of about 10 K.

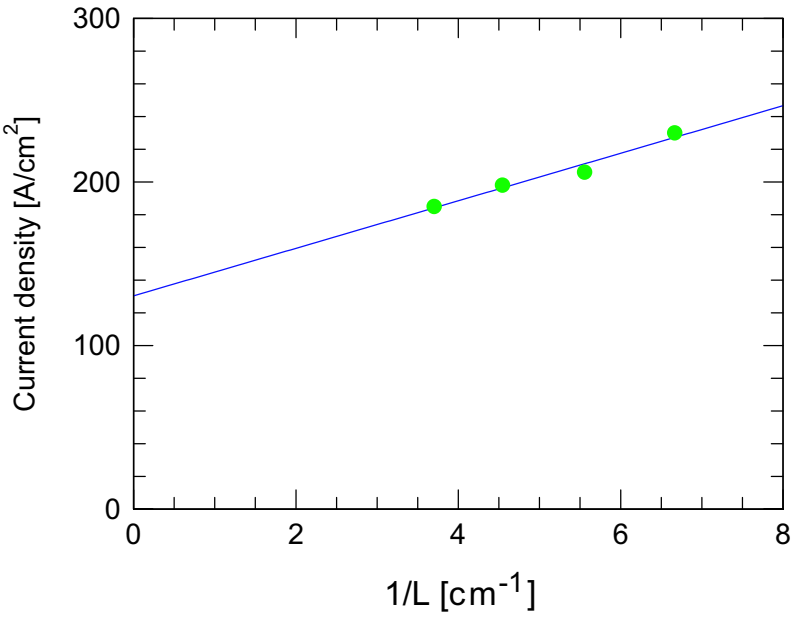

Figure 5.4: The pulsed threshold current density as a function of inverse laser length with backfacet coating measured at 10 K.

Assuming a linear dependence of the peak gain in current density, systematic threshold current density measurements of devices of various cavity lengths L enable the extraction of the material differential gain g_d and the waveguide loss α_w [83]. Using the data shown in Fig. 5.4, assuming a reflectivity coefficient $R_1 = 0.31$ and $R_2 = 0.98$ and the computed

value of the overlap factor $\Gamma = 38\,\%$, we can extract $g_d = 105\,\mathrm{cm/kA}$ and $\alpha_w = 5.1\,\mathrm{cm}^{-1}$, close to the calculated value (6.5 cm^{-1}).

As shown in Fig. 5.5, the same device could be operate in continuous wave with a threshold current density of $J_{\mathrm{th}} = 235\,\mathrm{A/cm}^2$ and a maximum collected power of 50 mW.

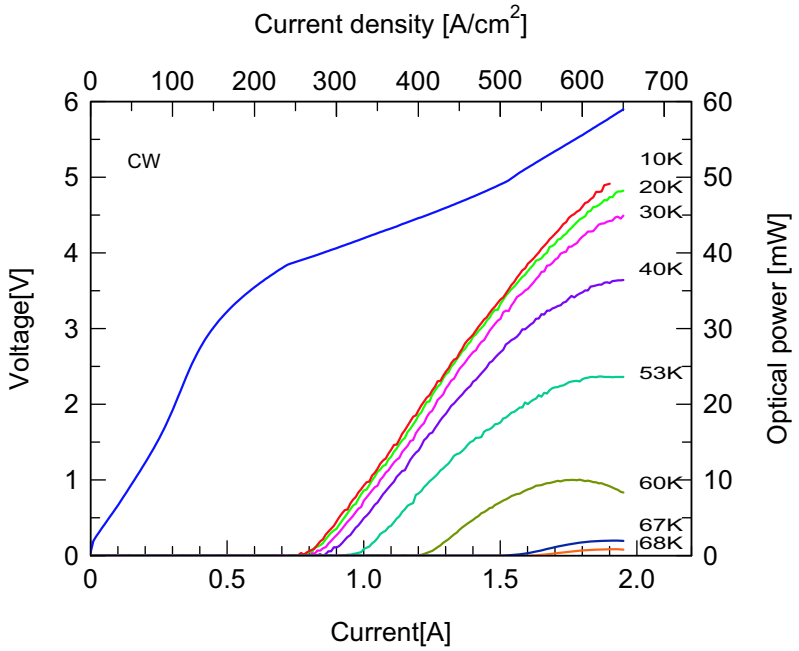

Figure 5.5: CW optical power from a single facet and bias of the same device (1.6-mm-long and 210μm-wide waveguide) as function of drive current for various heat sink temperatures.

The specific differential resistance, obtained by numerically differentiating the current density-voltage characteristics, is plotted as a function of injected current density in the Fig. 5.6 as a function of current density. For comparison, the same data taken in the previous device A2771 [22], is displayed along in the same graph. The data demonstrates that the thicker injection barrier reduces the current injected in the lower miniband before the devices achieves

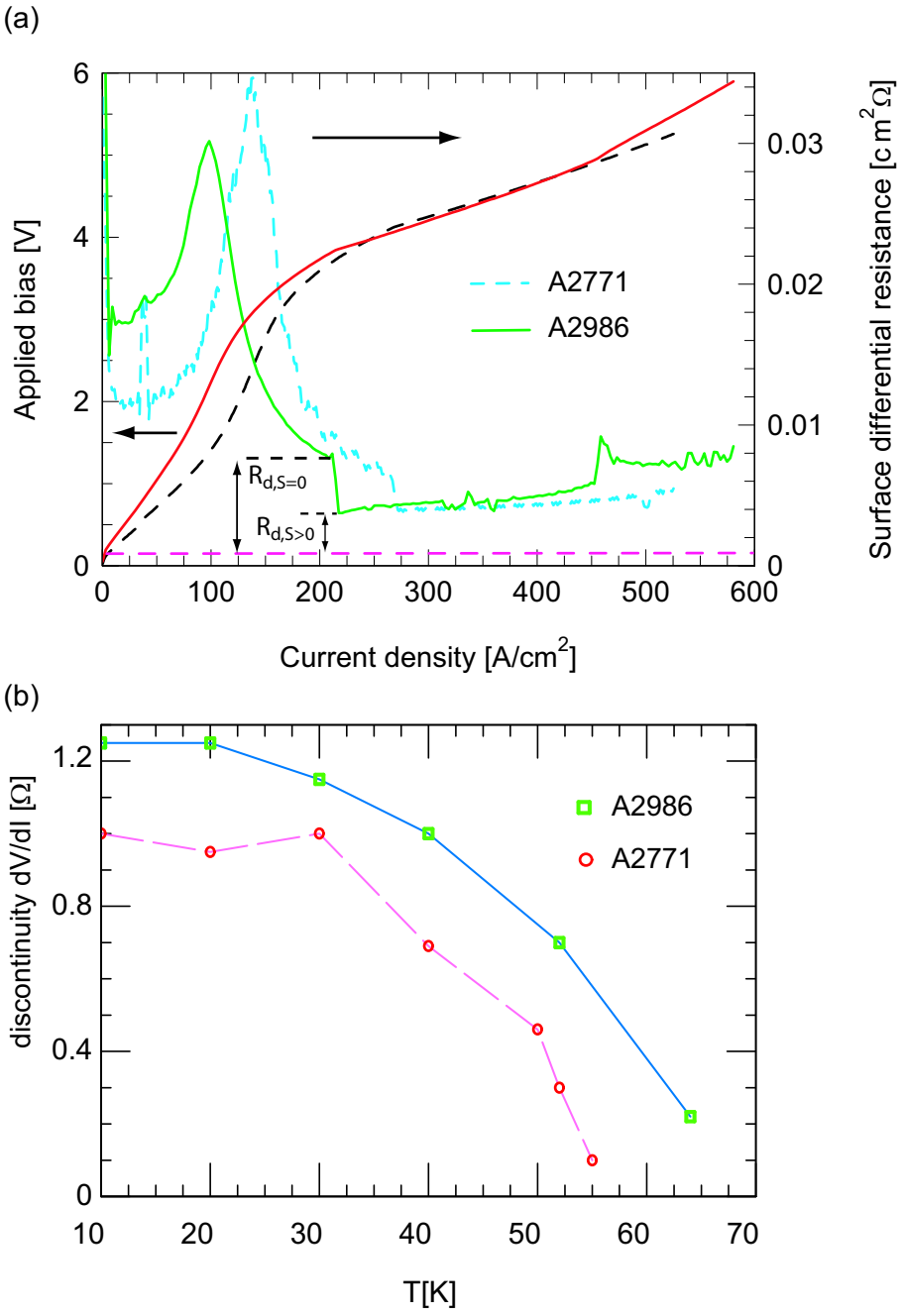

Figure 5.6: (a) Bias voltage as a function of injection current density and differential resistance deduced from the V-I curve of the A2986 (continuous line) and A2771 (dashed line) samples, the horizontal straight curve at $1 \times 10^{-3}\,\Omega\text{cm}^2$ is the residual series resistance R_s of the buried contact layer. (b) The discontinuity in differential resistance that occurs at CW threshold for both samples.

the proper band alignement, with the conductance peak reduced from 140 A/cm^2 to than 99 A/cm^2. Another parameter that has to be taken into account is the discontinuity in differential resistance that occurs at CW threshold. This number is both an indication of good injection efficiency and good ratio of lifetimes in the lasing structures [127].

From a comparison of this parameter for both structures, we verified that sample A2986 has a greater value of $\frac{dV}{dI}$ for any temperature. This can explain both the higher power emitted and the higher operating temperature in pulsed and CW modes.

Lifetimes and slope effeciency

We interpret these measurements assuming a simplifed three level model of the active region where n=3 and n=2 are the upper and lower states of the laser transition, respectively. Inspection of the rate equations that includes the photon field demonstrates the strong link between electron transport and photon emission in quantum cascade lasers. Using the Equ. 2.2.36 in stationary state ($\frac{dn}{dt} = 0$) and assuming an injection efficiency $\eta = 1$, the derivative of the upper state population, as a function of injected current density can be expressed as:

$$\frac{dn_3}{dJ} = \frac{\tau_3}{\mathrm{q}} \left(1 - \mathrm{g_c}(\mathrm{n_3} - \mathrm{n_2})\frac{\mathrm{dS}}{\mathrm{dJ}}\right) \tag{5.2.2}$$

where g_c (cm) is the gain cross-section (see Equ. 2.2.42) and S (cm^{-1} s^{-1}) is the photon flux per unit length per period given by [128][1]:

[1]The gain cross section σ defined in the article [128] is in units of cm^2. s^{-1} and is expressed as a function of g_c by $\sigma = g_c\ \bar{c}$.

$$S = \frac{1}{(\tau_{eff} + \tau_2)\,\alpha_{\text{tot}}}\left[\frac{J}{q}\tau_{eff} - \frac{\alpha_{tot}}{g_c}\right] \qquad With \qquad \tau_{eff} = \tau_3\,(1 - \tau_2/\tau_{32}) \tag{5.2.3}$$

From this expression one can deduced $\frac{dS}{dJ}$:

$$\frac{dS}{dJ} = \frac{1}{q\,\alpha_{\text{tot}}}\frac{\tau_{eff}}{\tau_{eff} + \tau_2} \tag{5.2.4}$$

Inserting this Eq. 5.2.4 into Eq. 5.2.2 We obtain the following expression:

$$\frac{dn_3}{dJ} = \frac{\tau_3}{\text{q}}\,(1 - \frac{\text{g}_\text{c}(\text{n}_3 - \text{n}_2)}{\alpha_{\text{tot}}}\frac{\tau_{\text{eff}}}{\tau_{\text{eff}} + \tau_2}) \tag{5.2.5}$$

Using the Equ. 2.2.36 in stationary state ($\frac{dS}{dt} = 0$) and assuming $\beta\frac{n_3}{\tau_{spont}} = 0$, We obtain

$$g_c(n_3 - n_2) = \alpha_{\text{tot}} \tag{5.2.6}$$

Substituting this expression into the Eq. 5.2.5, the derivative of the upper state population, as a function of injected current density can be expressed as:

$$\frac{dn_3}{dJ} = \frac{\tau_3}{\text{q}}\,(\frac{\tau_2}{\tau_{\text{eff}} + \tau_2}) \tag{5.2.7}$$

In the last equation, the effective lifetime may be extracted from the measurement of the differential gain g_d, using the Equ. 2.2.43, with $L_p = 116.2\,\text{nm}$, $\lambda = 87\,\mu\text{m}$, $Z_{23} = 8.8\,\text{nm}$, n = 3.6, $2\,\nu_{23} = 4.57\,\text{meV}$. We extract a value of $\tau_{eff} = 1.6\,\text{ps}$.

Assuming that differential resistance R_d (Fig. 5.6) is proportional to dn_3/dJ, the ratio of the differential conductance above ($S > 0$) and below ($S = 0$) threshold is just:

$$R_{d,S>0}/R_{d,S=0} = \frac{\tau_2}{\tau_{eff} + \tau_2} \tag{5.2.8}$$

It is a measurement of the population inversion obtained directly from the IV characteristics. To obtain the experimental value of this ratio, we must determine the residual series resistance R_s of the buried contact layer. As shematized in Fig. 5.7 the residual series resistance R_s (in units of $cm^2.\Omega$) can be expressed as

$$R_s = \frac{(R_1 + R_2)}{2} \times L\,D \tag{5.2.9}$$

Where L and D are the length and width of the device, respectively.

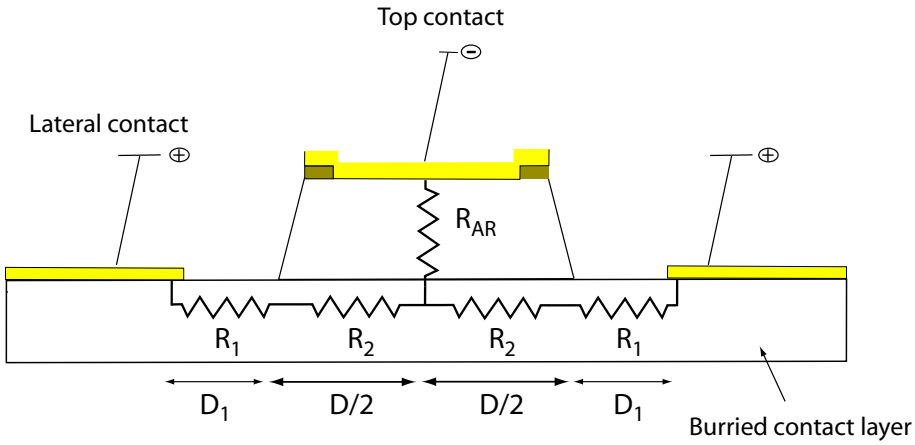

Figure 5.7: An approximative geometry model of the sample is used to determine the relation between V_{app}, V_{AR} and the residual series resistance of the buried contact layer.

Using the voltage of the active region V_{AR}, the series resistance R_1 and R_2, and the current I, the applied voltage V_{app} can be expressed as (Fig. 5.7)

$$V_{app} = \mathrm{V_{AR}} + \frac{\mathrm{R_1 + R_2}}{2} \times \mathrm{I} \tag{5.2.10}$$

Where $\mathrm{I} = (L\,\mathrm{D}\,\mathrm{J})$ is the current injected in the device, $R_1 = \rho D_1/Ld$ and $R_2 = \rho D/2Ld$ are the resistance associted to the buried contact layers, ρ and d are the resistivity and the thickness of the burried contact layers, respectively. Inserting these values in the equation. 5.2.10, the applied voltage V_{app} can be given as

$$V_{app} = \mathrm{V_{AR}} + \frac{\rho \mathrm{D_1\,J}}{2\mathrm{d}}\,\mathrm{D} + \frac{\rho\,\mathrm{J}}{4\mathrm{d}}\,\mathrm{D}^2 \tag{5.2.11}$$

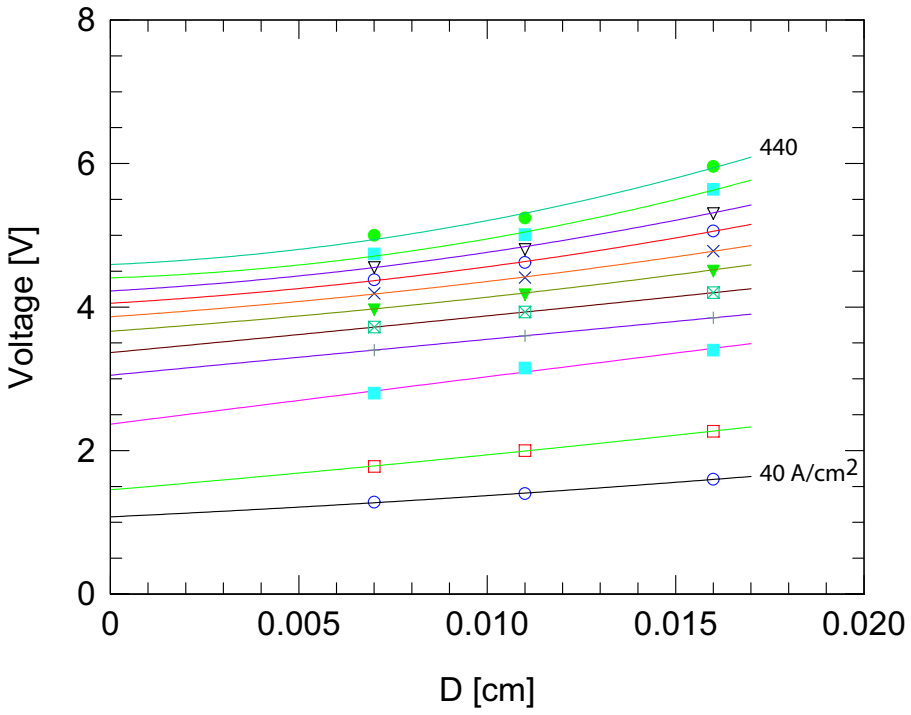

Figure 5.8: Bias voltage as a function of the waveguide width (V=f(D)). The series starts at 40 A/cm^2 and goes from the bottom to the upper in steps of 40 A/cm^2 up to 440 A/cm^2.

This Equ. 5.2.11 shows a parabolic dependence between the voltage applied to the device and the width D of the stripe laser. To deduce the active region voltage, IV curves were measured for 600 μm length stripes of various widths D between 70 and 160 μm and a fixed distance D_1. As shown in Fig. 5.8, at fixed current density, we reported the bias vs the waveguide width (WV); the intersection of the data curve parabolic fit with the axis of the bias gives the voltage of the active region at this current density. Knowing the distance D_1=45 μm and the thickness d = 700 nm, a resistivity ρ of ≈0.001 Ωcm is deduced from the parabolic fit. Now the extraction of the electron mobility μ_n is done from the expression $\mu_n = \frac{1}{n\,e\,\rho}$, where n = 2×10^{18} cm^{-3} is the carrier concentration of the burried contact layer and e is the electronic charge. A value of $\mu_n = 3125\,cm^2V^{-1}S^{-1}$ was deduced at 10 K.

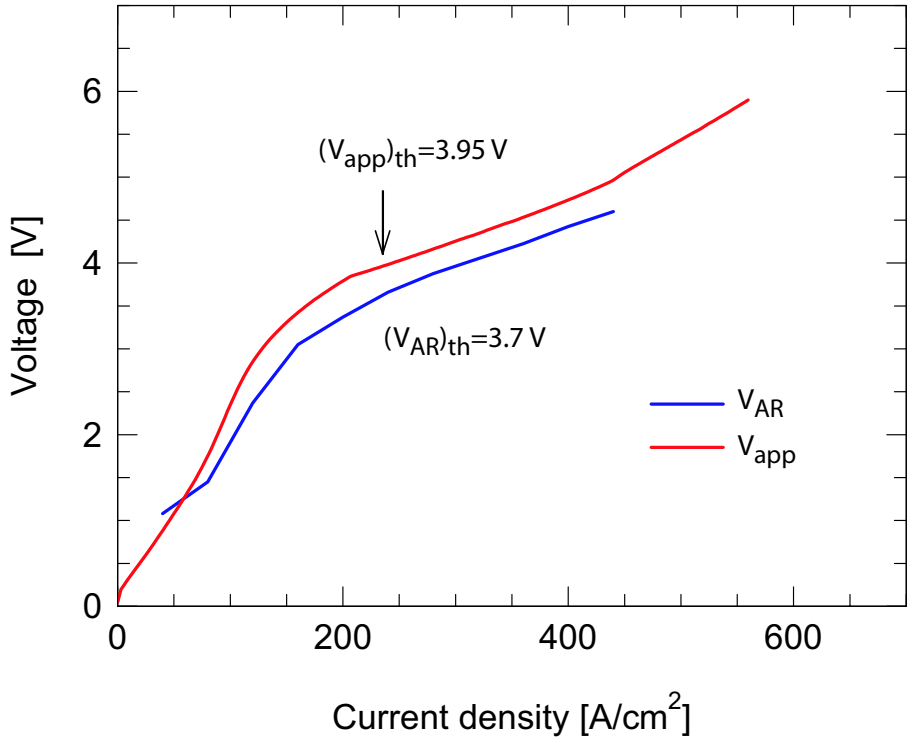

Figure 5.9: Bias voltage as a function of injection current density for applied and extrapolated voltages.

JV curve of the active region was extrapolated using different current density values shows an extrapolate threshold voltge of 3.7 V (Fig. 5.9). After a substraction of the series resistance of the device, measured from the scaling of the I-V characteristics with stripe width, a value of $R_{d,S>0}/R_{d,S=0} = 0.39$ is obtained. From this value, a direct estimate of the lower state lifetime $\tau_2 = 1\,\mathrm{ps}$ is obtained. The value of the population inversion at threshold yields a predicted value of the slope efficiency:

$$\frac{dP}{dI} = N_p \frac{h\nu}{q} \frac{\alpha_m}{\alpha_{tot}} \frac{\tau_{eff}}{\tau_{eff} + \tau_2} = 0.41\,\mathrm{W/A} \tag{5.2.12}$$

significantly larger than the measured one ($dP/dI = 0.05\,\mathrm{W/A}$).We attribute the discrepancy in the measured slope efficiency to a poor estimate of facet transmission and of the collection efficiency. Indeed, comparison with the previous devices A2771 where $R_{d,S>0}/R_{d,S=0} = 0.58$ show that an improvement of the quantity $(1 - R_{d,S>0}/R_{d,S=0})$, proportional to the slope efficiency, by a factor 1.45 is indeed accompanied by improvement of the slope efficiency by a factor of 1.40.

As shown in Fig. 5.10, Spectral measurements in CW above and below $J = 450\,\mathrm{A/cm^2}$ show that the JV behavior at this current density is due to an excitation of other lasing transverse modes of the cavity; however, larger stripes (210 μm) often allow excitation of higher-order transverse modes.

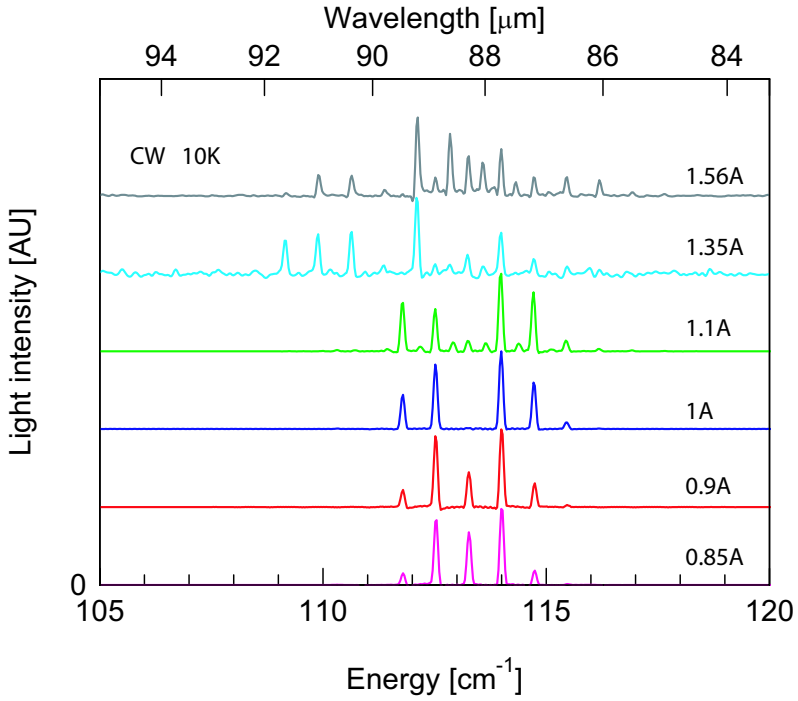

Figure 5.10: Spectra recorded at 10 K under continuous operation at six different injection currents. At low current levels the laser emits on a multimode; passing a certain threshold additional serie of modes appear in the spectra.

5.2.2 Lasers based on a bound-to-continuum transition emitting at $\lambda \simeq 130\,\mu$m

Laser design and characterization

The good performances obtained by the QC structures based on a bound-to-continuum transition emitting at $\lambda \simeq 87\,\mu$m suggested us to use the same concept for the fabrication of longer wavelength devices.

As shown in Fig. 5.11, the structure of sample A2985, designed for emission at about 9.6

meV ($\simeq 130\mu$m) is also based on a bound-to-continuum transition. This structure has been realized in the GaAs/$Al_{0.15}Ga_{0.85}$As material system and was fabricated to have identical SI-surface-plasmon waveguides as the original device (see Sec. 2.4.3).

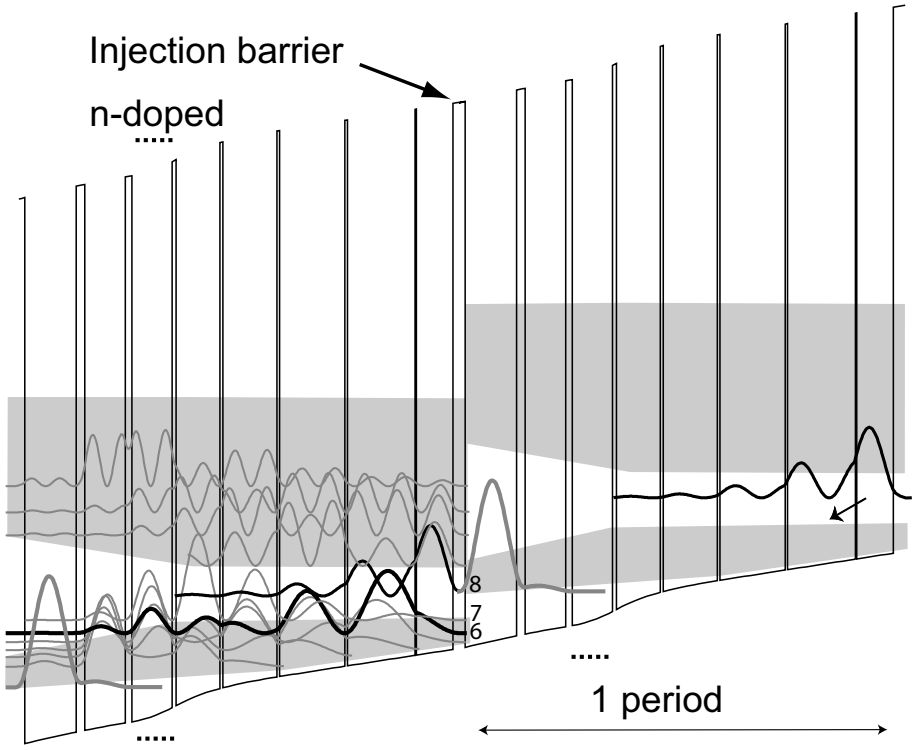

Figure 5.11: Computed conduction band profile at T=40 K of one stage of the structure (130 μm) under an average applied electric field of 2.55 kV/cm. The optical transition occurs between level n = 8, isolated in the minigap, and the state n = 6 of the lower miniband. The GaAs/$Al_{0.15}Ga_{0.85}$As layer sequence of one period of the active layers starting from the injection barrier is as follows: **4.0**/12/**0.5**/22.3/**0.8**/21.5/**0.9**/17.8/**1**/14.5/**1.3**/ <u>13.2</u>/**2.2**/13.4/**2.8**/17 where $Al_{0.15}Ga_{0.85}$As layers are in bold, GaAs in Roman and underlined number correspond to Si doped layer with $n = 2.5 \times 10^{16}\,\mathrm{cm}^{-3}$.

Typical light versus currents (L-I) curves from a 430 μm-wide and 3 mm long device with

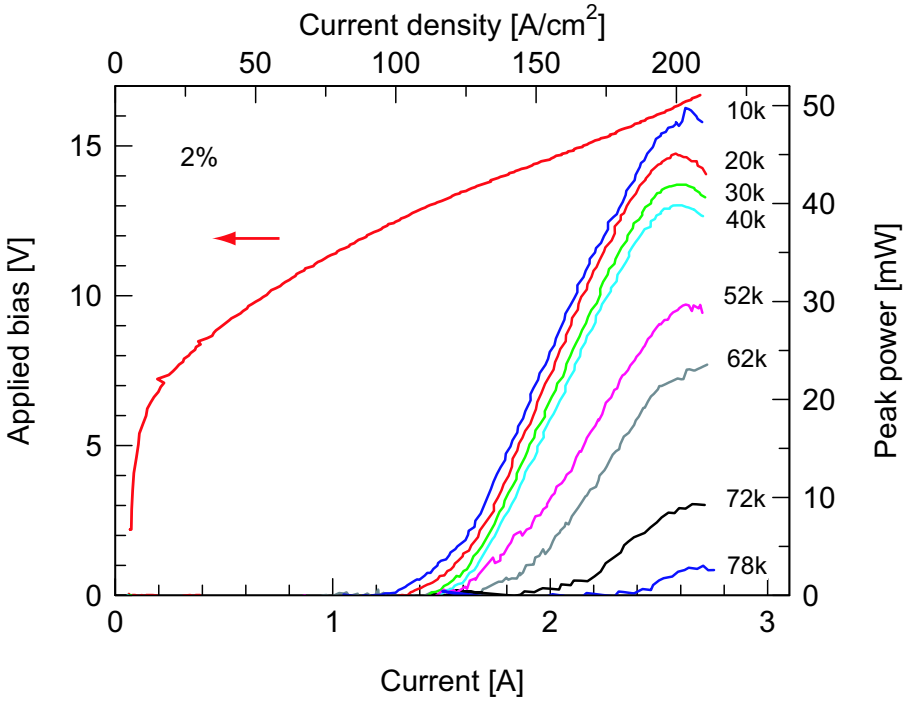

Figure 5.12: Light-current characteristics at different temperatures as measured from a 3-mm-long and 430 μm-wide laser stripe with backfacet coating.

backfacet coating are shown in Fig. 5.12 for temperatures ranging from 10 K up to 78 K. A very low threshold current density of $J_{\mathrm{th}} = 99\,\mathrm{A/cm^2}$ is achieved at 10 K. The maximum peak power at this temperature is 50 mW with a slope efficiency $dP/dI = 20\,\mathrm{mW/A}$. The device operates up to 80 K with a peak power of 30 μW. Analysis of the threshold current density versus cavity lengths (see Fig. 5.13), assuming $\Gamma = 16\,\%$, yields $\alpha_W = 4.5\,\mathrm{cm^{-1}}$, close to the experimental value of $\alpha_W = 3.3\,\mathrm{cm^{-1}}$.

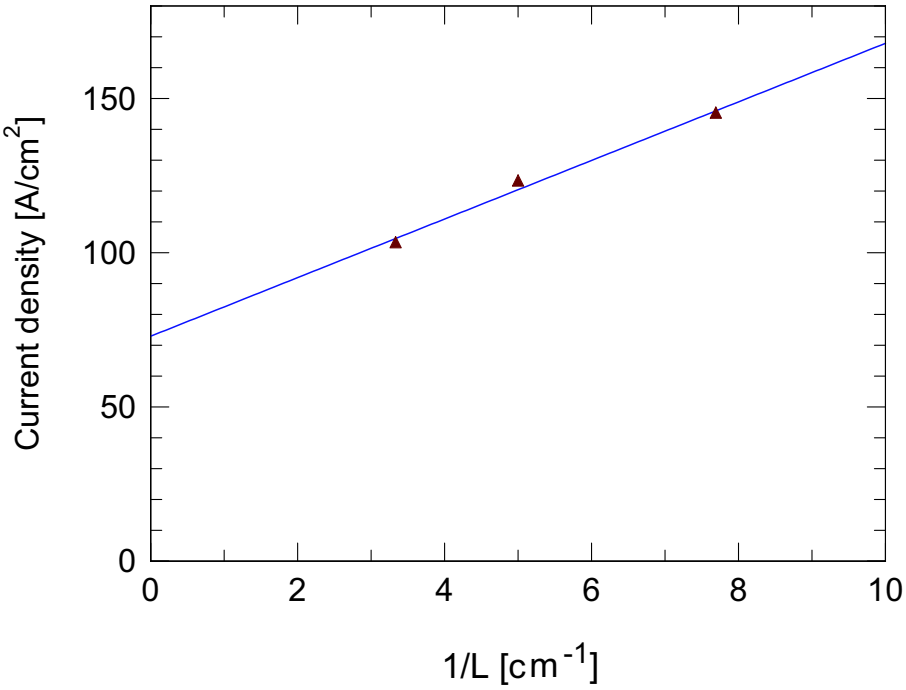

Figure 5.13: The pulsed thrshold current of sample A2985 as a function of inverse laser length with backfacet coating measured at 10 K.

The continuous wave operation was demonstrated in a 210 μm-wide and 2.1 mm long device with backfacet coating (ZnSe/Au) (Fig. 5.14). At 10 K the laser exhibited a threshold current of 656 mA ($J_{\mathrm{th}} = 148\,\mathrm{A/cm^2}$ at U = 8.3 V) and a slope efficiency $dP/dI = 30\,\mathrm{mW/A}$. A maximum optical power of 11.5 mW at 10 K was detected at a driving current of 1.2 A. Continuous wave operation was observed up to 53 K. A thermal resistance of 6 K/W is deduced from a comparison of the pulsed and continuous wave threshold current density.

As displayed in the Fig. 5.14 the voltage at which the device starts to lase is much higher (8.3 V) than the calculated value (2.9 V). We believe that this disagreement is caused by a residual series resistance of the order of 8.2 Ω ($3.6 \times 10^{-2}\Omega\,\mathrm{cm^2}$) originated from the bottom contact layer. The high resistance is explained by the lower doping $N_d = 9 \times 10^{17}\,\mathrm{cm^{-3}}$ of

the 0.6 μm thick bottom contact layer needed to minimize the waveguide losses (Fig. 5.15). For this reason we cannot deduce τ_2 from the ratio of dN_3/dJ (therefore dV/dJ) below and above threshold in this device.

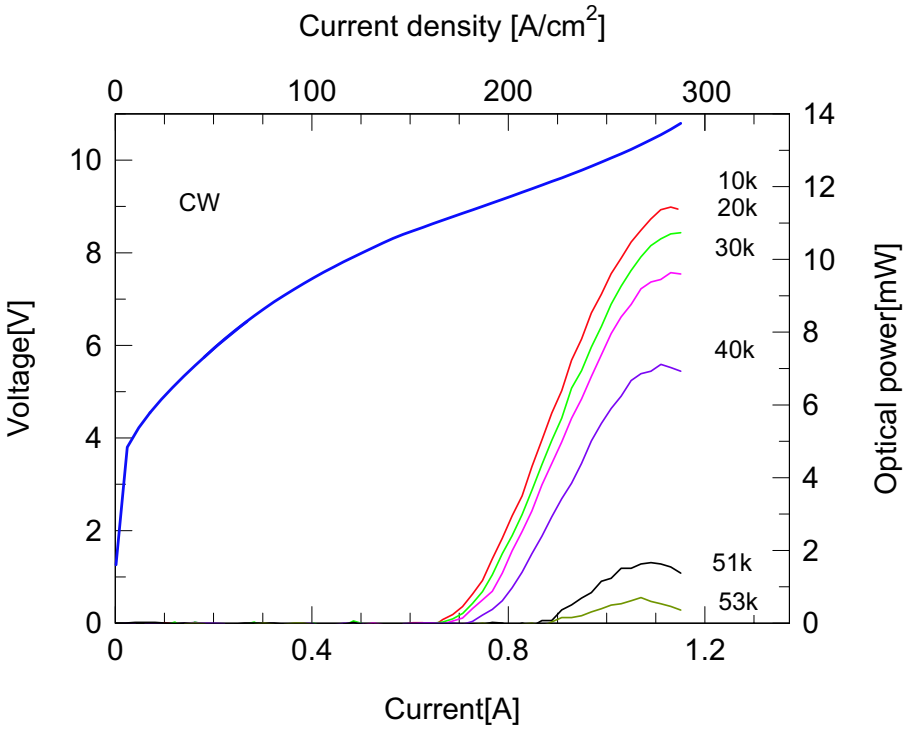

Figure 5.14: CW optical power from a single facet and bias of a 2.1 mm long and 200 μm wide laser stripe as function of drive current for various heat sink temperatures.

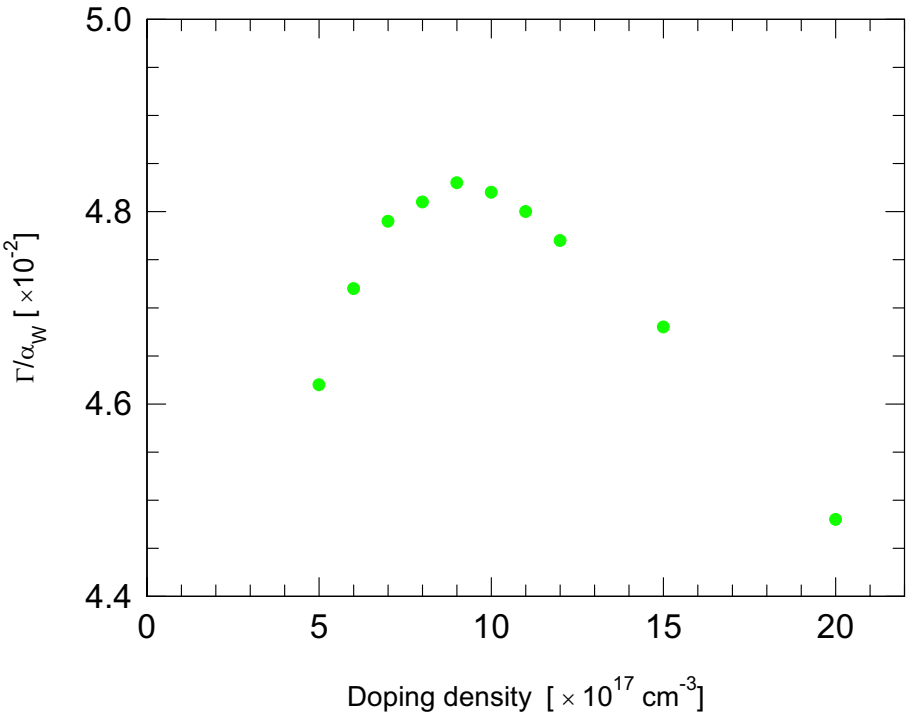

Figure 5.15: The ratio Γ/α_W of the overlap factor and the waveguide losses are shown versus the doping density of the 600 nm thick buried contact layers. The simulations have been performed for a far-infrared radiation at $\lambda = 130\mu m$, using the bulk Drude model, where scattering times of $\tau = 0.1$ ps and 0.5 ps were used for the heavily doped and lightly doped GaAs regions respectively. They show a maximum of the ratio Γ/α_W at N_d=9 $\times 10^{17}$.

Spectral measurements

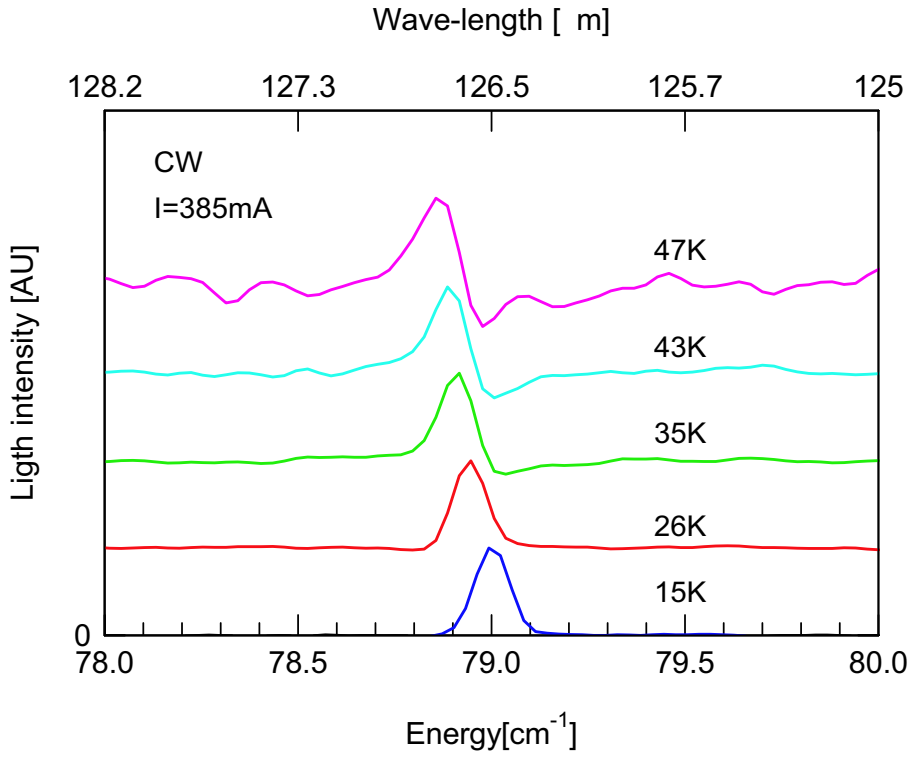

Figure 5.16: Lasing spectra of a 150 μm-wide and 1 mm-long QCL with high reflectivity back and frontfacet coating at different temperatures between 15 and 47 K. The curves are vertically displaced for clarity.

Spectral measurements are performed in CW operation at high-resolution ($0.09\,\mathrm{cm}^{-1}$) with a Nicolet fourier transform infrared (FTIR) spectrometer in rapid-scan mode. Figure. 5.16 shows the lasing spectra measured at different heat sink temperature. Single mode operation is observed at I = 385 mA for all temperatures. The emission wavelength shift towards smaller energies as the temperature increase from 15 K to 47 K. The temperature tuning coefficient of the lasing peak is constant over the entire temperature range, and its magnitude is $1/\lambda \times \Delta\lambda/\Delta T = 5.2 \times 10^{-5}\,\mathrm{K}^{-1}$.

Multimode emission for the same device was observed at T = 14 K at various currents between 283 and 385 mA (Fig. 5.17). The longitudinal mode spacing is $\Delta\lambda = 2.23\,\mu$m, knowing the cavity length, we can also compute an approximate value for the group effective refractive index in the laser cavity. This procedure yields $n_g = \lambda^2/2\,\Delta\lambda\,\mathrm{L} = 3.61$, which is in excellent agreement with the value reported in literature [129](n = 3.61).

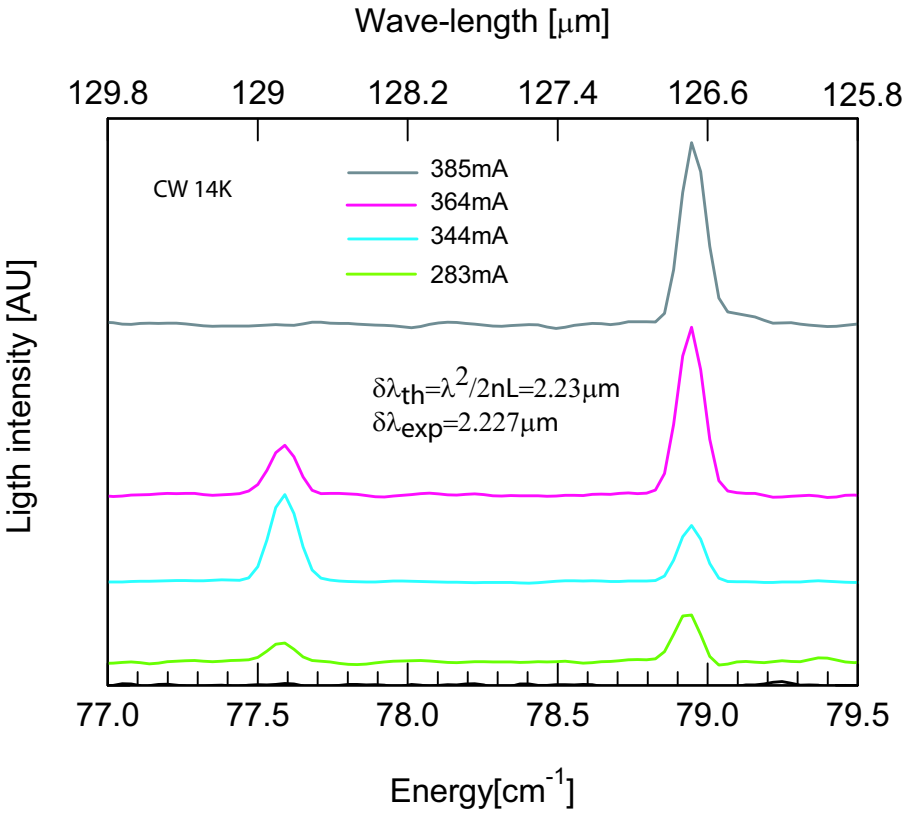

Figure 5.17: Spectra recorded at 10 K under continuous operation at four different injection currents. At low current levels the laser emits a multimode spectra; after a certain threshold the laser emits on a single mode.

5.3 Doping in terahertz GaAs/AlGaAs quantum cascade lasers

In order to improve the performance of terahertz QCLs and understand better the limitations of particular designs, further investigation of the influence of relevant physical parameters is required. One of the parameters which influences the physical properties of QC structures is the doping density. This parameter, has a remarkable influence on the transport as well as the waveguide losses and the wavelength emitted in the QCL's. In the mid-infrared [130, 131], a studies on this topic have attributed the effect of doping on the laser characteristics to a change the shape of the potential in the injector [132] as well as increase in the waveguide losses [133, 131]. In the terahertz, the studies have focused on changes in the maximum current [134] and the effect of the leakage current [135] as well as a general improvement of the laser performances. In this section, we studied experimentally the changes in the properties of GaAs/$Al_{0.15}Ga_{0.85}$As terahertz QCL's based on a bound-to-continuum design with sheet doping density.

5.3.1 Samples preparations

Four wafers (N295, N299, N301 and N310) of the GaAs/$Al_{0.15}Ga_{0.85}$As QCL's structure designed for emission at $\lambda \simeq 87$ μm ($h\nu \simeq 14.3$ meV) have been grown by molecular beam epitaxy (MBE) in the same growth series and using the same growth conditions. In these structures, a total of 120 periods of the active structure was grown on an undoped GaAs substrate, embedded in a waveguide based on a single interface plasmon and a thin (0.7 μm

thick) heavily doped buried contact layer .

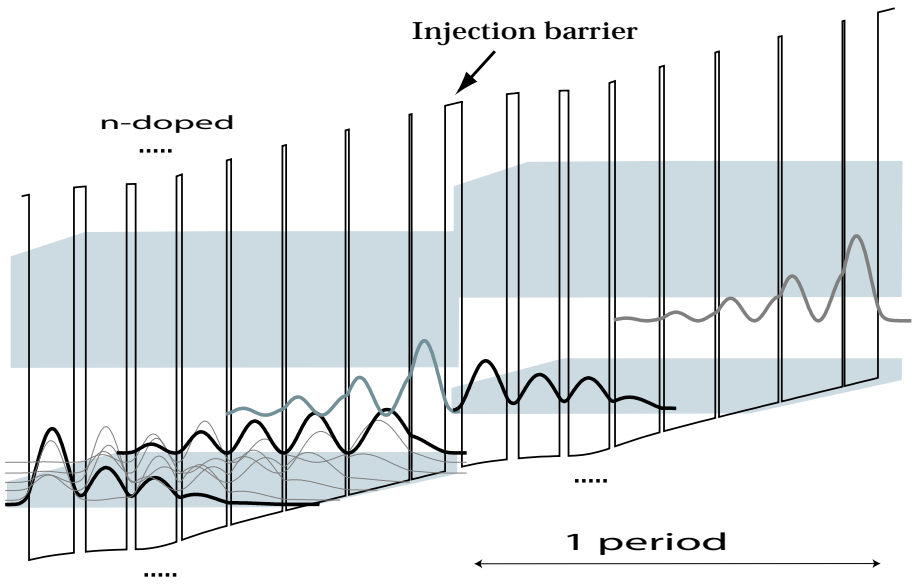

Figure 5.18: Computed conduction band profile at T=20 K of the structure under an average applied electric field of 3.1 kV/cm and an Si doped layer of $n = 4.2 \times 10^{16}\,\mathrm{cm}^{-3}$. The optical transition occurs between level n = 8, isolated in the minigap, and the state n = 7 of the lower miniband.

As shown Fig. 5.18, the layer sequence of the grown structures, in nanometers starting from the injection barrier, is: **4.5**/9/**0.6**/16.3/**0.9**/16/**1**/13.8/ **1.2**/12/**1.5**/ 11/ **2.4**/11/**3.2**/12.1 where $Al_{0.15}Ga_{0.85}As$ layers are in bold, GaAs in roman type and the underlined number corresponds to a Si doped layer. In these four samples, the doping level was systematically varied, such that the resulting sheet doping densities (n_s) yield respectively a 3.3×10^{10}, 4.4×10^{10}, 6.6×10^{10} and $8.8 \times 10^{10}\,\mathrm{cm}^{-2}$. After growth, the samples were processed as described in Sec. 3.2.1, cleaved in ridges of variable length with a width of approximately 210 μm, soldered with indium on a copper heatsink and mounted on the cold finger of a He

flow cryostat.

5.3.2 Doping characterisations

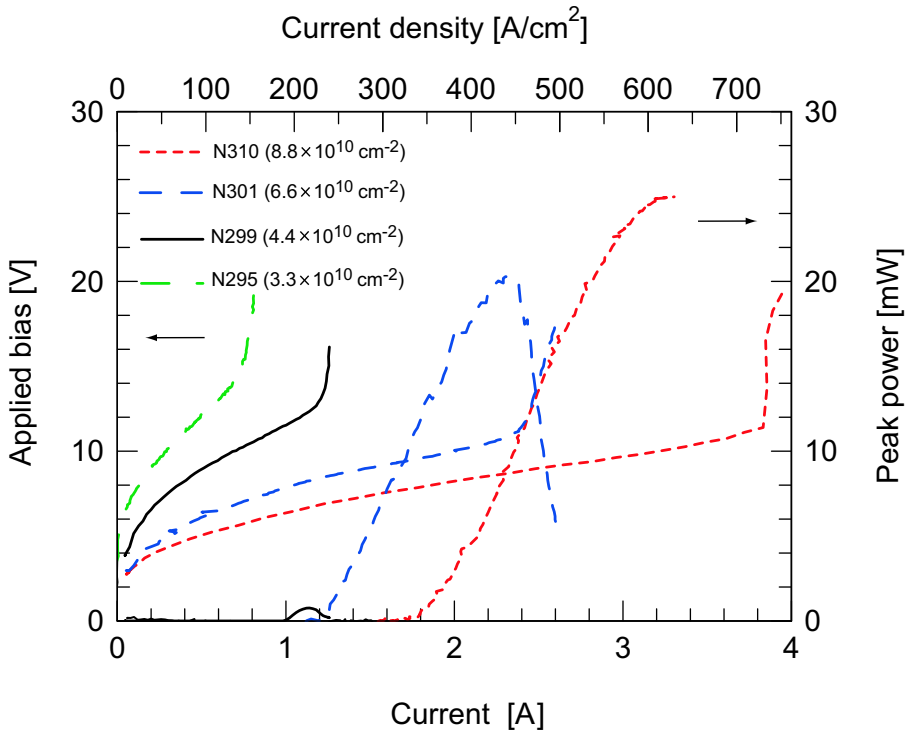

Figure 5.19: Peak optical output power and voltage versus injected current density in pulsed mode at a duty cycle of 2% of various sheet doping density, as indicated. The sample is processed into a 2.5-mm-long and 200 μm-wide waveguide.

Simultaneous measurements of the voltage and optical output power versus injection current were performed in pulsed mode for otherwise identical samples fabricated from the four different growths. A total number of thirty devices were measured. The reproducibilities in threshold current density for identical growth and device size was better than $\pm$15%. Results from four representative samples (210 μm wide and 2.5 mm-long) were reported in Fig. 5.19.

In these measurements, the terahertz emission is collected through a light pipe and sent to a broadband thermopile power meter. Laser operation is observed for the samples with a sheet doping larger or equal than $n_s \geq 4.4 \times 10^{10}$ cm^{-2}.

We first concentrate on the electrical characteristics of the devices. The current-voltage characteristics of the devices exhibit a very clear onset negative differential resistance that depends on the doping level of the sample; above this current the output optical power drops. The maximum injection current in a quantum cascade laser is limited by resonant tunneling [128], and is proportional to the sheet carrier density [77, 2]. To check this dependence, the current at the onset of negative differential resistance was plotted in Fig. 5.20 as a function of the sheet doping density. As expected, a linear dependence was found with a doping offset of about $n_{offset} = 2 \times 10^{10}$ cm^{-2}; i.e. a negligible current was extrapolated to flow for this value of doping. We interpret this offset as a residual p doping of the wafer of $N_A = 1.7 \times 10^{15}$ cm^{-3}. Capacitance-Voltage measurements on these structures also yield a lower doping level as the one intended, however the offset is smaller and corresponds to $n_s = 8 \times 10^9$ cm^{-2}, i.e an acceptor density $N_A = 7 \times 10^{14}$ cm^{-3}. The difference between these two values corresponds to electrons localized on impurities that do not participate to transport. Secondary ion mass spectrometry (SIMS) measurements were also performed; the results were however inconclusive as the measured impurity level was too close to the detection limit. The dependence of the maximum current with doping is more difficult to interpret because there is still no reliable computation of the upper state lifetime, in contrast with the mid-infrared case where optical phonon limited lifetimes may be assumed. However, assuming the strong coupling regime $\Omega^2 \tau_\perp \tau_{up} >> 1$ and neglecting the electron population

in the miniband at the exception of the lowest state, the upper state lifetime is given by the inverse of the derivative of the current density as a function of sheet doping density:

$$\tau_{up} = \frac{q_0}{2}\frac{dn_s}{dJ_{max}}, \tag{5.3.13}$$

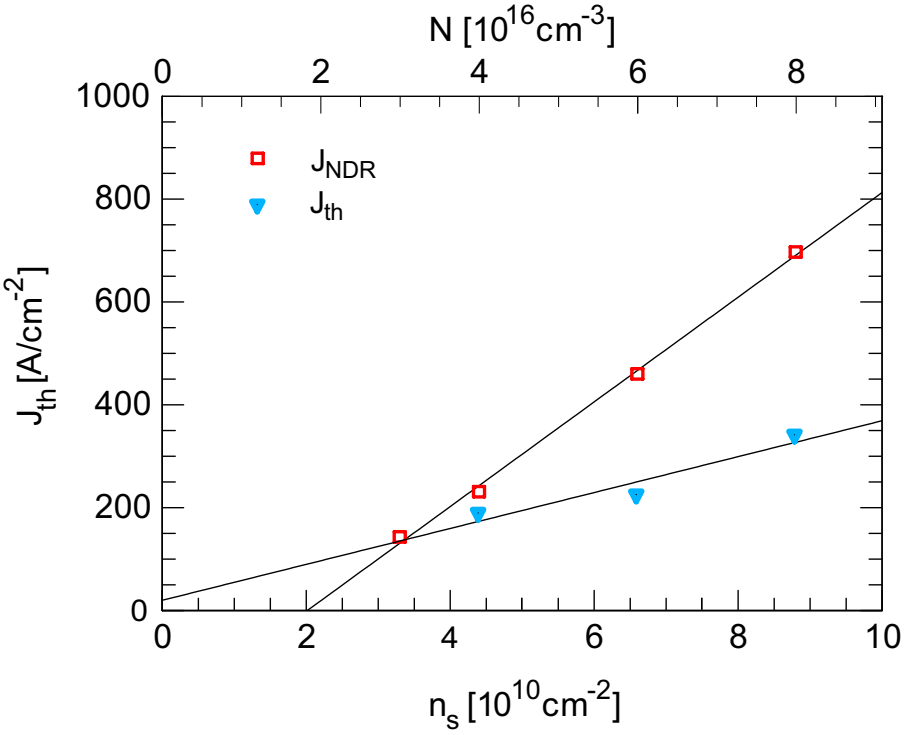

Figure 5.20: Threshold current density (J_{th}) and the maximum current density before appearance NDR (J_{NDR}) as a function of doping density.

For the values shown in Fig. 5.20 the lifetime we deduce is $\tau_{up} = 8\,\text{ps}$. This value is however significantly longer than the one $\tau = 1.6\,\text{ps}$ obtained for essentially identical structures by optical characterisation [23]; this strongly suggests that a significant population resides on the lower state of the laser transition and on the states of the injection miniband. In this

picture, the lifetime of 8 ps must be interpreted as the transport time across one period, including injection.

As shown in Fig. 5.19, the bias at the J_{th} decreases with increasing the sample doping, and the values are much larger (11.5, 8.4, and 6.9 V) than the calculated ones (4.38, 3.82 and 3.75 V respectively). This strong additional voltage drop, as well as its dependence on doping level, strongly suggest that a number of periods in the active region are depleted, as nominally identical structures, but grown in an other equipment and in an other growth run as demonstrated in Sec. 5.2.1 for the same structure, a threshold voltages very close to the computed ones.

5.3.3 Waveguide losses

The threshold current density of the devices also increases linearily with doping (Fig. 5.20), from a value of 187 A/cm^2 (N299) to a maximum of 340 A/cm^2 for sample N310. As in the mid-infrared case, this dependence could either be originating from a decrease of the upper state lifetime with doping due to an increase of electron-electron scattering or an increase in waveguide losses due to free carrier absorption. A strong variation in the upper state lifetime with doping is however unlikely as it would lead to a superlinear dependence of the maximum current with active region doping. To verify the importance of free carrier absorption, we measured the threshold current density as a function of inverse laser length, and extracted the waveguide losses from the fit [23]. In Fig. 5.21, we report the waveguide losses as a function of the sheet effective doping density (n_{eff}), where $n_{eff} = n_s$ - n_{offset}. As shown in Fig. 5.21, the experimental waveguide losses (6.2, 7.8 and 10.2 cm^{-1}) agree well

with the calculated values (6.6, 8.5 and 10.1 cm^{-1} respectively).

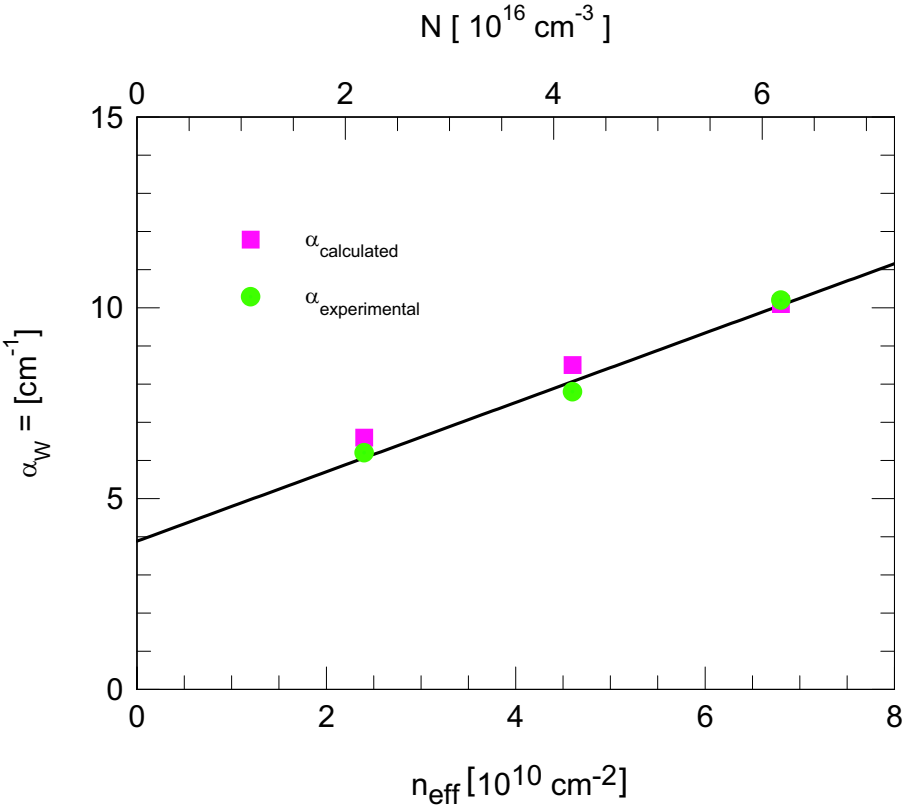

Figure 5.21: Experimental and calculated waveguide losses versus n_{eff}.

In the latter simulations, the waveguide losses are expressed as the sum of the losses of the empty waveguide α_0 (i.e. without active region) and of the additional free carrier losses of the active region: $\alpha_W = \alpha_0 + \Gamma\alpha_{AR}$. A value $\alpha_0 = 5.2$ cm^{-1} is obtained using the bulk Drude model, where scattering times of $\tau = 0.15$ ps and 0.5 ps were used for the heavily doped and lightly doped GaAs regions respectively.

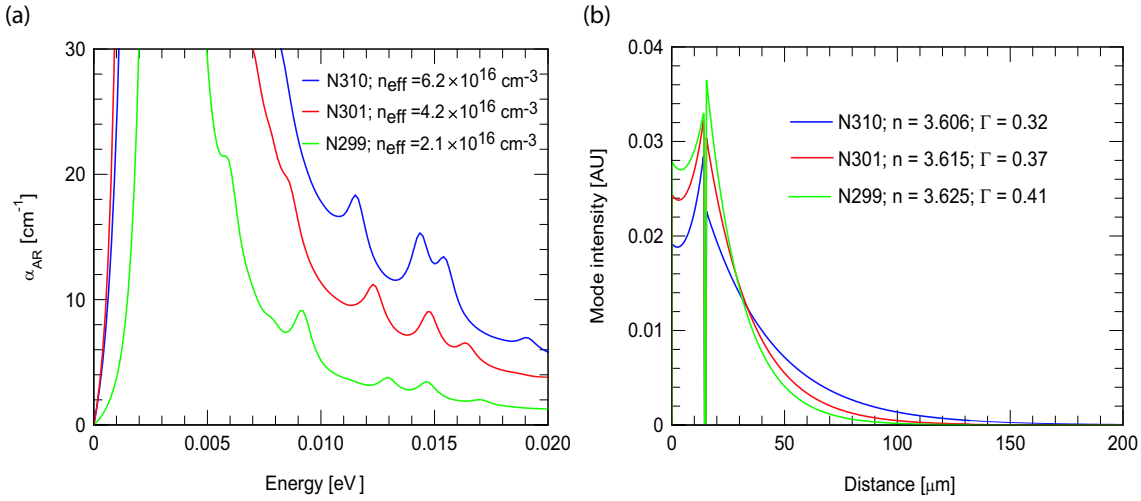

Figure 5.22: (a) The absorption of the all contributions of the intersubband absorption between all active region and injector states (α_{AR}) computed by solving Schrodinger and Poissons equations for three effective doping densities. (b) Calculated mode profiles of the waveguide for different doping densities of the active region: n_{eff} = 2.4 $\times 10^{10}\,\mathrm{cm}^{-2}$ (N299), 4.6 $\times 10^{10}\,\mathrm{cm}^{-2}$ (N301) and 6.8 $\times 10^{10}\,\mathrm{cm}^{-2}$ (N310). With decreasing doping density in the active region, the mode is pushed further into the substrate causing a reduction of the overlap factor.

The absorption of the active region α_{AR} is computed by summing all contributions of the intersubband absorption (assuming a full-width at half maximum of the transitions of 2 meV) between all active region and injector states. The states are computed self-consistently by solving Schrodinger and Poissons equations for the effective doping densities n_{eff} = 2.4, 4.6 and 6.8 $\times 10^{10}\,\mathrm{cm}^{-2}$ respectively (the right of Fig. 5.22), and a thermal electron distribution at a temperature T = 50 K is assumed. The overlap factor ($\Gamma = 0.41, 0.37$ and 0.32) is computed taking into account the decrease of the value of the refractive index with free

carrier concentration. The sum of these two terms is shown in Fig. 5.21; the good agreement shows convincingly that the increase in the threshold current densities with doping n_s is due to the increase of the waveguide losses.

However, in contrast to the threshold current density, the slope efficiency does not show the expected decrease with increased doping. In fact, the slope efficiency seems to exhibit a maximum at some intermediate doping, corresponding in our case to sample N301. This behavior, also observed in mid-infrared devices, is attributed to the onset of gain saturation close to the onset of negative differential resistance. As a result, the measurement of the slope efficiency cannot be used to reliably extract the waveguide losses.

5.3.4 Threshold current and spectra vs temperature measurements

Fig 5.23 shows the temperature dependence of the threshold current density $J_{th}(T)$ for the three lasing layers(samples dimensions are described in the caption of figure 5.23). The increase of $J_{th}(T)$ with temperature is attributed to the reduction of the upper state lifetime due to thermally activated LO-phonon and to thermal backfilling of the lower state [22]. The maximum operation temperature increases from 48 to 78 K with n_s as the maximum current increases faster than the threshold current. However a maximum is expected to be reached for larger dopings, when the backfilling will become significant.

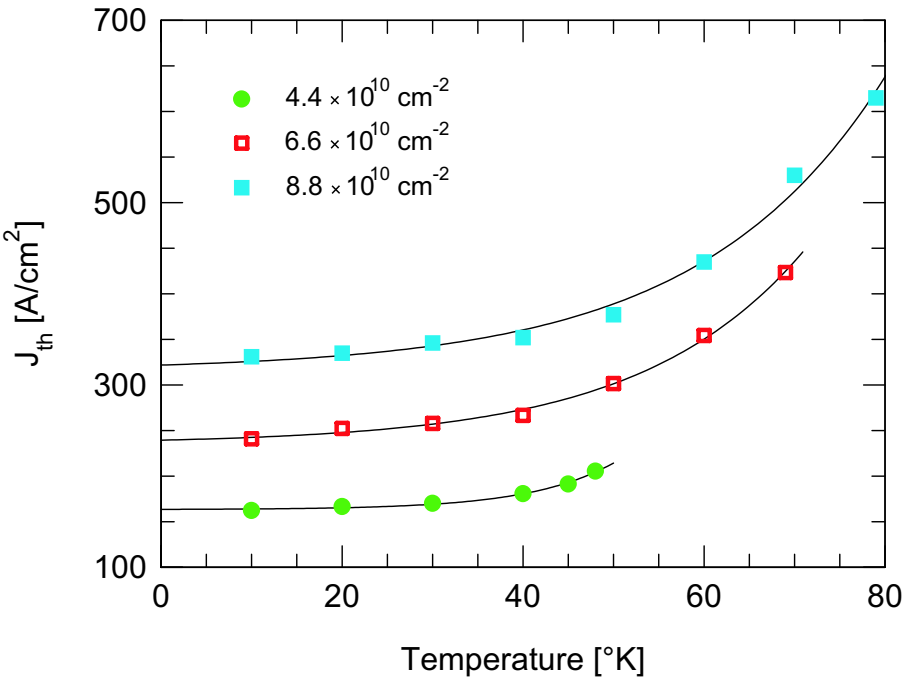

Figure 5.23: Comparison of the relative tempertature dependence of the threshold current density for the QCL's with different doping levels, as indicated. The solid lines correspond to fits of the data with the following relation $J_{th} = J_0 + J_1 \exp(T/T_0^*)$. Samples dimensions are 210 μm wide and 5.4, 1.8, and 2.5 mm-long for N299, N301, and N310 respectively. The improvements in the maximum operating temperature arise from successively increasing the sheet doping density. The squares show superior temperature dependence and a maximum operating temperature of 78 K.

The emission spectra were also studied in pulsed-mode (duty-cycle of 0.5 % and a repetition rate of 125 Khz and at a current above threshold $J = 1.2 \times J_{th}$) using a FTIR spectrometer (Nicolet 800) fitted with a DTGS pyroelectric detector and operated in rapid scan mode. The spectra are displayed in the Fig. 5.24 and show, as expected, an emitted photon energy that decreases with increasing doping as the threshold is reached for lower applied field. The

computed biases that correspond to the measured transition energies of 119.4 cm^{-1} (sample N299), 118.9 cm^{-1} (sample N301) 116.3cm^{-1} are respectively 4.75, 4.68 and 3.98 V.

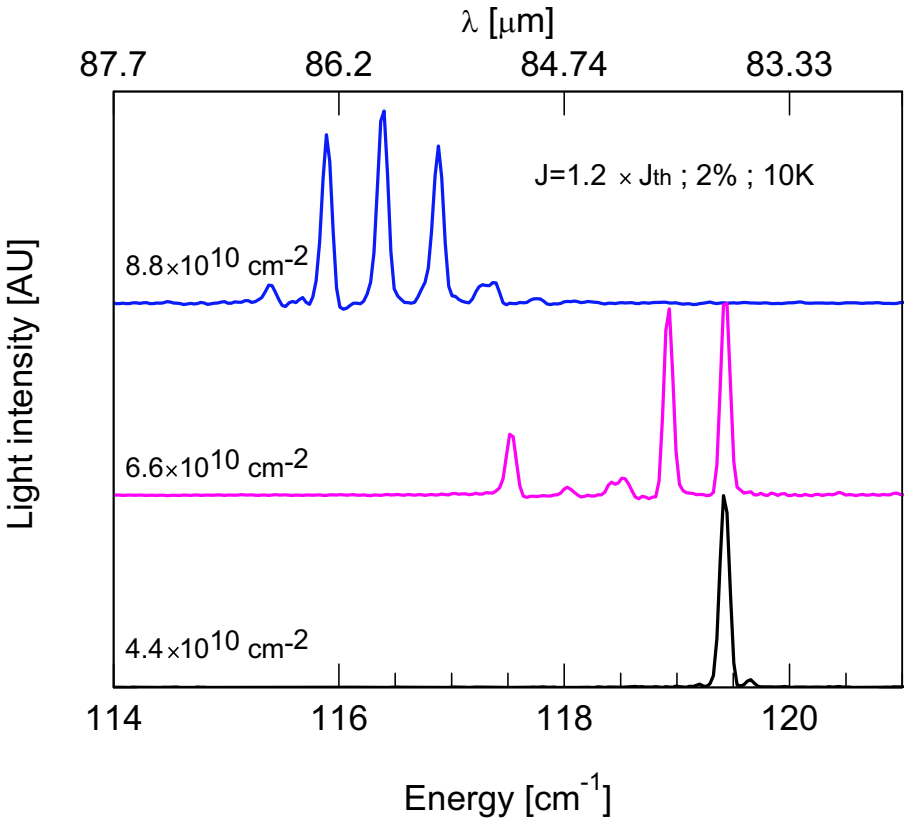

Figure 5.24: Lasing spectra of 210-μm-wide and 2.5 mm long QCL's(see Fig 5.19) taken at 10 K for different doping density (4.4, 6.6, 8.8 $\times$ $10^{10}\,cm^{-2}$), as indicated. The spectra are vertically displaced for clarity. The redschift observed is in agreement with the calculated optical transition.

5.4 Growth requirements

Because of the large number of layers, the large overall thickness (more than 10 μm) and the low average electron density (n = 2 $\times 10^{15} cm^{-3}$), the growth of THz QCLs is a very challeng-

ing task. At this point, however, it is not clear what the influence of the background doping of the growth equipement has on the performances of the structures. Such a study is being conducted on the University of Cambridge's equipement. We also performed a comparison of some parameters using our own growth equpement at the University of Neuchâtel. The mobility of a two-dimentional electron gas was used as an indication of the background doping of the two sets of equipement. In the dark, the mobility value at 4.2 K for a 40 nm spacer two-dimensional electron gas was consistently above $10^6 cm^2 V^{-1} s^{-1}$ for the material grown in Cambridge; the value of our equipement was significantly lower, $\mu = 3 \times 10^5 cm^2 V^{-1} s^{-1}$. It should be noted, however, that no optimization of the high electron mobility transistor structure was made for the sample grown in the equipement from Neuchâtel.

The two QCL structures discussed in section. 4.2 and 5.2.1 were also grown and processed at Neuchâtel. The structure based on the chirped superlattice (N85) did reach laser action. However, it operated only up to a maximum temperature of 35 K. Its threshold-current density (230 A cm^{-2} at 10 K) was higher to the one (137 A cm^{-2} at 10 K) measured in the structure grown in Cambridge (Fig. 4.7). Another structure identical to the device discussed in the section. 5.2.1, based on a bound-to-continuum transition and grown at Cambrigde (A2986), and at Neuchâtel (N301, N310) respectively, was also compared. The light-versus-current characterisatics at various temperatures of a representative device are shown in figure. 5.25.(b). The devices operates up to a temperature of 60 K and 78 K for N301 and N310, respectively. At that temperature a peak optical power up to 5 mW and 0.3 mW for N301 and N310, respectively is achieved.

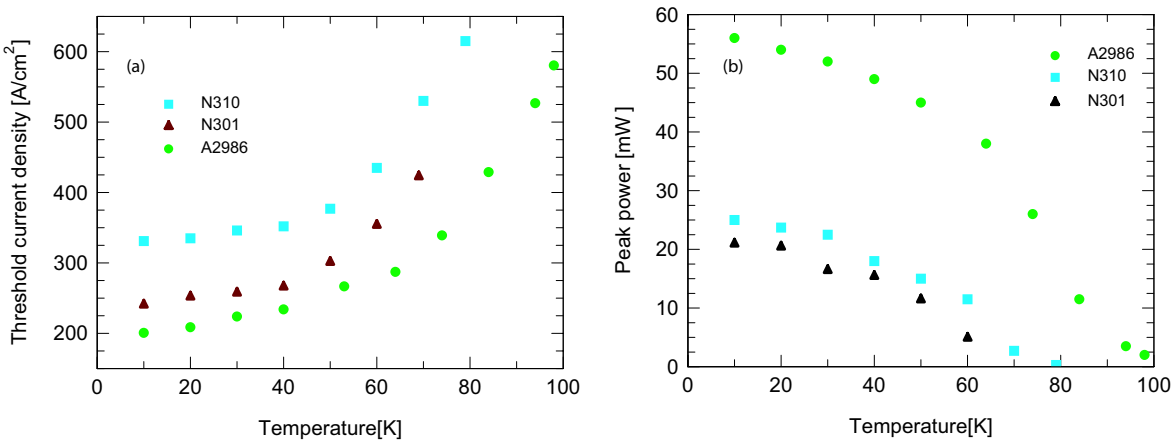

Figure 5.25: (a)Threshold current density and (b) peak power measured for samples N301, N310 grwon in Neuchâtel and A2986 grown in Combridge. We attribute the slightly lower performance of sample N301 and N310 to the larger background doping of the epitaxial growth system at the time it was grown.

A systematic comparison of the threshold-current densities is performed in figure. 5.25.(a). As shown in this figure, the results obtained with the three samples are similar, with better overall performances for sample A2986 from Cambridge. We attribute this difference to a higher background doping of our MBE equipment.

Chapter 6

Third generation of THz QCL's.

6.1 Introduction.

In order to improve the maximum operation temperature and the emitted power of the THz QC lasers, a new structure that combines the advantages of the bound-to-continuum approach with an optical phonon extraction was designed. A high-optical-power at $\lambda \simeq 74\,\mu$m wavelengths (100 mW at 10 K) has been demonstrated using this active region QC design and will be discussed in this chapter. 6.

6.2 Design and operation of GaAs/AlGaAs QCL's

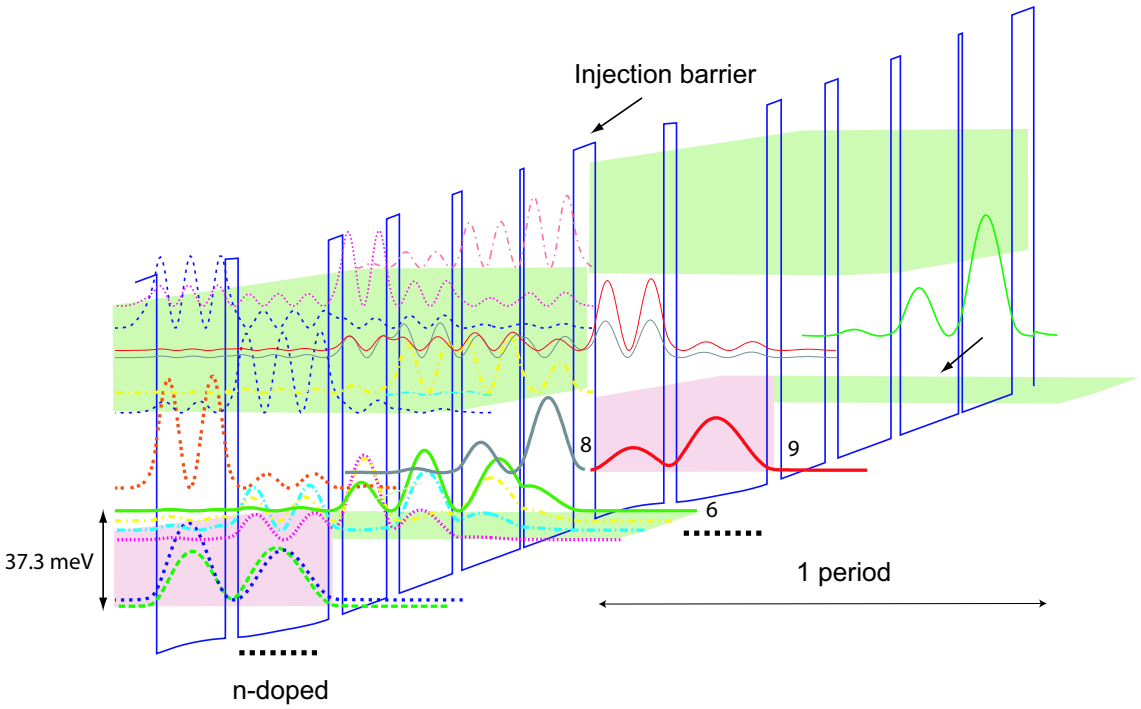

Figure 6.1: Computed conduction band profile at T = 10 K of one stage of the structure under an average applied electric field of 6.1 kV/cm. The GaAs-$Al_{0.15}Ga_{0.85}As$ layer sequence of one period of the active layers starting from the injection barrier is as follows: **4.6**/10.5/**0.8**/12.3/**2.0**/11.2/**2.7**/9.3/**3.0**/ 19.1/**2.7**/14.5/ where $Al_{0.15}Ga_{0.85}As$ layers are in bold, GaAs are in Roman underlined number correspond to Si doped layer with $n = 6 \times 10^{16}\,\mathrm{cm}^{-3}$.

The design, which is shown in Fig. 6.1, consists of four-coupled quantum wells active region followed by a two-coupled quantum wells injector region ($n_s = 11.4 \times 10^{10}$ cm^{-2}). A 3 nm extraction barrier separates the injection/relaxation zone from the active zone. Its consists of a 19.1 nm and 14.5 nm GaAs well separated by a 2.7 nm $Al_{0.15}Ga_{0.85}As$ barrier. The

energy difference of the two anticrossed states n = 1 and n = 6 is kept close (37.8 meV) to the LO-phonon energy to assure fast depopulation of the state n = 6. The injection barrier is 4.6 nm thick. The optical transitiuon is diagonal and takes place between state n = 8 and n = 6. At 6.1 kV/cm, the calculated energy transition E_{86} is 15.7 meV and the optical matrix element is $Z_{86} = 5.5$ nm. The miniband width of relaxation/injection region decrease close to the injection barriers and the upper state level is well-separated from the higher-lying states of the superlattice, lying in its first minigap. For these reason, the injection efficiency is not reduced by electron injection into higher energy states of the superlattice. As a consequence, thermally activated leakage of electrons into heigher energy states of the superlattice should be significantly reduced in this laser structure. We believe that this design feature notably improves the high temperature operation, also the slope efficiency and the peak power of the laser.

6.3 Experimental results

Two devices (N464 and N465) were grown by molecular beam epitaxy using GaAs and $Al_{0.15}Ga_{0.85}As$ alloys lattice matched on semi-insulating GaAs substrates with 300-nm $Al_{0.3}$-$Ga_{0.7}As$ etch-stop layers to accommodate processing for either SI-surface-plasmon or metal-metal waveguides and consist of a 120 period active region. The lower contact layer was 700-nm thick and doped at 3×10^{18} cm^{-3}. The sheet doping densities n_s are respectively a 11.4×10^{10} and 5.7×10^{10} cm^{-2}. The samples were processed as a single plasmon waveguide (Sec. 2.4.3) to have large peak power, which is not possible in a metal-metal waveguide

because of its strong mirror reflectivity. Afterward the devices are cleaved in variable length with a width between 70 μm and 210 μm, soldered with indium on a copper heatsink and mounted on the cold finger of a He flow cryostat.

6.3.1 Samples N464

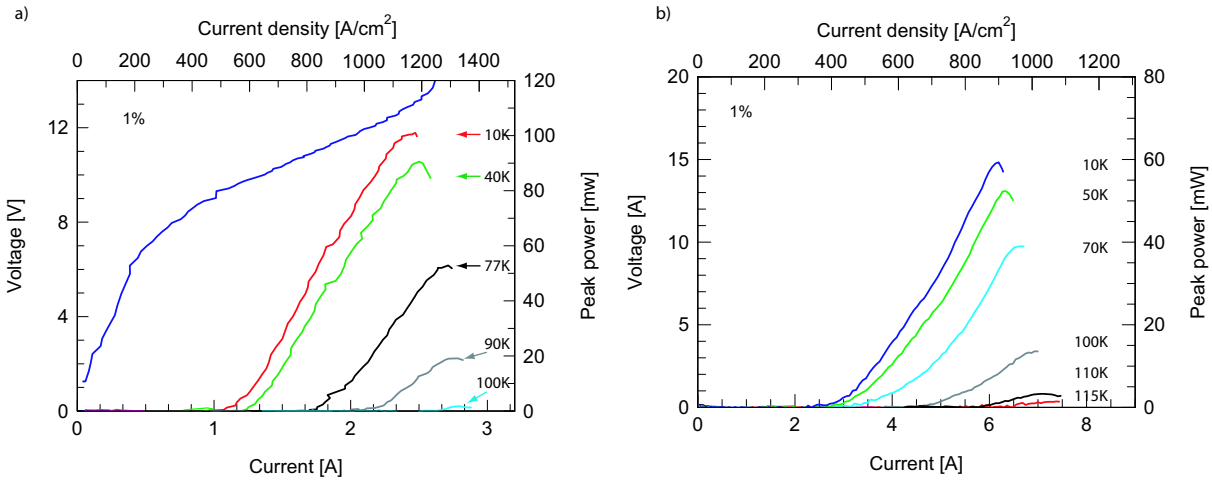

Figure 6.2: Peak optical output power versus injected current in pulsed mode at a duty cycle of 1 % at various temperatures from a 1 mm long, 210-mm-wide single plasmon laser ridge (a) and a 4.3-mm-long and 160 μm-wide waveguide (b).

For the N464 sample (n_s = 11.4 × 10^{10} cm^{-2}), devices are driven with 100 ns-long current pulses and a duty cycle of 1 %. For devices needed an injection current below 3.2 A, the electrical power is provided by a HP-8114A pulse generator. In pulsed mode, the threshold current is J_{th}= 520 A/cm^{-2} at 10 K, and lasing continued up to a maximum temperature of T_{max} = 100 K. Lasing ceases at the maximum current J_{max} = 1250 A/cm^{-2} when the injection subbands become misaligned, and the device enters into a negative differential resistance (NDR) region. The collected peak power at 10 K of 1 mm long and 210 μm-wide

device reaches a value of 101 mW. Still more than 2 mW is detected at 100 K (Fig. 6.2.(a)). In this device, the lasing threshold occurs at a bias of 9.5 V, and NDR is reached slightly above 13.5 V, which correspond roughly 79 mV/module and 112 mV/module respectively. This is consistently much larger than the design value of 55 mV/module. The differerence is likely due to parasitic resistance associated with the lateral contacts. Due to the large current injection needed for a 160 μm-wide and 4.3 mm long device, a commercial pulse generator (Alpes Lasers, TPG 128 pulser, and a LDD 100 power supply) was used, delivering 100-ns-long current pulses at a repetition rate of 100 KHz. The round observed in the Li curves is due to the change of shape of the electrical pulse during measurements (Fig. 6.2.(b)). Indeed, an additional current due to the rectangular shape of electric pulse is measured, producing a shift of current measured. Increasing the electric bias, the shape of pulse becomes square and the shift of current is reduced. As compared with the results obtained from the 1 mm long device (Fig. 6.2.(a)), the maximum temperature is improved to 115 K and the threshold current density is reduced to 365 A/cm^{-2} (Fig. 6.2.(b)). The improvement in temperature performance and in threshold current density compared to the smaller device (T_{max} = 100 K and J_{th}= 495 A/cm^{-2} at 10 K for 1 mm long and 160 μm-wide device) is due to the increase in cavity length. Increasing the cavity length from 1 mm to 4.3 mm reduced the mirror losses from α_m = 6 cm^{-1} to 1.4 cm^{-1}. Given the threshold condition (Eq. 2.2.46), and using the calculated values of Γ = 0.37 and α_W = 8.9 cm^{-1}, this increase in cavity length therefore reduces the threshold material gain g_{th} from 40 to 28 cm^{-1}. Although J_{th} in these devices is significantly larger than in bound-to-continuum QCLs (Sec. 5.2.1, and 5.3.4), these devices also have a large dynamic current range of 400-500 A/cm^2 above threshold, which results in

large output powers.

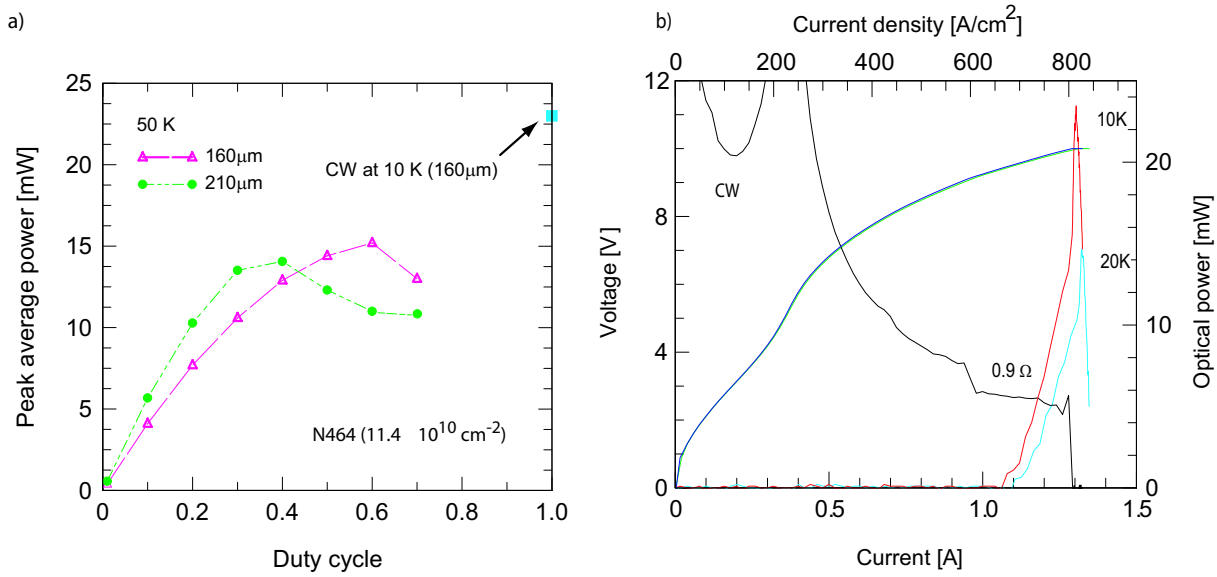

Figure 6.3: a) Average power data as a function of duty cycle taken at 10 K. The cavity length are 1-mm with a stripe width of 210 and 160 μm-wide waveguides. A high reflecting coating are deposited on one facet allowed to reduce the mirror losses down to 6 cm^{-1}. b) Continuous wave optical output power of a 1-mm-long, 160-mm-wide single plasmon waveguide device together with differential resistance (left axis). At 800 A/cm^2, the continuous wave operation is stopped due to device heating.

Figure. 6.3.a displays the maximum average power data taken for pulses of increasing width repeated at 100 KHz. The maximum average power increases for duty cycles below 40 %, but for longer pulses, the power drops due to heating. Although 11 mW maximum average power was observed at 70 % duty cycle, the device burned out in continuous wave (cw) mode due to device heating. For a 160μm-wide, 1-mm-long coated ridge, a maximum average power of 13 mW was observed at 70 % duty cycle and continuous wave operation was briefly observed for approximately 3 s before heat buildup in the cryostat stopped operation (fig. 6.3.b). A

peak pulsed power of 73 mW was observed in pulsed mode for this device at 10 K.

The high threshold current densities are the main reason which prevents continuous wave (cw) operation of optical phonon extraction based design. The maximum injection current in a quantum cascade laser is limited by resonant tunneling (Equ. 5.3.13), and is proportional to the sheet carrier density (Equ. 2.1.35). In order to reduce the current densities in the active region, the same design has been growth in N465 device at low sheet doping density ($5.7 \times 10^{10}\,\mathrm{cm}^{-2}$). The results of this device will be discussed in details in the following section.

6.3.2 Samples N465

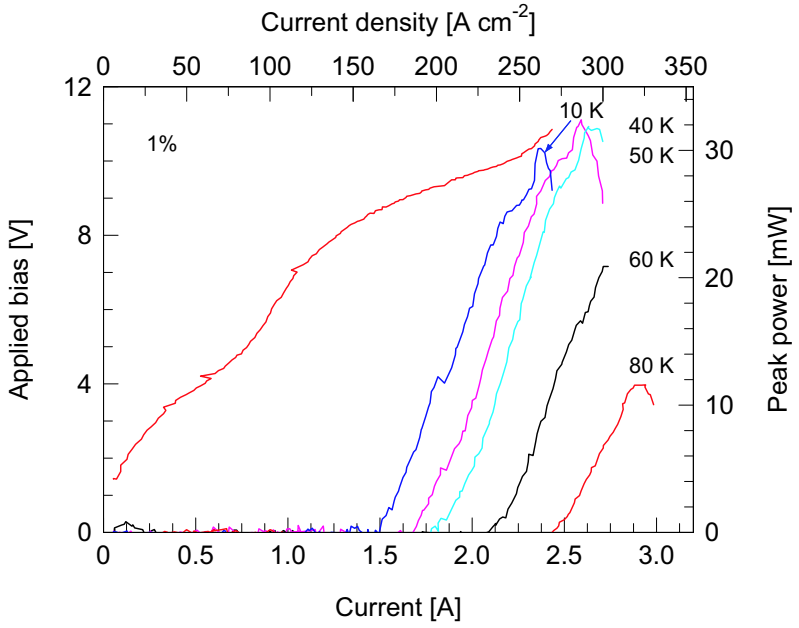

Figure 6.4: L-I and V-I taken in pulsed mode for 210-μm-wide, 4.3mm-long ridge after the evaporation of a HR coating on the backfacet. Data was measured using 100-ns pulses repeated at 100 kHz.

The light versus current (L-I) characteristics were collected in both pulsed and CW modes from device N465 and are plotted, in Fig. 6.4 and Fig. 6.5, respectively. In pulsed mode, for 4.3mm-long and 210-μm-wide laser, the threshold current was j_{th} = 166 A/cm^2 at 10 K, and lasing continued up to a maximum temperature of T$_{max}$ = 80 K. The maximum emitted peak power was 32.4 and 11.7 mW with a slope efficiency dP/dI equal to 38 and 26 mW/A at, respectively, 10 and 80 K. In cw mode, lasing could be reached in smaller devices, yielding a maximum operating temperature of 40 K with peak powers of the order of 8 mW for a 1.7-mm-long, 160 mm-wide laser ridge provided of high reflectivity backfacet coating (Fig. 6.5). This results represents an improvement of 20 K compared to the devices with high dopind density (N464: $6 \times 10^{16}\,\mathrm{cm}^{-3}$).

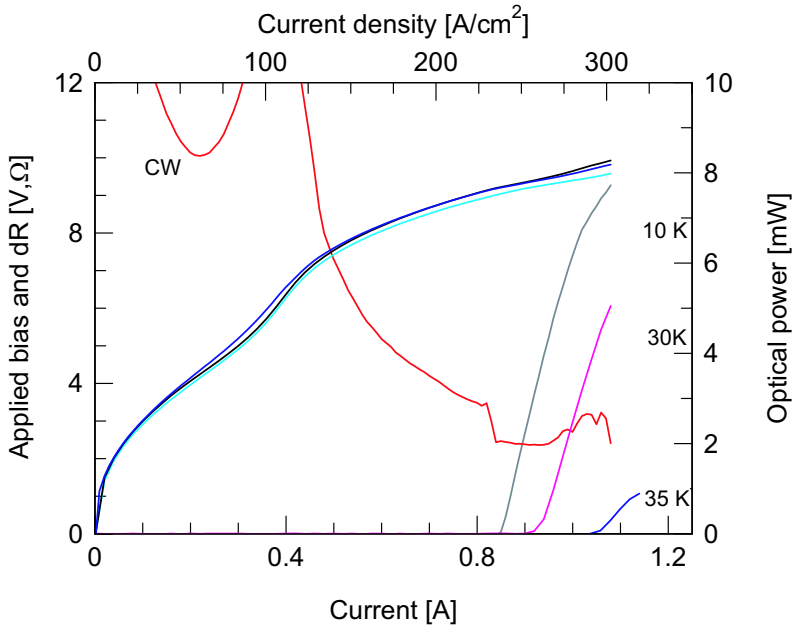

Figure 6.5: Devices with low doping in the active region (N465: $3 \times 10^{16}\mathrm{cm}^{-3}$) worked in continuous wave up to 40 K. emitted power has been measured with a calibrated thermopile from a 1.7-mm-long, 210-mm-wide waveguide laser ridge.

Despite our expectations, these two devices show no particular temperature improvement to the best performance from bound-to-continuum designs, which typically lase up to 70 K in CW operation (Fig. 5.5 and Ref. [136]). Assuming the same thermal conductivity as our previously results (Sec. 5.2.1), the lower cw temperature range could be explained by the higher electrical power dissipated due to a threshold bias that results to be 9.2 V, 2.4 times higher than in the bound-to-continuum case. Inspection of the CW-LI curve at 40 K confirms this hypothesis, clearly showing a power saturation due to thermal rollover. The differential resistance shows a discontinuity at threshold with a size of 1 Ω which is lower than the value of 1.2 Ω obtained from a device with similar dimensions and a bound-to-continuum transition-based active region. As shown theoretically [127], the size of this discontinuity is ultimately limited by the ratio of the upper to lower state lifetimes. However, contrary to expectation, the lower ratio of lifetimes in the optical phonon extraction based designs indicates a poor selective injection and depopulation processes.

6.3.3 Comparison

The values of threshold current density J_{th} measured in pulsed mode are plotted versus temperature for both devices in Fig. 6.6. As shown in this figure, the difference in terms of performance between the high and low-sheet doping densities QCLs is not negligible. For comparison, the threshold current density between 10 and 80 K is lower in N465 than in N464 device of about 50 %. Note that the measured slope efficiency is only 35 mW/A for the low doping density samples (N465), which is lower of 65 % than for N464 (101 mW/A). Although our device does not reach high enough temperature for a good fit, a value of T_0 =

107 K and 134 K are obtained for N465 and N464, respectively. For N464 device, a value of $T_0 = 74$ K is obtained if the highest temperature points are used.

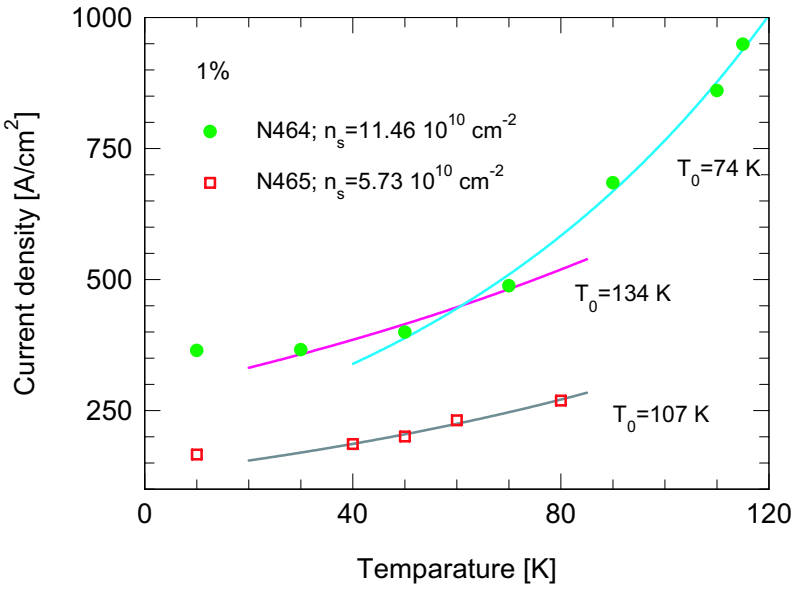

Figure 6.6: Threshold current density as a function of the heatsink temperature in pulsed mode for both devices (N464 and N465). The curves correspond to the usual exponential fit $j_{th} = j_0 exp(T/T_0)$.

The dependence of the threshold and maximum current densities with the sheet doping density are reported in figure. 6.7. From 5.7 $\times 10^{10}$ to 11.4 $\times 10^{10} cm^{-2}$ sheet doping density, the maximum current densities J_{max} increases three times. A doping offset of about $n_{offset} = 2.6 \times 10^{10} cm^{-2}$ was extracted from the intersection of the linear fit of maximum current densities data curve with the axis of sheet doping density. We interpret this offset as a p-type background residual doping of the order of $N_A = 2.8 \times 10^{15}\,\mathrm{cm}^{-3}$, which is higher by a factor of 1.3 than the value extracted from the devices growth in another run and using the same MBE machine (Sec. 5.3.2).

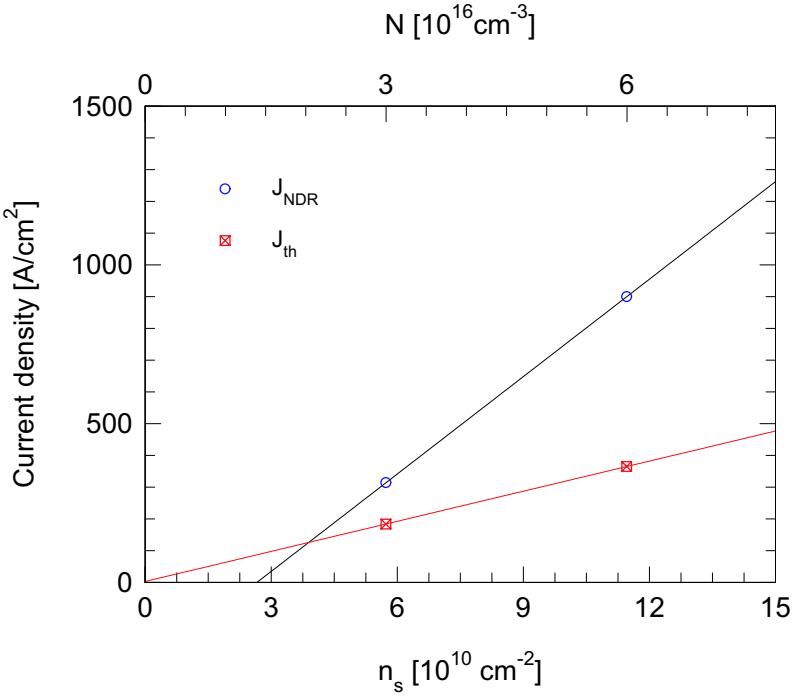

Figure 6.7: Threshold current density (J_{th}) and the maximum current density before appearance NDR (J_{NDR}) as a function of doping density.

The origin of this difference is not completely clear. In reality, the p-type background concentration in GaAs growth layers differ to that in AlGaAs barriers. Therefore, an alternative possible explanation for the difference in the background doping can be the different thickness per period of the GaAs or AlGaAs layers between the both series of growth A (N310, N301, N299) and B (N464, N465). The background impurity concentration in GaAs layers was about 1.7 higher in the serie B than in the serie A. This large difference proves that the major background impurity is not coming from the GaAs growth layers. However, in AlGaAs barriers, we find a p-type background concentration of about 1.64 10^{16} cm^{-3} in the serie B which is close to that of serie A, where a value of 1.31 $\times$ 10^{16} cm^{-3} is found. The

ratio between these two values is 1.2, this indicates that the major background impurity is coming from the AlGaAs growth layers. In addition, a long time separation ($\approx$ 1 year) is however separating these growths and growth conditions are therefore not identical leading to slightly different background residual doping.

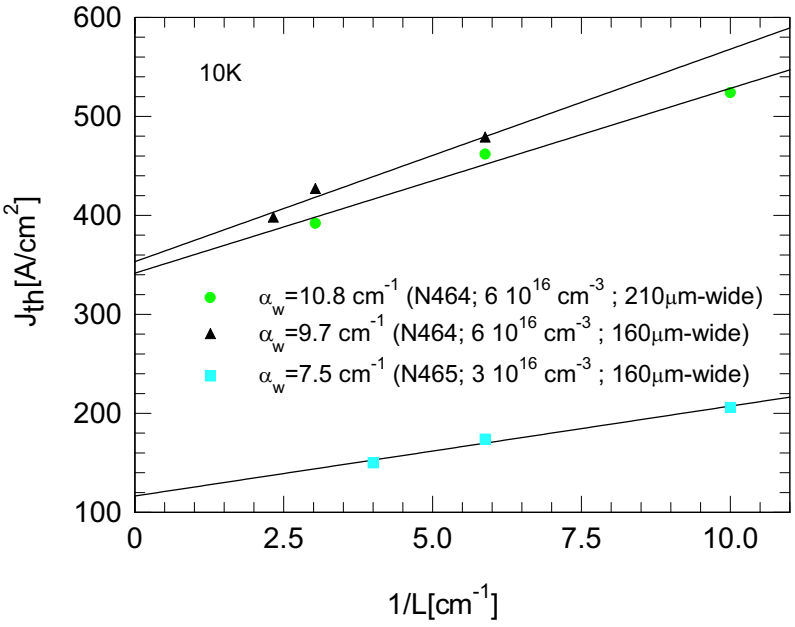

Figure 6.8: Threshold current density vs inverse laser length with backfacet coating for both samples (N464 and N465) measured at 10 K.

The threshold current density of the devices also increases with doping, from a value of 185 A/cm^2 (N465) to a maximum of 365 A/cm^2 for sample N464. As discussed in the Sec. 5.3.2, we attributed this increase to the decrease of the upper state lifetime with doping due to an increase in waveguide losses due to free carrier absorption. To verify the importance of free carrier absorption, we measured the threshold current density as a function of inverse laser length, and extracted the waveguide losses from the fit (Sec. 5.2.1). Using the data shown in the Fig. 6.8, assuming the computed reflectivity coefficient $R_1 = 0.31$ and $R_2 = 0.98$

and the computed value of the overlap factor $\Gamma = 37\,\%$ for N464 and N465, we can extract $g_d = 75\,\mathrm{cm/kA}$, $\alpha_w = 9.7\,\mathrm{cm}^{-1}$ and $g_d = 64\,\mathrm{cm/kA}$, $\alpha_w = 7.5\,\mathrm{cm}^{-1}$ for 160-μm wide-ridge of N464 and N465 respectively.

In Fig. 6.9, we report the waveguide losses as a function of the sheet doping density (n_s). As shown in this figure, the experimental waveguide losses (7.5 and 9.7 cm^{-1}) agree well with the calculated values (6.5 and 8.9 cm^{-1} respectively). The calculated waveguide is obtained using the bulk Drude model with the same parameters used in Sec. 5.3.3.

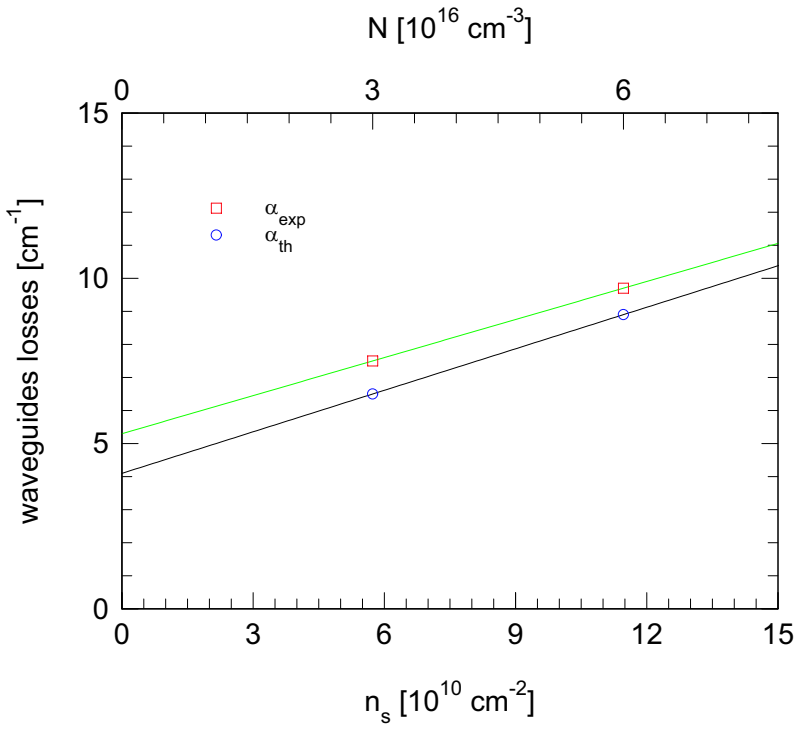

Figure 6.9: experimental and calculated waveguide losses versus n_s. The waveguide losses are calculated using the Drude model with $\tau = 0.5$ ps for the active region, 0.15 ps for the heavily doped regions, and 0.05 ps for gold.

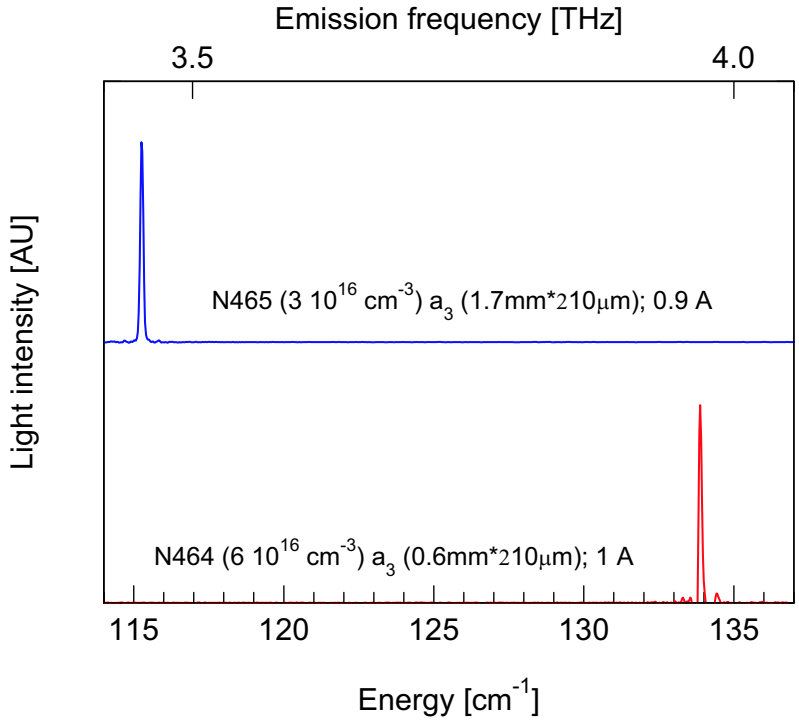

Figure 6.10: Lasing spectra of 210-μm-wide and 1.7 and o.6 mm long for N465 and N464 QCL's respectively taken at 10 K for different doping density (5.7, 11.4 $\times$ $10^{10}\,\mathrm{cm}^{-2}$), as indicated. The spectra are vertically displaced for clarity. The redschift observed is in agreement with the calculated optical transition.

The emission spectrum of these samples were also studied in pulse-mode (duty-cycle of 0.5 % and a repetition rate of 100 Khz and at a current above threshold $J = 1.2 \times \mathrm{J_{th}}$) using a FTIR spectrometer fitted with DTGS pyroelectric detector in rapid scan mode. The spectra are displayed in the Fig. 6.10 and show, an emitted photon energy that shifts with increasing n_s by about 2.3 meV to higher energies. Note that this change of the lasing energy due to the doping variation is more than one order of magnitude larger than variations of E_{86} across a wafer. Furthermore, since we verified the structural parameters of the QCLs by

x-ray diffraction, we can also exclude that the variation of E_{86} is caused by fluctuations of the layer thickness or Al content. The computed biases that correspond to the measured transition energies of 115.3 cm^{-1} (sample N465), 133.9 cm^{-1} (sample N464) are respectively 6.4 and 6.7 V, which are lower than the experimental value (9.3 and 10.4 V respectively).

Chapter 7

Distributed feedback terahertz quantum cascade lasers.

7.1 Introduction.

Distributed feedback (DFB) QC lasers provide a very elegant and reliable method to achieve a single-mode operation. It is the grating period rather than the laser gain spectrum which determines the single-mode emission wavelength. In this chapetr, single mode emitting device is presented at wavelengths range between 83 and 90.5 μm that also use a loss-coupled grating. The QCL material used for this work is described in detail in section. 5.2.1 and consists of a GaAs/$Al_{0.15}Ga_{0.85}As$ active region based on a bound-to-continuum design emitting at $\lambda = 87\mu$m. The device was processed using a SI-surface-plasmon waveguide. The Bragg grating are defined by either etching and refilling with hard backed resist or etching and metal coverage (Sec. 3.2.2).

7.2 Loss-coupled distributed feedback far-infrared Quantum Cascade lasers.

The device was processed into SI-surface-plasmon waveguides, where a loss-coupled gratings manufactured using an etching and refilling with hard backed resist (Sec. 3.2.2).

7.2.1 spectra as a function of grating period.

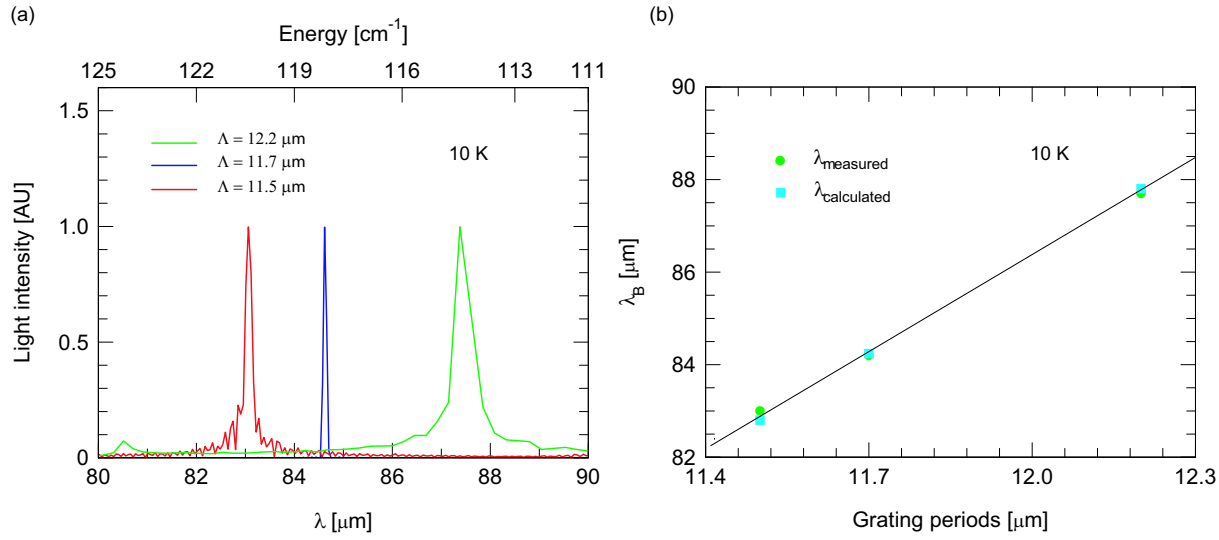

Figure 7.1: (a) Lasing spectra of DFB QC laser as a function of different grating periods. (b) Good agreemnet is obtained between the calculated (squares symbols) and the experimental (cycles symbols) bragg wavelengths as a function of the grating periods. The slope of the line fit to the data, give $n_{eff} = 3.40$ close to the calculated value (3.68).

Spectral measurements were performed in pulsed mode operation with pulse lengths of 100 ns and a duty cycle of 0.008 %. They were measured under vacuum with a home-made

Fourier transform infrared (FTIR) spectrometer in step-scan mode using a liquid-helium-cooled Si bolometer as detector. In Fig. 7.1(a), typical emission spectra are shown for a 1.7 mm long and 160 μm wide DFB laser for different grating periods. Single mode operation is observed for three grating periods (11.5, 11.7 and 12.2 μm). The Bragg wavelength relation is illustrated in the Fig. 7.1(b) which shows the measured Bragg wavelength as a function of grating period. An effective refractive index of 3.40 can be extracted, which is close to the calculated value (3.68). For the other grating periods (11.9, 12, 12.4 and 12.5 μm), devices do not lase and a problem related to the etch is suspected.

7.2.2 Liiv curves.

The light-current characteristics in pulsed mode for a laser operating with a grating periodicity of $\Lambda = 11.7\mu m$ are shown in Fig. 7.2(a). The devices were driven with 160 ns-long current pulses and a duty cycle of 2 %. The terahertz emission was collected through a light pipe and sent to a broadband thermopile power meter. At 10 K, the measured slope efficiency (dP/dT =12 mW/A) and maximum optical power (P_{max} = 6 mW) are much smaller than the values obtained in equivalent Fabry-Perot (FP) devices (dP/dT = 56 mW/A and P_{max} = 56 mW). Furthermore, at 10 K, the threshold current density increased to $J_{th} = 352\,A/cm^2$, compared to ($J_{\rm th} = 235\,A/cm^2$), in the FP laser. This degradation of performance is a result of reduction of the ratio Γ/α_W from 5.9×10^{-2} in FP devices to 4.8×10^{-2} in DFB devices[1]. The transport characteristics of the two FP and DFB devices are reported in the

[1]The ratio of Γ/α_W in DFB devices is calculated using the bulk Drude model and assuming a refractive index of n=2 for the resin.

Fig. 7.2(b). Because of the etching and refilling of the grating with hard baked resist, the current is injected into the active region only from the non-etched part of the grating, therefore the effective surface of current injection is a fraction of the total ridge surface. The device achieves proper band alignment at 99 A/cm^2 in FP and 165 A/cm^2 in DFB and the ratio of the two current densities is 165/99 =1.7, yielding an effective surface of injection for the DFB device 40 % smaller than the FP one.

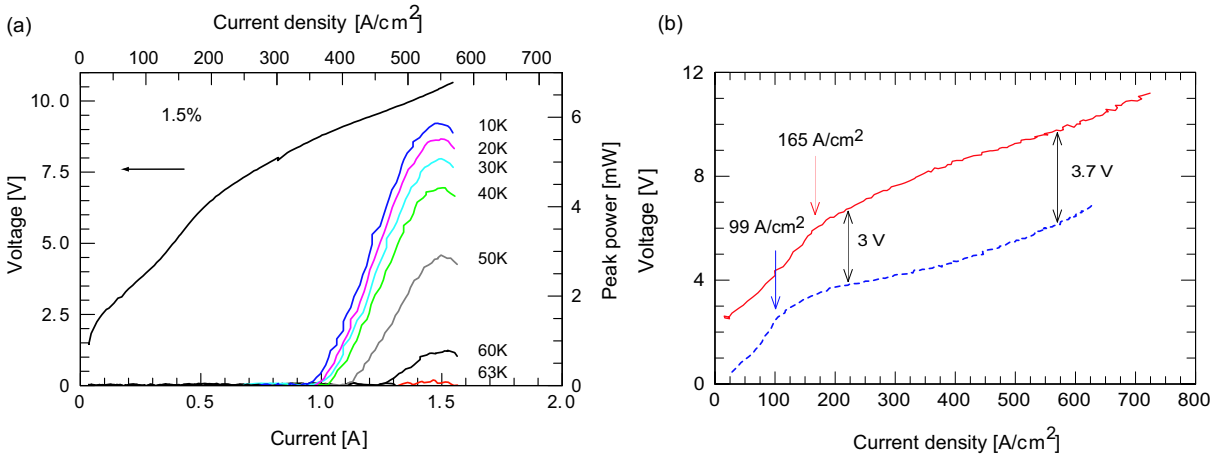

Figure 7.2: (a) Liiv curves of the laser operating at $\Lambda = 11.7$ μm measured at different temperatures. (b) Applied bias as a function of injection current in pulsed mode of the DFB (continuous line) and FP (dashed line) devices.

7.2.3 Lasing spectra

The laser spectra were then measured with an FTIR spectrometer in rapid scan mode using a DTGS pyroelectric detector. Single mode operation is observed for all driving currents (Fig. 7.3(a)). Figure. 7.3(b) shows the lasing spectra at temperatures between 20 to 60 K. Single mode operation was also observed for all temperatures. We determined the line width

to be below of 0.09 cm^{-1}, which corresponds to the resolution limit of our experimental setup. In addition, the temperature tuning coefficient of the lasing peak was found to be constant over the entire temperature range, and its magnitude was $1/\lambda \times \Delta\lambda/\Delta T = 2 \times 10^{-5} K^{-1}$.

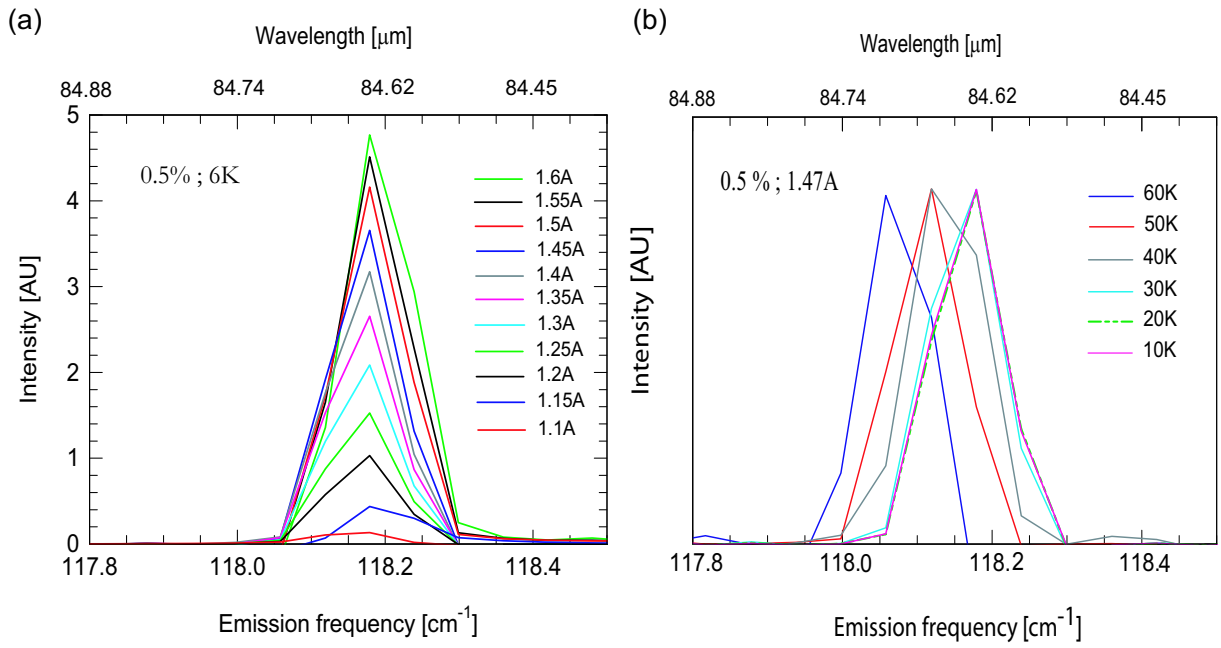

Figure 7.3: (a) Spectra of the laser operating at $\Lambda = 11.7$ μm measured at different current injection. (b) shows lasing spectra of the same device taken at different temperatures between 20 and 60 K.

7.3 Continuous wave operation of distributed feedback terahertz quantum cascade lasers.

In previous section, we have demonstrated the possibility of single mode QCLs based on a bound-to-continuum device, emit at three (83.0, 84.2, 87.7 μm) wavelengths and also use a loss-coupled grating. In this case, the device burned out in continuous wave (cw) mode

due to the high threshold current density ($\geq$ 365 A/cm^2) which is likely related to the quality of the processing devices, such as the grating, the waveguide configuration and the contamination of the GaAs surface by the resine. The single-wavelength emission in CW operation has the advantage of a very narrow line-width [119], which is essential for high-resolution spectroscopy of trace gases at low pressure. For this reason an improvement in the quality of the processing devices is still needed to achieve CW operation. In this section, we report a continuous wave single-mode operation of terahertz distributed feedback QCLs at wavelengths of 85.2, 86.9 and 87.2 μm. The grating is based on the combination of wet chemical etching and metal coverage. To avoid contamination of the GaAs surface, the step of refilling with hard baked resist of last processing fabrication is removed. Pulsed and continuous wave operation of single-mode terahertz quantum cascade lasers using this concept were first demonstrated in 2005 [137]. It should be noted that this technique is different from the other DFB terahertz QCLs fabricated using lateral corrugation in a metal-metal ridge waveguide [138].

7.3.1 Optical measurements

Spectral measurements were performed in pulsed mode operation with pulse lengths of 100 ns and a duty cycle of 8 $\times$ 10^{-5}. They were measured under vacuum with a home-made Fourier transform infrared (FTIR) spectrometer in step-scan mode using a liquid-helium-cooled Si bolometer as detector. Fig. 7.4, shows typical emission spectra for a 1.25 mm-long and 110 μm-wide DFB laser for different grating periods. Single mode operation is observed for six grating periods (11.7, 11.9, 12, 12.1, 12.2 and 12.5 μm). The reason for devices with

11.5 and 12.4 μm periodicities failure to lase was likely due to a problem related to the etch of the grating.

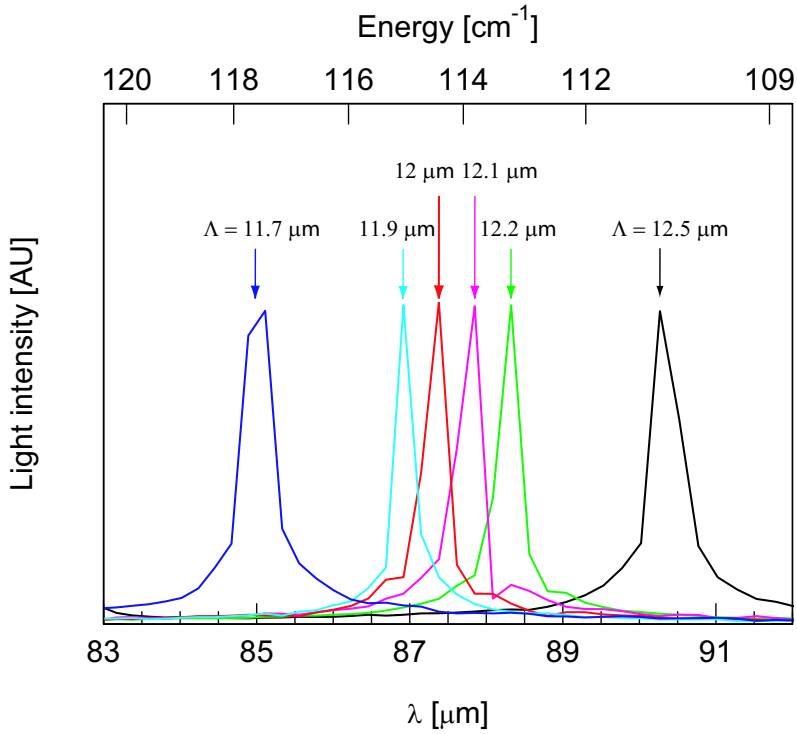

Figure 7.4: Lasing spectra of DFB QCL in pulsed mode for different grating periods.

Laser emission in CW operation was also observed from the DFB processed devices at high-resolution ($0.09\,\mathrm{cm}^{-1}$) with a Nicolet fourier transform infrared (FTIR) spectrometer in rapid-scan mode (Fig. 7.5). Single mode operation is observed for 11.7, 11.9 and 12.1 μm grating periods. The emission wavelength shift as a function of the grating period. For the other grating periods (12, 12.4 and 12.5 μm), devices do not lase in continuous wave and a problem is related to the large current densities ($\geq$ 460 A/cm^2).

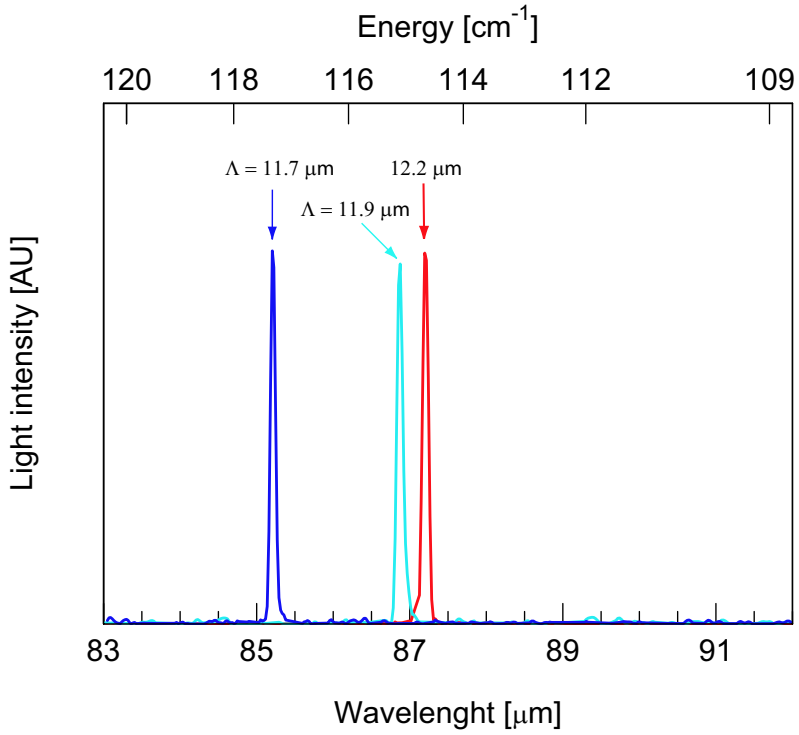

Figure 7.5: Lasing spectra of DFB QCL in CW operation for different grating periods.

The Bragg wavelength relation is illustrated in the inset of Fig. 7.6, which shows the measured Bragg wavelength versus grating period. In pulsed operation, a clear linear variation is observed and an effective refractive index of 3.65 can be extracted, which is in agreement to the calculated value (3.68). In CW operation, the agreement between the experimental and calculated Bragg wavelength is satisfactory for the three grating periods (Λ=11.7, 11.9 and 12.1 μm).

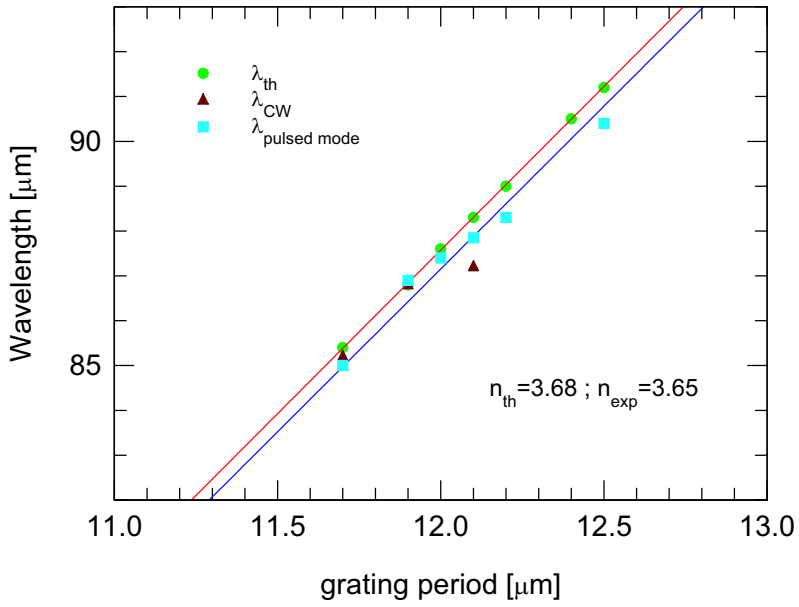

Figure 7.6: Good agreement is obtained between calculated (circles) and experimental Bragg wavelengths in pulsed (squares) and CW operation (triangles) against grating period.

Light-current curves, and applied bias against injection current of DFB laser with 11.7 μm grating period are measured in CW operation at different temperatures (Fig. 7.7(a)). The maximum CW single-mode output power at 10 K is 7.7 mW, the slope efficiency dP/dI = 26 mW/A, and the threshold current density $J_{\mathrm{th}} = 383\,\mathrm{A/cm^2}$. These, as well as the pulsed operation values, compare well to recent QC-DFB lasers using etching and refilling with hard baked resist. Finally, Fig. 7.7(b) shows the lasing spectra at temperatures between 10 and 40 K. We observed single mode in CW operation for all temperatures and, in particular, at maximum power for each individual temperature. The temperature tuning is well described by a linear expression up to 40 K and its magnitude was $1/\lambda \times \Delta\lambda/\Delta\mathrm{T} = 2.2 \times 10^{-5}\mathrm{K}^{-1}$.

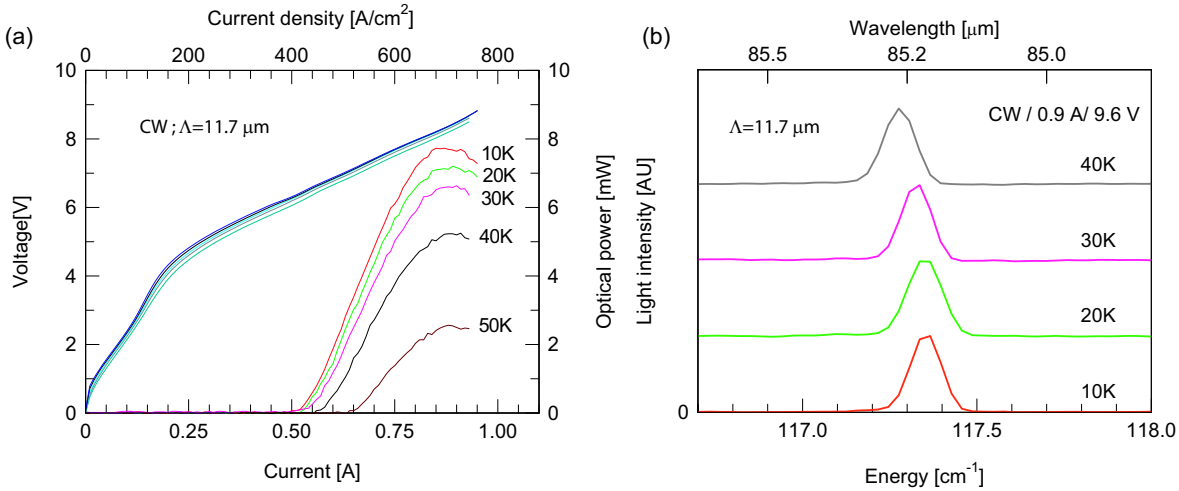

Figure 7.7: (a) CW optical power from a single facet and bias of a 110 μm-wide and 1.25 mm-long DFB QCL as function of drive current for various heat sink temperatures. (b) Lasing spectra of the same device measured at different temperatures.

Luminescence spectrum for a grating period $\Lambda = 11.9\mu m$, measured below lasing threshold allowed a relatively precise measurement of the Bragg reflector's stop-band width (fig. 7.8(a)). The spontaneous emission peaks around 115 cm^{-1}, exhibits a regular FabryPerot modes with a spacing of $\approx$ 0.94 cm^{-1} (cavity length: 1.25 mm). To distinguish the main stop band from all other minor peaks of the spontaneous spectrum, the position of the peaks are reported as a function of its number ($E_{peakpostion}$ = f(n)) (circles) (Fig. 7.8(b)). The measured data below and above 115 cm^{-1} are well fitted by a linear function y_1 and y_2, respectively. The data extracted from the difference quantity ($E_{peakpostion}$ - y_1) (squares), shows a gap at 115 cm^{-1} due to the stop-band. The stop-band width value extracted from this figure was $\approx$ 0.27 cm^{-1} for the first-order DFB laser. From this value, we determined the coupling coefficients of the grating to be $\kappa = \Delta\lambda\pi n_{eff}/\lambda^2 = 3$ cm^{-1}. which is larger than the computed value

obtained from the coupled mode approach [139, 111, 121]:

$$\kappa = \left| \frac{\pi \Delta n_{eff}}{4 n_{eff} \Lambda} + i \frac{\Delta \alpha_W + \Delta \Gamma g_{th}}{4} \right| = 0.55 cm^{-1} \tag{7.3.1}$$

where $\Delta n_{eff} = 3 \times 10^{-3}$, $\Delta \alpha_W = 0.47 cm^{-1}$ and $\Delta \Gamma = 0.025$ are the differences of the modal refractive index (n_{eff}=3.679), waveguide attenuation coefficient ($\alpha_W = 6.5 cm^{-1}$) and confinement factor ($\Gamma = 0.38$) between the grating grooves and plateaus. $\Lambda = 11.9 \mu m$ is the first-order grating priod and $g_{th} = 26 cm^{-1}$ is the gain coefficient at laser threshold calculated from $g_{th}\Gamma = \alpha_{tot}$ relation where $\alpha_{tot} = 10.1 cm^{-1}$ is the total losses.

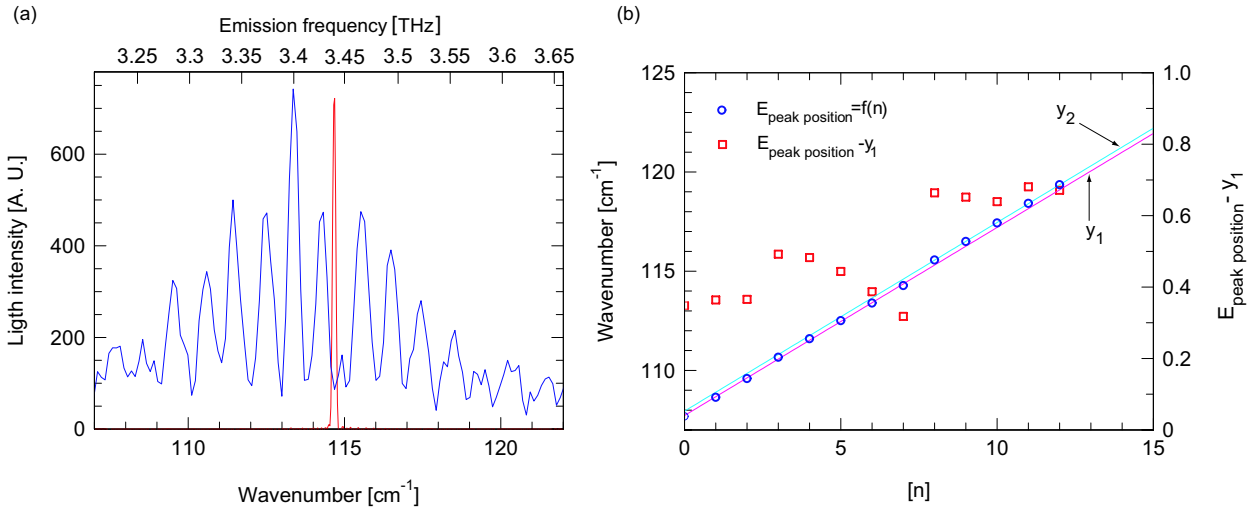

Figure 7.8: (a) Spontaneous emission spectrum of a 110 μm-wide and 1.25 mm long DFB QC laser for Λ=11.9 μm grating period measured at 10 K. (b) position of peak as a function of its number n.

In comparison to our previous DFB QC lasers(Sec 7.2), the new devices have unprecedented peak output power levels of 14.5 mW and 7.7 mW in pulsed and CW operation, respectively, measured at 10K. However, the disadvantage to this approach is that, contrary to the our

previous DFB laser where the single mode operation is observed for all driving currents and for all temperatures, a multimode spectra appeares at high current ($\geq$ 550 A/cm^2) and temperatures ($\geq$ 50 K) which due to the low coupling coefficient.

7.3.2 far-field measurements

Beam profiles of the laser light from DFB QC device were characterized at 545 A/cm^2 current density with a pyroelectric detector. The spatial profile of THz beams has been performed in two dimensions by measuring the laser ligth on a spherical region orthogonal to the propagation direction of the THz beam.

Device with 11.7 μm grating periodicity, is attached to the copper cold plate of a helium flow cryostat at a distance of 5 mm from the 60 mm diamater quartz crystal window. The QCLs are operated in the long-pulsed mode with 3000 $\times$ 333 ns-long current pulses at 11.1 μs intervals, providing an overall duty factor of 1.5 $\times$ 10^{-2} at a frequency of 15 Hz, in order to enable the use of a room temperature pyroelectric detector, together with a lock-in amplifier for noise reduction. The detector, with a 2 mm diameter sensor, is placed in a two-axis rotation system (θ and φ angle parallel and perpendicular to the growth layer plane respectively), in order to cover both vertical and horizontal beam profiles. The emission has been monitored with the detector at 25 mm distance from the QCL.

Fig. 7.9(a) show the orientation of the sample expressed in angular coordinates (θ and φ), where θ and φ having as origin the center of the positive x-axis direction. The beam patterns is obtained by measuring the distribution of intensities reaching the detector when it moves in the horizontal plane on a φ angle ($-60 \leq \varphi \leq +60$) centered at the front facet of the

sample and having as origin the positive direction of x-axis. A second rotation angle, in the plane parallel to the growth layer, allows to characterize the distribution intensity of laser in the vertical direction. The angular resolution for both directions is 2° and 3° for θ and φ respectively.

The terahertz emission is collected with a collection efficiency η_{coll} given by

$$\eta_{coll} = \frac{\Omega_{\theta_{\max},\varphi_{\max}}}{\Omega_{\theta=\pi,\varphi=\pi}} \tag{7.3.2}$$

Where $\Omega_{\theta_{max},\varphi_{max}}$ is the solid angle that, seen from the center of a sphere, includes a given area on the surface of that sphere. Taking account of the Gaussian distribution ($\exp(-\frac{\theta^2}{2\sigma^2})$) shown in Fig. 7.10, $\Omega_{\theta_{max},\varphi_{max}}$ can be written as:

$$\Omega_{\Theta_{max},\varphi_{max}} = \int\int_{\mathrm{S}} \frac{\mathrm{dA}}{\mathrm{r}^2} = \int_{\frac{-\theta_{\max}}{2}}^{\frac{+\theta_{\max}}{2}} \cos\theta \, \exp(-\frac{\theta^2}{2\sigma_1^2}) \, \mathrm{d}\theta \int_{\frac{-\varphi_{\max}}{2}}^{\frac{+\varphi_{\max}}{2}} \exp(-\frac{\varphi^2}{2\sigma_2^2}) \, \mathrm{d}\varphi \tag{7.3.3}$$

Where dA is the differential area of a surface of the detector, r is the distance from the QCL to the detector. From this equation, we can calculated $\Omega_{\theta=\pi,\varphi=\pi}$ with $\theta_{max} = \varphi_{max} = \pi$. Using eq. 7.3.3 and replacing each parameter by its value we find $\eta_{coll} \approx 3\,\%$.

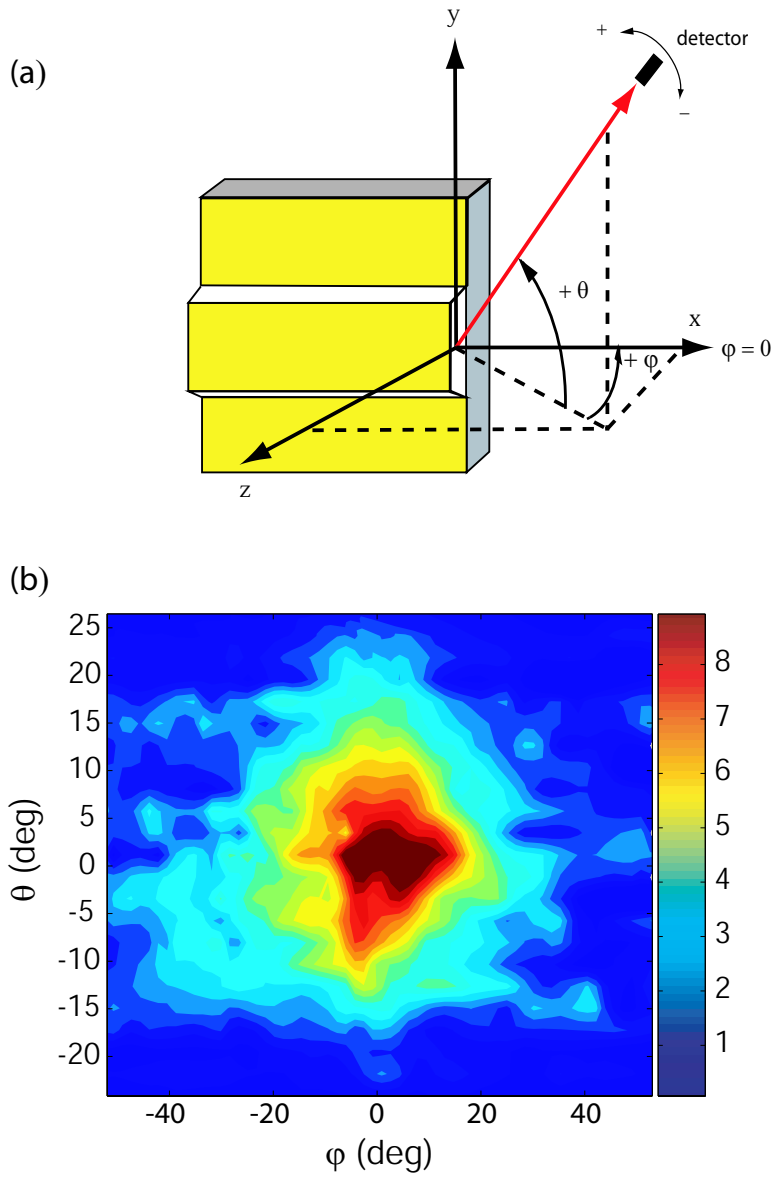

Figure 7.9: (a) This figure gives the definition of the angular coordinates for the orientation of the samples. The x-axis is perpendicular to the cryostat window. (b) Beam profile for a 1.25-mm-long Quantum Cascade DFB laser with Λ=11.7 μm grating period measured at 10 K. The measurements were taken at 750 A injection current with 0.015 % duty cycle.

Fig. 7.9(b) show the measured beam patterns distibution in a plane orthogonal to the prop-

agation direction of the THz beam. A clear intensity maximum in the pointing direction ($\theta = \varphi = 0$) of the laser is shown and it decreases smoothly in the two directions as gaussian profile.

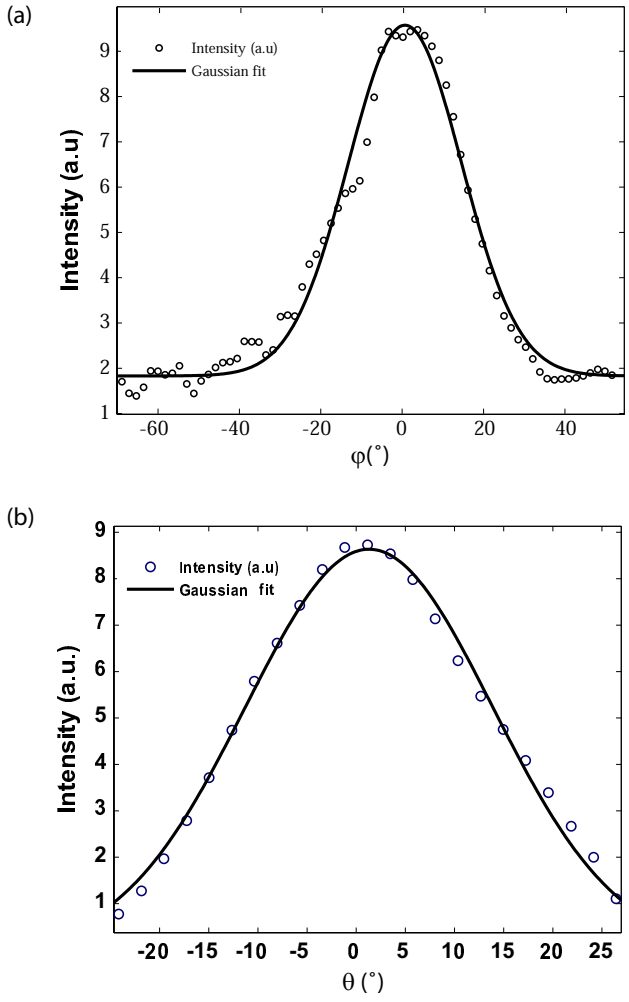

Figure 7.10: The section of the far-field distributions in the parallel (for φ=0; (a)) and perpendicular(θ=0; (b)) grown layers directions, represented by a Gaussian profile (Solid line) with standard deviation $\sigma_1 = 13°$ (0.22 radian) and $\sigma_2 = 17°$ (0.29 radian) for the function of variable θ and φ, repectively.

The section of the far-field distributions in the two directions parallel (for φ=0; Fig. 7.10.(a)

and perpendicular (θ=0; Fig. 7.10.(b)) to the grown layers exhibited a Gaussian profile with standard deviation $\sigma_1 = 13°$ (0.22 radian) and $\sigma_2 = 17°$ (0.29 radian) for the function of variable θ and φ, repectively. The far-field angle is of 27° full-width at half-maximum (FWHM) in the in-plane direction and 38° perpendicular to the layers, proving that the device oscillates in its fundamental lateral and transverse mode.

Chapter 8

InGaAs-AlInAs/InP terahertz quantum cascade laser.

8.1 Introduction.

Because they are based on intersubband transitions in quantum wells, quantum cascade lasers (QCL's) may be realized in principle in a large variety of material systems. The stringent requirements on the maturity of the growth technology had initially limited the choice to InGaAs/AlInAs/InP [46], GaAs/AlGaAs [9]. As the performances of lasers based on these two material systems were compared, and also compared to other prospective materials such as Si/Ge [140], it became clear that the effective mass of the material played a key role in the potential performances. Specifically, a low effective mass means large oscillator strength, lower sensitivity to interface roughness (because the structures are larger for any given transition energy) and for III-V compounds a weaker electron-optical phonon coupling.

These considerations, as well as the prospect of very large conduction band discontinuities, stimulated the developement of quantum cascade lasers based on InAs/GaSb [71, 72]. In contrast, quantum cascade lasers operating in the terahertz range have so far all been fabricated using the GaAs/AlGaAs material system [19, 20]. The advantages of this system for long-wavelength operation are a very mature growth technology, as proven by the record 2D gas mobilities ($> 10^7 cm^2/(Vs)$) [141] achieved at a GaAs/AlGaAs interface and a lattice match condition irrespective of composition. It is difficult to derive an absolute figure of merit for a material for a quantum cascade laser. However, one indication is the comparison of quantum cascade lasers operating at $\lambda \approx 10\mu$m, a photon energy sufficiently low that the conduction band discontinuity should not play a role in the comparison between $Al_{0.45}Ga_{0.65}As$/GaAs and $In_{0.52}Al_{0.48}As/In_{0.53}Ga_{0.47}As$. At 300K, the best published threshold current density is about $J_{th} = 9\,\mathrm{kA/cm^2}$ for the GaAs-based device [142], whereas the lowest value for the $In_{0.52}Al_{0.48}As/In_{0.53}Ga_{0.47}As$ is about $2.6\,\mathrm{kA/cm^2}$. The understanding is that approximately half of the improvement originates from a waveguide that exhibits lower losses and half from the improvement in lifetimes and oscillator strength. In this chapter, we show that, in principle, such gain could also be achieved in the Terahertz region of the spectrum, raising the prospect of higher temperature operation for these devices.

8.2 Waveguide design.

Electroluminescence of $In_{0.52}Al_{0.48}As$-$In_{0.53}Ga_{0.47}As$/InP structures in the THz has already been demonstrated in structures with a vertical transition in a single quantum well [143,

144] as well as in a chirped superlattice structure [123]. However, we will show that the waveguide design must also be slightly changed. In fact, a key feature of the $In_{0.52}Al_{0.48}As$-$In_{0.53}Ga_{0.47}As$/InP material is the relatively large refractive index difference $\Delta n \approx 0.36$ between the active region (which, for the case of Terahertz quantum cascade lasers, will consist mainly of $In_{0.53}Ga_{0.47}As$) and the InP substrate. For this reason, waveguides based on the confinement of the light by a buried contact layer will not work efficiently because this layer will be at the interface between two materials with a relatively large refractive index difference. The example of such a situation is shown in Fig. 8.1 where such a potential waveguide is shown. Very large losses ($\alpha_W = 52\,\mathrm{cm}^{-1}$) and a poor confinement factor are obtained ($\Gamma = 0.39$). A possibility for an efficient waveguide is to revert to the solution originally proposed by Sirtori et al. [102] where the mode is guided both by a metal *and* the refractive index difference between the core of the waveguide and the cladding material. However, in contrast with the latter work, a doped substrate cannot be used as the bottom contact since it would create unacceptably large losses($\alpha_W > 100\,\mathrm{cm}^{-1}$). We elected to use a high-mobility two dimentional gas as the mean to inject laterally the current while creating little additional losses($\alpha_W = 15\,\mathrm{cm}^{-1}$). The refractive index profile, as well as the computed mode intensity, is shown for such a waveguide in Fig. 8.1. A figure of merit for a waveguide is the ratio of overlap factor per active region period divided by waveguide loss Γ_P/α_w. Our $In_{0.52}Al_{0.48}As$-$In_{0.53}Ga_{0.47}As$/InP waveguide compares very favorably to a equivalent GaAs-based waveguide. Considering the numbers for the empty waveguide (i.e. active region loss not taken into account), this number is $\Gamma_P/\alpha_w = 9.2 \times 10^{-4}\,\mathrm{cm}$, significantly larger than the equivalent value for a GaAs-based waveguide $\Gamma_P/\alpha_w = 4.5 \times 10^{-4}\,\mathrm{cm}$ [94]. Layer thicknesses

and doping are described in the caption of Fig. 8.1(for the waveguide).

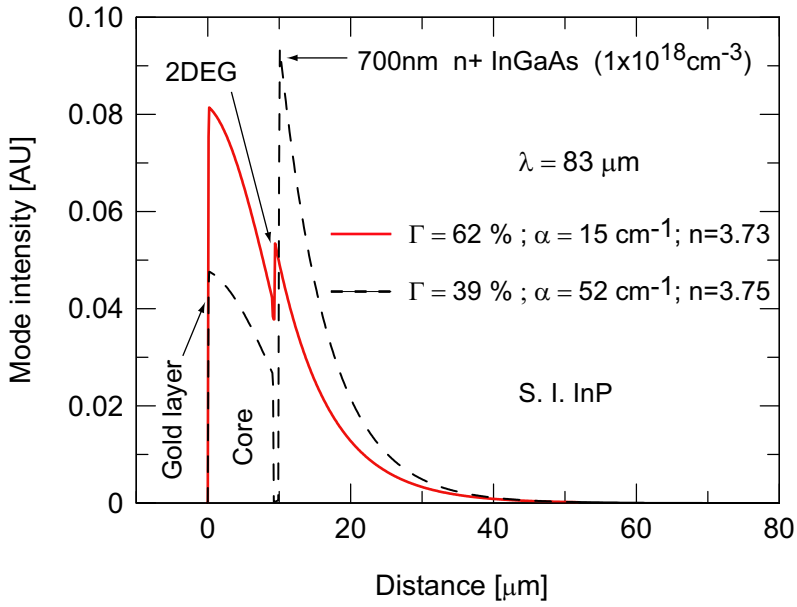

Figure 8.1: Solid line: Optical mode intensity profile in an $In_{0.52}Al_{0.48}As$-$In_{0.53}Ga_{0.47}As$/InP waveguide structure. Solid line is the mode computed assuming the current is injected by a two-dimentional electron gas (2DEG). For comparison, the mode computed assuming a $In_{0.53}Ga_{0.47}As$ heavily doped buried contact layer is also shown (dashed line). The growth, on a semi-insulating InP substrate, starts by a two dimentional electron gas formed successively of 2 1/2 period of a 5 nm $In_{0.53}Ga_{0.47}As$ / 5 nm $In_{0.52}Al_{0.48}As$ superlattice, a 120 nm thick undoped $In_{0.52}Al_{0.48}As$ layer, a 5 nm thick doped ($n = 2 \times 10^{18}\,cm^{-3}$) $In_{0.52}Al_{0.48}As$ layer, an undoped 10 nm thick $In_{0.52}Al_{0.48}As$ spacer layer, and finishing by a an undoped 100 nm thick $In_{0.53}Ga_{0.47}As$ layer. The growth follows by 70 periods of the active region, and followed by an undoped, 40 nm thick $In_{0.53}Ga_{0.47}As$ layer. The latter consists of a an undoped 5 nm thick $In_{0.52}Al_{0.48}As$ layer, an undoped, 1 nm thick $In_{0.53}Ga_{0.47}As$ layer, a 60 nm thick heavily doped ($n = 1.5 \times 10^{19}\,cm^{-3}$) $In_{0.53}Ga_{0.47}As$ contact layer.

8.3 Stucture based on a Bound-to-cntinuum transition with optical phonon extraction.

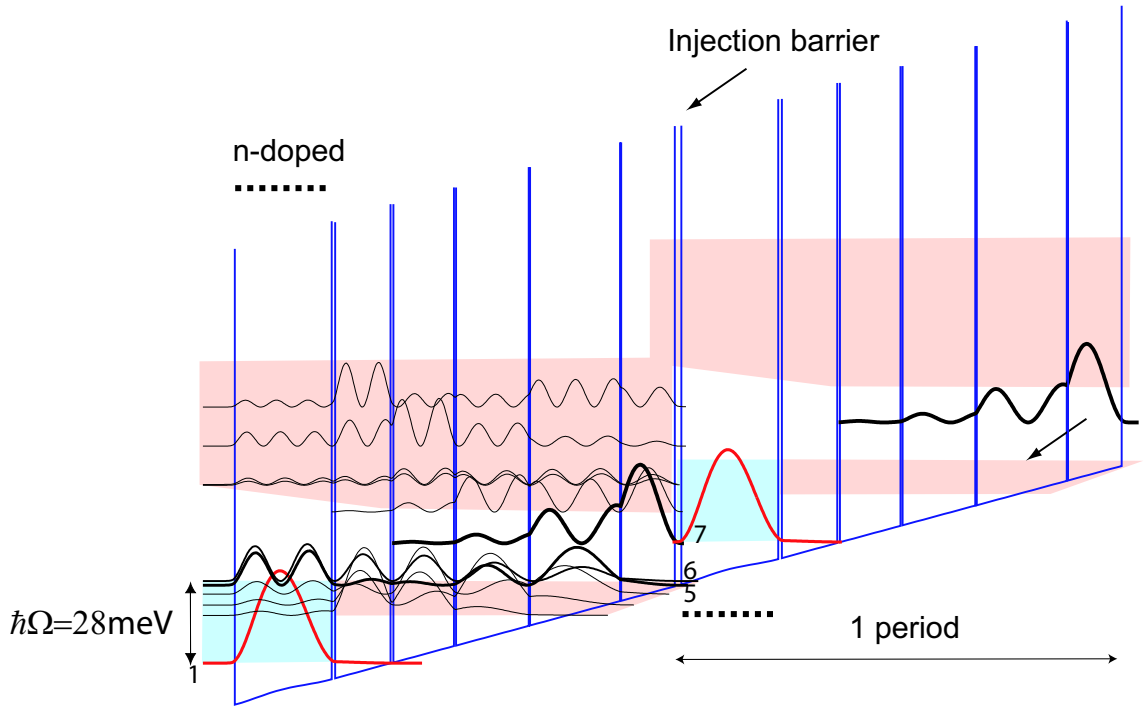

Figure 8.2: Computed conduction band profile at T=10K of one stage of the structure under an average applied electric field of 3.3 kV/cm. The $In_{0.52}Al_{0.48}As$-$In_{0.53}Ga_{0.47}As$ layer sequence of one period of the active layers starting from the injection barrier is as follows: **1.9**/15.5/**0.3**/26.0/**0.4**/21.0/**0.6**/17.5/**0.8**/16.0/**1.0**/ 28.0/ where $In_{0.52}Al_{0.48}As$ layers are in bold, $In_{0.53}Ga_{0.47}As$ are in Roman and the underlined number correspond to Si doped layer with $n = 2.2 \times 10^{16}\,\mathrm{cm}^{-3}$.

For the active region, a structure based on a combination of bound-to-continuum transition and optical phonon extraction was choosen, as GaAs terahertz quantum cascade lasers based on such a design recently demonstrated high performance operation [94]. The calculated

conduction band profile of two active regions connected by an injector is shown in (Fig. 8.2). The energy separation between the lower state of the laser transition and the lower state of the injector, $E_{61} \simeq 28\,\text{meV}$ is designed to be close to the LO-phonon energy ($E_{LO} \simeq 32$ meV for InGaAs), so that fast LO-phonon scattering can depopulate level 6. Electrons are collected in the collector/injector state $n = 1$ and resonantly tunnel into the $n = 7$ upper laser state . The radiative transition is interwell (spatially diagonal), and takes place between state n = 7 and n = 6 as well as n = 5. The combined oscillator strength of these two transition is $f_{7(65)} = 29.5$. At $T = 80K$, computation of the optical phonon scattering yields an upper state lifetime of $\tau_7 = 4.7$ ps. This again compares favorably to the GaAs active region operating at the same photon energy, where the equivalent oscillator strength is $f_{9(87)} = 23$ and the lifetime $\tau_9 = 3.2$ ps [94].

The lasers are grown by Molecular Beam Epitaxy (MBE) on a semi-insulating InP substrate consist of 70 periods active region grown on top of an two-dimentional electron gas. Layer thicknesses and doping are described in the caption of Fig. 8.2 (for the active region).

8.4 Samples processing.

The devices were processed by wet etching using $H_3PO_4/H_2O_2/H_2O$ (1:4:1) to form (70, 110, 160 and 210 μm) wide ridges. Two bottom contacts are then evaporated on both sides of the stripes (Ge/Au/Ag/Au 12/27/50/400 nm alloyed at 400 °C during 1 minute). A Ti/Au confining layer is furthermore evaporated completely covering the top of the stripe. Substrate thinning down to 250 μm, and backside metallization (Ti/Au), complete the processing of

the devices. They are then cleaved in laser bars of various lengths, soldered on a copper mounts using Indium and wire bonded. The samples were mounted on the cold finger of a He flow cryostat.

8.5 Experimental measurements.

8.5.1 Optical spectra.

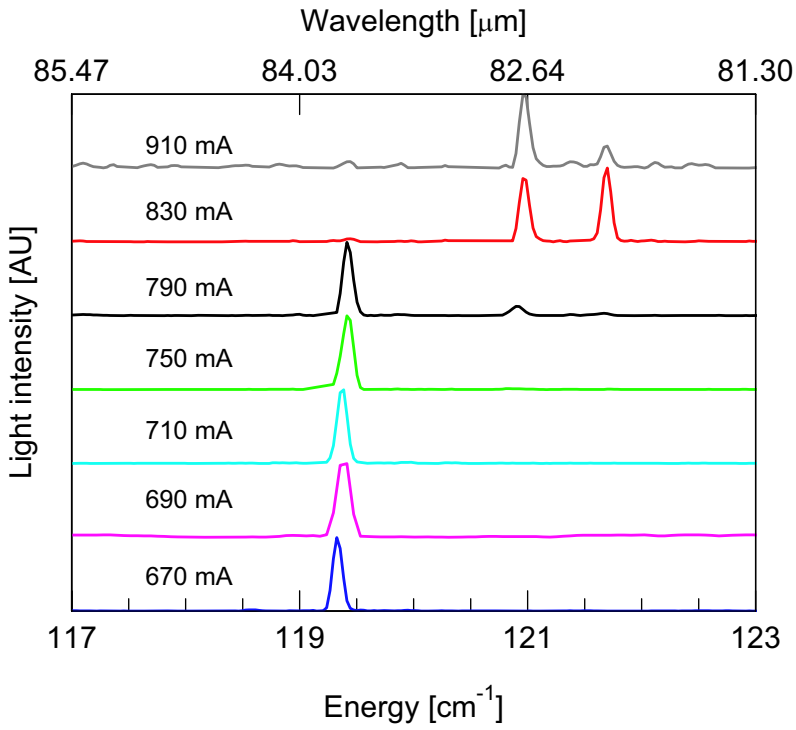

Figure 8.3: Spectra recorded at heat sink temperature of 10 K from a 1.25 mm long and 110 μm wide device under pulsed excitation with a duty cycle of 2 at different currents. The threshold curent of the deviceis 630 mA. Spectra are offset for clarity.

The optical spectra were measured at low temperature (T = 10K). Shown in Fig. 8.3 is a series of spectra for increasing drive current for a 1.25mm long and 110μm wide device. For these spectra, the device was driven with 627 $\times$ 192 ns-long current pulses at 1.92 μs intervals, providing an overall duty factor of 5 $\times$ 10^{-2} at a frequency of 413 Hz. As shown in Fig. 8.3, a clear narrowing of the spectrum is observed above 300 mA, with device achieving laser threshold at a drive current of 630 mA.

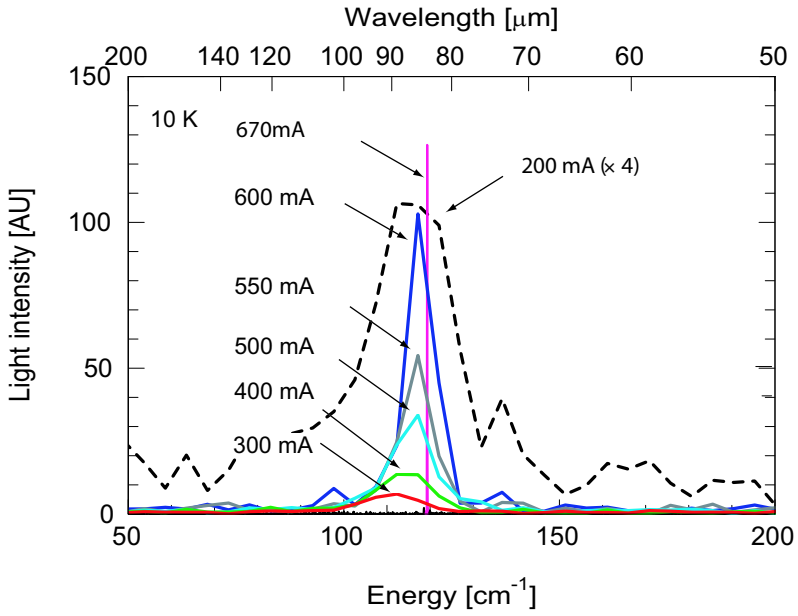

Figure 8.4: Solid line, emission spectra measured as a function of current for a 110 μm-wide and 1.25 mm-long device. For comparison, the same measurement performed from the side of a device that has been cleaved along the length of the stripe is shown (dashed line). Inset: High resolution spectra of the same laser taken above threshold. The spectra are vertically displaced for clarity.

As a comparison, the electroluminescence extracted from a device cleaved along the length of the stripe is also shown in the same figure. In this geometry, cavity effects are efficiently

supressed and the true luminescence linewidth of the transition, equals to 2.8 meV in our case, may be extracted. No narrowing was observed in this case. The inset of fig. 8.3 displays high resolution spectra (0.09 cm^{-1}) of the same device measured above threshold. Depending on current, a monomode or multimode operation is achieved. The spacing of the modes corresponds to a group effective index of 3.67. The computed group index value is significantly higher and equal to 3.93. The discrepancy between the measured and the computed values of the effective index is not understood but may stem from the uncertainty in the refractive index values used to compute the effective mode index. Individual modes were found to tune with temperature with a coefficient equal to $1/\lambda \times \Delta\lambda/\Delta T = 2.4 \times 10^{-5}\,\mathrm{K}^{-1}$.

8.5.2 Liiv curves.

The light and voltage-current characteristics of the same device are shown in Fig. 8.5 for temperatures ranging from 10 K up to 45 K. The collected peak power at 10 K reaches a value of 250 μW, with a slope efficiency (dP/dT = 1.3 mW/A) and a threshold current density of $J_{\mathrm{th}} = 460\,\mathrm{A/cm^2}$. A low duty factor of 8 $\times$ 10^{-5} was used in these measurements, in order to avoid saturation of the Si bolometer detector. The measured voltage at threshold (5.6 V) is larger than the one expected (2.9 V) for our 70 period active region. The difference is attributed to the serie resistance of the two-dimentional electron gas. In fact, an extrapolation of the bias voltage at constant current density versus laser ridge width indeed yields a voltage (2.8 V) very close to the theoretical value.

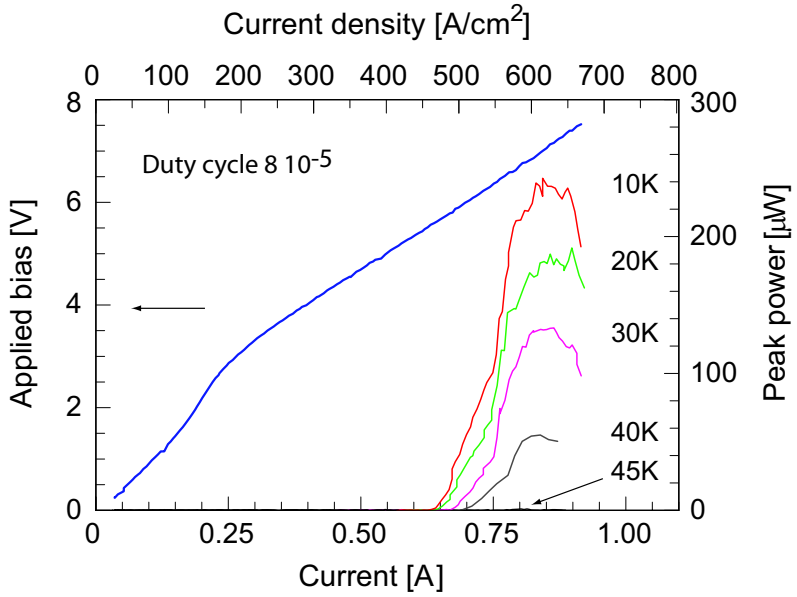

Figure 8.5: Peak optical output power versus injected current in pulsed mode at a duty cycle of 0.008 % at various temperatures, as indicated. The sample is processed into a 1.25-mm-long and 110 μm-wide waveguide.

8.5.3 Waveguide losses.

Assuming a linear dependence of the peak gain in current density, systematic threshold current density measurements of devices of various cavity lengths L enable the extraction of the material differential gain g_d and the waveguide loss α_w [83]. Using the data shown in the Fig. 8.6(b), assuming the computed reflectivity coefficient ($R_1 = 0.31$) and the overlap factor ($\Gamma = 62\,\%$), we can extract a value of the differential gain coefficient $g_d = 192\,\mathrm{cm/kA}$ and a waveguide loss of $\alpha_w = 45\,\mathrm{cm}^{-1}$. Both values are much larger than the one usually observed in GaAs-based terahertz quantum cascade lasers. A typical value of differential material gain for a bound-to-continuum active region at a similar wavelength yield $g_d = 105\,\mathrm{cm/kA}$ [23].

As mentionned in the introduction, the factor of two between differential gain in the two materials is expected and is also the one observed in mid-infrared quantum cascade lasers. Assuming (in a somewhat arbitrary manner) lifetimes limited by optical phonon at T = 80K, as well as the computed values of the dipole matrix elements, the computed value of differential gain coefficient for our structure is $195cm/kA$ and agrees well with the measured one.

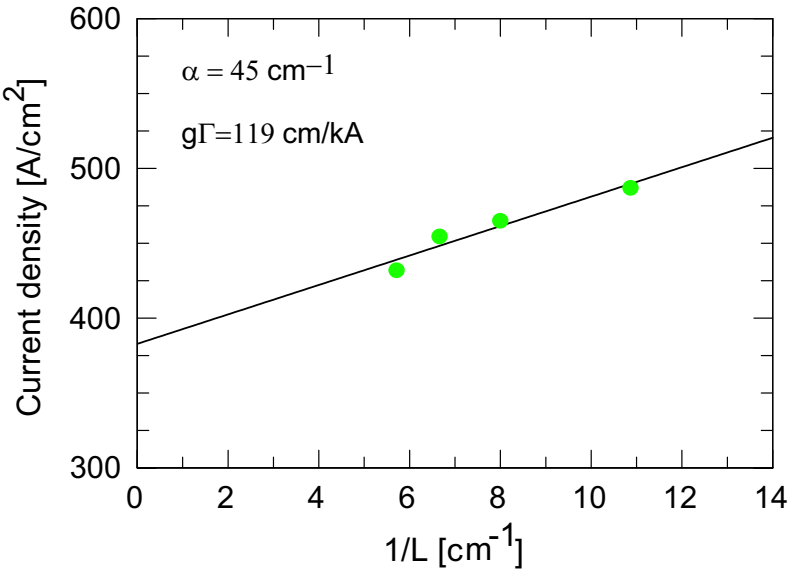

Figure 8.6: Pulsed threshold current as a function of inverse laser length measured at 10 K.

In contrast, the measured waveguide loss $\alpha_w = 45\,\mathrm{cm}^{-1}$ is much larger than the value measured in GaAs-based quantum cascade lasers where $\alpha_w = 5cm^{-1}$ is routinely achieved (see for example [23]). It is also larger than the computed value of $\alpha_w = 15cm^{-1}$. The reason for this discrepancy is not clear, but could be attributed to a larger than expected background doping level and lower in-plane mobility. Absorption due to tails of the optical

phonons, broadened by the alloy disorder may also play a role.

Chapter 9

Conclusion.

In summary, in this thesis, I have given an in-depth discussion of the THz QC lasers and have reported experimental data on various designs and on different materials systems. Continuous wave operation was first demonstrated at THz frequencies in the chirped-superlattice QC structures using a low waveguides losses with an optimized samples processing. Laser action at 4.6 THz ($\lambda = 64$ μm) is reached with a low threshold current density of $J_{th} = 137$ A/cm^2 at T = 10 K. Despite this low threshold density, this chirped superlattice design displayed disappointing temperature behavior. The highest operating temperature was only 60 K. This is likely a result of thermal backfilling of the lower radiative and a weak population inversion.

Active region based on a bound-to-continuum transition have achieved dramatic performance improvements for a THz QCL, due to the long lifetime and good injection efficiency of the upper radiative state and the excellent extraction efficiency of the lower radiative state. A high power Quantum Cascade Lasers operating above liquid nitrogen temperature at

$\lambda \simeq 87$ and $130\,\mu$m has been demonstrated using this concept. For $\lambda \simeq 87\,\mu$m (3.4 THz), 56 mW peak power in pulsed operation and 50 mW continuous wave operation at 10 K are demonstrated. The highest lasing temperature is 103 K in pulsed mode. At $\lambda \simeq 130\,\mu$m (2.3 THz), a peak power of 50 mW was achieved and devices operated in continuous wave reached a maximum temperature of 53 K with an optical power of 11.5 mW at T = 10 K. Lifetimes are extracted from the scaling of the transport and laser parameters as a function of size using a simple rate equation model. An experimental study of the lasing and transport properties of GaAs/$Al_{0.15}Ga_{0.85}$As QCLs based on this design are also investigated with varying sheet doping density n_s. As in the mid-infrared, both maximum current and threshold currents increase linearly with doping in bound-to-continuum Thz QCLs; the key influence on the threshold current density does originates from the increase of the waveguide losses due to free carrier absorption. The performance level can be improved in many ways, including the optimization of the doping in the active region as well as the excellent growth quality.

To improve the population inversion at high temperatures, a new class of terahertz quantum cascade lasers based on a bound-to-continuum transition combined with an optical phonon extraction was designed. This depopulation method is different in character than the mini-band depopulation used for the prior chirped superlattice and bound-to-continuum transition based designs. LO-phonon scattering provides an efficient and temperature insensitive depopulation mechanism, and an intrinsic protection from thermal backfilling effects due to the large ($\geq$36 meV) energy separation between the lower radiative state and the injector. Both properties are important in allowing higher temperature operation at longer wavelengths. Lasing at 4 THz (74 μm) was observed in a device with a semi-insulating-surface-plasmon

waveguide in pulsed mode up to 115 K. The peak pulsed optical power of 100 mW and a slope efficiency of 95 mW/A were obtained at 10 K. However, in Continuous wave operation, these devices show no particular temperature improvement to the best performance from bound-to-continuum designs, which typically lase up to 70 K. This is attributed to the higher electrical power dissipated due to a threshold bias which is 2.4 times higher than in the bound-to-continuum case.

Single-mode emitting devices are demonstrated at wavelengths range between 83 and 90.5 μm that also use a loss-coupled grating. The Bragg grating are defined by either etching and refilling with hard backed resist or etching and metal coverage. For the first one, single mode operation is observed for all driving currents and for all temperatures but no CW operation is achieved due to the high threshold current density ($\geq$ 365 A/cm^2). For the second, continuous wave single mode operation of distributed feedback quantum cascade lasers are demonstrated at wavelengths of 85.2, 86.9 and 87.2 μm. However, the disadvantage to this approach is that, a multimode spectra appeares at high current and temperatures which due to the low coupling coefficient. For the two approach, a tuning rate of about $2 \times 10^{-5}\ K^{-1}$ is obtained. A measured of far field beam pattern of the distributed feedback quantum cascade lasers shows strong intensity centered on the QCL pointing direction which is a signature of monomode spectrum.

Operation of a quantum-cascade laser based on the $In_{0.52}Al_{0.48}As$-$In_{0.53}Ga_{0.47}As$/InP material is demonstrated at a frequency of 3.6 Terahertz (83 μm) using an active region based on a bound-to-continuum transition combined with an optical phonon extraction. The optical waveguide exploits a combination of metallic and dielectric confinement. Threshold current

density of 460 A/cm^2 at 10 K and a maximum operating temperature of 45 K are achieved. The device achieved a differential gain about twice than the one obtained in GaAs structures at a similar wavelength. However, it is still hampered by large waveguide losses (α_W = 45 cm^{-1}). Despite this degradation of the highest temperature performence, this work experimentally demonstrates the general validity of quantum cascade laser principales by showing laser action in a heterostructure material different from the one used until now in terahertz quantum cascade lasers.

Acknowledgements

I would like to first thank my thesis director, Prof. Jérôme Faist, for giving me the opportunity to work on this project and for advising me along the way. I thank him also for his constant encouragement, his continuous support and enthusiasm.

I would like to thank Prof. Daniel Hofstetter (University of Neuchâtel) and Dr. Hideaki Page (Teraview, Cambridge, U.K) for reading the manuscript and taking part to the examination committee.

I am really grateful to Prof. Edmund Linfield of the University of Leeds and especially to Prof. David Ritchie and Dr. Harvey Beere of the Cavendish Laboratory for the excellent quality of the epitaxial growth samples produced during our collaborations in the Wanted project.

Thanks to Dr. Marcella Giovannini, Mr. Nicolas Hoyler and Dr. Mattias Beck for the excellent layers coming from our in-house MBE grower.

Many thanks to Docteur Giacomo Scalari , my collegue on the THz project, who spent more than four years between labs, offices, clean room and conferences with me in good mood, deserves a full load of acknowledgments for the hours spent together and the numerous discussions about QC physics, many thanks for his careful reading and remarks on this

thesis.

I am grateful as well to the members (past and present) of the Mesoscopic Physics Group for their contributions and for the excellent atmosphere in the group: Thierry Aellen, Richard Moulini, Tobias Gresch, Romain Terazzi, Christoph Walther, Milan Fischer, Lorenzo Sirigu, Maria Amanti, Harry Willenberg, Michel Rochat, Dmitri Yarekha Yuriy and Maxi.

I also wish to thank Farid Bouabada for his help with measurements and characterizations of some devices during his Master work.

It is my pleasure to thank the Hofstetter group and Alpes Lasers who shared the labs, are also thanked for their good collaboration! Thanks a lot to Marcel, Yargo, Fabrizio, Esther, Antoine, Stephane, Hege, Lubos, Sophie.

Thanks also to the technical and administrative staffs of the Institute of Physics who really made my life easier during this time.

I am particularly indebted to my family for her generous support during my studies. I want to thank my brother Naceur for his encouragement during my THESE. Thanks to all of my friends who I haven't mentioned.

This work was supported in part by the European IST project WANTED, by the Swiss National Science foundation center NCCR Quantum Photonics and by the Agilent technologies.

Bibliography

[1] L. Esaki and R. Tsu. Superlattice and negative differential conductivity in semiconductors. *IBM J. Res. Develop.*, 14(61):61–65, 1970.

[2] R.F. Kazarinov and R.A. Suris. Possibility of the amplification of electromagnetic waves in a semiconductor with a superlattice. *Sov. Phys. Semicond.*, 5(4):707–709, 1971.

[3] L.C. West and S.J. Eglash. First observation of an extremely large-dipole infrared transition within the conduction band of a gaas quantum well. *Appl. Phys. Lett.*, 46(12):1156–1158, 1985.

[4] F. Capasso, K. Mohammed, and A.Y. Cho. Resonant tunneling through double barriers, perpendicular quantum transport phenomena in superlattices, and their device applications. *IEEE J. Quantum Electron.*, 22(9):1853–1869, 1986.

[5] J. Faist, F. Capasso, C. Sirtori, D.L. Sivco, and A.Y. Cho. Quantum cascade lasers. In H.C. Liu and F. Capasso, editors, *Intersubband transitions in quantum wells: Physics and device applications II*, volume 66, chapter 1, pages 1–83. Academic Press, 2000.

[6] J. Faist, F. Capasso, C. Sirtori, D.L. Sivco, A.L. Hutchinson, and A.Y. Cho. Continuous wave operation of a vertical transition quantum cascade laser above t=80 k. *Appl. Phys. Lett.*, 67(21):3057–3059, 1995.

[7] J. Faist, F. Capasso, C. Sirtori, D.L. Sivco, J.N. Baillargeon, A.L. Hutchinson, S.G. Chu, and A.Y. Cho. High power mid-infrared ($\lambda \sim 5$ μm) quantum cascade lasers operating above room temperature. *Appl. Phys. Lett.*, 68(26):3680–3682, 1996.

[8] J. Faist, C. Gmachl, F. Capasso, C. Sirtori, D.L. Sivco, J.N. Baillargeon, and A.Y. Cho. Distributed feedback quantum cascade lasers. *Appl. Phys. Lett.*, 70(20):2670–2672, 1997.

[9] C. Sirtori, P. Kruck, S. Barbieri, P. Collot, J. Nagle, M. Beck, J. Faist, and U. Oesterle. Gaas/al$_x$ga$_{1-x}$as quantum cascade lasers. *Appl. Phys. Lett.*, 73(24):3486–3488, 1998.

[10] R. Colombelli, F. Capasso, C. Gmachl, A.L. Hutchinson, D.L. Sivco, A. Tredicucci, M.C. Wanke, A.M. Sergent, and A.Y. Cho. Far-infrared surface-plasmon quantum-cascade lasers at 21.5 μm and 24 μm wavelengths. *Appl. Phys. Lett.*, 78(18):2620–2622, 2001.

[11] M. Beck, D. Hofstetter, T. Aellen, J. Faist, U. Oesterle, M. Ilegems, E. Gini, and H. Melchior. Continuous wave operation of a mid-infrared semiconductor laser at room temperature. *Science*, 295:301–305, 2002.

[12] L. Diehl, D. Bour, S. Corzine, J. Zhu, G. Höfler, B.G. Lee, C.Y. Wang, M. Troccoli, and F. Capasso. Pulsed- and continuous-mode operation at high temperature of strained quantum-cascade lasers grown by metalorganic vapor phase epitaxy. *Appl. Phys. Lett.*, 88:041102–1–041102–3, 2006.

[13] M. Rochat, J. Faist, M. Beck, U. Oesterle, and M. Ilegems. Far-infrared ($\lambda = 88\ \mu$m) electroluminescence in a quantum cascade structure. *Appl. Phys. Lett.*, 73(25):3724–3726, 1998.

[14] B.S. Williams, B. Xu, Q. Hu, and M.R. Melloch. Narrow-linewidth terahertz intersubband emission from three-level systems. *Appl. Phys. Lett.*, 75(19):2927–2929, 1999.

[15] J. Ulrich, R. Zobl, K. Unterrainer, G. Strasser, and E. Gornik. Magnetic-field-enhanced quantum-cascade emission. *Appl. Phys. Lett.*, 76(1):19–21, 2000.

[16] M. Helm, P. England, E. Colas, F. DeRosa, and S.J. Allen. Intersubband emission from semiconductor superlattices excited by sequential resonant tunneling. *Phys. Rev. Lett.*, 63(1):74–77, 1989.

[17] R. Köhler, A. Tredicucci, F. Beltram, H.E. Beere, E.H. Linfield, A.G. Davies, and D.A. Ritchie. High-intensity interminiband terahertz emission from chirped superlattices. *Appl. Phys. Lett.*, 80(11):1867–1869, 2002.

[18] S. Blaser, M. Rochat, M. Beck, J. Faist, and U. Oesterle. Far-infrared emission and stark-cyclotron resonances in a quantum cascade structure based on photon-assisted tunneling transition. *Phys. Rev. B*, 61(12):8369–8374, 2000.

[19] R. Köhler, A. Tredicucci, F. Beltram, H.E. Beere, E.H. Linfield, A.G. Davies, D.A. Ritchie, R.C. Iotti, and F. Rossi. Terahertz semiconductor-heterostructure laser. *Nature*, 417:156–159, 2002.

[20] M. Rochat, L. Ajili, H. Willenberg, J. Faist, H. Beere, G. Davies, E. Linfield, and D. Ritchie. Low-threshold terahertz quantum-cascade lasers. *Appl. Phys. Lett.*, 81(8):1381–1383, 2002.

[21] L. Ajili, G. Scalari, D. Hofstetter, M. Beck, J. Faist, H. Beere, G. Davies, E. Linfield, and D. Ritchie. Continuous-wave operation of far-infrared quantum cascade lasers. *IEE Elect. Lett.*, 38(25):1675–1676, 2002.

[22] G. Scalari, L. Ajili, J. Faist, H. Beere, E. Linfield, D. Ritchie, and G. Davies. Far-infrared ($\lambda \simeq 87\mu$m) bound-to-continuum quantum-cascade lasers operating up to 90 k. *Appl. Phys. Lett.*, 82(19):3165–3167, 2003.

[23] L. Ajili, G. Scalari, J. Faist, H. Beere, E. Linfield, D. Ritchie, and G. Davies. High power quantum-cascade lasers operating at $\lambda \sim 87$ and 130 μm. *Appl. Phys. Lett.*, 85(18):3986–3988, 2004.

[24] L. Ajili, G. Scalari, N. Hoyler, M. Giovannini, and J. Faist. Ingaasalinas/inp terahertz quantum cascade laser. *Appl. Phys. Lett.*, 87:141107–1–141107–3, 2005.

[25] B.S. Williams, S. Kumar, H. Callebaut, Q. Hu, and J.L. Reno. Terahertz quantum-cascade laser operating up to 137k. *Appl. Phys. Lett.*, 83(25):5142–5144, 2003.

[26] S. Kumar, B.S. Williams, Q. Hu, and J.L. Reno. 1.9 thz quantum-cascade lasers with one-will injector. *Appl. Phys. Lett.*, 88:121123–1–121123–3, 2006.

[27] C. Walther, G. Scalari, J. Faist, H. Beere, and D. Ritchie. Low frequency terahertz quantum cascade laser operating from 1.6 to 1.8 thz. *Appl. Phys. Lett.*, 89:231121–, 2006.

[28] C. Worrall, J. Alton, M. Houghton, S. Barbieri, H.E. Beere, D. Ritchie, and C. Sirtori. Continuous wave operation of a superlattice quantum cascade laser emitting at 2 thz. *Optics Express*, 14(1):171–181, 2006.

[29] G. Scalari, C. Walther, J. Faist, H. Beere, and D. Ritchie. Electrically switchable, two-color quantum cascade laser emitting at 1.39 and 2.3 thz. *Appl. Phys. Lett.*, 88(14):141102–1–141102–3, 2006.

[30] M. Nagel, P.H. Bolivar, M. Brucherseifer, and H. Kurz. Integrated thz technology for label-free genetic diagnostics. *Appl. Phys. Lett.*, 80:154–156, 2001.

[31] P.H. Bolivar, M. Nagel, F. Richter, M. Brucherseifer, H. Kurz, A. Bosserhoff, and R. Buttner. Label-free thz sensing of genetic sequences: towards 'thz biochips'. *Philos. T. Roy. Soc. A*, 362:323–333, 2004.

[32] R. Huber, F. Tauser, A. Brodschelm, M. Bichler, G. Abstreiter, and A. Leitenstorfer. How many-particle interactions develop after ultrafast excitation of an electron-hole plasma. *Nature*, 414:286–289, 2001.

[33] P.H. Siegel. Terahertz technology. *IEEE Trans. Microwave Theory Tech.*, 50(03):910–928, 2002.

[34] J.D. Crowley, C. Hang, R.E. Dalrymple, D.R. Tringali, F.B. Fank, L. Wandinger, and H.B. Wallace. 140 ghz indium phosphide gunn diode. *IEE Elect. Lett.*, 30(06):499–500, 1994.

[35] H. Eisele. Conventional and novel approaches to rf power generation with two-terminal devices at terahertz frequencies. In *2002 IEEE Tenth International Conference on Terahertz Electronics Proceedings.*, pages 13–18, 2002.

[36] H. Eisele, M. Naftaly, and R. Kamoua. Generation of submillimeter-wave radiation with gaas tunnett diodes and inp gunn devices in a second or higher harmonic mode. *Intern. J. Infrared Millim.Waves*, 26(01):1–14, 2005.

[37] M. Tschernitz and J. Freyer. 140ghz gaas double-read impatt diodes. *IEE Elect. Lett.*, 31(07):582–583, 1995.

[38] E.R. Brown, J.R. Soderstrom, C.D. Parker, L.J. Mahoney, K.M. Molvar, and T.C. McGill. Oscillations up to 712 ghz in inas/alsb resonant-tunneling diodes. *Appl. Phys. Lett.*, 58:2291–2293, 1991.

[39] W. Knap, J. Lusakowski, T. Parenty, S. Bollaert, A. A.Cappy, V. Popov, and M.S. Shur. Terahertz emission by plasma waves in 60 nm gate high electron mobility transistors. *Appl. Phys. Lett.*, 84(13):2331–2333, 2004.

[40] S. Komiyama. Far-infrared emission from population-inverted hot-carrier system in p-ge. *Phys. Rev. Lett.*, 48:271–274, 1982.

[41] H. Hubers, S. Pavlov, and V. Shastin. Terahertz lasers based on germanium and silicon. *Semicond. Sci. Technol.*, 20:S211–S221, 2005.

[42] Y.P. Gousev, I.V. Korolev, K. Korolev, V.P. Sinis, M.S. Kagan, E.E. Haller, M.A. Odnoblyudov, I.N. Yassievitch, and K.A. Chao. Widely tunable continuous-wave thz laser. *Appl. Phys. Lett.*, 75:757–759, 1999.

[43] M.S. Kagan, I.V. Altukhov, V.P. Sinis, S.G. Thomas, K.L. Wang, K. Chao, and I.N. Yassievich. Terahertz emission of sige/si quantum wells. *Thin Solid Films*, 380:237–239, 2000.

[44] A. Blom, M.A. Odnoblyudov, H.H. Cheng, and I.N. Yassievich. Mechanism of terahertz lasing in sige/si quantum wells. *Appl. Phys. Lett.*, 79:713–715, 2001.

[45] S.G. Pavlov, R.K. Zhukavin, E.E. Orlova, V.N. Shastin, A.V. Kirsanov, H.W. Hubers, K. Auen, and H. Riemann. Stimulated emission from donor transitions in silicon. *Phys. Rev. Lett.*, 84(22):5220–5223, 2000.

[46] J. Faist, F. Capasso, D.L. Sivco, C. Sirtori, A.L. Hutchinson, and A.Y. Cho. Quantum cascade laser. *Science*, 264:553–556, 1994.

[47] A. Staprans, E.W. Mccune, and J.A. Ruetz. High-power linear-beam tubes. *IEE Proc. Optoelectron.*, 61:299–330, 1973.

[48] M. Inguscio, G. Moruzzi, K.M. Evenson, and D.A. Jennings. A review of frequency measurements of optically pumped lasers from 0.1 to 8 thz. *J. Appl. Phys.*, 60(12):161–191, 1986.

[49] E. Brown, K. McIntosh, K. Nichols, and C. Dennis. Photomixing up to 3.8 thz in low-temperature-grown gaas. *Appl. Phys. Lett.*, 66(3):285–287, 1995.

[50] D.M. Mittleman, R.H. Jacobsen, and M.C. Nuss. T-ray imaging. *IEEE J. Quantum Electron.*, 2(03):679–692, 1996.

[51] B.B. Hu and M.C. Nuss. Imaging with terahertz waves. *Opt. Lett.*, 20(16):1716–1718, 1995.

[52] T. Loffler, T. Bauer, K.J. Siebert, H.G. Roskos, A. Fitzgerald, and S. Czasch. Terahertz dark-field imaging of biomedical tissue. *Optics Express*, 9(12):616 –621, 2001.

[53] R.A. Cheville and D. Grischkowsky. Far-infrared terahertz time-domain spectroscopy of flames. *Opt. Lett.*, 20(15):1646–1648, 1995.

[54] B. Ferguson, S.H. Wang, D. Gray, D. Abbot, and X.C. Zhang. T-ray computed tomography. *Opt. Lett.*, 27(15):1312–1314, 2002.

[55] O. Mitrofanov, M. Lee, J.W. Hsu, I. Brener, R. Harel, J.F. Federici, J.D. Wynn, L.N. Pfeiffer, and K.W. West. Collection-mode near-field imaging with 0.5 thz pulses. *IEEE J. Select. Topics Quantum Electron.*, 7(04):600 –607, 2001.

[56] P.Y. Han, G.C. Cho, and X.C. Zhang. Time-domain transillumination of biological tissues with terahertz pulses. *Opt. Lett.*, 25(4):242–244, 2000.

[57] R. Martini, C. Gmachl, J. Falciglia, F.G. Curti, C.G. Bethea, F. Capasso, E.A. Whittaker, R. Paiella, A. Tredicucci, A.L. Hutchinson, D.L. Sivco, and A.Y. Cho. High-speed modulation and free-space optical audio/video transmission using quantum cascade lasers. *IEE Elect. Lett.*, 37(3):102–103, 2001.

[58] S. Blaser, D. Hofstetter, M. Beck, and J. Faist. Free-space optical data link using peltier-cooled quantum cascade laser. *IEE Elect. Lett.*, 37(12):778–780, 2001.

[59] E. Rosencher and B. Vinter. *Optoélectronique*. Masson, Paris, 1998.

[60] C. Weisbuch and B. Vinter. *Quantum semiconductor structures*. Academic Press, San Diego, CA, 1991.

[61] G. Bastard. Superlattice band structure in the envelope-function approximation. *Phys. Rev. B*, 24(10):5693–5697, 1981.

[62] G. Bastard. Theoretical investigations of superlattice band structure in the envelope-function approximation. *Phys. Rev. B*, 25(12):7584–7597, 1982.

[63] M.A. Littlejohn, J.R. Hauser, and T.H. Glisson. Velocity-field characteristics of gaas with γ_6^c-l_6^c-x_6^c conduction-band ordering. *J. Appl. Phys.*, 48(11):4587–4590, 1977.

[64] D.F. Nelson, R.C. Miller, and D.A. Kleinman. Band nonparabolicity effects in semiconductor quantum wells. *Phys. Rev. B*, 35(14):7770–7773, 1987.

[65] U. Ekenberg. Nonparabolicity effects in a quantum well: Sublevel shift, parallel mass, and landau levels. *Phys. Rev. B*, 40(11):7714–7726, 1989.

[66] S.L. Chuang. *Physics of Optoelectronic Devices*. John Wiley & Sons, Inc, 1995.

[67] I.H. Tan, G.L. Snider, L.D. Chang, and E.L. Hu. A self-consistent solution of schrdingerpoisson equations using a nonuniform mesh. *J. Appl. Phys.*, 68(08):4071–4076, 1990.

[68] G. Bastard. *Wave mechanics applied to semiconductor heterostructures*. Les éditions de physique, Les Ulis, France, 1988.

[69] C. Sirtori, F. Capasso, J. Faist, and S. Scandolo. Nonparabolicity and a sum rule associated with bound-to-bound and bound-to-continuum intersubband transitions in quantum wells. *Phys. Rev. B*, 50(12):8663–8674, 1994.

[70] M. Helm. The basic physics of intersubband transitions. In H.C. Liu and F. Capasso, editors, *Intersubband transitions in quantum wells: Physics and device applications I*, volume 62, chapter 1, pages 1–99. Academic Press, 2000.

[71] K. Ohtani and H. Ohno. Inas/alsb quantum cascade lasers operating at 10 μm. *Appl. Phys. Lett.*, 82(7):1003–1005, 2003.

[72] R. Teissier, D. Barate, A. Vicet, C. Alibert, A.N. Baranov, X. Marcadet, C. Renard, M. Garcia, C. Sirtori, D. Revin, and J. Cockburn. Room temperature operation of inas/alsb quantum cascade lasers. *Appl. Phys. Lett.*, 85(02):167–169, 2004.

[73] R. Ferreira and G. Bastard. Evaluation of some scattering times for electrons in unbiased and biased single-and multiple-quantum-well structures. *Phys. Rev. B*, 40(2):1074–1086, 1989.

[74] S.C. Lee and I. Galbraith. Intersubband and intrasubband electronic scattering rates in semiconductor quantum wells. *Phys. Rev. B*, 59(24):15796–15805, 1999.

[75] D.Y. Oberli, D.R. Wake, M.V. Klein, J. Klem, T. Henderson, and H. Morkoc. Time-resolved raman scattering in gaas quantum wells. *Phys. Rev. Lett.*, 59(6):696–699, 1987.

[76] M.C. Tatham, J.F. Ryan, and C.T. Foxon. Time-resolved raman measurements of intersubband relaxation in gaas quantum wells. *Phys. Rev. Lett.*, 63(15):1637–1640, 1989.

[77] R.F. Kazarinov and R.A. Suris. Electric and electromagnetic properties of semiconductors with a superlattice. *Sov. Phys. Semicond.*, 6(1):120–131, 1972.

[78] A. Yariv. *Quantum electronics*. John Wiley & Sons, New-York, 3^{rd} edition, 1989.

[79] C. Gmachl, F. Capasso, A. Tredicucci, D.L. Sivco, R. Köhler, A.L. Hutchinson, and A.Y. Cho. Dependence of the device performance on the number of stages in quantum-cascade lasers. *IEEE J. Select. Topics Quantum Electron.*, 5(3):808–816, 1999.

[80] H.C. Liu. A novel superlattice infrared source. *J. Appl. Phys.*, 63(8):2856–2858, 1988.

[81] A. Kastalsky, V.J. Goldman, and J.H. Abeles. Possibility of infrared laser in a resonant tunneling structure. *Appl. Phys. Lett.*, 59(21):2636–2638, 1991.

[82] J. Ulrich, R. Zobl, N. Finger, K. Unterrainer, G. Strasser, and E. Gornik. Terahertz-electroluminescence in a quantum cascade structure. *Physica B*, 272:216–218, 1999.

[83] C. Sirtori, J. Faist, F. Capasso, D.L. Sivco, A.L. Hutchinson, and A.Y. Cho. Quantum cascade laser with plasmon-enhanced waveguide operating at 8.4 μm wavelength. *Appl. Phys. Lett.*, 66(24):3242–3244, 1995.

[84] A. Tredicucci, F. Capasso, C. Gmachl, D.L. Sivco, A.L. Hutchinson, A.Y. Cho, J. Faist, and G. Scamarcio. High-power inter-miniband lasing in intrinsic superlattices. *Appl. Phys. Lett.*, 72(19):2388–2390, 1998.

[85] J. Faist, F. Capasso, C. Sirtori, D.L. Sivco, A.L. Hutchinson, M.S. Hybertsen, and A.Y. Cho. Quantum cascade lasers without intersubband population inversion. *Phys. Rev. Lett.*, 76(3):411–414, 1996.

[86] M. Helm. Infrared spectroscopy and transport of electrons in semiconductor superlattices. *Semicond. Sci. Technol.*, 10:557–575, 1995.

[87] R. Köhler, A. Tredicucci, F. Beltram, H.E. Beere, E.H. Linfield, A.G. Davies, and D.A. Ritchie. Low-threshold quantum-cascade lasers at 3.5 thz ($\lambda = 85\mu$m). *Opt. Lett.*, 28(10):810–812, 2003.

[88] A. Tredicucci, F. Capasso, C. Gmachl, D.L. Sivco, A.L. Hutchinson, and A.Y. Cho. High performance interminiband quantum cascade lasers with graded superlattices. *Appl. Phys. Lett.*, 73(15):2101–2103, 1998.

[89] J. Faist, M. Beck, T. Aellen, and E. Gini. Quantum cascade lasers based on a bound-to-continuum transition. *Appl. Phys. Lett.*, 78(2):147–149, 2001.

[90] M. Rochat, D. Hofstetter, M. Beck, and J. Faist. Long-wavelength ($\lambda \sim 16\mu$m), room-temperature, single-frequency quantum-cascade lasers based on a bound-to-continuum transition. *Appl. Phys. Lett.*, 79(26):4271–4273, 2001.

[91] B.S. Williams, H. Callebaut, S. Kumar, Q. Hu, and J.L. Reno. 3.4-thz quantum cascade laser based on longitudinal-optical-phonon scattering for depopulation. *Appl. Phys. Lett.*, 82(7):1015–1017, 2003.

[92] B.S. Williams, S. Kumar, Q. Hu, and J.L. Reno. Operation of terahertz quantum-cascade lasers at 164 k in pulsed mode and at 117 k in continuous-wave mode. *Optics Express*, 13:3331–3339, 2005.

[93] R. Kohler, A. Tredicucci, C. Mauro, F. Beltram, H.E. Beere, E.H. Linfield, A.G. Davies, and D.A. Ritchie. Terahertz quantum-cascade lasers based on an interlaced photon-phonon cascade. *Appl. Phys. Lett.*, 84(8):1266–1268, 2004.

[94] G. Scalari, N. Hoyler, M. Giovannini, and J. Faist. Terahertz bound-to-continuum quanutm-cascade lasers based on optical-phonon scattering extraction. *Appl. Phys. Lett.*, 86:181101–1–181101–3, 2005.

[95] H. Kogelnik and C. Shank. Coupled-wave theory of distributed feedback lasers. *J. Appl. Phys.*, 43(05):2327–2335, 1972.

[96] J. Faist, F. Capasso, D.L. Sivco, A.L. Hutchinson, S.G. Chu, and A.Y. Cho. Short wavelength ($\lambda \sim 3.4$ μm) quantum cascade laser based on strained compensated ingaas/alinas. *Appl. Phys. Lett.*, 72(6):680–682, 1998.

[97] C. Sirtori, P. Kruck, S. Barbieri, H. Page, J. Nagle, M. Beck, J. Faist, and U. Oesterle. Low-loss al-free waveguides for unipolar semiconductor lasers. *Appl. Phys. Lett.*, 75(25):3911–3913, 1999.

[98] G. Strasser, S. Gianordoli, L. Hvozdara, W. Schrenk, K. Unterrainer, and E. Gornik. Gaas/algaas superlattice quantum cascade lasers at $\lambda \sim 13$ μm. *Appl. Phys. Lett.*, 75(10):1345–1347, 1999.

[99] C. Becker, C. Sirtori, H. Page, G. Glastre, V. Ortiz, X. Marcadet, M. Stellmacher, and J. Nagle. Alas/gaas quantum cascade lasers based on large direct conduction band discontnuity. *Appl. Phys. Lett.*, 77(4):463–465, 2000.

[100] L.R. Wilson, P.T. Keightley, J.W. Cockburn, M.S. Skolnick, J.C. Clark, R. Grey, and G. Hill. Controlling the performance of gaas-algaas quantum-cascade lasers via barrier height modifications. *Appl. Phys. Lett.*, 76(7):801–803, 2000.

[101] L.R. Wilson, J.W. Cockburn, M.J. Steer, D.A. Carder, M.S. Skolnick, M. Hopkinson, and G. Hill. Decreasing the emission wavelength of gaas-algaas quantum cascade lasers by the incorporation of ultrahin ingaas layers. *Appl. Phys. Lett.*, 78(4):413–415, 2001.

[102] C. Sirtori, C. Gmachl, F. Capasso, J. Faist, D.L. Sivco, A.L. Hutchinson, and A.Y. Cho. Long-wavelength (λ = 8-11.5 μm) semiconductor lasers with waveguides based on surface plasmons. *Opt. Lett.*, 23(17):1366–1368, 1998.

[103] A. Tredicucci, C. Gmachl, M.C. Wanke, F. Capasso, A.L. Hutchinson, D.L. Sivco, S.G. Chu, and A.Y. Cho. Surface plasmon quantum cascade lasers at $\lambda \sim 19\mu$m. *Appl. Phys. Lett.*, 77(15):2286–2288, 2000.

[104] C. Gmachl, F. Capasso, A. Tredicucci, D.L. Sivco, A.L. Hutchinson, and A.Y. Cho. Long wavelength ($\lambda \simeq 13\mu$m) quantum cascade lasers. *IEE Elect. Lett.*, 34(11):1103–1104, 1998.

[105] A. Tredicucci, C. Gmachl, F. Capasso, D.L. Sivco, A.L. Hutchinson, and A.Y. Cho. Long wavelength superlattice quantum cascade lasers at $\lambda = 17$ μm. *Appl. Phys. Lett.*, 74(5):638–640, 1999.

[106] A. Tredicucci, C. Gmachl, F. Capasso, A.L. Hutchinson, D.L. Sivco, and A.Y. Cho. Single-mode surface-plasmon laser. *Appl. Phys. Lett.*, 76(16):2164–2166, 2000.

[107] R. Colombelli, A. Straub, F. Capasso, C. Gmachl, M.I. Blakey, A.M. Sergent, S.N. Chu, K.W. West, and L.N. Pfeiffer. Terahertz electroluminescence from superlattice quantum cascade structures. *J. Appl. Phys.*, 91(6):3526–3529, 2002.

[108] M. Rochat, M. Beck, J. Faist, and U. Oesterle. Measurement of far-infrared waveguide loss using a multisection single-pass technique. *Appl. Phys. Lett.*, 78(14):1967–1969, 2001.

[109] C. Sirtori, A. Tredicucci, F. Capasso, J. Faist, D.L. Sivco, A.L. Hutchinson, and A.Y. Cho. Dual-wavelength emission from optically cascaded intersubband transitions. *Opt. Lett.*, 23(6):463–465, 1998.

[110] C. Gmachl, J. Faist, J.N. Baillargeon, F. Capasso, C. Sirtori, D.L. Sivco, S.G. Chu, and A.Y. Cho. Complex-coupled quantum cascade distributed-feedback laser. *IEEE Photon. Technol. Lett.*, 9(8):1090–1092, 1997.

[111] C. Gmachl, F. Capasso, J. Faist, A.L. Hutchinson, A. Tredicucci, D.L. Sivco, J.N. Baillargeon, S.G. Chu, and A.Y. Cho. Continuous-wave and high-power pulsed operation of index-coupled distributed quantum cascade laser at $\lambda \sim 8.5$ μm. *Appl. Phys. Lett.*, 72(12):1430–1432, 1998.

[112] D. Hofstetter, J. Faist, M. Beck, and U. Oesterle. Surface-emitting 10.1 μm quantum-cascade distributed feedback lasers. *Appl. Phys. Lett.*, 75(24):3769–3771, 1999.

[113] D. Hofstetter, J. Faist, M. Beck, A. Muller, and U. Oesterle. Demonstration of high-performance 10.16 μm quantum cascade distributed feedback lasers fabricated without epitaxial regrowth. *Appl. Phys. Lett.*, 75(5):665–667, 1999.

[114] W. Schrenk, N. Finger, S. Gianordoli, L. Hvozdara, G. Strasser, and E. Gornik. Gaas/algaas distributed feedback quantum cascade lasers. *Appl. Phys. Lett.*, 76(3):253–255, 2000.

[115] W. Schrenk, N. Finger, S. Gianordoli, E. Gornik, and G. Strasser. Continuous-wave operation of distributed feedback alas/gaas superlattice quantum-cascade lasers. *Appl. Phys. Lett.*, 77(21):3328–3330, 2000.

[116] K. Namjou, S. Cai, E.A. Whittaker, J. Faist, C. Gmachl, F. Capasso, D.L. Sivco, and A.Y. Cho. Sensitive absorption spectroscopy with a room-temperature distributed-feedback quantum-cascade laser. *Opt. Lett.*, 23(3):219–221, 1998.

[117] S.W. Sharpe, J.F. Kelly, J.S. Hartmann, C. Gmachl, F. Capasso, D.L. Sivco, J.N. Baillargeon, and A.Y. Cho. High-resolution (doppler-limited) spectroscopy using quantum-cascade distributed-feedback lasers. *Opt. Lett.*, 23(17):1396–1398, 1998.

[118] A.A. Kosterev, R.F. Curl, F.K. Tittel, C. Gmachl, F. Capasso, D.L. Sivco, J.N. Baillargeon, A.L. Hutchinson, and A.Y. Cho. Methane concentration and isotopic composition measurements with a mid-infrared quantum-cascade laser. *Opt. Lett.*, 24(23):1762–1764, 1999.

[119] R.M. Williams, J.F. Kelly, J.S. Hartman, S.W. Sharpe, M.S. Taubman, J.L. Hall, F. Capasso, C. Gmachl, D.L. Sivco, J.N. Baillargeon, and A.Y. Cho. Kilohertz linewidth from frequency-stabilized mid-infrared quantum cascade lasers. *Opt. Lett.*, 24(24):1844–1846, 1999.

[120] M. Nägele, D. Hofstetter, J. Faist, and M.W. Sigrist. Low power quantum-cascade laser photoacoustic spectrometer for trace-gas monitoring. *Analytical Sciences*, 17(4):497–499, 2001.

[121] R. Köhler, C. Gmachl, A. Tredicucci, F. Capasso, D.L. Sivco, S.G. Chu, and A.Y. Cho. Single-mode tunable pulsed, and continuous wave quantum-cascade distributed feedback lasers at $\lambda \sim 4.6$ - 4.7 μm. *Appl. Phys. Lett.*, 76(9):1092–1094, 2000.

[122] C. Gmachl, F. Capasso, A. Tredicucci, D.L. Sivco, J.N. Baillargeon, A.L. Hutchinson, and A.Y. Cho. High power, continuous-wave, current-tunable, single-mode quantum-cascade distributed-feedback lasers at $\lambda \sim 5.2$ and $\lambda \sim 7.95$ μm. *Opt. Lett.*, 25(4):230–232, 2000.

[123] M. Rochat. *Far-infrared emission in quantum cascade structures.* PhD thesis, Université de Neuchâtel, 2002. unpublished.

[124] L. Ajili, J. Faist, H. Beere, D. Ritchie, G. Davies, and E. Linfield. Loss-coupled distributed feedback far-infrared quantum cascade lasers. *IEE Elect. Lett.*, 41(07):419–420, 2005.

[125] S. Blaser, M. Rochat, L. Ajili, M. Beck, J. Faist, H.E. Beere, A.G. Davies, E.H. Linfield, and D.A. Ritchie. Terahertz interminiband emission and magneto-transport measurements from a quantum cascade chirped superlattice. *Physica E*, 13(2-4):854–857, 2002.

[126] R. Köhler, R.C. Iotti, A. Tredicucci, and F. Rossi. Design and simulation of terahertz quantum cascade lasers. *Appl. Phys. Lett.*, 79(24):3920–3922, 2001.

[127] S. Blaser, L. Diehl, M. Beck, J. Faist, U. Oesterle, J. Xu, S. Barbieri, and F. Beltram. Characterization and modeling of quantum cascade lasers based on photon-assisted tunneling transition. *IEEE J. Quantum Electron.*, 37(3):448–455, 2001.

[128] C. Sirtori, F. Capasso, J. Faist, A.L. Hutchinson, D.L. Sivco, and A.Y. Cho. Resonant tunneling in quantum cascade lasers. *IEEE J. Quantum Electron.*, 34(9):1722–1729, 1998.

[129] E.D. Palik. Gallium arsenide (gaas). In Edward D. Palik, editor, *Handbook of optical constants of solids*, pages 429–443. Academic Press, Inc., Orlando, Florida, 1985.

[130] M. Giehler, R. Hey, H. Kostial, S. Cronenberg, T. Ohtsuka, and L. Schrottke. Lasing properties of gaas/(al,ga)as quantum-cascade lasers as a function of injector doping density. *Appl. Phys. Lett.*, 82(5):671–673, 2003.

[131] M. Giehler, H. Kostial, R. Hey, and H.T. Grahn. Effect of free-carrier absorption on the threshold current density of gaas/ (al,ga)as quantum-cascade lasers. *J. Appl. Phys.*, 96(9):4755–4761, 2004.

[132] V.D. Jovanovic, D. Indjin, N. Vukmirovic, Z. Ikonic, P. Harrison, E.H. Linfield, H. Page, X. Marcadet, C. Sirtori, C. Worrall, H.E. Beere, and D.A. Ritchie. Mechanisms of dynamic range limitations in gaas/algaas quantum-cascade lasers: Influence of injector doping. *Appl. Phys. Lett.*, 86:211117–1–211117–3, 2005.

[133] S. Lee, M. Giehler, R. Hey, T. Ohtsuka, A. A.Wacker, and H.T. Grahn. Dependence of lasing properties of gaas/$\mathrm{al}_x\mathrm{ga}_{1-x}$as quantum cascade lasers on injector doping density: theory and experiment. *Semicond. Sci. Technol.*, 19:45–47, 2004.

[134] H.C. Liu, M. Wächter, D. Ban, Z.R. Wasilewski, M. Buchanan, G.C. Aers, J.C. Cao, S.L. Feng, B.S. Williams, and Q. Hu. Effect of doping concentration on the performance of terahertz quantum-cascade lasers. *Appl. Phys. Lett.*, 87:141102–1–141102–3, 2005.

[135] J. Alton, S. Barbieri, C. Worral, M. Houghton, H.E. Beere, E.L. Linfield, and D.A. Richie. Optimum resonant tunnelling injection and influence of doping density on the performance of thz bound-to-continuum cascade lasers. In *SPIE Proceedings, Terahertz and Gigahertz Electronics and Photonics IV*, volume 5727, pages 65–73, 2005.

[136] S. Barbieri, J. Alton, H. Beere, J. Fowler, E. Linfield, and D. Ritchie. 2.9 thz quantum cascade lasers operating up 70 k in continuous wave. *Appl. Phys. Lett.*, 85(10):1674–1676, 2004.

[137] L. Mahler, A. Tredicucci, R. Köhler, F. Beltram, H.E. Beere, E.H. Linfield, and D.A. Ritchie. High-performance operation of single-mode terahertz quantum cascade lasers with metallic gratings. *Appl. Phys. Lett.*, 87:181101–1–181101–3, 2005.

[138] B.S. Williams, S. Kumar, Q. Hu, and J.L. Reno. Distributed-feedback terahertz quantum-cascade lasers with laterally corrugated metal waveguides. *Opt. Lett.*, 30(21):2909–2911, 2005.

[139] D. Herriot, H. Kogelnik, and R. Kompner. Off-axis paths in spherical mirror interferometers. *Appl. Opt.*, 3:523–525, 1964.

[140] G. Dehlinger, L. Diehl, U. Gennser, H. Sigg, J. Faist, K. Ensslin, D. Grützmacher, and E. Müller. Intersubband electroluminescence from silicon-based quantum cascade structures. *Science*, 290:2277–2280, 2000.

[141] L. Pfeiffer, K.W. West, H.L. Storner, and K.W. Baldwin. Electron mobilities exceeding 10^7 cm^2/v s in modulation-doped gaas. *Appl. Phys. Lett.*, 55(18):1888–1890, 1989.

[142] C. Pflügl, W. Schrenk, S. Anders, G. Strasser, C. Becker, C. Sirtori, Y. Bonetti, and A. Muller. High-temperature performance of gaas-based bound-to-continuum quantum-cascade lasers. *Appl. Phys. Lett.*, 83(23):4698–4700, 2003.

[143] M. Rochat, M. Beck, J. Faist, U. Oesterle, and M. Ilegems. Electrically pumped terahertz quantum well sources. *Physica E*, 7(1-2):44–47, 2000.

[144] S. Blaser, M. Rochat, M. Beck, D. Hofstetter, and J. Faist. Terahertz intersubband emission in strong magnetic fields. *Appl. Phys. Lett.*, 81(1):67–69, 2002.

Appendix A

Samples parameters

The layer sequence of one period of the different samples measured during this thesis are given in the following tables, starting from the injection barrier. Also indicated are the doping levels, the nominal sheet density n_s induced by this doping and the number of periods N_p. The doped layers are underlined and the thickness of the barriers are in bold. Sample names staring with an "A" come from the Cavendish laboratory in Cambridge, UK. Samples whose identifier starts with "N" come from the inhouse MBE facility of the Faist group at the University of Neuchâtel, CH. The devices are grown in the GaAs/$Al_{0.15}Ga_{0.85}As$ material system, except for the samples N509 , which is grown in the $In_{0.52}Al_{0.48}As$-$In_{0.53}Ga_{0.47}As$ material system.

Sample	Layer sequence of one period, thickness in nm. Barriers layers are in bold, n-doped layers are underlined.	n [cm^{-3}]	n_s [cm^{-2}]	N_a [cm^{-3}]	N_p
A2672	**3.0**/18.6/**0.7**/15.4/**0.5**/13.6/**2.3**/12.8/**1.8**/ 11.8/**2.3**/10.8/**3.2**/10.4	$1.6 \cdot 10^{16}$	$3.98 \cdot 10^{10}$	$3.71 \cdot 10^{15}$	120
A2771	**3.5**/9.0/**0.6**/16.3/**0.9**/16.0/**1.0**/13.8/**1.2**/12.0/**1.5**/ 11.0/**2.4**/11.0/**3.2**/12.1	$2.5 \cdot 10^{16}$	$2.75 \cdot 10^{10}$	$2.38 \cdot 10^{15}$	120
A2985	**4.0**/12/**0.5**/22.3/**0.8**/21.5/**0.9**/17.8/**1**/14.5/**1.3**/ 13.2/**2.2**/13.4/**2.8**/17	$2.5 \cdot 10^{16}$	$3.3 \cdot 10^{10}$	$2.27 \cdot 10^{15}$	120
A2986	**4.2**/9.0/**0.6**/16.3/**0.9**/16.0/**1.0**/13.8/**1.2**/12.0/**1.5**/ 11.0/**2.4**/11.0/**3.2**/12.1	$3 \cdot 10^{16}$	$3.3 \cdot 10^{10}$	$2.83 \cdot 10^{15}$	120
N295	**4.2**/9.0/**0.6**/16.3/**0.9**/16.0/**1.0**/13.8/**1.2**/12.0/**1.5**/ 11.0/**2.4**/11.0/**3.2**/12.1	$3 \cdot 10^{16}$	$3.3 \cdot 10^{10}$	$2.83 \cdot 10^{15}$	120
N299	**4.2**/9.0/**0.6**/16.3/**0.9**/16.0/**1.0**/13.8/**1.2**/12.0/**1.5**/ 11.0/**2.4**/11.0/**3.2**/12.1	$4 \cdot 10^{16}$	$4.4 \cdot 10^{10}$	$3.78 \cdot 10^{15}$	120
N301	**4.2**/9.0/**0.6**/16.3/**0.9**/16.0/**1.0**/13.8/**1.2**/12.0/**1.5**/ 11.0/**2.4**/11.0/**3.2**/12.1	$6 \cdot 10^{16}$	$6.6 \cdot 10^{10}$	$5.68 \cdot 10^{15}$	120
N310	**4.2**/9.0/**0.6**/16.3/**0.9**/16.0/**1.0**/13.8/**1.2**/12.0/**1.5**/ 11.0/**2.4**/11.0/**3.2**/12.1	$8 \cdot 10^{16}$	$8.8 \cdot 10^{10}$	$7.57 \cdot 10^{15}$	120
N464	**4.6**/10.5/**0.8**/12.3/**2.0**/11.2/**2.7**/9.3/**3.0**/ 19.1/**2.7**/14.5	$6 \cdot 10^{16}$	$11.4 \cdot 10^{10}$	$12.2 \cdot 10^{15}$	120
N465	**4.6**/10.5/**0.8**/12.3/**2.0**/11.2/**2.7**/9.3/**3.0**/ 19.1/**2.7**/14.5	$3 \cdot 10^{16}$	$5.7 \cdot 10^{10}$	$6.1 \cdot 10^{15}$	120
N509	**1.9**/15.5/**0.3**/26.0/**0.4**/21.0/**0.6**/17.5/**0.8**/16.0/**1.0**/ 28.0	$2.2 \cdot 10^{16}$	$6.16 \cdot 10^{10}$	$4.77 \cdot 10^{15}$	70

Table A.1: Layer sequence of THz QC samples.

Published work

1. S. Blaser, M. Rochat, **L. Ajili**, M. Beck, J. Faist, H. Beere, A. Davies, E. Linfield, and D. Ritchie, Terahertz interminiband emission and magneto-transport measurements from a quantum cascade chirped superlattice, Physica E **13**, 854–857 (2002).

2. M. Rochat, **L. Ajili**, H. Willenberg, J. Faist, H. Beere, G. Davies, E. Linfield and D. Ritchie, Low-threshold terahertz quantum-cascade lasers, Appl. Phys. Lett. **81**, 1381–1383 (2002).

3. **L. Ajili**, G. Scalari, D. Hofstetter, M. Beck, J. Faist, H. Beere, G. Davies, E. Linfield, and D. Ritchie, Continuous-wave operation of far-infrared quantum cascade lasers, IEE Elect. Lett. **38**, 1675-1676 (2002).

4. G. Scalari, S. Blaser, M. Rochat, **L. Ajili**, H. Willenberg, D. Hofstetter, J. Faist, H. Beere, A. Davies, E. Linfield and D. Ritchie, Low threshold THz QC lasers in strong magnetic field, Proceeding of the 26th International Conference on the Physics of Semiconductors, CD– (2002).

5. **L. Ajili**, G. Scalari, H. Willenberg, D. Hofstetter, M. Beck, J. Faist, H. Beere, G. Davies, E. Linfield, and D. Ritchie, Continuous wave operation of far-infrared quantum cascade lasers, Proceedings of the 29th International Symposium on Compound Semiconductors, 439–442 (2003).

6. G. Scalari, **L. Ajili**, J. Faist, H. Beere, E. Linfield, D. Ritchie, and G. Davies, Far-infrared ($\lambda \simeq 87\mu$m) bound-to-continuum quantum-cascade lasers operating up to 90 K, Appl. Phys. Lett. **82**, 3165–3167 (2003).

7. G. Scalari, S. Blaser, **L. Ajili**, J. Faist, H. Beere, E. Linfield, D. Ritchie, and G. Davies, Population inversion by resonant magnetic confinement in terahertz quantum-cascade lasers, Appl. Phys. Lett. **83**, 3453–3455 (2003).

8. G. Scalari, S. Blaser, **L. Ajili**, M. Rochat, H. Willenberg, D. Hofstetter, J. Faist, H. Beere, G. Davies, E. Linfield, and D. Ritchie, Population inversion enhancement by resonant magnetic confinement in THz quantum cascade lasers, Proceedings of the 29th International Symposium on Compound Semiconductors, 371–374 (2003),

9. **L. Ajili**, G. Scalari, J. Faist, H. Beere, E. Linfield, D. Ritchie, and G. Davies, High power quantum-cascade lasers operating at $\lambda \sim 87$ and 130 μm, Appl. Phys. Lett. **85**, 3986–3988 (2004),

10. S. Barbieri, J. Alton, H. Beere, E. Linfield, D. Ritchie, S. Whithington, G. Scalari, **L. Ajili**, and J. Faist, Heterodyne mixing of two far-infrared quantum cascade lasers by use of a point-contact Schottky diode, Opt. Lett. **29**, 1632–1634 (2004),

11. J. Faist, **L. Ajili**, G. Scalari, M. Giovannini, M. Beck, M. Rochat, H. Beere, G. Davies, E. Linfield, and D. Ritchie, Terahertz quantum cascade lasers, Philos. T. Roy. Soc. A **362**, 215–229 (2004),

12. D.C. Larrabee, G.A. Khodaparast, F.K. Tittel, J. Kono, G. Scalari, **L. Ajili**, J. Faist, H. Beere, G. Davies, E. Linfield, D. Ritchie, Y. Nakajima, M. Nakai, and S. Sasa, Application of terahertz quantum-cascade lasers to semiconductor cyclotron resonance, Opt. Lett. **29**, 122–124 (2004),

13. **L. Ajili**, J. Faist, H. Beere, E. Linfield, D. Ritchie, and G. Davies, Loss-coupled distributed feedback far-infrared quantum cascade lasers, IEE Elect. Lett. **41**, 419–420 (2005),

14. **L. Ajili**, G. Scalari, N. Hoyler, M. Giovannini, and J. Faist, InGaAsAlInAs/InP terahertz quantum cascade laser, Appl. Phys. Lett. **87**, 141107-1–141107-3 (2005),

15. H. Beere, J. Fowler, J. Alton, E. Linfield, D. Ritchie, R. Kohler, A. Tredicucci, G. Scalari, **L. Ajili**, J. Faist, S. Barbieri, MBE growth of terahertz quantum cascade lasers, J. Cryst. Growth **278**, 756–764 (2005),

16. D. Chamberlin, P. Robrish, W. Trutna, G. Scalari, M. Giovannini, **L. Ajili**, J. Faist, H. Beere, and D. Ritchie, Dual-wavelength THz imaging with quantum cascade lasers, Proc. SPIE **5727**, 107–114 (2005),

17. D. Chamberlin, P. Robrish, W. Trutna, G. Scalari, M. Giovannini, **L. Ajili**, and J. Faist, Imaging at 3.4 THz with a quantum-cascade laser, Appl. Opt. **44**, 121–125 (2005),

18. G. Scalari, S. Blaser, L. Sirigu, M. Graf, **L. Ajili**, J. Faist, H. Beere, E. Linfield, D. Ritchie, and G. Davies, Terahertz quantum cascade laser emitting at 160 μm in strong magnetic field, AIP Conference Proceedings, 27th International Conference on the Physics of semiconductors (ICPS-27) **772**, 1573–1574 (2005),

19. **L. Ajili**, G. Scalari, N. Hoyler, M. Giovannini, and J. Faist, Doping in quantum cascade lasers. II. GaAs/$Al_{0.15}Ga_{0.85}As$ terahertz devices, J. Appl. Phys. **100**, 043102-1–043102-3 (2006),

20. Fabrizio R. Giorgetta, E. Baumann, M. Graf, **L. Ajili**, N. Hoyler, M. Giovannini, J. Faist, D. Hofstetter, P. Krtz, and G. Sonnabend, 16.5 μm quantum cascade detector using miniband transport, Appl. Phys. Lett. **90**, 231111 (2007),